Computational Modelling in Bio-Based Heterogeneous Catalysis

Max Quayle

A thesis submitted for the degree of
Doctor of Philosophy.

Cardiff University

September 2025

Summary

Since the advent of the Industrial Revolution, the cost of society's dependence on fossil fuels has only continued to grow. For humanity to have any hope of outgrowing its reliance on non-renewable feedstocks, it is critical that the mechanistic chemistry behind heterogeneous catalysis is properly understood so that sustainable catalytic processes may be developed. In the hope of contributing towards this goal, this thesis is a comprehensive computational study of the catalytic conversion of bio-based platform molecules. Particular emphasis has been devoted to the hydrogenation, reductive amination, and pyrolysis of biomass derivatives over platinum group metal and metal oxide catalysts. By constructing density functional theory (DFT) models of key intermediates and their associated transition states, accessible pathways for the hydrogenation of both the chain C=C bond and furanic ring system of the furfural derivative ALD-1 were identified over Pd(111). In agreement with experiment, chain hydrogenation was shown to be facile over Pt(111) and Ru(0001), but not ring hydrogenation. Partial charge analysis revealed that the distribution of electron density across the adsorbate played a critical role in the selectivity of these catalysts. This work was then extended to the reductive amination of furfural derivatives over Pd(111) and Ru(0001), where accessible mechanisms were identified for the formation and hydrogenation of imine intermediates. A final DFT study on the ceria-catalysed pyrolysis of sinapic acid (SA) confirmed that the disappearance of C=O and O–H vibrational modes in experimental infrared spectra was caused by SA's decarboxylation to 4-vinylsyringol. By complementing all calculations with experimental data, it is the hope of the author that this thesis will help inform the development of sustainable syntheses and deepen our collective understanding of bio-based heterogeneous catalysis.

Publications

Chapter 3

M. Quayle, Z. Wu, M. Pera-Titus, and A. Roldan. *Mechanistic Insights Into the Catalytic Hydrogenation of Furfural Derivatives over Pd and Ru Surfaces.* J. Catal. **2026**. Manuscript has been accepted for publication.

Chapter 5

T. Kulik, N. Nastasiienko, B. Palianytsia, M. Quayle, A. Nastasiienko, P. R. Davies, D. Wass, and A. Roldan. *Catalytic Pyrolysis of Sinapic Acid on Nanoceria: Surface Complexes, Valorisation of Products, Experimental, and Atomistic Approaches.* ChemSusChem. **2025**, 19, (1), e202501249. https://doi.org/10.1002/cssc.202501249

Other Publications During PhD

• F. Morteo-Flores, M. Quayle, A. Salom-Català, M. Pera-Titus, and A. Roldan. *First-Principles Microkinetic Study of the Catalytic Hydrodeoxygenation of Guaiacol on Transition Metal Surfaces.* ChemCatChem. **2023**, 15 (24), e202301549. https://doi.org/10.1002/cctc.202300671

• C. Squarzoni, N. Kania, M. Dearg, M. Quayle, H. Hu, T. J. A. Slater, A. Folli, A. Roldan, M. Pera-Titus, and A. Ponchel. *Nanoceria as an Efficient and Cost-Effective Metal-Free Catalyst for the Oxidation of Alcohols.* ACS Sustainable Chem. Eng. **2025**, 13 (39), 16348-16363. https://doi.org/10.1021/acssuschemeng.5c05061

• Y. Li, Y. Zhou, M. Quayle, S. An, A. Roldan, and X. Xia. *Defect Modified Mo-based MXenes for HER Application: A DFT Study.* Phys. Chem. Chem. Phys. **2025**. Manuscript has been submitted for publication.

Acknowledgements

First and foremost, I would like to thank my supervisors, Alberto Roldan and Marc Pera-Titus. Your guidance, support, and inexhaustible reservoirs of patience were pillars of support throughout my studies, and I am honoured to have had the opportunity to learn from the example of such brilliant researchers.

Among the scientists I've had the privilege of working with at Cardiff, I would like to pay special tribute to Anu Bala, Hermione Beer, Cameron Beevers, Owain Beynon, Alexandre Boucher, Gabriel Bramley, Amit Chaudhari, Maicon Delarmelina, Andrea Folli, Eva Ford, Ola Gorecka, Alejandro Gracia Gil, Avalon Halgreen, Akash Hiregange, Mohammad Islam, Lara Kabalan, Igor Kowalec, Tetiana Kulik, Stefano Leoni, Shumin Li, Andrew Logsdail, Xiuyuan Lu, Zhongwei Lu, Eimear McCarthy, Fabian Morteo-Flores, James Platts, Lucas Rivera Blair, Matthew Robinson, Antoni Salom-Català, Maciej Sikora, Pavel Stishenko, Oscar Van Vuren, David Vázquez Parga, Jack Warren, David Willock, and Zhuoli Wu. This thesis would have never seen the light of day without your invaluable help.

In addition, I would like to thank Mahmoud Akhtar, Heather Amos, Bethan King, Caru Shanahan, George Summers, Richard Webb, and the rest of the administrative team at the School of Chemistry for four years of tireless support. Completing this thesis with COVID lurking in the shadows would have been a waking nightmare without your hard work behind the scenes, and I will always appreciate your collective efforts in keeping both students and staff safe throughout the pandemic.

For helping fund my research, I would like to thank the UKRI Interdisciplinary Centre for Circular Chemical Economy and the Isle of Man Department of Education, Sport, and Culture. In particular, I would like to thank Helen Ward for her invaluable help with my PhD stipend. I would also like to thank Supercomputing Wales, the Materials and Molecular Modelling Hub, and the Materials Chemistry Consortium (MCC) for providing me with the computational resources and technical support necessary to complete this thesis.

For keeping me sane throughout my studies, there are three friend groups I would like to thank. First, from the Isle of Man: Peter Daniels, Juan Mercer, Callum Nickson, Marc Swales, and George Willoughby. Second, from across the Irish Sea and beyond: Jacob Bradford-Parker, Conal Carleton, Maisie Carter, Jordan Casstles, and Leo Forde. And third, from the darkest corners of the Celtic world, where neither man nor beast dare tread (especially Peel): Keenan Allen, Sinéad Allen, Peter Daniels (again), and Zach Long. The stories we have weaved together will stay with me for the rest of my life, and I thank you all for accepting a perpetually sleep-deprived chemist as one of your own.

Finally, I would like to dedicate this thesis to those I love more than mere words could ever fully express. To Mum, Dad, Amy, Alfie, and my darling fiancée, Phos. For everything.

“Just because you can explain it doesn’t mean it’s not still a miracle.”
— Terry Pratchett

Contents

Figures

Schemes

Abbreviations

AO	Atomic orbital
bcc	Body-centred cubic
BOA	Born-Oppenheimer approximation[1]
CI-NEB	Climbing image nudged elastic band method of Henkelman *et al.*[2]
DDEC6	Density Derived Electrostatic and Chemical net atomic charge approach, 6th version[3,4]
DFT	Density functional theory
DFT-D3(0)	Zero-damped D3 dispersion correction of Grimme *et al.*[5]
DOS	Density of states
DTA	Differential thermal analysis
E1	Unimolecular elimination
E2	Bimolecular elimination
FCA	Frozen core approximation
fcc	Face-centred cubic
FT-IR	Fourier transform infrared spectroscopy
GGA	Generalised gradient approximation
hcp	Hexagonal close-packed
HDO	Hydrodeoxygenation
IR	Infrared
KS-DFT	Kohn-Sham density functional theory[6]
LDA	Local density approximation
LSDA	Local spin density approximation
MEP	Minimum energy pathway
ML	Machine learning
MO	Molecular orbital
MP2	Second-order Møller–Plesset perturbation theory[7]
NAC	Net atomic charges
NEB	Nudged elastic band method
NIST	National Institute of Standards and Technology
PBE	Perdew, Burke, and Ernzerhof functional[8]
PDOS	Projected density of states
PES	Potential energy surface
PGM	Platinum group metals

PW91	Perdew-Wang functional of 1991[9]
QMC	Quantum Monte-Carlo
revPBE	Revised Perdew, Burke, and Ernzerhof functional of Zhang and Yang[10]
RIXS	Resonant inelastic X-ray scattering
RPA	Random phase approximation of Langreth and Perdew[11]
RPBE	Revised Perdew, Burke, and Ernzerhof functional of Hammer *et al.*[12]
S_N2	Bimolecular nucleophilic substitution
TGA	Thermogravimetric analysis
THFA	Tetrahydrofurfuryl alcohol
TPD-MS	Temperature programmed desorption-mass spectrometry
TS	Transition state
TST	Transition state theory
TZ	Triazole
VASP	Vienna Ab Initio Simulations Package[13,14]
XAS	X-ray absorption spectroscopy
ZPE	Zero-point energy

Mathematical Symbols

A	Surface area
$\boldsymbol{a_1}, \boldsymbol{a_2}, \boldsymbol{a_3}$	Primitive lattice vectors in real space
a, b, c	Lattice constants
B	Bulk modulus
$\boldsymbol{b_1}, \boldsymbol{b_2}, \boldsymbol{b_3}$	Reciprocal lattice vectors
C_{LO}	Lieb-Oxford constant[15]
C_n^{AB}	nth-order dispersion coefficient based on the atomic charge and polarisability of atoms A and B
c	Speed of light in a vacuum ≈ 2.9979×10^8 m s^{-1}
$D(E)$	Density of states for an electron in a solid with energy E
$d_n^{D3(0)}$	DFT-D3(0) damping function[5]
E	Energy
E_*	Ground-state energy of a naked surface
$E[\rho]$	Kohn-Sham electron density functional[6]
E_{ads}	Adsorption energy
E_{BLK}	Ground-state energy of bulk material
$E_C^f[\rho]$	Correlation energy of functional f

$E_{disp}^{D3(0)}$	DFT-D3(0) pairwise corrective term[5]
$E_{dc}[\{n\}]$	DFT+U double counting functional
$E_{DFT+U}[\rho]$	DFT+U functional
E_F	Fermi level
E_G	Band gap
E_{HF}	Hartree-Fock energy[16,17]
$E_{Hub}[\{n\}]$	Hubbard model functional
E_{SUR}	Ground-state energy of the relaxed surface
$E_X^f[\rho]$	Exchange energy of functional f
$E_{XC}^f[\rho]$	Exchange-correlation energy of functional f
E_Y	Ground-state energy of an unbound compound Y
E_{Y*}	Ground-state energy of adsorbate Y bound to a surface
e	Euler's number ≈ 2.7183
$\boldsymbol{e}$	Elementary charge ≈ 1.6022×10^{19} C
$F(g_X)$	PBE enhancement factor[8]
$F_{i,d}$	Force exerted on atom i following a displacement along Cartesian direction d
G	Gibbs free energy
g_C	PBE gradient parameter[8]
$\widehat{H}$	Hamiltonian operator
$\mathbf{H}$	Hessian
$\mathbf{H}_{\boldsymbol{mw}}$	Mass-weighted Hessian
$\hat{h}_i$	Kohn-Sham one-electron operator
I	Infrared intensity
i	$\sqrt{-1}$
J	DFT+U exchange parameter
$\boldsymbol{k}$	$\boldsymbol{k}$ point / wave vector
m	Magnetic moment
m/z	Mass-to-charge ratio
$\bar{\boldsymbol{N}}$	Dimer method correction vector[18,19]
N_1, N_2, N_3	Monkhorst-Pack subdivisions
$n_i = n_i^{\uparrow} + n_i^{\downarrow}$	Number of spin-up electrons plus the number of spin-down electrons possessed by atom i
n_{pd}	Particle density
$O(f(x))$	Big O algorithmic scaling factor of $f(x)$
p	Pressure
$\boldsymbol{p}(i \times j \times k)$	Periodic slab model with i, j, and k repetitions of the unit cell along the x-, y-, and z-axes, respectively
Q	Normal mode coordinates
$\boldsymbol{q}$	Position vector corresponding to a dimer method[18,19] trial structure
q_A	Net atomic charge of atom A

R_{AB}	Distance between atoms A and B
R_{AB}^{cut}	DFT-D3(0) cut-off radius[5]
$\boldsymbol{r}$	Position
r_s	Wigner-Seitz radius
$\hat{S}$	Spherical averaging operator
S_e	Spin-degeneracy factor
s_n	DFT-D3(0) global scaling parameter[5]
T	Temperature
T_{ni}	Kinetic energy of non-interacting electrons
U	DFT+U Coulombic parameter
U_{eff}	DFT+U effective Coulombic parameter ($U - J$)
$u(\boldsymbol{r})$	Periodic phase factor for Bloch wave functions[20]
$\boldsymbol{u}_{\xi}$	Dimer axis[18,19]
V_{cell}	Unit cell volume
V_{ee}	Classical electron-electron repulsion potential
V_F	Final volume
V_I	Initial volume
V_{ne}	Nuclear-electron interaction
V_{XC}	Exchange correlation potential
$w^{DDEC6}(\boldsymbol{r})$	DDEC6 weight function[3,4]
$X_{i,d}$	ith eigenvector along Cartesian direction d
Z_k	Atomic number of the kth nucleus
z_A	Nuclear charge of atom A
α_n	DFT-D3(0) steepness parameter[5]
Γ	Gamma point
γ	Surface energy
Δ	Change of a variable (e.g. $\Delta G =$ change in Gibbs free energy)
δ_{ij}	Kronecker relation of i and j
$\delta(x)$	Dirac delta function
$\varepsilon_n(\boldsymbol{k})$	One-electron energy eigenstate at energy level n
ε_X	"Extra" term integrated alongside the local electron density when calculating the exchange energy
ϵ	Dimer method step size[18,19]
ζ	Relative degree of spin polarisation
κ	PBE[8] and RPBE[12] gradient constant = 0.804
μ	PBE[8] and RPBE[12] gradient constant = 0.220
ν_i	ith vibrational mode
π	Pi ≈ 3.1416
ρ	Electron density

$\rho_{\uparrow}(\boldsymbol{r})$ and $\rho_{\downarrow}(\boldsymbol{r})$	Density of spin-up electrons and spin-down electrons, respectively
$\rho_A(\boldsymbol{r}_A)$	Local electron density of atom A at position $\boldsymbol{r}_A$
$\rho_A^{ion}(\boldsymbol{r})$	Reference electron density for atom A
ϕ_1	Dimer method rotation angle, initial step[18,19]
ϕ_{min}	Dimer method rotation angle, minimisation[18,19]
χ_i	Molecular orbital occupied by the ith electron
χ_P	Pauling electronegativity[21]
ψ	Time-independent wave function
Ω	Scalar triple product
∇_i^2	Laplacian with respect to the coordinates of the ith electron
$\nabla\rho$	Gradient of the electron density
$\mathbf{1}$	Identity matrix

Compounds

Abbreviation	Name	Structure
4VS	4-vinylsyringol	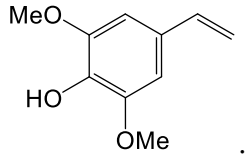
ALD-1	(*E*)-1-(furan-2-yl)-5-methylhex-1-en-3-one	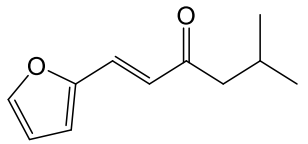
ALD-2	1-(furan-2-yl)-5-methylhexan-3-one	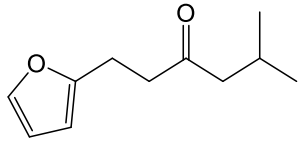
ALD-3	5-methyl-1-(tetrahydrofuran-2-yl)hexan-3-one	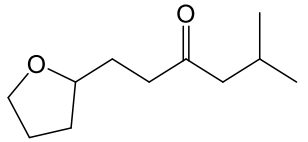
EtOAc	ethyl acetate	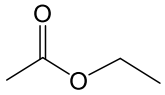
MIBK	methyl isobutyl ketone	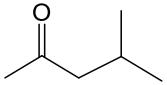
SA	sinapic acid	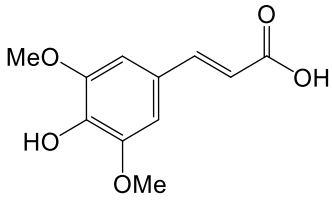

1. Introduction

Synthetic chemistry has a crisis on its hands. Humanity's dependence on non-renewable feedstocks such as petroleum and natural gas has come at a grave environmental cost. If current consumption trends are not reversed, the planet's reserves of fossil fuels are expected to be depleted within the next hundred years.[22] Chemists no longer have the luxury of waiting for the problem to fix itself. Renewable alternatives to traditional feedstocks must be developed if synthetic chemistry as we know it is to survive.

This chapter begins with a brief introduction on the properties and uses of biomass and its derivatives in **Section 1.1**. This is followed by a review of prominent materials in heterogeneous catalysis in **Section 1.2**. A review on the role of computational modelling in contemporary catalysis research is provided in **Section 1.3.** A discussion of bio-based catalysis in industry is given in **Section 1.4**. Finally, a broad structural outline of the thesis as a whole is provided in **Section 1.5**.

1.1. Biomass

Biomass, broadly defined as non-fossilised matter derived from living organisms,[23] is one of the most abundant sources of renewable platform chemicals known to the physical sciences. Unlike fossil fuels, which take millions of years to replenish, biomass can be regenerated on human timescales, offering a sustainable source of hydrocarbons that can then be processed into fuels, solvents, and high-value platform chemicals.[24–27]

While an exhaustive list of biomass sources would be impossible to compile, a selection of common examples is provided in **Figure 1.1**. Aquatic sources of biomass such as algae and seaweed can be used to synthesise textile dyes.[28,29] The waste and carcasses of animals in the livestock industry are valuable sources of fertilisers,[30,31] fuel,[32,33] and adhesives.[34] Bio-based waste generated by factories and urban settlements can be used to manufacture paper products,[35,36] polymers,[37] and cosmetic items such as shampoos.[38]

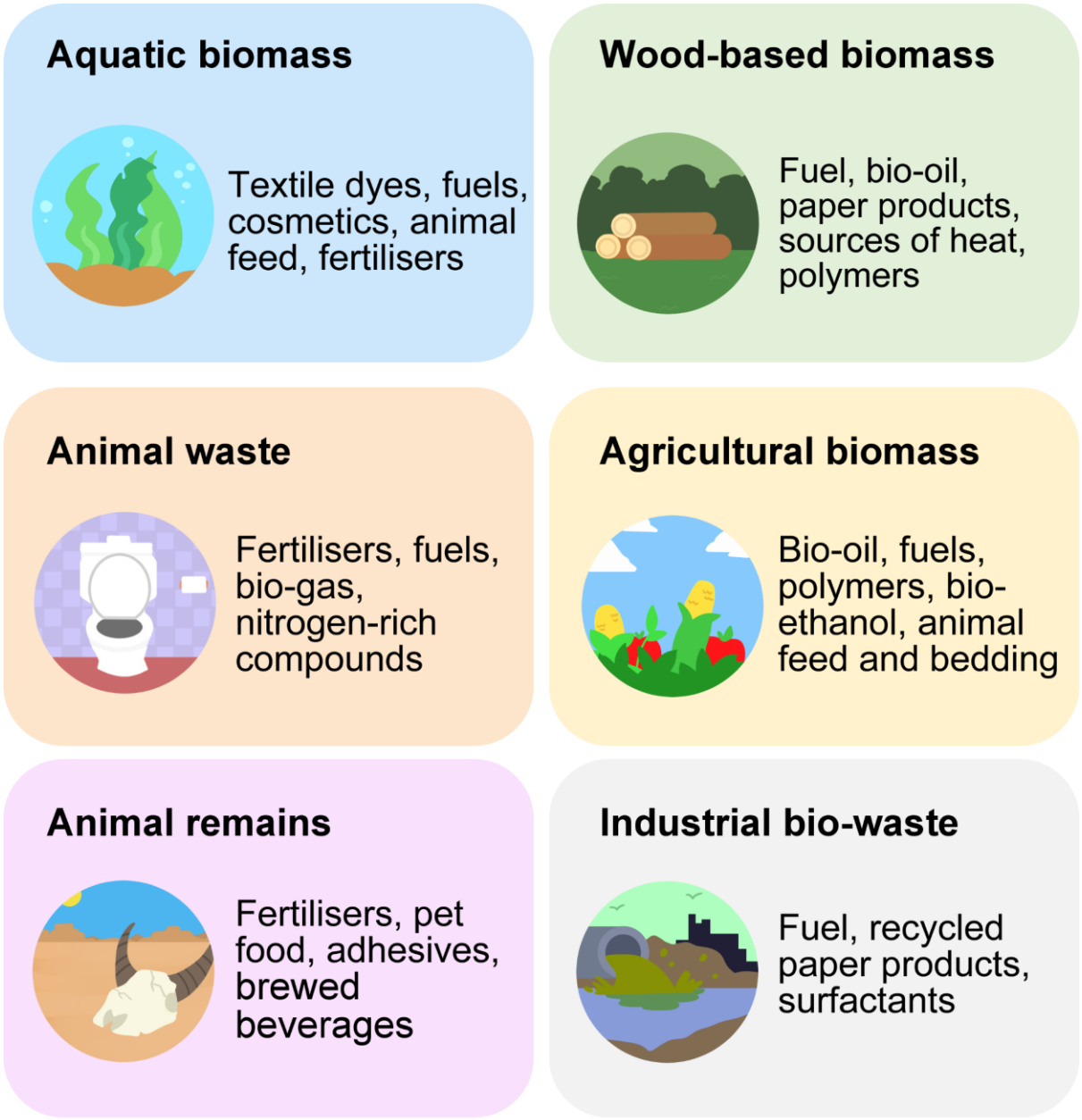

Figure 1.1. Selection of biomass sources and uses.

Two particularly abundant sources of high-value feedstocks are wood-based biomass (e.g. sawdust, branches, leaves, lumber shavings) and biomass from the agricultural sector (e.g. fruit and vegetable waste, straw, crop husks). Large quantities of wood-based biomass are generated as by-products of the forestry, construction, and printing industries. While the most widespread and traditional use of both resources has been direct combustion for heat,[39] the chemical composition of wood-based and agricultural biomass allows for the generation of a wide selection of useful and valuable compounds. Both materials can be transformed into bio-oil, a liquidised natural feedstock used as a fuel and as a source of monomers for the production of

plastics.[40–42] Synthetic chemists have learned to exploit the high quantities of lignocellulose (**Section 1.1.2**) present in both wood-based and agricultural biomass, allowing for the generation of solvents,[24,43] platform chemicals,[44] and medicinal compounds.[45,46]

1.1.1. Furfural

One example of a platform chemical that can be synthesised from agricultural biomass is furfural, a colourless, almond-scented liquid commonly used as a precursor in organic synthesis.[47,48] In many ways, furfural is a model reagent for sustainable catalysis. It is relatively easy to store and transport, it can be recovered inexpensively and renewably from cereal grains, and cheap ways to extract it from food waste have been known since the 1920s.[49–51] While freshly prepared furfural will darken and discolour if exposed to oxygen over long periods of time, this process is slow and can be easily mitigated by storing furfural under its own vapour pressure immediately after distillation.[48,52]

Furfural and its derivatives play a critical role in modern industrial chemistry. As shown in **Scheme 1.1**, furfural can be hydrogenated to furfuryl alcohol, a crucial component in the production of rocket fuel and dyes in the textile industry.[53–55] It can also be oxidised to both maleic acid, a precursor to polyester resins in the automotive industry,[56] and 2-furoic acid, a compound used in the production of renewable flavouring agents.[57,58] Furthermore, furfural's ring system allows it to participate as a diene in Diels-Alder reactions; a property that can be exploited by synthetic chemists to generate high-value feedstocks such as benzaldehyde.[59,60]

Furfural readily partakes in aldol condensation reactions through its aldehyde group,[47,61,62] allowing for the formation of a wide variety of unsaturated derivatives. These compounds have proven to be highly receptive to reductive amination, a family of reactions in which carbonyls are reduced to amines via imine intermediates.[47,63] Advances in the field of synthetic organic chemistry have shown that the yield and stereochemistry of amines produced in this fashion can be optimised with great precision. For instance, it was shown in 2019 by Jiang *et al.*[64] that a family of THF-derived amines could be synthesised from furfural derivatives using NH_3 and molecular hydrogen over a Pd/Al_2O_3 catalyst. In the same year, Yuan *et al.*[63] showed similar success using the furfural derivative 5-hydroxymethylfurfural (HMF) as a starting reagent and Ni_6AlO_x as a recyclable catalyst.

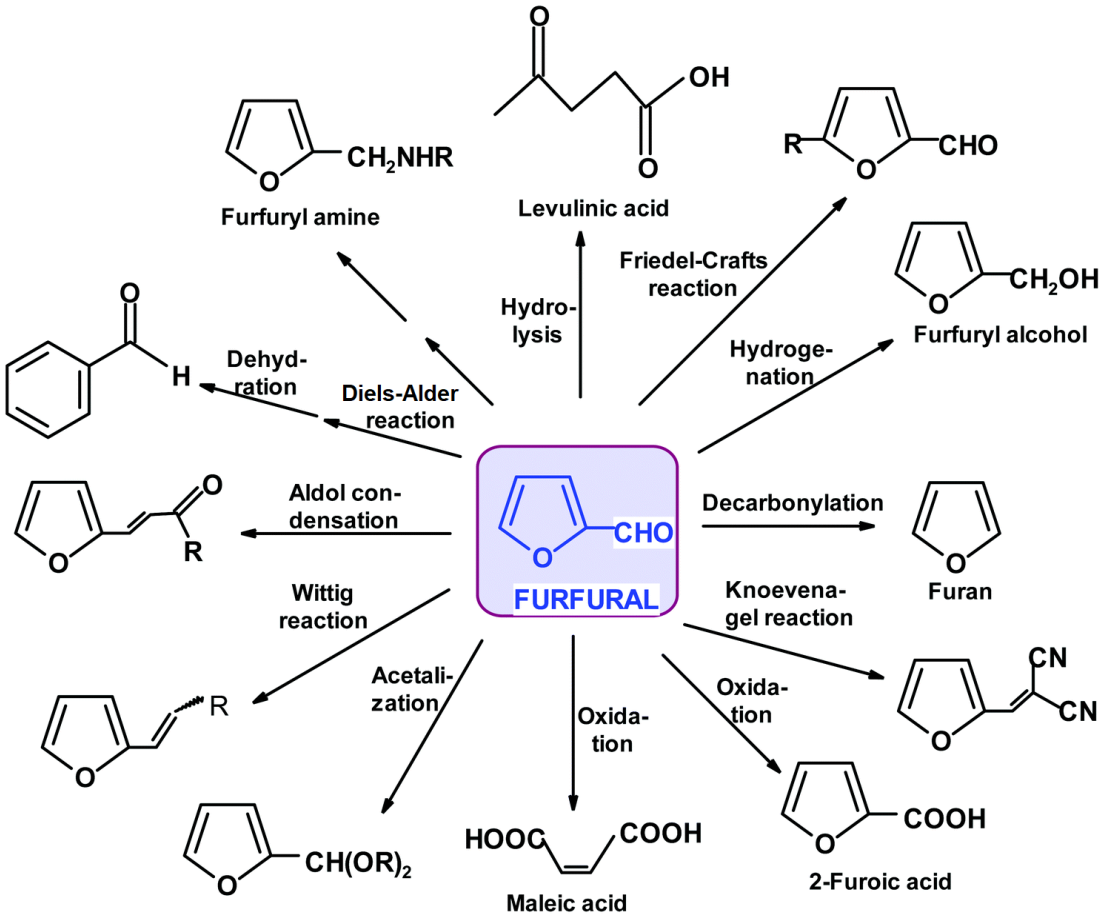

Scheme 1.1. Furfural and a selection of its most common derivatives. Adapted from Bielski and Grynkiewicz (2021).[59]

1.1.2. Lignocellulosic Biomass

Lignocellulose, the primary structural component of plant cell walls, is a highly abundant source of bio-based platform chemicals. Due to lignocellulose's presence in every species of plant with a vascular system,[65] unprocessed lignocellulosic biomass has a cost close to zero, and it can be cheaply refined into valuable feedstocks. Since at least 2005,[27] ethanol derived from lignocellulose has had a lower purchase cost than petroleum,[24,26] and as fossil fuel supplies continue to dwindle, it is likely that its affordability will only increase over time.

The exact composition of lignocellulosic biomass varies from plant to plant, but it typically consists of three major components: (1) cellulose, a linear structural polymer that prevents cell walls from collapsing in on themselves;[66] (2) hemicellulose, an amorphous heteropolymer composed of a wide variety of sugar residues; and (3) lignin, a class of phenolic polymers that fortifies the strength and hardness of the cell

walls, protects the plant from UV radiation, and facilitates the transport of water and salt in the plant's vascular system.[67–70]

The differences in chemical composition between these three materials is reflected in how varied their applications are in industry. The sugars in cellulose and hemicellulose can be fermented into biofuels[24,66] and used as feedstocks for the synthesis of biodegradable polymers.[71] The composition of lignin is highly dependent on the species, age, and part of the plant that it's sourced from,[72] but it has gained recognition as a valuable and renewable source of aromatic compounds such as sinapic acid (SA), an unsaturated ketone found in fruit[73,74] with potent antioxidant properties[75] that is being investigated as a treatment for Alzheimer's and Parkinson's disease.[76] Lignin's amorphous structure makes it a challenging material to computationally model (**Section 1.3**), but model compounds such as SA can be used in such simulations to gain valuable insights into lignin's chemical properties.

1.2. Heterogeneous Catalysis

Alongside the search for renewable organic feedstocks, much attention has been directed towards the development of heterogeneous catalysts for biomass processing and refinement. For humanity to have any hope of moving towards a society in which high-value chemicals can be sustainably produced on an industrial scale, the art and science of catalyst development must be mastered. Platinum group metals (PGMs) such as Pd, Pt, and Ru have proven especially popular in the field of heterogeneous catalysis. Each of these elements offers a unique blend of activity, selectivity, and stability, leading to an outpour of research on their catalytic properties. While the CO_2 emissions associated with the mining and processing of PGMs must be accounted for in any life-cycle analysis of a catalytic process,[77] a substantial portion of the negative environmental impact is generally offset by the durability and reusability of PGMs, as well as the ease with which they can be recovered from scrap metal.[78] For over a decade, recycling processes for spent PGM catalysts have existed with recovery rates as high as 95%,[79,80] and due to the pressing economic demand for PGMs in the electronic and automotive sectors,[81,82] it is likely that the efficiency of these processes will increase as the Earth's supplies of PGM-bearing ore dwindle.

1.2.1. Pd

Of all the elements in the d-block, Pd has proven to be one of the most popular heterogeneous catalysts for hydrogenation[83–86] and C–C cross coupling.[87–89] In the context of biomass processing, Pd catalysts have shown exceptional selectivity and activity in the hydrogenation of furfural and its derivatives,[47,64,90] as well as other platform chemicals derived from biomass.[86,91,92]

As reported by Alibegovic *et al.*[93] (**Scheme 1.2**), composite Pd-Fe_3O_4 nanoparticles are highly selective catalysts for the hydrogenation of furfural to furfuryl alcohol, with both selectivity and conversion exceeding 99%. Pd has also proven especially useful as a component in reductive amination catalysts due to its ability to activate molecular hydrogen and ammonia,[94,95] allowing for the sustainable production of amines of a high value in the agricultural and pharmaceutical sectors.[96–98]

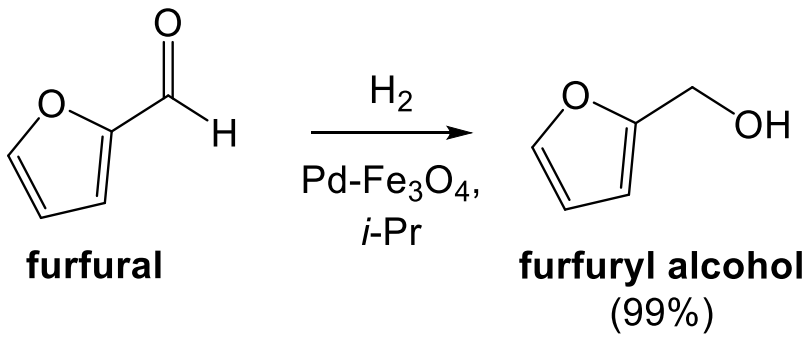

Scheme 1.2. Hydrogenation of furfural to furfuryl alcohol over Pd-Fe_3O_4 nanoparticles.[93] Reaction conditions: *i*-propanol (48 mL), H_2 (6 MPa), 120 °C, 450 min.

1.2.2. Pt

Although Pt is less commonly used than Pd for hydrogenation catalysis, it still plays a crucial role in biomass upgrading due to its ability to facilitate deoxygenation and oxidation. Pt has been frequently utilised as a catalyst in the hydrodeoxygenation of bio-based aldehydes[99,100] and ketones,[101,102] a process used to upgrade the energy density of bio-oil (**Section 1.4**).[103] Pt is particularly adept at oxidising carbon monoxide and unburned hydrocarbons in car exhaust fumes, leading to its widespread adaption as a component in catalytic converters.[104,105] Levulinic acid, a platform chemical featured in **Scheme 1.1** that can be derived from biomass by subjecting furfural to hydrolysis,[59,106] was shown by Touchy *et al.*[107] (**Scheme 1.3**) to readily undergo solvent-free reductive amination over Pt and molybdenum oxide nanoparticles coloaded with

titania (Pt-MoO_x/TiO_2), allowing for the formation of a wide variety of five-membered heterocycles.

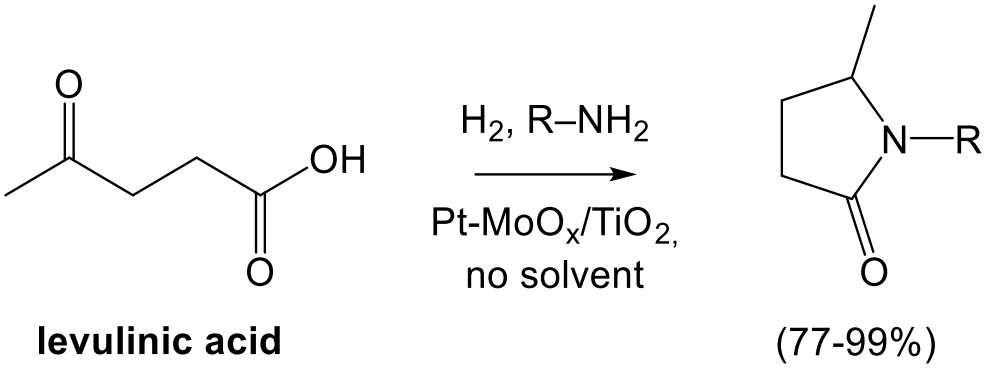

Scheme 1.3. General scheme for the solvent-free reductive amination of levulinic acid over Pt-MoO_x/TiO_2 nanoparticles.[107] Reaction conditions: Pt-MoO_x/TiO_2 (0.1 mol%), H_2 (3 bar), 100 °C, 20 h.

1.2.3. Ru

Ru has been one of the least expensive of the PGMs for at least half a decade (**Figure 1.2**),[108] making it an attractive and affordable catalyst for industrial-scale processes. Ru is particularly effective at cleaving C–O bonds[109,110] and is substantially more oxophilic than both Pd and Pt.[111] In homogeneous catalysis, Ru's oxophilicity and access to a wide range of oxidation states has been exploited to create a range of highly Lewis acidic complexes for liquid-phase catalysis.[112,113] It has also proven to be a useful and relatively inexpensive material in heterogeneous catalysis. A study by Mu *et al.*[114] on the upgrading of bio-based pyrolysis oils found that Ru was less susceptible to catalytic spoilage than Pd and Pt due to its low selectivity towards by-products associated with coke formation. Dendrimer-encapsulated Ru nanoparticles were shown by Nemanashi *et al.*[115] to be an excellent catalyst for the hydrogenation of levulinic acid to γ-valerolactone (**Scheme 1.4**), with 100% conversion and a selectivity towards γ-valerolactone exceeding 99%.

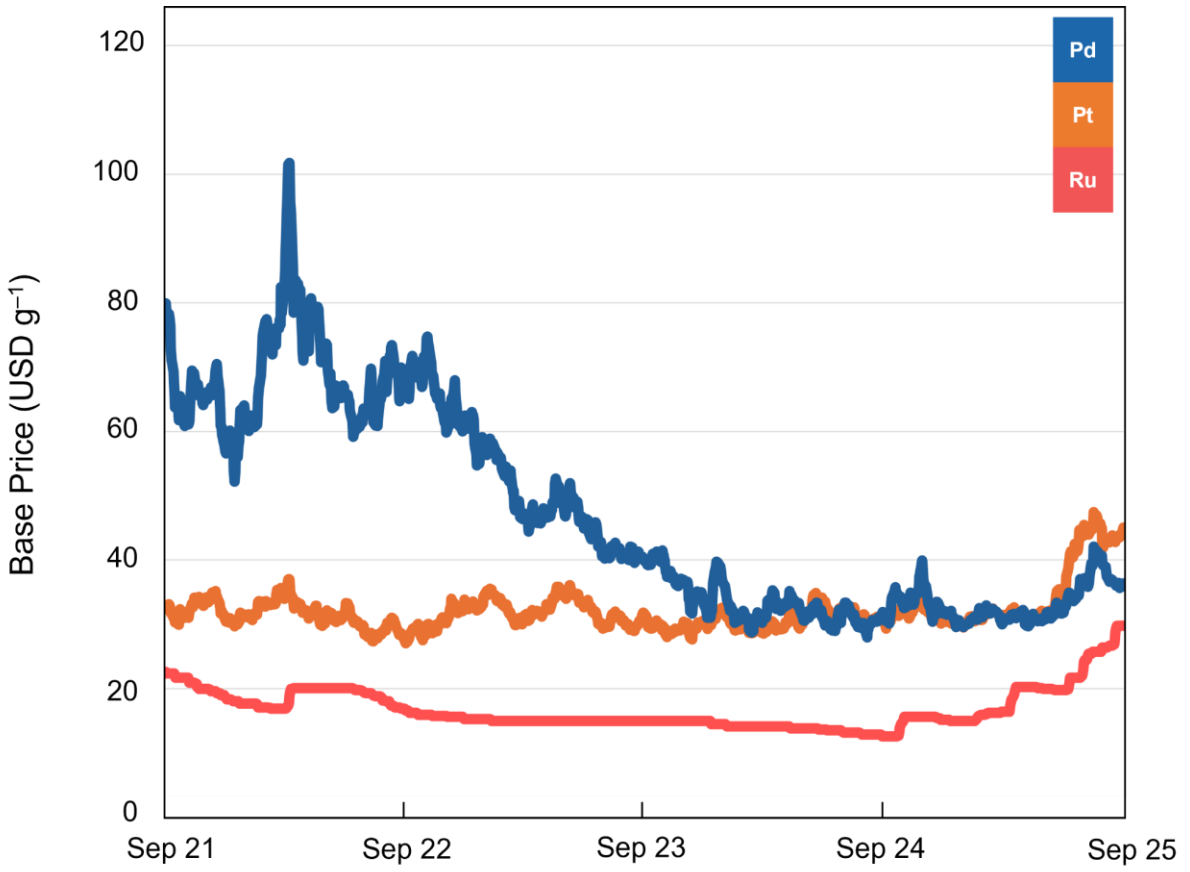

Figure 1.2. Average global base prices of Pd (blue), Pt (orange) and Ru (red) from 1 September 2021 to 1 September 2025. Data collated from the Johnson Matthey PGM price database.[108]

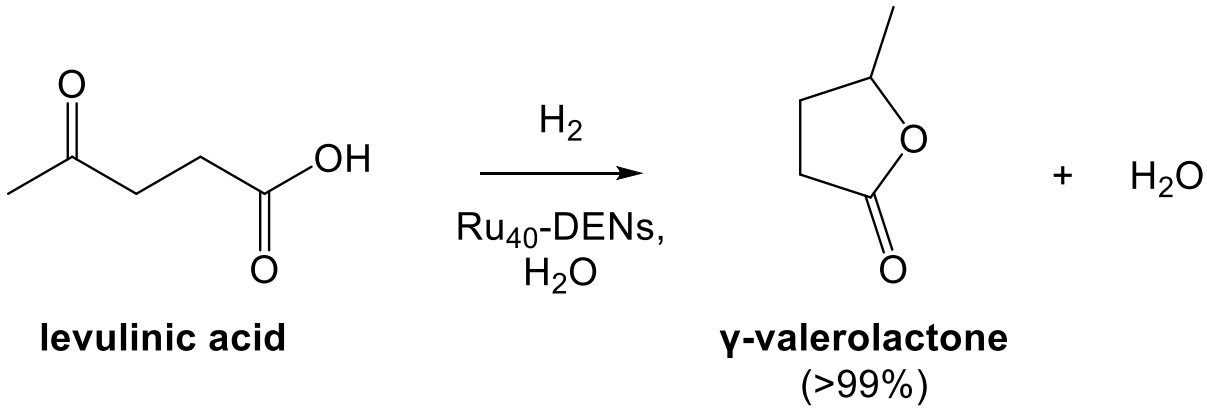

Scheme 1.4. General scheme for the catalytic hydrogenation of levulinic acid to γ-valerolactone.[115] Reaction conditions: catalyst (0.5 mol%), levulinic acid (2 mmol), H_2 (10 bar), 150 °C, 5 h.

1.2.4. Ceria

While PGMs remain the most popular materials in heterogeneous catalysis, metal oxides have also shown promise in this regard. Ceria (CeO_2) is a metal oxide that has garnered attention in recent years for its unique redox chemistry.[116–118] While historically

used as a support for transition metals,[119,120] ceria nanoparticles have shown promise as catalysts in their own right; particularly, in the field of biomass pyrolysis. Shao *et al.*[121] reported that ceria facilitates the generation of oxygenated carbonyl compounds, while Wan *et al.*[122] highlighted its ability to selectively catalyse the production of linear ketones from waste plant matter.

1.3. Computational Catalysis

The study of heterogeneous catalysis at the atomic level has been transformed over the past few decades due to the advent of computational chemistry. The development of density functional theory (DFT) and substantial increases in both the power and affordability of computers since the 1980s have allowed researchers to model chemical reactions at unparalleled levels of accuracy. While exact solutions to the multi-electronic Schrödinger equation remain unattainable,[123] modern DFT modelling allows for the calculation of key properties (**Figure 1.3**) such as binding configurations, adsorption energies, charge distributions, surface energies, electronic structure, and activation energies.[3,4,124] Many of these properties are extremely difficult to measure experimentally, giving computational modellers a unique advantage at understanding catalytic processes at the atomic scale.

In contemporary research, experimental studies of heterogeneous catalysts are frequently complimented with DFT modelling work so that hypotheses relating to reaction mechanisms, selectivity, and adsorption configurations can be supported until they can be confirmed or disproven by experiment. For instance, by constructing a DFT model of an adsorbate binding to the surface of a catalyst, analysis of the adsorbate's charge distribution and electronic structure can provide valuable insights into its reactivity. Mechanisms can also be validated by modelling the transition states associated with pairs of elementary steps, allowing for the calculation and comparison of activation energies.

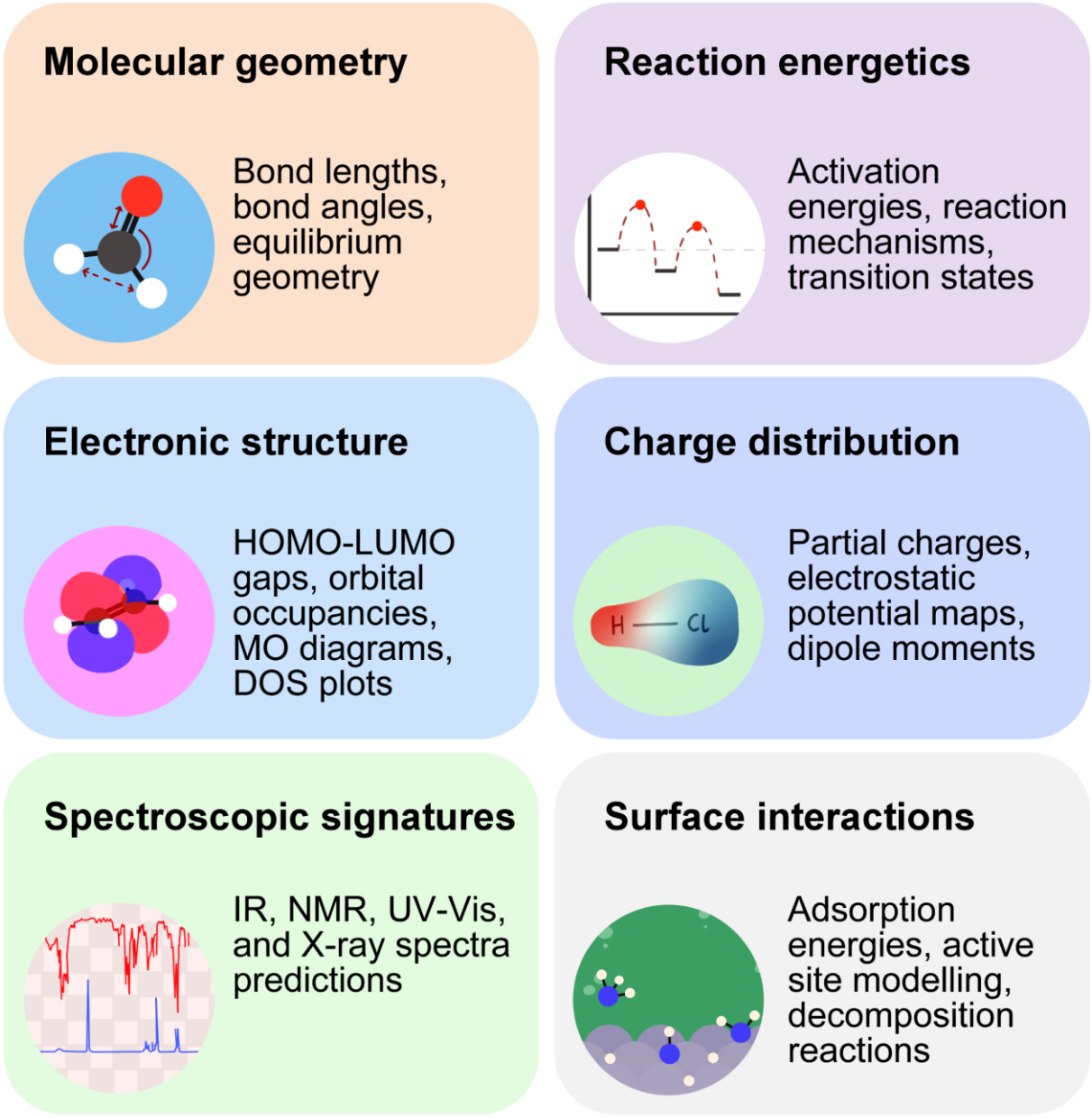

Figure 1.3. A selection of chemical properties that can be modelled at the DFT level by computational chemists.

DFT models of heterogeneous systems have yielded profound insight in the field of hydrogenation catalysis; particularly, over the facets of transition metal nanoparticles. For instance, a DFT mechanistic study by Narayanan, Kaushik, and Gupta[125] on the hydrogenation of furfural over Ru(0001) (**Scheme 1.5**) revealed a mechanism with a low activation energy (E_A = +74.2 kJ mol^{-1}) for its reduction to tetrahydrofurfuryl alcohol (THFA), a renewable solvent used in the textiles industry.[126,127] Ring hydrogenation was shown to optimally proceed through the initial reduction of the C4=C5 double bond.

The corresponding route, in which the C2=C3 bond was hydrogenated (E_A = +129.2 kJ mol^{-1}), had an activation energy nearly 75% higher than the optimal pathway.

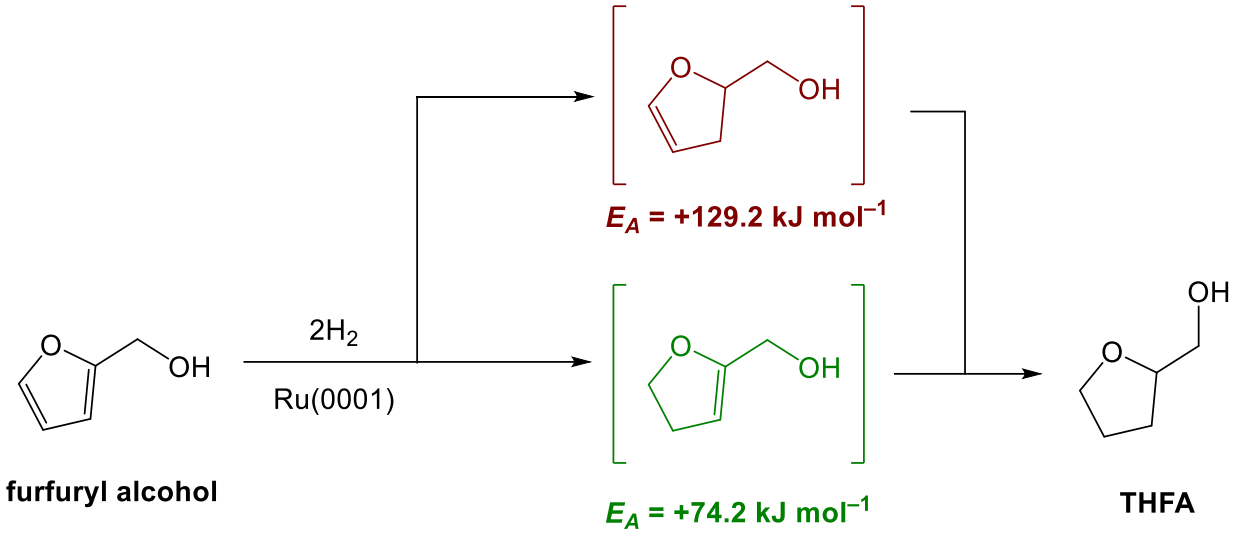

Scheme 1.5. Hydrogenation of furfuryl alcohol to THFA over Ru(0001). Activation energies calculated at the PBE-D3(0) level[5,9] in VASP.[13,14]

Other computational studies of catalytic hydrogenation have used DFT modelling software to determine the binding configurations of key intermediates over transition metal surfaces. A microkinetic study by Cao *et al.*[128] on the Pt-catalysed hydrogenation of (*E*)-crotonaldehyde, a common wastewater pollutant in the petrochemical industry,[129,130] identified a novel, low energy 1,4-addition mechanism (**Figure 1.4**) for its reduction to but-1-en-1-ol (E_A = +42.3 kJ mol^{-1}); an intermediate that quickly tautomerises to the dominant product, butyraldehyde.[131,132]

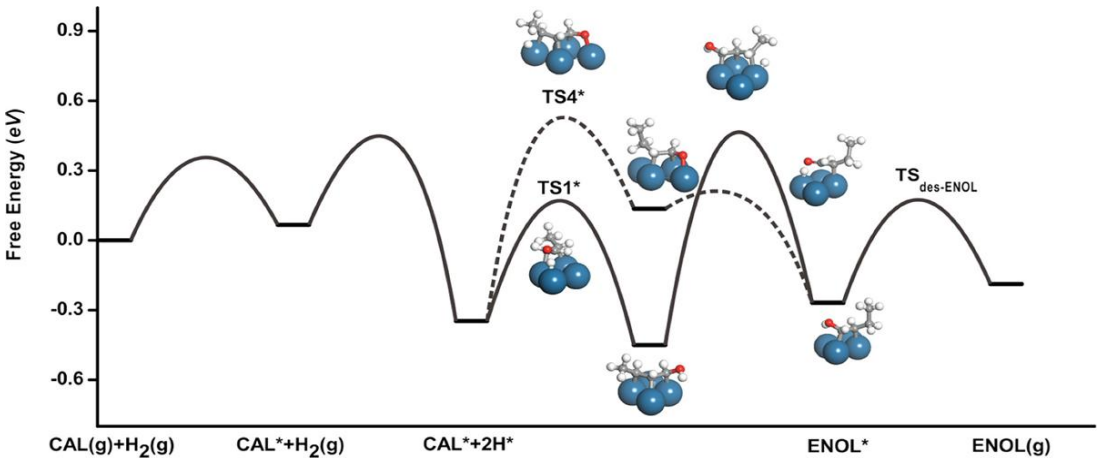

Figure 1.4. Free energy profile of the reduction of crotonaldehyde (CAL) to but-1-en-1-ol (ENOL). Hydrogenation can either proceed via 1,4-addition (solid line) or 4,1-addition (dashed). Adapted from Cao *et al.* (2011).[128]

1.4. Industrial Bio-Based Catalysis

Waste generated by the forestry and food sectors such as the stalks of cereal grains, sawdust, leaves, and fruit peels remain an under-utilised source of valuable platform chemicals.[133–135] Workers in these sectors, particularly those in developing countries with little recycling infrastructure in place,[136,137] often treat biomass as low-value refuse to be burned for heat or sent to landfill. Beyond the negative effects on local ecosystems that result from this approach, there are compelling economic incentives for investing in biomass conversion facilities. As shown in **Figure 1.5**, lignocellulosic biomass can be converted into a range of valuable products. Microorganisms can ferment the sugars present in biomass to ethanol, a widely used solvent and biofuel.[39] They can also decompose organic waste via anaerobic digestion into a sustainable and nutrient-rich fertiliser known as digestate.[138] Biomass can undergo gasification (i.e. incomplete combustion in an environment of limited oxygen) to syngas, a gaseous mixture of H_2 and CO used both as a heating source and a feedstock for platform chemicals such as methanol and ammonia.[139,140]

Bio-oil is generally produced from biomass in two ways. In hydrothermal liquefaction, wet biomass is converted into bio-oil by processing it in superheated water; usually, at temperatures and pressures exceeding 250 °C and 4 MPa, respectively.[141] Alternatively, bio-oil can be sourced from wood-based biomass by subjecting it to pyrolysis (i.e. heating it at high temperatures in an inert environment). Char, a black, carbon-based residue produced by pyrolysis, has been historically discarded as a waste product, but it in turn can be used as an additive in soils to counteract acidity and improve water retention.[142,143]

Considerable attention has been devoted to the potential applications of bio-oil in the transport, agricultural, and chemical sectors. However, “raw” bio-oil has several properties that make it an undesirable feedstock in comparison with petroleum-based compounds. These properties include, but are not limited to, low thermal stability;[144,145] high tendency towards coke formation;[146] low calorific value, limiting its utility as a source of heat;[144,147] and high acidity, a property that can lead to the corrosion of machinery and storage containers.[148] Many of these issues are exacerbated if the oil is rich in oxygenated compounds such as carboxylic acids and ketones, as they can catalyse undesirable polymerisation side reactions.[149]

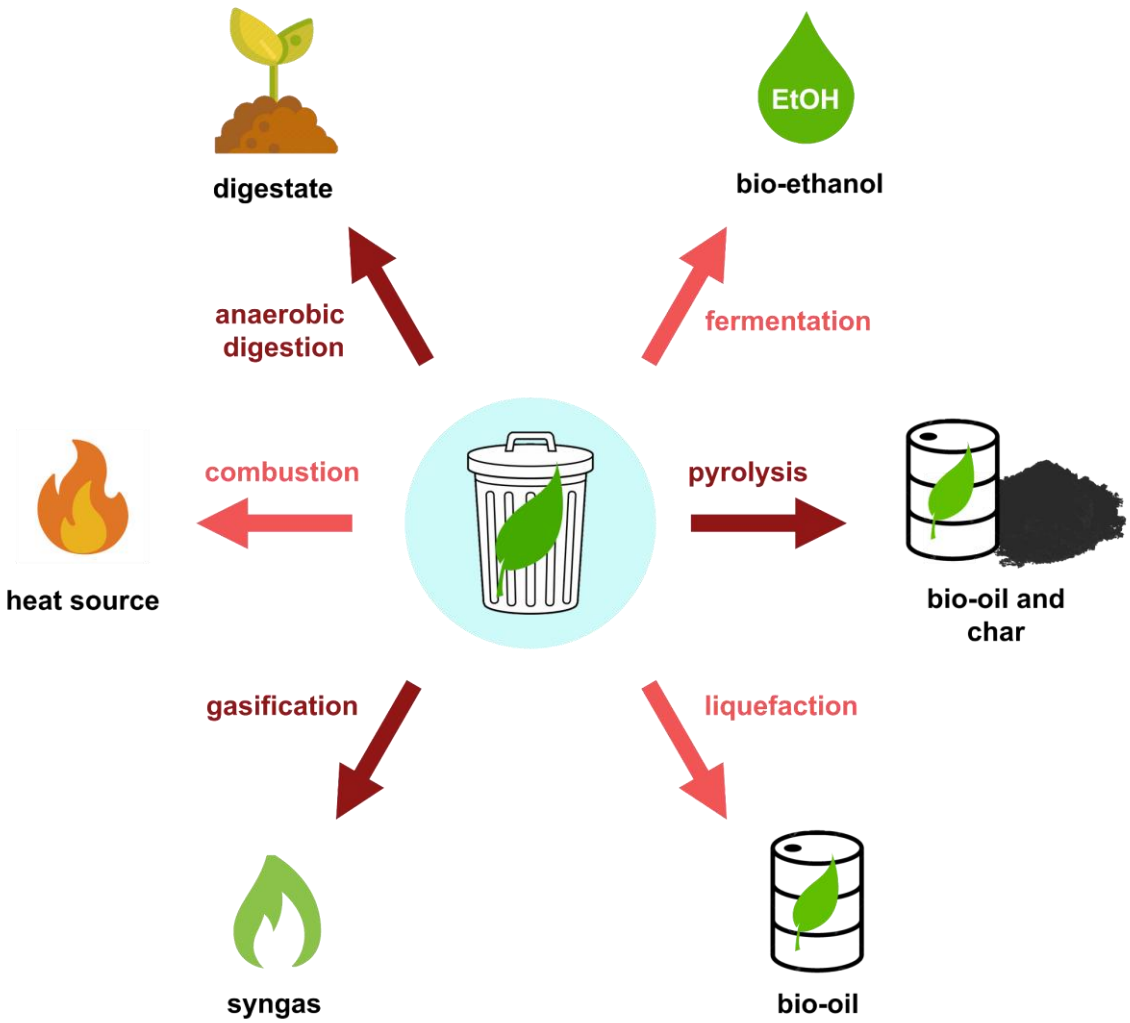

Figure 1.5. A selection of lignocellulosic biomass conversion routes and their associated products.

To combat this, bio-oil can be "upgraded" by subjecting it to hydrodeoxygenation (HDO), a catalytic process in which oxygen is removed from the oil in the form of water under an atmosphere of hydrogen gas. By decreasing the total oxygen content of bio-oil, HDO can increase its energy density by as much as 46 MJ kg^{-1},[103] bringing its calorific value in line with petroleum-based fuels. A representative reaction of this process is the hydrodeoxygenation of guaiacol to benzene (**Scheme 1.6**), a process usually performed over transition metal catalysts in industry.[150–154] A DFT study by Morteo-Flores *et al.*[153] identified a low-energy pathway for guaiacol HDO over Ni(111), in which guaiacol is first demethylated to catechol, followed by deoxygenation to phenol, and a final hydrogenolysis to the product. While this mechanism has yet to be confirmed experimentally over Ni-based catalysts, kinetic studies of guaiacol HDO have confirmed that the DFT mechanism is preferred over Pt/ZrO_2,[155] showing that the

production of catechol was four orders of magnitude faster than the direct hydrogenolysis of guaiacol to phenol. This highlights the importance of catechol as a crucial intermediate and the power of DFT as a tool for evaluating the mechanistic character of catalytic reactions.

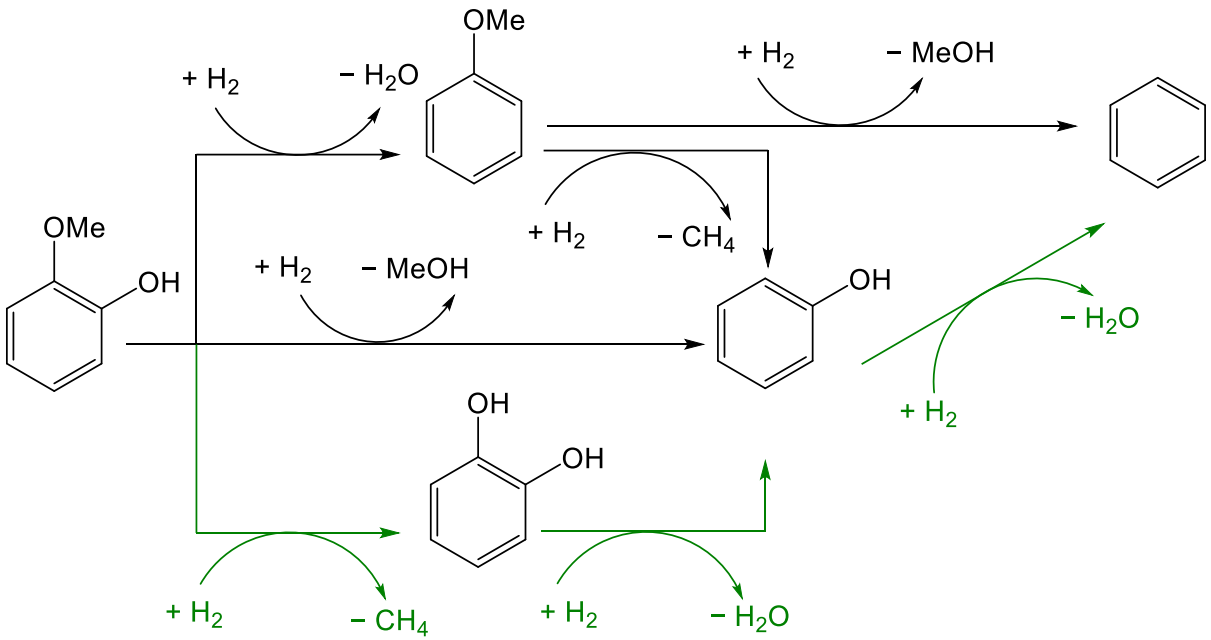

Scheme 1.6. Three potential mechanisms for guaiacol HDO to benzene. Mechanism favoured by DFT for guaiacol HDO over Ni(111) highlighted in green.

1.5. Thesis Outline

This thesis focuses of the applications of DFT modelling in the study of bio-based heterogeneous catalysis, with particular emphasis on two processes: (1) the hydrogenation and subsequent amination of furfural derivatives and (2) the pyrolysis of model compounds from lignocellulosic biomass over nanoceria. By constructing DFT models of key intermediates associated with these reactions, this work seeks to deepen our collective understanding of how catalyst choice can affect the selectivity and yield of bio-based processes. The results of the author's calculations will then be compared against experiment, thus combining theoretical and practical chemistry to construct a robust framework for the design of catalysts capable of converting renewable feedstocks to high-value platform chemicals.

Chapter 2 is a review of the computational methods that form the theoretical foundation of this thesis. The following three chapters cover the simulations work conducted over the course of the author's doctoral studies. **Chapter 3** is an

investigation of the catalytic hydrogenation of the furfural derivative (*E*)-1-(furan-2-yl)-5-methylhex-1-en-3-one (ALD-1) over Pd(111) and Pt(111) (**Figure 1.6**). Particular attention is given to the energetics and mechanistic pathways governing the hydrogenation of chain C=C bonds and the furanic ring, as well as to the role of charge distribution in influencing catalyst selectivity.

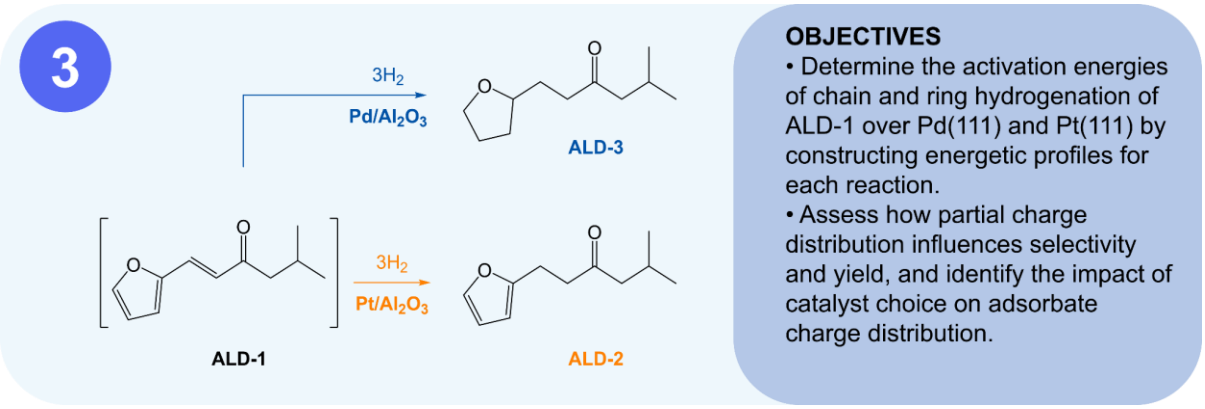

Figure 1.6. Objectives of **Chapter 3**.

Chapter 4 is a continuation of this work that focuses on the reductive amination of the hydrogenation product 5-methyl-1-(tetrahydrofuran-2-yl)hexan-3-one (ALD-3) to its corresponding amine, IMI-3, over Pd(111) and Ru(0001) (**Figure 1.7**). **Chapter 5** turns to the catalytic pyrolysis of biomass over CeO_2(111) (**Figure 1.8**). Using sinapic acid (SA) as a model compound for lignocellulosic biomass, this chapter aims to investigate the contributions of different compounds to infrared spectra taken during pyrolysis, as well as study the mechanistic chemistry underpinning SA's decarboxylation to 4-vinylsyringol (4VS). The thesis then concludes with **Chapter 6**, which summarises the key findings of the author's doctoral research and offers a selection of recommendations for future work in the field.

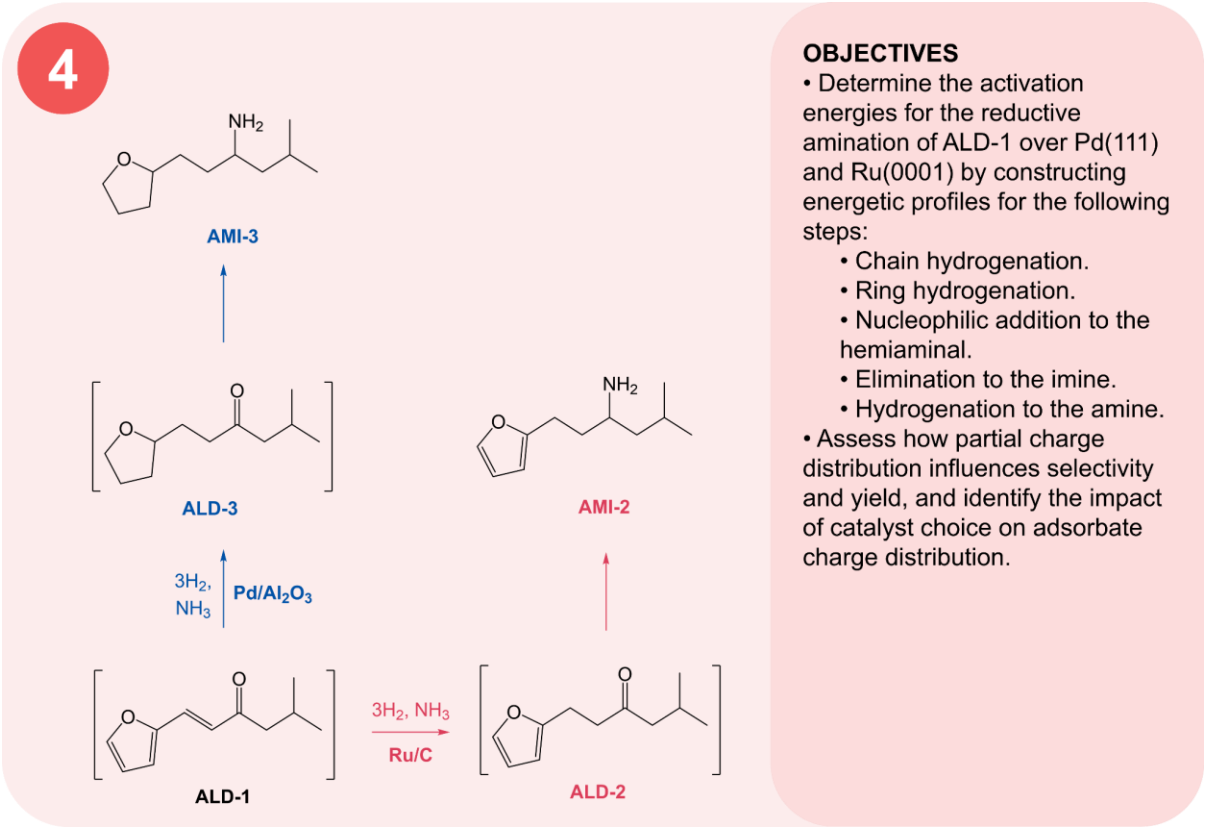

Figure 1.7. Objectives of **Chapter 4.**

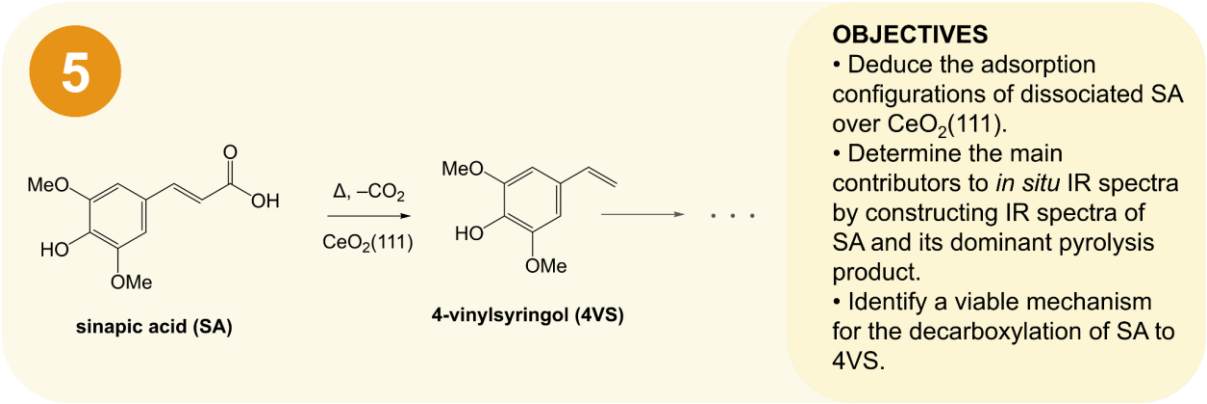

Figure 1.8. Objectives of **Chapter 5**.

1.6. References

1. M. Born and R. Oppenheimer, *Ann. Phys.*, **1927**, 389, 457–484.
2. G. Henkelman, B. P. Uberuaga and H. Jónsson, *J. Chem. Phys.*, **2000**, 113, 9901–9904.
3. T. A. Manz and N. Gabaldon Limas, *RSC Adv.*, **2016**, 6, 47771–47801.
4. N. Gabaldon Limas and T. A. Manz, *RSC Adv.*, **2016**, 6, 45727–45747.
5. S. Grimme, J. Antony, S. Ehrlich and H. Krieg, *J. Chem. Phys.*, **2010**, 132.
6. W. Kohn and L. J. Sham, *Phys. Rev.*, **1965**, 140, A1133–A1138.
7. C. Møller and M. S. Plesset, *Phys. Rev.*, **1934**, 46, 618–622.
8. J. P. Perdew, K. Burke and M. Ernzerhof, *Phys. Rev. Lett.*, **1996**, 77, 3865.
9. J. P. Perdew, K. Burke and Y. Wang, *Phys. Rev. B*, **1996**, 54, 16533–16539.
10. Y. Zhang and W. Yang, *Phys. Rev. Lett.*, **1998**, 80, 890–890.
11. D. C. Langreth and J. P. Perdew, *Phys. Rev. B*, **1980**, 21, 5469–5493.
12. B. Hammer, L. B. Hansen and J. K. Nørskov, *Phys. Rev. B*, **1999**, 59, 7413–7421.
13. J. Hafner and G. Kresse, in *Properties of Complex Inorganic Solids*, Springer, **1997**, pp. 69–82.
14. G. Kresse and D. Joubert, *Phys. Rev. B*, **1999**, 59, 1758.
15. E. H. Lieb and S. Oxford, *Int. J. Quantum Chem.*, **1981**, 19, 427–439.
16. D. R. Hartree, *Math. Proc. Camb. Philos. Soc.*, **1928**, 24, 89–110.
17. V. Fock, *Z. Für Phys.*, **1930**, 61, 126–148.
18. G. Henkelman and H. Jónsson, *J. Chem. Phys.*, **1999**, 111, 7010–7022.
19. A. Heyden, A. T. Bell and F. J. Keil, *J. Chem. Phys.*, **2005**, 123, 224101.
20. F. Bloch, *Z. Für Phys.*, **1929**, 52, 555–600.
21. L. Pauling, *The Nature of the Chemical Bond*, Cornell University Press, 3rd edn., **1960**.
22. S. Shafiee and E. Topal, *Energy Policy*, **2009**, 37, 181–189.
23. S. V. Vassilev, D. Baxter, L. K. Andersen and C. G. Vassileva, *Fuel*, **2010**, 89, 913–933.
24. L. R. Lynd, X. Liang, M. J. Biddy, A. Allee, H. Cai, T. Foust, M. E. Himmel, M. S. Laser, M. Wang and C. E. Wyman, *Curr. Opin. Biotechnol.*, **2017**, 45, 202–211.
25. M. Gu, Q. Xia, X. Liu, Y. Guo and Y. Wang, *ChemSusChem*, **2017**, 10, 4102–4108.
26. L. R. Lynd, G. T. Beckham, A. M. Guss, L. N. Jayakody, E. M. Karp, C. Maranas, R. L. McCormick, D. Amador-Noguez, Y. J. Bomble, B. H. Davison, C. Foster, M. E. Himmel, E. K. Holwerda, M. S. Laser, C. Yu Ng, D. G. Olson, Y. Román-Leshkov, C. T. Trinh, G. A. Tuskan, V. Upadhayay, D. R. Vardon, L. Wang and C. E. Wyman, *Energy Environ. Sci.*, **2022**, 15, 938–990.
27. C. E. Wyman, B. E. Dale, R. T. Elander, M. Holtzapple, M. R. Ladisch and Y. Y. Lee, *Bioresour. Technol.*, **2005**, 96, 1959–1966.
28. M. Azeem, N. Iqbal, R. A. Mir, S. Adeel, F. Batool, A. A. Khan and S. Gul, *J. Appl. Phycol.*, **2019**, 31, 3941–3948.
29. A. Wiraningtyas, P. A. Mutmainnah and M. Perkasa, *Orient. J. Chem.*, **2020**, 36, 964.
30. Z. He, P. H. Pagliari and H. M. Waldrip, *Pedosphere*, **2016**, 26, 779–816.
31. J. J. Hoyos-Sebá, N. P. Arias, J. Salcedo-Mendoza and V. Aristizábal-Marulanda, *Chem. Eng. Process. - Process Intensif.*, **2024**, 196, 109660.
32. M. Hájek, A. Vávra, H. de Paz Carmona and J. Kocík, *Catalysts*, **2021**, 11, 1118.

33. D. Mariuzza, J.-C. Lin, M. Volpe, L. Fiori, S. Ceylan and J. L. Goldfarb, *Biomass Bioenergy*, **2022**, 157, 106329.
34. N. C. Schellmann, *Stud. Conserv.*, **2007**, 52, 55–66.
35. P. Bajpai, *Recycling and Deinking of Recovered Paper*, Elsevier, **2024**.
36. A. Polyportis, R. Mugge and L. Magnier, *Resour. Conserv. Recycl.*, **2022**, 186, 106533.
37. O. Das, K. Babu, V. Shanmugam, K. Sykam, M. Tebyetekerwa, R. E. Neisiany, M. Försth, G. Sas, J. Gonzalez-Libreros, A. J. Capezza, M. S. Hedenqvist, F. Berto and S. Ramakrishna, *Renew. Sustain. Energy Rev.*, **2022**, 158, 112054.
38. I. Brito, S. M. Ferreira and L. Santos, *Cosmetics*, **2023**, 10, 140.
39. S. Brethauer and M. H. Studer, *CHIMIA*, **2015**, 69, 572–572.
40. M. P. Ruiz, J. Mijnders, R. Tweehuysen, L. Warnet, M. van Drongelen, S. R. A. Kersten and J.-P. Lange, *ChemSusChem*, **2019**, 12, 4395–4399.
41. R. Moita and P. C. Lemos, *J. Biotechnol.*, **2012**, 157, 578–583.
42. X. Hu and M. Gholizadeh, *Renew. Sustain. Energy Rev.*, **2020**, 134, 110124.
43. A. M. Niziolek, O. Onel, Y. A. Guzman and C. A. Floudas, *Energy Fuels*, **2016**, 30, 4970–4998.
44. G. Machado, S. Leon, F. Santos, R. Lourega, J. Dullius, M. E. Mollmann and P. Eichler, *Nat. Resour.*, **2016**, 07, 115–129.
45. N. Nićiforović and H. Abramovič, *Compr. Rev. Food Sci. Food Saf.*, **2014**, 13, 34–51.
46. H. Kuwahara, A. Kanazawa, D. Wakamatu, S. Morimura, K. Kida, T. Akaike and H. Maeda, *J. Agric. Food Chem.*, **2004**, 52, 4380–4387.
47. S. Jiang, W. Ramdani, E. Muller, C. Ma, M. Pera-Titus, F. Jerôme and K. De Oliveira Vigiera, *ChemSusChem*, **2020**, 13, 1699–1704.
48. K. J. Zeitsch, *The Chemistry and Technology of Furfural and Its Many By-Products*, Elsevier, **2000**.
49. H. J. Brownlee, *Ind. Eng. Chem.*, **1927**, 19, 422–424.
50. H. J. Brownlee and C. S. Miner, *Ind. Eng. Chem.*, **1948**, 40, 201–204.
51. K. L. MacIntosh and S. K. Beaumont, *Top. Catal.*, **2020**, 63, 1446–1462.
52. A. Gandini, *Polym. Chem.*, **1977**, 47–96.
53. A. O. Iroegbu and S. P. Hlangothi, *Chem. Afr.*, **2019**, 2, 223–239.
54. T. Kim, R. S. Assary, C. L. Marshall, D. J. Gosztola, L. A. Curtiss and P. C. Stair, *ChemCatChem*, **2011**, 3, 1451–1458.
55. N. P. Cheremisinoff, *Industrial Solvents Handbook*, CRC Press, 2nd edn., **2003**.
56. B. Trivedi, *Maleic Anhydride*, Springer Science & Business Media, **2013**.
57. A. Escobar, Á. Sathicq, L. Pizzio, M. Blanco and G. Romanelli, *Process Saf. Environ. Prot.*, **2015**, 98, 176–186.
58. G. D. Yadav and A. R. Yadav, *Chem. Eng. J.*, **2014**, 243, 556–563.
59. R. Bielski and G. Grynkiewicz, *Green Chem.*, **2021**, 23, 7458–7487.
60. R. C. Cioc, M. Lutz, E. A. Pidko, M. Crockatt, J. C. Van Der Waal and P. C. A. Bruijnincx, *Green Chem.*, **2021**, 23, 367–373.
61. O. Kikhtyanin, V. Kelbichová, D. Vitvarová, M. Kubů and D. Kubička, *Catal. Today*, **2014**, 227, 154–162.
62. M. C. Hernández-Soto, A. Erigoni, C. Segarra, F. Rey, U. Díaz, E. Gianotti, I. Miletto and M. Pera-Titus, *Appl. Catal. Gen.*, **2022**, 643, 118710.
63. H. Yuan, J. P. Li, F. Su, Z. Yan, B. T. Kusema, S. Streiff, Y. Huang, M. Pera-Titus and F. Shi, *ACS Omega*, **2019**, 4, 2510–2516.
64. S. Jiang, C. Ma, E. Muller, M. Pera-Titus, F. Jérôme and K. De Oliveira Vigier, *ACS Catal.*, **2019**, 9, 8893–8902.

65. F. H. Isikgor and C. Remzi Becer, *Polym. Chem.*, **2015**, 6, 4497–4559.
66. S. M. Read and T. Bacic, *Science*, **2002**, 295, 59–60.
67. H. Sadeghifar and A. Ragauskas, *Polymers*, **2020**, 12, 1134.
68. F. Shu, B. Jiang, Y. Yuan, M. Li, W. Wu, Y. Jin and H. Xiao, *Biomacromolecules*, **2021**, 22, 4905–4918.
69. M. Schuetz, A. Benske, R. A. Smith, Y. Watanabe, Y. Tobimatsu, J. Ralph, T. Demura, B. Ellis and A. L. Samuels, *Plant Physiol.*, **2014**, 166, 798–807.
70. W.-J. Liu, H. Jiang and H.-Q. Yu, *Green Chem.*, **2015**, 17, 4888–4907.
71. M. Söderqvist Lindblad, E. Ranucci and A.-C. Albertsson, *Macromol. Rapid Commun.*, **2001**, 22, 962–967.
72. M. Poletto, *Lignin: Trends and Applications*, BoD – Books on Demand, **2018**.
73. Y.-C. Wang, Y.-C. Chuang and Y.-H. Ku, *Food Chem.*, **2007**, 102, 1163–1171.
74. W. R. Russell, A. Labat, L. Scobbie, G. J. Duncan and G. G. Duthie, *Food Chem.*, **2009**, 115, 100–104.
75. F. Natella, M. Nardini, M. Di Felice and C. Scaccini, *J. Agric. Food Chem.*, **1999**, 47, 1453–1459.
76. M. Farzan, B. Abedi, I. Bhia, A. Madanipour, M. Farzan, M. Bhia, A. Aghaei, I. Kheirollahi, M. Motallebi, H. Amini-Khoei and Y. N. Ertas, *ACS Chem. Neurosci.*, **2024**, 15, 2966–2981.
77. B. J. Glaister and G. M. Mudd, *Miner. Eng.*, **2010**, 23, 438–450.
78. C. Hagelüken, *Platin. Met. Rev*, **2012**, 56, 29–35.
79. H. Dong, J. Zhao, J. Chen, Y. Wu and B. Li, *Int. J. Miner. Process.*, **2015**, 145, 108–113.
80. B. C. Hagelüken, *Platin. Met. Rev.*, **2012**, 56, 29–35.
81. J. Zhang, M. P. Everson, T. J. Wallington, F. R. I. Field, R. Roth and R. E. Kirchain, *Environ. Sci. Technol.*, **2016**, 50, 7687–7695.
82. S. Zhang, X. He, Y. Ding, Z. Shi and B. Wu, *Renew. Sustain. Energy Rev.*, **2024**, 204, 114821.
83. S. M. Rogers, C. R. A. Catlow, C. E. Chan-Thaw, A. Chutia, N. Jian, R. E. Palmer, M. Perdjon, A. Thetford, N. Dimitratos, A. Villa and P. P. Wells, *ACS Catal.*, **2017**, 7, 2266–2274.
84. W. Kim and S. H. Moon, *Catal. Today*, **2012**, 185, 2–16.
85. C. P. O'Brien, K. Dostert, S. Schauermann and H. Freund, *Chem. Eur. J.*, **2016**, 22, 15856–15863.
86. W. Dedsuksophon, K. Faungnawakij, V. Champreda and N. Laosiripojana, *Bioresour. Technol.*, **2011**, 102, 2040–2046.
87. P. Ruiz-Castillo and S. L. Buchwald, *Chem. Rev.*, **2016**, 116, 12564–12649.
88. M. Kashihara and Y. Nakao, *Acc. Chem. Res.*, **2021**, 54, 2928–2935.
89. M. C. D'Alterio, È. Casals-Cruañas, N. V. Tzouras, G. Talarico, S. P. Nolan and A. Poater, *Chem. – Eur. J.*, **2021**, 27, 13481–13493.
90. L. Gao, Z. Jiang, I. Miletto, E. Gianotti, E. Rebmann, L. Baussaron, F. Jiang and M. Pera-Titus, *Chem. Eng. J.*, **2023**, 473, 145021.
91. G. Liu, T. Nie, Z. Song, X. Sun, T. Shen, S. Bai, T. Yu, L. Zheng and Y.-F. Song, *Adv. Funct. Mater.*, **2024**, 34, 2411284.
92. H. Ning, Y. Chen, Z. Wang, S. Mao, Z. Chen, Y. Gong and Y. Wang, *Chem*, **2021**, 7, 3069–3084.
93. K. Alibegovic, D. G. Morgan, Y. Losovyj, M. Pink, B. D. Stein, N. V. Kuchkina, E. S. Serkova, K. E. Salnikova, Z. B. Shifrina, V. G. Matveeva, E. M. Sulman and L. M. Bronstein, *ChemistrySelect*, **2017**, 2, 5485–5491.

94. J. Mazarío, Z. Raad, P. Concepción, C. Cerdá-Moreno and M. E. Domine, *Catal. Sci. Technol.*, **2020**, 10, 8049–8063.
95. N. Wang, J. Liu, X. Li and L. Ma, *Catal. Commun.*, **2023**, 175, 106620.
96. S. A. Lawrence, *Amines: Synthesis, Properties and Applications*, Cambridge University Press, **2004**.
97. J. Hack, N. Maeda and D. M. Meier, *ACS Omega*, **2022**, 7, 39520–39530.
98. W. Zawodny and S. L. Montgomery, *Catalysts*, **2022**, 12, 595.
99. D. Shi and J. M. Vohs, *ACS Catal.*, **2015**, 5, 2177–2183.
100. J. R. McManus, E. Martono and J. M. Vohs, *ACS Catal.*, **2013**, 3, 1739–1750.
101. M. B. Griffin, G. A. Ferguson, D. A. Ruddy, M. J. Biddy, G. T. Beckham and J. A. Schaidle, *ACS Catal.*, **2016**, 6, 2715–2727.
102. R. Ramos, Z. Tišler, O. Kikhtyanin and D. Kubička, *Catal. Sci. Technol.*, **2016**, 6, 1829–1841.
103. X. Xu, C. Zhang, Y. Liu, Y. Zhai and R. Zhang, *Chemosphere*, **2013**, 93, 652–660.
104. I. Chidunchi, M. Kulikov, R. Safarov and E. Kopishev, *Heliyon*, **2024**, 10.
105. F. R. Muñoz, C. P. Ramírez, J. Meza and T. Crouch, *Miner. Econ.*, **2024**, 37, 681–700.
106. Y. Zhang and Y. Shen, *Appl. Catal. B Environ.*, **2024**, 343, 123576.
107. A. S. Touchy, S. M. A. Hakim Siddiki, K. Kon and K. Shimizu, *ACS Catal.*, **2014**, 4, 3045–3050.
108. *PGM Prices and Trading*, Johnson Matthey. Last accessed 15 September 2025. https://matthey.com/products-and-markets/pgms-and-circularity/pgm-management.
109. L. Dong, J. Xia, Y. Guo, X. Liu, H. Wang and Y. Wang, *J. Catal.*, **2021**, 394, 94–103.
110. Y. Zeng, S. Zhang, L. Lin, N. Wang, Z. Jiang, C. Zeng, X. Tu and K. Yan, *Chem. Eng. J.*, **2024**, 495, 153612.
111. K. P. Kepp, *Inorg. Chem.*, **2016**, 55, 9461–9470.
112. M. P. Boone and D. W. Stephan, *J. Am. Chem. Soc.*, **2013**, 135, 8508–8511.
113. E. P. Kündig, C. M. Saudan and G. Bernardinelli, *Angew. Chem. Int. Ed.*, **1999**, 38, 1219–1223.
114. W. Mu, H. Ben, X. Du, X. Zhang, F. Hu, W. Liu, A. J. Ragauskas and Y. Deng, *Bioresour. Technol.*, **2014**, 173, 6–10.
115. M. Nemanashi, J.-H. Noh and R. Meijboom, *Appl. Catal. Gen.*, **2018**, 550, 77–89.
116. M. Melchionna and P. Fornasiero, *RSC Appl. Interfaces*, **2024**, 1, 70–79.
117. D. R. Mullins, S. H. Overbury and D. R. Huntley, *Surf. Sci.*, **1998**, 409, 307–319.
118. A. Trovarelli, *Catalysis by Ceria and Related Materials*, World Scientific, **2002**, vol. 2.
119. H.-M. Kim, Y.-H. Lee, M.-J. Park and D.-W. Jeong, *Int. J. Hydrog. Energy*, **2023**, 48, 29142–29152.
120. T. Montini, M. Melchionna, M. Monai and P. Fornasiero, *Chem. Rev.*, **2016**, 116, 5987–6041.
121. S. Shao, C. Liu, X. Xiang, X. Li, H. Zhang, R. Xiao and Y. Cai, *Renew. Energy*, **2021**, 177, 1372–1381.
122. Y. Wan, K. Ding, J. C.-H. Lam, D. Zhong and S. Zhang, *Fuel Process. Technol.*, **2023**, 241, 107584.
123. C. J. Cramer, *Essentials of Computational Chemistry: Theories and Models*, John Wiley & Sons, 2nd edn., **2004**.

124. P. Chen, Y. Gao and M. R. Castell, *Appl. Phys. Lett.*, **2020**, 117, 1–5.
125. A. K. Narayanan, D. Kaushik and S. Gupta, *J. Phys. Chem. C*, **2024**, 128, 18265–18272.
126. N. Merat, C. Godawa and A. Gaset, *J. Chem. Technol. Biotechnol.*, **1990**, 48, 145–159.
127. L. Chen, J. Ye, Y. Yang, P. Yin, H. Feng, C. Chen, X. Zhang, M. Wei and D. G. Truhlar, *ACS Catal.*, **2020**, 10, 7240–7249.
128. X.-M. Cao, R. Burch, C. Hardacre and P. Hu, *J. Phys. Chem. C*, **2011**, 115, 19819–19827.
129. T. Liu, J. Zuo, Z. Shen and Y. Zhou, *J. Environ. Manage.*, **2022**, 303, 114090.
130. T. Liu, Z. Shen, Y. Zhou and J. Zuo, *Process Saf. Environ. Prot.*, **2023**, 178, 1161–1169.
131. T. Ishida, F. Hirata and S. Kato, *J. Chem. Phys.*, **1999**, 110, 3938–3945.
132. C. S. Cucinotta, A. Ruini, A. Catellani and A. Stirling, *ChemPhysChem*, **2006**, 7, 1229–1234.
133. N. Tripathi, C. D. Hills, R. S. Singh and C. J. Atkinson, *Npj Clim. Atmospheric Sci.*, **2019**, 2, 35.
134. O. K. Saheed, P. Jamal, M. I. A. Karim, Md. Z. Alam and S. A. Muyibi, *J. King Saud Univ. - Sci.*, **2016**, 28, 143–151.
135. K. Theerarattananoon, F. Xu, J. Wilson, R. Ballard, L. Mckinney, S. Staggenborg, P. Vadlani, Z. J. Pei and D. Wang, *Ind. Crops Prod.*, **2011**, 33, 325–332.
136. S. Pandey, *SN Appl. Sci.*, **2022**, 4, 168.
137. P. J. H. van Beukering and J. C. J. M. van den Bergh, *Resour. Conserv. Recycl.*, **2006**, 46, 1–26.
138. Đ. Kovačić, Z. Lončarić, J. Jović, D. Samac, B. Popović and M. Tišma, *Appl. Sci.*, **2022**, 12, 9216.
139. A. L. Boehman and O. L. Corre, *Combust. Sci. Technol.*, **2008**, 180, 1193–1206.
140. K. Göransson, U. Söderlind, J. He and W. Zhang, *Renew. Sustain. Energy Rev.*, **2011**, 15, 482–492.
141. D. C. Elliott, P. Biller, A. B. Ross, A. J. Schmidt and S. B. Jones, *Bioresour. Technol.*, **2015**, 178, 147–156.
142. Z. Dai, X. Zhang, C. Tang, N. Muhammad, J. Wu, P. C. Brookes and J. Xu, *Sci. Total Environ.*, **2017**, 581–582, 601–611.
143. F. Razzaghi, P. B. Obour and E. Arthur, *Geoderma*, **2020**, 361, 114055.
144. X. Hu and M. Gholizadeh, *J. Energy Chem.*, **2019**, 39, 109–143.
145. X. Xu, Z. Li, Y. Sun, E. Jiang and L. Huang, *Energy Fuels*, **2018**, 32, 3477–3487.
146. M. Gholizadeh, R. Gunawan, X. Hu, F. de Miguel Mercader, R. Westerhof, W. Chaitwat, M. M. Hasan, D. Mourant and C.-Z. Li, *Fuel Process. Technol.*, **2016**, 148, 175–183.
147. Z. Xiong, Y. Wang, S. S. A. Syed-Hassan, X. Hu, H. Han, S. Su, K. Xu, L. Jiang, J. Guo, E. E. S. Berthold, S. Hu and J. Xiang, *Energy Convers. Manag.*, **2018**, 163, 420–427.
148. X. Zhang, Z. Guo and W. Chen, *Energies*, **2017**, 10, 590.
149. X. Hu, Y. Wang, D. Mourant, R. Gunawan, C. Lievens, W. Chaiwat, M. Gholizadeh, L. Wu, X. Li and C.-Z. Li, *AIChE J.*, **2013**, 59, 888–900.
150. K. Agrawal, A. Roldan, N. Kishore and A. J. Logsdail, *Catal. Sci. Technol.*, **2022**, 12, 843–854.

151. D. Gao, C. Schweitzer, H. T. Hwang and A. Varma, *Ind. Eng. Chem. Res.*, **2014**, 53, 18658–18667.
152. J. Chang, T. Danuthai, S. Dewiyanti, C. Wang and A. Borgna, *ChemCatChem*, **2013**, 5, 3041–3049.
153. F. Morteo-Flores, M. Quayle, A. Salom-Català, M. Pera-Titus and A. Roldan, *ChemCatChem*, **2023**, 15, e202300671.
154. F. Morteo-Flores and A. Roldan, *ChemPhysChem*, **2022**, 23, e202100583.
155. A. Gutierrez, R. K. Kaila, M. L. Honkela, R. Slioor and A. O. I. Krause, *Catal. Today*, **2009**, 147, 239–246.

2. Computational Theory

This chapter begins with a brief review of the most common approximations in computational chemistry (**Section 2.1**), followed by a discussion on the theoretical background and applications of density functional theory in **Sections 2.2** and **2.3**. Finally, the chapter concludes with a short discussion of transition state search methods in **Section 2.4**.

2.1. Common Approximations

The non-relativistic energy of any chemical system can be analytically determined by solving the time-independent Schrödinger equation:

$$\hat{H}\psi = E\psi \tag{2.1}$$

where $\hat{H}$ is the Hamiltonian operator, E is the non-relativistic energy of the system, and ψ is the time-independent wave function. In spite of its apparent simplicity, **Equation 2.1** cannot be solved analytically for any chemical system with two or more electrons.[1,2] Consequently, theoreticians must make several approximations when trying to solve the Schrödinger equation for realistic systems. These approximations are a necessary compromise, and they form the theoretical foundation of almost every algorithm employed in contemporary computational chemistry research.

2.1.1. The Born-Oppenheimer Approximation

Since its formulation in the 1920s,[3] the Born-Oppenheimer approximation (BOA) has cemented itself as one of the theoretical foundations of quantum chemistry. Under the BOA, nuclear and electronic motion are assumed to be separable from one another, drastically reducing the computational complexity of the Schrödinger equation for many-electron systems. The justification for this assumption is that electrons are 1,836 times lighter than protons,[4,5] and thus move on much slower timescales. Consequently, nuclei can be treated as static with respect to the electrons during electronic structure calculations.

Due to the enormous computational speedup that results from the BOA, it is often applied without question in a wide range of quantum chemical calculations, particularly

those involving systems with large numbers of nuclei. However, in the words of Edward Condon,[6] Born and Oppenheimer's 1927 paper is "among those difficult ones that are more often cited than read." If misapplied, the BOA can introduce non-negligible errors, especially in systems where electronic and nuclear motion are strongly coupled.[7] The BOA is known to break down for excitations in metallic structures, and applying it carelessly when modelling semiconducting materials such as graphene can lead to errors in the electronic structure.[8] Fortunately, while the BOA is by no means applicable to every chemical system, it remains a sensible approximation for most systems of interest in catalysis, and will thus be applied for all calculations in this thesis.

2.1.2. The Frozen Core Approximation

The BOA is a prerequisite for several other approximations considered necessary for computational surface chemistry; chief among them, the frozen core approximation (FCA). Under the FCA, it is assumed that the core orbitals of each atom in the system do not change shape. The physical justification for this approximation is that the chemistry of an element is largely dictated by the electrons in its valence orbitals. Core electrons, which experience much stronger attraction to the nucleus, have a negligible effect on bond formation compared to the valence electrons.[9] As a result, the shape and energy of core orbitals are relatively insensitive to changes in molecular geometry, and their relaxation contributes minimally to the total energy. For large atoms, neglecting the relaxation of the core orbitals can significantly reduce the computational cost of geometry optimisation.

Due to the large numbers of atoms (and in turn, the large numbers of electrons) that would otherwise have to be modelled to properly simulate the chemical properties of metal surfaces, the FCA is generally considered to be an essential approximation for most systems of interest in catalysis. However, for high-precision simulations work, theoretical chemists must proceed with caution; particularly, if the work in question involves condensed matter. When atoms are brought closer to one another during crystal formation, the increase in the kinetic energy of core electrons gives rise to non-negligible changes in the shape of the core orbitals.[10,11] This effect will be even more pronounced if the system contains heavy elements such as Bi, where electrons in the core orbitals can reach velocities exceeding 75% of the speed of light.[12,13] Due to relativistic effects, the mass of the electrons in the Bi 1s orbitals will increase by 26%,

leading to the orbital's radius contracting by approximately 20%.[14] Wang *et al.*[15] showed that applying the FCA in DFT models of Tl, Bi, and Po lead to substantial errors in the excitation and ionisation energies. Fortunately, in typical catalytic systems, errors induced by the FCA are typically small in comparison to the kinetic energy changes of the valence electrons, and can generally be neglected out of practical necessity.[10]

2.2. Density Functional Theory

In a ground-breaking paper in 1964,[16] Pierre Hohenberg and Walter Kohn showed that the energy of any chemical system can be expressed exactly as a functional of its electron density. This energy functional $E[\rho]$ can be expressed as a sum of four terms:

$$E[\rho] = T_{ni} + V_{ne} + V_{ee} + E_{XC} \tag{2.2}$$

where T_{ni} is the kinetic energy of the non-interacting electrons, V_{ne} is the nuclear-electron interaction, V_{ee} is the classical electron-electron repulsion, and E_{XC} is the exchange correlation energy. It can be shown[17] that the set of molecular orbitals χ_i that minimises $E[\rho]$ must satisfy the following eigenvalue equation:

$$\hat{h}_i \chi_i = \varepsilon_i \chi_i \tag{2.3}$$

where ε_i is the energy of a single electron in the ith molecular orbital. The Kohn-Sham one-electron operator ($\hat{h}_i$) can be expressed as follows:

$$\hat{h}_i = -\frac{1}{2}\nabla_i^2 - \sum_k^N \frac{Z_k}{|\boldsymbol{r_i} - \boldsymbol{R_k}|} + \int \frac{\rho(\boldsymbol{r'})}{|\boldsymbol{r_i} - \boldsymbol{r'}|}\,\mathrm{d}\boldsymbol{r'} + V_{XC} \tag{2.4}$$

where N is the total number of nuclei in the system, Z_k is the atomic number of the kth nucleus, ∇_i^2 is the Laplacian taken with respect to the coordinates of the electron at $\boldsymbol{r_i}$, and $|\boldsymbol{r_i} - \boldsymbol{R_k}|$ is the absolute difference in position between the ith electron and the kth nucleus. A dummy integration variable $\boldsymbol{r'}$ is used to calculate the classical

electrostatic repulsion between the electron at $\boldsymbol{r_i}$ and the rest of the system. The final term in **Equation 2.4** is the functional derivative V_{XC}, usually referred to as the exchange correlation potential:

$$V_{XC} = \frac{\delta E_{XC}}{\delta \rho} \tag{2.5}$$

Equations 2.2 to **2.5** form the bedrock of Kohn-Sham density functional theory (KS-DFT).[18] It should be highlighted that DFT is both broader and older than the Kohn-Sham formalism, and that "pure DFT" calculations can be undertaken independently of these constraints.[19–21] However, the vast majority of computational chemistry papers that have made use of DFT post-1980 implicitly assume the use of the Kohn-Sham formalism. Consequently, the "KS-" prefix will be dropped for the remainder of this thesis.

Provided the terms on the right-hand side of **Equation 2.4** are known, the ground state energy of any chemical system can be determined analytically, providing theoretical chemists with exact solutions to the Schrödinger equation. Unfortunately, while Hohenberg and Kohn's proof conclusively shows that the energy of a system *can* be expressed as a functional of its electron density, it tells us nothing about *how* these functionals can be determined through experiment; or even, more troublingly, if they can be experimentally determined at all.[17] The largest practical barrier associated with DFT and the reason that, in practice, it remains an inexact technique, is that E_{XC} is unknown for the vast majority of chemical systems, save for a handful of extremely simplified models. As such, computational chemists have no choice but to approximate E_{XC}, either through semi-empirical methods, or by modifying $E[\rho]$ in more fundamental ways to account for additional variables alongside the electron density.

DFT did not find much early success in theoretical chemistry. While primitive DFT packages gave good quantitative predictions for metallic surfaces, they failed to model covalent systems to sufficient degrees of accuracy. For DFT models of catalytic systems, the BOA and FCA are often enforced out of practical necessity, further frustrating any efforts to solve the Schrödinger equation analytically for bulk matter. However, since the development of GGA functionals in the 1980s (**Section 2.3**), modern DFT software packages have been able to model chemical systems to extremely high degrees of accuracy; particularly, in surface chemistry, where most

systems of interest involve large numbers of atoms. In recognition of its success, DFT has become one of the most heavily cited research topics in the history of the physical sciences. Of the ten most cited papers in peer-reviewed physics journals between 1980 and 2010, eight focused on DFT, including all of the papers in the top three.[22–25]

2.2.1. Exchange and Correlation Energies

The exchange correlation energy is typically evaluated by constructing an exchange correlation functional $E_{XC}[\rho]$, which can be expressed as the sum of the exchange energy $E_X[\rho]$ and the correlation energy $E_C[\rho]$:

$$E_{XC}[\rho] = E_X[\rho] + E_C[\rho] \tag{2.6}$$

$E_X[\rho]$ is a measure of energy that arises from the violation of the Pauli exclusion principle.[17] Under this principle, no two electrons in the same atom can have the same set of quantum numbers. When atoms move towards each other, electrons in identical quantum states are repelled from one another in a process known as Pauli repulsion. $E_C[\rho]$, the correlation energy, is a harder property to describe in a physically intuitive manner, but it can be loosely defined as a measure of how the movement of a single electron is affected by the movement of all of the other electrons in the system.[26] In the language of Hartree-Fock theory,[27,28] a formalism that reduces all electron-electron interactions to an average "mean-field" potential, the correlation energy can be expressed as follows:

$$E_C[\rho] = E - E_{HF} \tag{2.7}$$

where E_{HF} is the Hartree-Fock energy of the system and E is the true, non-relativistic energy of the system.

Until the 1980s, DFT functionals were typically based on the groundwork of the local density approximation (LDA). The key assumption of the LDA is that the local electron density of the system is treated as if it were perfectly homogenous at all occupied points in space. Under these constraints, the exchange correlation energy of the entire system can be solely determined from the electron density ρ at any position $\boldsymbol{r}$. In

atomic units, exchange functionals that arise from this assumption (E_X^{LDA}) typically take the following form:

$$E_X^{LDA} = C \int \rho^{4/3}(\boldsymbol{r})\, \mathrm{d}\boldsymbol{r} \tag{2.8}$$

for some constant C. Due to the variation that can arise in their construction, no analogous expression exists for LDA correlation functionals (E_C^{LDA}), but historically, they were constructed by fitting the functional to the results of quantum Monte-Carlo (QMC) calculations.[17,29,30]

A shortcoming of the LDA is that it implicitly assumes that spin-up and spin-down electrons contribute equally to the exchange correlation energy of the system. A more sophisticated variant of the LDA called the local spin density approximation (LSDA) accounts for this by replacing the $\rho^{4/3}(\boldsymbol{r})$ term with the sum of the individual spin densities raised to the $\frac{4}{3}$th power:

$$E_X^{LSDA} = C \int \left(\rho_\uparrow^{4/3}(\boldsymbol{r}) + \rho_\downarrow^{4/3}(\boldsymbol{r})\right) \mathrm{d}\boldsymbol{r} \tag{2.9}$$

By the end of the 1980s, LSDA functionals had made their LDA counterparts largely obsolete, as they could model atoms with unpaired electrons in their valence shells to unparalleled degrees of accuracy.[31] However, there are fundamental oversimplifications in both the LDA and LSDA that must be addressed; namely, the assumption that the electron density of a chemical system will ever be perfectly homogeneous at every point in space, even for a single frame of a calculation. Up until the 1980s, LSDA functionals were generally considered satisfactory for metals, as the electron density is distributed relatively evenly across the surface. However, for organic systems, LSDA functionals overestimate the strengths of covalent bonds, sometimes by as much as 100 kJ mol^{-1}.[32] For heterogeneous catalysis, this is an unacceptable compromise, and more accurate functionals must be employed if the system is to be accurately modelled computationally.

The functionals used in this work are based on a more complex variant of the LSDA known as the generalised gradient approximation (GGA). In GGA functionals, the

gradient of the electron density ($\nabla\rho$) is included as a variable alongside the density itself. As well as modelling covalent bonds more accurately, GGA functionals have generally eclipsed LSDA functionals for metals, as they do not share the LSDA's tendency to overbind metal atoms to one another, leading them to often underestimate properties such as lattice constants (**Section 2.2.6**).[33]

2.2.2. PBE

It is estimated that more than 300 DFT functionals were developed between 1980 and 2020.[34,35] As the discipline of computational chemistry continues to evolve, it is inevitable that the number and quality of these functionals will increase, but few have had as large an impact on the field as PBE, a GGA functional developed by Perdew, Burke, and Ernzerhof in 1996.[25] On the cusp of its thirtieth anniversary, PBE remains one of the most popular DFT functionals in the field of molecular modelling. It is a popular benchmark in computational chemistry research; both in the development of new functionals and the training of machine learning models designed to predict molecular or material properties from first principles.

One of PBE's biggest strengths is its generality. At the time of its release, PBE was one of the first GGA functionals to be largely free of empirical parameters. Almost all of the parameters invoked in the construction of PBE are derived from boundary conditions in solid state physics or are fundamental constants of nature, lending it a robustness that makes it broadly applicable across a wide range of fields. The PBE correlation energy (E_C^{PBE}) can be expressed as follows:

$$E_C^{PBE} = \int \rho(\boldsymbol{r}) \cdot (\rho_\uparrow^{4/3}(r_s,\zeta) + \rho_\downarrow^{4/3}(r_s,\zeta) + H(r_s,\zeta,g_C)d\boldsymbol{r} \tag{2.10}$$

where $r_s = (3/4\pi n_{pd})^{1/3}$ is the Wigner-Seitz radius, n_{pd} is the particle density of the system, and $\zeta = (\rho_\uparrow - \rho_\downarrow)/\rho$ is the system's relative degree of spin polarisation.[25,36] The gradient contribution term H invokes a dimensionless parameter g_C that ensures the preservation of physical behaviour as the gradient of the electron density tends to infinity. The PBE exchange energy (E_X^{PBE}) is as follows:

$$E_X^{PBE} = \int \rho(\boldsymbol{r}) \cdot \varepsilon_X^{PBE}(\boldsymbol{r})\, d\boldsymbol{r} = \int \frac{-3\rho(\boldsymbol{r})e^2 k_F}{4\pi} \cdot F(g_X)\, d\boldsymbol{r} \tag{2.11}$$

where e is the elementary charge and $k_F = \sqrt[3]{3\pi^2 \cdot \rho(\boldsymbol{r})}$ is the Fermi wave vector. The enhancement factor $F(g_X)$, a function of a second dimensionless gradient contribution term g_X, ensures that the PBE exchange energy obeys a litany of specialised boundary conditions relating to spin scaling and diamagnetic susceptibility.[37–40] The mathematical details of these conditions are largely beyond the scope of this thesis, and are discussed in greater detail in Perdew, Burke, and Ernzerhof (1996).[25] However, one boundary condition that warrants further discussion is the local Lieb-Oxford criterion,[41] a bound for the indirect part of the Coulomb repulsion energy. It should be highlighted that, at the time of PBE's development, $C_{LO} \leq 1.68$ was the strongest known bound for the Lieb-Oxford constant, but this bound has since been tightened to $1.44 \leq C_{LO} \leq 1.64$.[42–45] The local Lieb-Oxford criterion holds if the following inequality is met at all points of real space:

$$\rho(\boldsymbol{r}) \cdot \varepsilon_X(\boldsymbol{r}) \geq -C_{LO}\rho^{4/3}(\boldsymbol{r}) \tag{2.12}$$

where $\varepsilon_X(\boldsymbol{r})$ is the "extra" term that undergoes integration alongside the local electron density when calculating the exchange energy; in the case of **Equation 2.11**, $\varepsilon_X^{PBE}(\boldsymbol{r})$. Following the work of Becke,[46] all of the necessary criteria for a physically accurate exchange energy can be satisfied by calculating $F(g_X)$ as follows:

$$F_{PBE}(g_X) = 1 + \kappa - \frac{\kappa}{1 + \frac{\mu {g_X}^2}{\kappa}} \tag{2.13}$$

where $\mu = 0.220$ and $\kappa = 0.804$ are dimensionless constants. With these values of μ and κ, the upper bound of $F_{PBE}(g_X)$ is locked to 1.804, a value that satisfies the local Lieb-Oxford criterion for all possible charge densities.

2.2.3. revPBE and RPBE

Within eighteen months of the publication of Perdew, Burke, and Ernzerhof's work in *Physical Review Letters*, a one-page response to the paper by Zhang and Yang[47] was published in the same journal. In less than 400 words, the authors demonstrated that the molecular atomisation energies could be modelled more accurately by neglecting

the local Lieb-Oxford criterion and raising the value of κ to 1.245; an empirical value derived by fitting the exchange-only ground state energies of single atoms from helium to argon to the exact exchange-only energies of Engel and Vosko.[48] The new functional, now known as revPBE, reduced the mean absolute error of molecular atomisation energy calculations by nearly 40%. While revPBE can generate Coulomb repulsion energies that break the local Lieb-Oxford criterion in rare instances, its exchange term E_X^{revPBE} satisfies a weaker upper bound known as the *integrated* Lieb-Oxford criterion (**Equation 2.14**). As highlighted by revPBE's developers,[47] most systems that satisfy the integrated bound will satisfy the local Lieb-Oxford criterion in practice, but the possibility remains that the local bound may be violated at some region of space whilst still satisfying the integrated bound due to compensatory regions of electron density elsewhere in the system.

$$\int \rho(\boldsymbol{r}) \cdot \varepsilon_X^{PBE}(\boldsymbol{r})\, d\boldsymbol{r} \geq E_{XC} \geq -C_{LO} \int \rho^{4/3}\, d\boldsymbol{r} \tag{2.14}$$

Within a year of revPBE's release, the revised-Perdew-Burke-Ernzerhof functional (RPBE) was developed by Hammer *et al.*[49] The design philosophy of the RPBE development team was to create a functional that could reproduce the accuracy of revPBE whilst satisfying the local Lieb-Oxford criterion. This was achieved by changing the form of the enhancement factor:

$$F_{RPBE}(g_X) = 1 + \kappa\left(1 - \mathrm{e}^{-\mu g_X{}^2/\kappa}\right) \tag{2.15}$$

where $\mu = 0.220$ and $\kappa = 0.804$, following Perdew, Burke, and Ernzerhof's original formulation. A graphical comparison of how strictly the enhancement factors of PBE, revPBE, and RPBE obey the local Lieb-Oxford criterion is provided in **Figure 2.1**.

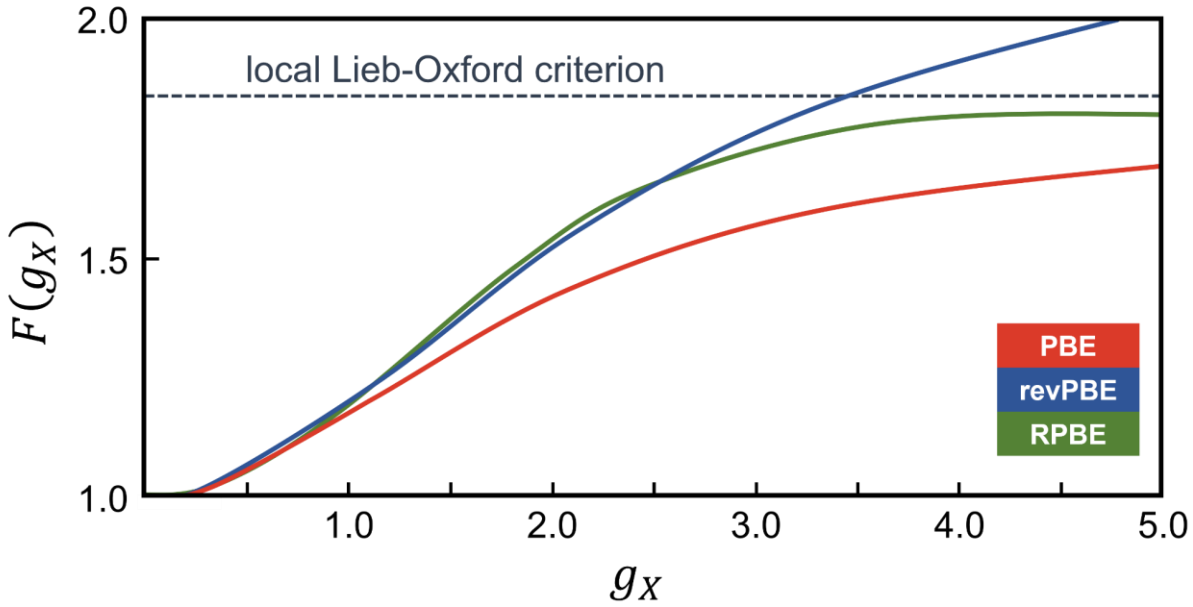

Figure 2.1. The degree to which the enhancement factors of PBE (red), revPBE (blue), and RPBE (green) obey the local Lieb-Oxford criterion. Both $F(g_X)$ and g_X are dimensionless. Data taken from Hammer *et al.* (1999).[49]

2.2.4. DFT-D3(0)

While the development of PBE and its derivatives has been heralded as a breakthrough in the field of computational chemistry, it has been known for several decades that GGA functionals fail to account for long-range interactions such as the London dispersive force.[50] To properly account for this shortcoming, a common solution is to introduce an additive corrective term that can be calculated separately once the DFT ground state energy has been determined. A popular example is the "zero-damped" DFT-D3(0) dispersion correction, developed by Grimme *et al.*[51] as a successor to the group's DFT-D1[52] and DFT-D2[53] methods. For each pair of atoms A and B in a system separated by a distance R_{AB}, the pairwise corrective term $E_{disp}^{D3(0)}$ is calculated as follows:

$$E_{disp}^{D3(0)} = -\frac{1}{2}\sum_{A\neq B}\sum_{n=6,8} s_n \frac{C_n^{AB}}{R_{AB}^n} d_n^{D3(0)}(R_{AB}) \qquad (2.16)$$

where s_n is a global scaling parameter that is dependent on the choice of DFT functional, and C_n^{AB} is an nth-order dispersion coefficient based on the atomic charge and polarisability of A and B. The factor of $-\frac{1}{2}$ is present to prevent double counting

any of the atom pairs. A damping function $d_n^{D3(0)}$ is employed to prevent the double-counting of correlation effects at intermediate distances:

$$d_n^{D3(0)} = \frac{1}{1 + 6\left(r_{AB} \,/\, (s_n R_{\mathrm{AB}}^{cut})\right)^{-\alpha_n}} \tag{2.17}$$

where R_{AB}^{cut} is a pre-determined cut-off radius for A and B, and α_n is an empirical "steepness parameter" that ensures physicality at typical covalent bond distances.

2.2.5. DFT+U

Strongly correlated electrons are poorly represented by GGA functionals.[54] When studying f-block materials (e.g. rare earth oxides), GGA functionals struggle to accurately model localised electronic states.[55] If unaccounted for, this deficiency can lead to errors in the electronic band structure and the incorrect assignment of oxidation states. The DFT+U method accounts for this failure by introducing an additive term to the DFT energy. For a set of n electrons, $E_{DFT+U}[\rho]$ is calculated as follows:

$$E_{DFT+U}[\rho] = E_{DFT}[\rho] + E_{Hub}[\{n\}] - E_{dc}[\{n\}] \tag{2.18}$$

where E_{Hub} is the Hubbard model,[56] a functional that helps describe electron localisation in strongly correlated materials. The double-counting corrective energy E_{dc} is a subtractive term that removes interactions already accounted for in the standard DFT energy.

Since the development of DFT+U in the 1990s, several implementation methods have been suggested. The exact construction of E_{dc} can vary widely depending on which DFT+U implementation method is used, but the rotationally invariant method of Liechtenstein *et al.*[57] is one of the oldest. Under this formalism, the double counting term is constructed from two semi-empirical terms: the Coulombic parameter U and the exchange parameter J. In the computational literature, these parameters are often expressed through a single constant, $U_{eff} = U - J$.[58] When calculating E_{dc} (**Equation 2.19**), the following sum is evaluated for each spin-up ($n_i^{\uparrow}$) and spin-down ($n_i^{\downarrow}$) electron across every ith atom, where $n_i = n_i^{\uparrow} + n_i^{\downarrow}$.

$$E_{dc}[\{n_{ij}\}] = \sum_i \frac{1}{2} U n_i (n_i - 1) - \frac{1}{2} J [n_i^{\uparrow}(n_i^{\uparrow} - 1) + n_i^{\downarrow}(n_i^{\downarrow} - 1)] \quad (2.19)$$

A major drawback of the DFT+U formalism is that U_{eff} is highly system specific. Sensible values for U and J can only be determined for a given material through extensive testing, and individual U_{eff} values must be obtained for every element in the system; typically, by fitting the results of benchmark calculations to experimental observables such as band gaps and reaction enthalpies.[59,60] This dependency on semi-empirical tuning undermines the generality and transferability of DFT+U, and limits its usefulness when modelling novel systems with little experimental data to benchmark against. In such cases, modellers may turn to post-GGA methods that can model strongly correlation to a higher degree of accuracy. Examples of such methods include second-order Møller–Plesset perturbation theory (MP2)[61,62] and the random phase approximation (RPA) of Langreth and Perdew.[63] Unfortunately, these methods are severely limited by computational cost. MP2 and RPA are severely limited by computational cost,[64] making them impractical for large periodic systems. As such, despite its limitations, DFT+U remains the more practical choice, and will be the primary method employed for the modelling of strongly correlated materials within this work.

2.2.6. Brillouin Zones and k Points

Despite several decades of computational and theoretical advances, performing DFT calculations on systems with more than a few hundred electrons remains prohibitively computationally expensive. Fortunately, for periodic materials such as metals and ionic crystals, this limitation can be overcome by only performing DFT calculations on the system's unit cell and infinitely repeating it three dimensions. This approach, known as periodic DFT, is one of the most cost-effective ways to accurately model the electronic structure of bulk materials and catalytic systems.

The length of the sides of a three-dimensional unit cell can be expressed in three lattice constants: a, b, and c. For face-centred cubic (fcc) and body-centred cubic (bcc) crystal structures, the unit cell will take the form of a perfect cube. As every side of the cell is uniform in length, only one constant is needed to define it ($a = b = c$). For

hexagonal closed packed (hcp) structures, the unit cell takes the shape of a hexagonal column. Despite this added complexity, only one additional lattice constant is needed to completely describe a hcp unit cell. By setting $a = b$ equal to the basal parameter of the cell and c to its height, the dimensions of the cell can be exactly specified with only two constants (**Figure 2.2**).

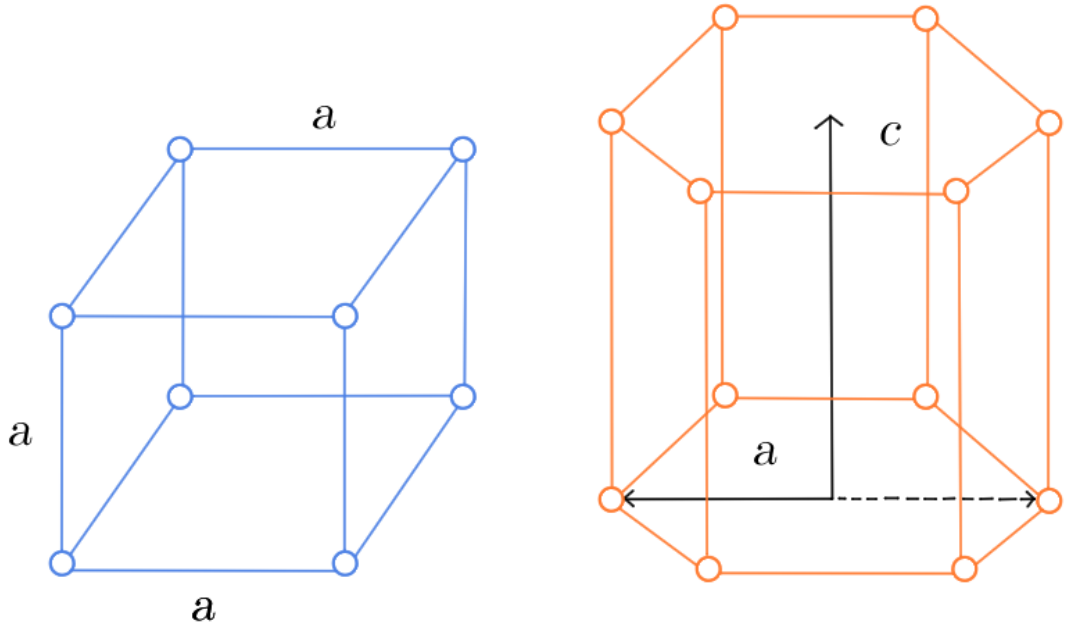

Figure 2.2. Lattice constants for fcc (blue) and hcp (orange) unit cells.

Once the unit cell has been optimised, the full surface may be constructed using the slab model. Under the constraints of this approach, the metal is represented with a periodic supercell, consisting of repeated layers of atoms stacked on top of one another. A large column of empty space known as the vacuum layer is then added to the topmost layer to limit any interaction between the atoms in the top layer and bottom layer. A slab representation of Pd(111) is given in **Figure 2.3**.

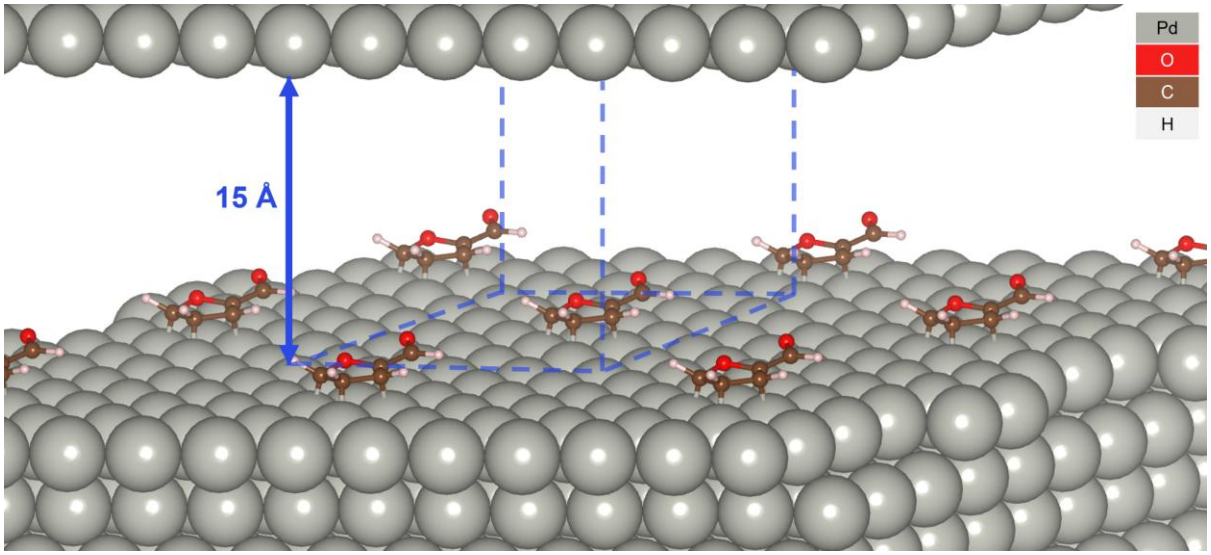

Figure 2.3. *p*(5×5×5) slab model of furfural adsorbed on Pd(111) with 15 Å of vacuum, repeated in a 3×3×2 pattern in Cartesian space. The boundaries of the unit cell are highlighted in blue.

The Brillouin zone of a lattice, commonly referred to as the *first* Brillouin zone in mathematics, is generated by projecting the primitive cell of a lattice in reciprocal space. Graphical representations of the Brillouin zones for bcc, fcc, and hcp crystal systems are given in **Figure 2.4**. Points of high symmetry in a Brillouin zone are known as critical points. An example is the point at the Brillouin's zone centre, known in solid state physics as the Γ-point.

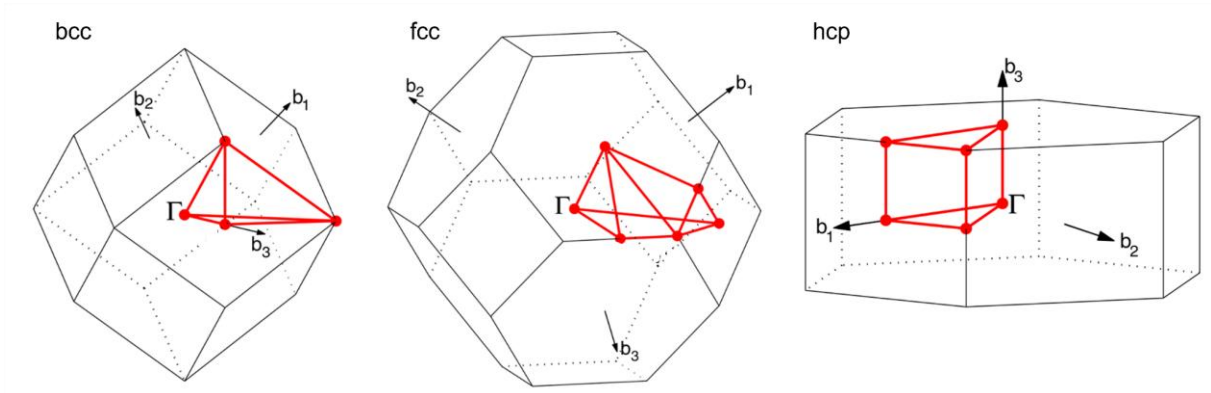

Figure 2.4. Brillouin zones for bcc, fcc and hcp crystal systems. Critical points are highlighted in red. Adapted from Setwayan and Curtarolo (2010).[65]

When a lattice $\boldsymbol{L}$ is projected into reciprocal space, its projection $\boldsymbol{M}$ must satisfy the following relation:

$$e^{i\boldsymbol{L}\cdot\boldsymbol{M}} = \mathbf{1} \tag{2.20}$$

where $\mathbf{1}$ is an identity matrix. For a three-dimensional lattice $\boldsymbol{L} = \boldsymbol{a_1} + \boldsymbol{a_2} + \boldsymbol{a_3}$ whose sides are defined by a set of primitive vectors $\{\boldsymbol{a_1}, \boldsymbol{a_2}, \boldsymbol{a_3}\}$ (i.e. the smallest set of vectors that can generate all possible vectors in the lattice), its projection in reciprocal space $\boldsymbol{M} = \boldsymbol{b_1} + \boldsymbol{b_2} + \boldsymbol{b_3}$ can be generated as follows:

$$\boldsymbol{b_1} = \frac{2\pi}{\Omega}\boldsymbol{l_2} \times \boldsymbol{a_2} \tag{2.21}$$

$$\boldsymbol{b_2} = \frac{2\pi}{\Omega}\boldsymbol{a_1} \times \boldsymbol{a_3} \tag{2.22}$$

$$\boldsymbol{b_3} = \frac{2\pi}{\Omega}\boldsymbol{a_1} \times \boldsymbol{a_2} \tag{2.23}$$

where $\Omega = \boldsymbol{a_1} \cdot (\boldsymbol{a_2} \times \boldsymbol{a_3}) = \boldsymbol{a_2} \cdot (\boldsymbol{a_3} \times \boldsymbol{a_1}) = \boldsymbol{a_3} \cdot (\boldsymbol{a_1} \times \boldsymbol{a_2})$ is the scalar triple product. It should be highlighted that the factor of 2π is an optional addition to **Equations 2.21 – 2.23**. While the factor is included by convention in solid state physics, it is often dropped in X-ray crystallography.[66,67] An advantage of constructing a set of primitive vectors in this fashion is that, for any $\boldsymbol{b_i}$ and $\boldsymbol{a_j}$, the orthogonality relation (**Equation 2.24**) will be automatically satisfied, where δ_{ij} is the Kronecker delta (**Equation 2.25**).

$$\boldsymbol{b_i} \cdot \boldsymbol{a_j} = 2\pi\delta_{ij} \tag{2.24}$$

$$\delta_{ij} = \begin{cases} 1 & i = j \\ 0 & i \neq j \end{cases} \tag{2.25}$$

As shown by Ashcroft and Mermin,[66] $\{\boldsymbol{b_1}, \boldsymbol{b_2}, \boldsymbol{b_3}\}$ is also a set of primitive lattice vectors for the Brillouin zone. Consequently, any three-dimensional vector in reciprocal space $\boldsymbol{x}$ can be expressed as the linear sum $\boldsymbol{x} = x_1\boldsymbol{b_1} + x_2\boldsymbol{b_2} + x_3\boldsymbol{b_3}$ for some set of constants $\{x_1, x_2, x_3\}$, thus providing a convenient framework for the

analysis of periodic wave functions. In accordance with Bloch's theorem (**Equation 2.26**),[68] the time-independent wave function $\psi(\boldsymbol{r})$ associated with each electron in a perfect crystal must be expressible in the following form for some vector $\boldsymbol{k}$ known in solid state physics as the wave vector, and a periodic function of position in real space $u(\boldsymbol{r})$ with the same periodicity as the crystal.

$$\psi(\boldsymbol{r}) = u(\boldsymbol{r}) \cdot \mathrm{e}^{\mathrm{i}\boldsymbol{k}\boldsymbol{r}} \tag{2.26}$$

Wave vectors and the periodic functions associated with them are not unique for given wave functions. In fact, for any valid wave function, an infinite number of solutions to **Equation 2.26** can be generated by setting $\boldsymbol{k} = \boldsymbol{k} + \boldsymbol{k}'$, where $\boldsymbol{k}'$ is any lattice vector of the system in reciprocal space. However, the Brillouin zone of the lattice can be uniquely defined by a linearly independent set of reciprocal lattice vectors $\boldsymbol{b_1}$, $\boldsymbol{b_2}$, and $\boldsymbol{b_3}$. Therefore, by restricting sampling of the reciprocal lattice to the Brillouin zone, the resultant wave vectors will form a linearly independent basis set. These wave vectors can then be used to generate solutions to the individual Schrödinger equations associated with the electrons in the system without redundancy. In this context, wave vectors are more commonly referred to in the computational chemistry literature as $\boldsymbol{k}$ points. Under the Monkhorst-Pack scheme,[69] the partition scheme used in all calculations in this thesis, uniform grids of $\boldsymbol{k}$ points are generated as linear combinations of $\boldsymbol{b_1}$, $\boldsymbol{b_2}$, and $\boldsymbol{b_3}$:

$$\boldsymbol{k} = \frac{2n_1 + 1 - N_1}{2N_1}\boldsymbol{b_1} + \frac{2n_2 + 1 - N_2}{2N_2}\boldsymbol{b_2} + \frac{2n_3 + 1 - N_3}{2N_3}\boldsymbol{b_3} \tag{2.27}$$

where N_1, N_2, and N_3 define the number of subdivisions along each reciprocal lattice vector for all integers $0 \leq n_i \leq N_i - 1$.

If N_1, N_2, and N_3 are large, more points along the reciprocal lattice vectors will be sampled, giving a more accurate representation of the Brillouin zone, but this can lead to impractically long convergence times. Conversely, smaller grids lead to quicker convergence, but can introduce significant sampling errors. With this in mind, researchers must make a careful compromise between physical accuracy and computational cost when specifying values for N_1, N_2, and N_3.

2.3. Applications of DFT to Catalysis

Once a suitable exchange correlation functional and a robust $\boldsymbol{k}$ point partition scheme have been selected, DFT modelling software can be used to model heterogeneous catalytic systems at the quantum mechanical level. This section outlines how DFT can be applied to compute a selection of key physical and chemical properties relevant to catalysis. Experimental parameters such as the bulk modulus of a catalyst (**Section 2.3.1**), the surface energy of its facets (**Section 2.3.2**), and the adsorption energy of any reactants or intermediates (**Section 2.3.3**) can be calculated directly from DFT calculations, even for catalytic systems where measuring these quantities experimentally remains a practical impossibility. Purely computational descriptors such as net atomic charge (**Section 2.3.4)** and projected density of states plots (**Section 2.3.5)** can also be used to provide further insight into the electronic structure of the catalyst and its interactions with adsorbates.

2.3.1. Bulk Modulus

The isothermal bulk modulus (B) of a solid is a measure of its resistance to uniform compression at constant temperature. Due to the relative ease with which bulk moduli can be measured both experimentally and computationally, they are often used as benchmarks in computational chemistry and solid state physics. The bulk modulus of a solid can be measured experimentally by applying a pressure p and measuring the change in volume at constant temperature T:

$$B = \left(\frac{pV_I}{V_I - V_F}\right)_T \tag{2.28}$$

where V_I and V_F are the initial and final volumes of the material, respectively. Computationally, the bulk modulus can be determined by conducting a series of geometry optimisation calculations on the material's unit cell, each at a slightly different volume near the equilibrium geometry. By plotting the energy as a function of volume, the bulk modulus can be determined by using an equivalent form of **Equation 2.28** that takes the second derivative of the energy at equilibrium:

$$B = V_0 \left(\frac{d^2 E}{dV^2} \right)_{V=V_0} \tag{2.29}$$

where V_0 is the equilibrium volume of the unit cell.

2.3.2. Surface Energy

Surface energy is defined as the energy required to cleave a particular surface from the bulk material. For a completely relaxed metal slab, its surface energy γ can be calculated as follows:

$$\gamma = \frac{E_{SUR} - nE_{BLK}}{2A} \tag{2.30}$$

where E_{SUR} is the ground-state energy of the slab, n is the total number of atoms in the slab, E_{BLK} is the per atom ground-state energy of the bulk, and A is the surface area of the exposed plane. As the face is exposed on both the top and bottom of the slab, a factor of $\frac{1}{2}$ is present to avoid double counting the surface energy.

Given the practical difficulties involved in preparing perfect surfaces along given crystal planes, absolute values for surface energy are difficult to measure experimentally.[70,71] As such, they are commonly expressed in the analytical literature as ratios of one another (e.g. $\gamma_{Pd(111)}/\gamma_{Pd(001)}$). However, predicted values for γ from periodic DFT calculations have shown good agreement with these ratios, which can be experimentally determined via scanning tunnelling microscopy.[72]

2.3.3. Adsorption Energy

In heterogeneous catalysis, it is often useful to calculate the adsorption energy (E_{ads}) of the adsorbates over a given catalyst. Following Sabatier's principle,[73] the adsorption of active species to a catalyst is a critical factor when determining the rate of a heterogeneous process. The catalyst must bind the reactants strongly enough to activate them, but not so strongly that it inhibits product desorption. A large and negative E_{ads} signifies that adsorption is exoergic, implying strong binding interactions

between the adsorbate and the catalyst. Conversely, a positive E_{ads} indicates endoergic and thermodynamically unfavourable adsorption.

For a given system where a substrate Y binds to the surface of a catalyst, E_{ads} is defined as follows:

$$E_{ads} = E_{Y*} - E_{*} - E_{Y} \tag{2.31}$$

where E_{Y*} is the ground state energy of Y adsorbed to the surface, E_{*} is the ground state energy of the naked surface, and E_{Y} is the ground state energy of the unbound substrate.

2.3.4. Charge Analysis

After geometry optimisation, it is often useful to conduct a second round of analysis to determine the distribution of electronic charge across individual atoms. Methods for the assignment of net atomic charges (NACs) have been available since the 1950s, but the computational chemistry community has yet to reach a consensus on the "best" method for NAC determination. Mulliken charge analysis,[74] one of the oldest charge partition methods in quantum chemistry, is fast and easy to implement, but this comes at the cost of a heavy dependency on basis set choice. Counter-intuitively, Mulliken charge analysis generally becomes less accurate as the quality and size of the basis set improves, leading to poor predictions for tightly optimised systems.[75–77] The Hirshfeld method,[78] developed in response to Mulliken's work in 1977, is both more accurate and far less dependent on the modeller's choice of basis set, but is known to underestimate molecular dipole moments and the charge densities on metal centres.[79] In 1985, the field was further advanced by the development of the Bader method,[80,81] a scheme that assigns partial charges by dividing the electron density into a collection of "atomic basins" centred on the nuclei in the system and assessing the NAC of each basin. For converged electronic structures, the Bader method is independent of basis set,[82] but dense $\boldsymbol{k}$ point grids are needed to accurately determine the NACs; a requirement that can incur significant computational cost for large systems.[83,84] Furthermore, even if the electron density is thoroughly sampled, covalent bonds with large dipole moments (e.g. O–H) are poorly handled by the Bader method's basin

partition scheme, often leading to the gross overestimation of NACs associated with these bonds.[85,86]

One of the most robust methods in the field of charge analysis is the density derived electronic and chemical (DDEC) family of population analysis schemes, first developed by Manz and Scholl in 2010.[87,88] As of 2016, the most recently developed method in this family is DDEC6.[89,90] NACs generated with DDEC6 are completely independent of basis set, and the method has performed favourably in systemic reviews of charge analysis schemes.[91,92] Unlike other high-ranking charge analysis methods such as the natural population analysis of Reed *et al.*,[93] DDEC6 analysis was designed to work regardless of the periodicity of the system, and can be easily conducted for periodic structures through the population analysis package CHARGEMOL.[87–90] In all DDEC methods, the NAC of a given atom A (q_A) is calculated by evaluating the following contour integral:

$$q_A = z_A - \oint \rho_A(\boldsymbol{r}_A)\,\mathrm{d}\boldsymbol{r}_A \tag{2.32}$$

where z_A is the nuclear charge of atom A and $\rho_A(\boldsymbol{r}_A)$ is the local electron density of the atom at $\boldsymbol{r}_A$. The manner in which $\rho_A(\boldsymbol{r}_A)$ is evaluated depends on the specific DDEC method employed. In DDEC6, it is approximated as follows:

$$\rho_A(\boldsymbol{r}_A) \approx \rho_A^{ion}(\boldsymbol{r}_A) \cdot \hat{S}\left[\frac{\rho(\boldsymbol{r})}{w^{DDEC6}(\boldsymbol{r})}\right]_{\boldsymbol{r}_A} \tag{2.33}$$

where $\rho_A^{ion}(\boldsymbol{r})$ is a reference electron density for atom A in a specified ionic state, taken from an pre-tabulated library.[88] $w^{DDEC6}(\boldsymbol{r})$ is a weight function that accounts for overlapping regions of electron density between individual atoms. The operator $\hat{S}$ computes the "spherical average" of the local electron density about $\boldsymbol{r}_A$, thus ensuring that $\rho_A(\boldsymbol{r}_A)$ is spatially continuous and spherically symmetrical. Further detail on spherical averaging is provided in Manz and Limas (2016).[89]

2.3.5. DOS and PDOS

The density of states (DOS) of a solid $D(E)$ is a measure of the number of different states that an electron with energy E can occupy. For a periodic system with n accessible energy levels, the DOS can be expressed as a sum of a series of integrals across the Brillouin zone with respect to each $\boldsymbol{k}$ point:

$$D(E) = \frac{S_e V_{cell}}{8\pi^3} \sum_n \int_{BZ} \delta(E - \varepsilon_n(\boldsymbol{k}))\, d\boldsymbol{k} \tag{2.34}$$

where V_{cell} is the volume of the unit cell, and $\varepsilon_n(\boldsymbol{k})$ is the one-electron energy eigenstate (i.e. the solution to **Equation 2.3**) at energy level n. The spin-degeneracy factor S_e is set to 1 for spin-polarised systems, where each energy eigenstate contributes to a spin-up or spin-down electron, and to 2 for spin-degenerate systems, where each energy eigenstate contributes to a pair of electrons with opposite spins.[94] The Dirac delta function $\delta(x)$ (**Equations 2.35** – **2.37**) is used to ensure that only eigenstates $\varepsilon_n(\boldsymbol{k}) = E$ contribute to $D(E)$.

$$\delta(x) = \begin{cases} \infty & x = 0 \\ 0 & x \neq 0 \end{cases} \tag{2.35}$$

$$\int_{-\infty}^{\infty} \delta(x) = 1 \tag{2.36}$$

$$\int_{-\infty}^{\infty} f(x) \cdot \delta(x - a) = f(a) \tag{2.37}$$

Due to the large number of unoccupied energy eigenstates that may contribute to $D(E)$ for a given solid, experimentally measuring the "complete" $D(E)$ of solid materials remains a challenging problem in condensed matter physics. However, occupied states can be studied through photo-emission spectroscopy (PES). This is typically easiest at energy levels close to the Fermi level (E_F), the minimum energy required to add a single electron to a solid. Above 0 K, the occupancy of energy levels close to the Fermi level can be measured using the Fermi-Dirac distribution (**Equation 2.38**), a function that calculates the probability that a level with energy E will be occupied by

an electron at temperature T. As shown in **Figure 2.5**, this probability is equal to 0.5 at $E = E_F$.

$$F(E) = \left(1 + e^{\frac{E-E_F}{k_B T}}\right)^{-1} \tag{2.38}$$

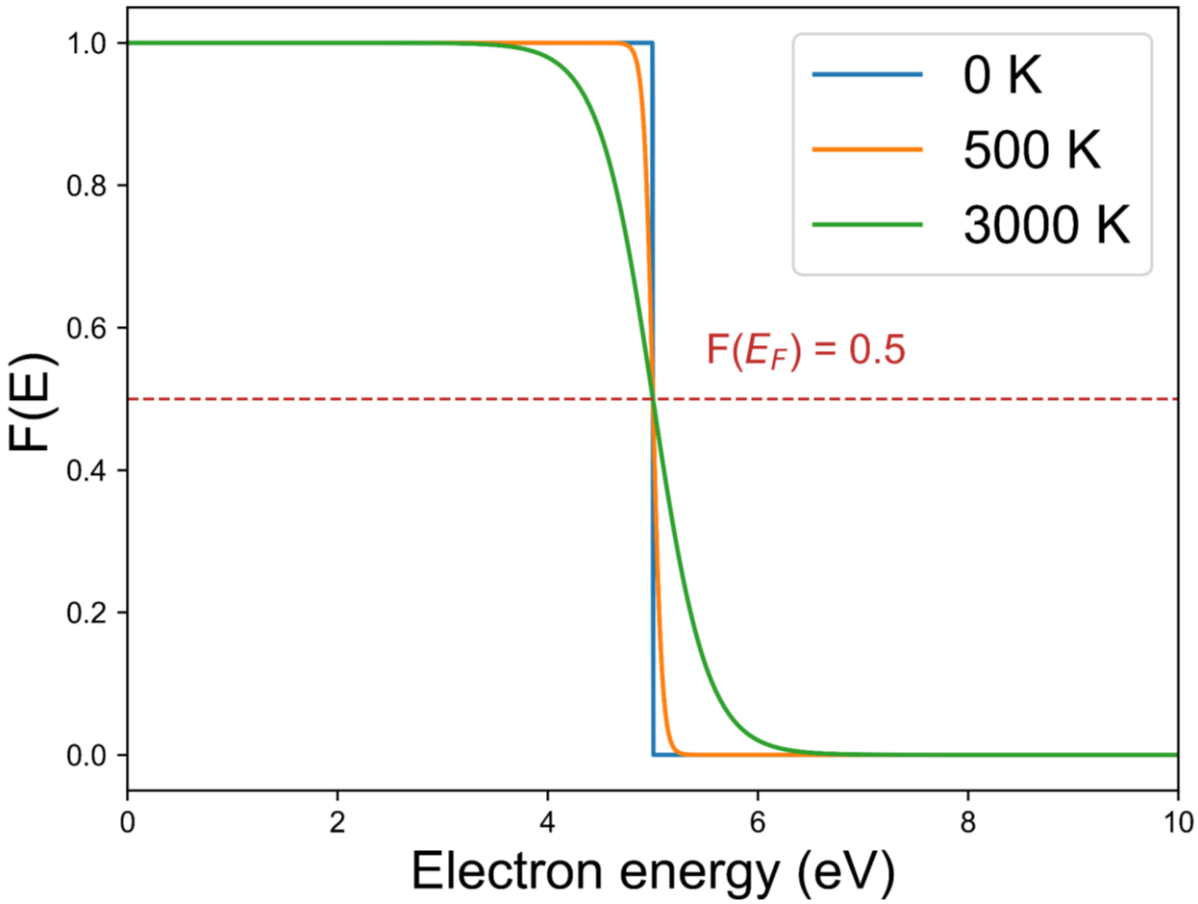

Figure 2.5. Fermi-Dirac distribution plots for a model system with a Fermi level of 5 eV. Plots taken at 0 K (blue), 500 K (orange), and 3000 K (green).

On its own, the Fermi-Dirac distribution will predict the occupancy of an energy level, but unless the compound's band structure has been thoroughly characterised beforehand, it cannot be used to deduce the contributions of specific atomic orbitals (AOs). For pure, homogeneous materials, AO occupation can be determined via X-ray absorption spectroscopy (XAS)[95–97] and resonant inelastic X-ray scattering (RIXS),[98,99] but these techniques are limited by their cost, high sensitivity to phase inhomogeneity, and their impracticality for beam-sensitive materials such as organic matter and zeolites.[100–102] Alternatively, the results of an electronic structure DFT calculation with a suitably dense $\boldsymbol{k}$ point grid[103] can be used to construct a projected

density of states (PDOS) plot, a computational technique that decomposes the DOS into a series of contributions from individual AOs. As well as allowing for the calculation of the band gap between different orbitals, PDOS plots can be used to analyse the binding character[104,105] and degree of orbital hybridisation[96,106,107] present in catalytic systems. For instance, highly populated d-orbitals close to the Fermi level are indicative of strong metallic character,[104] and a strong degree of p-d hybridisation in transition metal oxides has been shown to correlate with enhanced electronic conductivity and catalytic performance.[108,109]

2.3.6. The Langmuir-Hinshelwood and Eley-Rideal Mechanisms

Bimolecular reactions over heterogeneous catalysts typically proceed via one of two mechanisms. Under the Langmuir-Hinshelwood mechanism (**Figure 2.6a**), two reagents A and B adsorb to the catalyst and react with one another over the surface. The product, AB, then desorbs from the catalyst. Meanwhile, under the Eley-Rideal mechanism (**Figure 2.6b**), also known as the Langmuir-Rideal mechanism, one of the reagents adsorbs to the surface and is then attacked by the other directly from the gas or liquid phase. As highlighted by Prins,[110] the term “Eley-Rideal” is a historical misnomer, and originally referred to a mechanism in D.D. Eley’s doctoral thesis, in which one reagent was chemisorbed to the catalyst, while the other was physisorbed.[110–112] However, in contemporary usage, the term has been broadened to refer to all reactions in which one reagent is non-chemisorbed, and will thus be used in this fashion for the remainder of this thesis.

Generally, it is uncommon for Eley-Rideal kinetics to outcompete Langmuir-Hinshelwood kinetics in heterogeneous catalysis.[113–115] As the reagent approaches a surface, the probability it will enter an energetic well associated with chemisorption increases.[113,116] The probability of a mechanism being dominated by Langmuir-Hinshelwood kinetics further increases if the reagents are known to form strong bonds with the catalysts. Consequently, it was assumed that the kinetic profile of all reactions in this thesis would be dominated by the Langmuir-Hinshelwood mechanism.

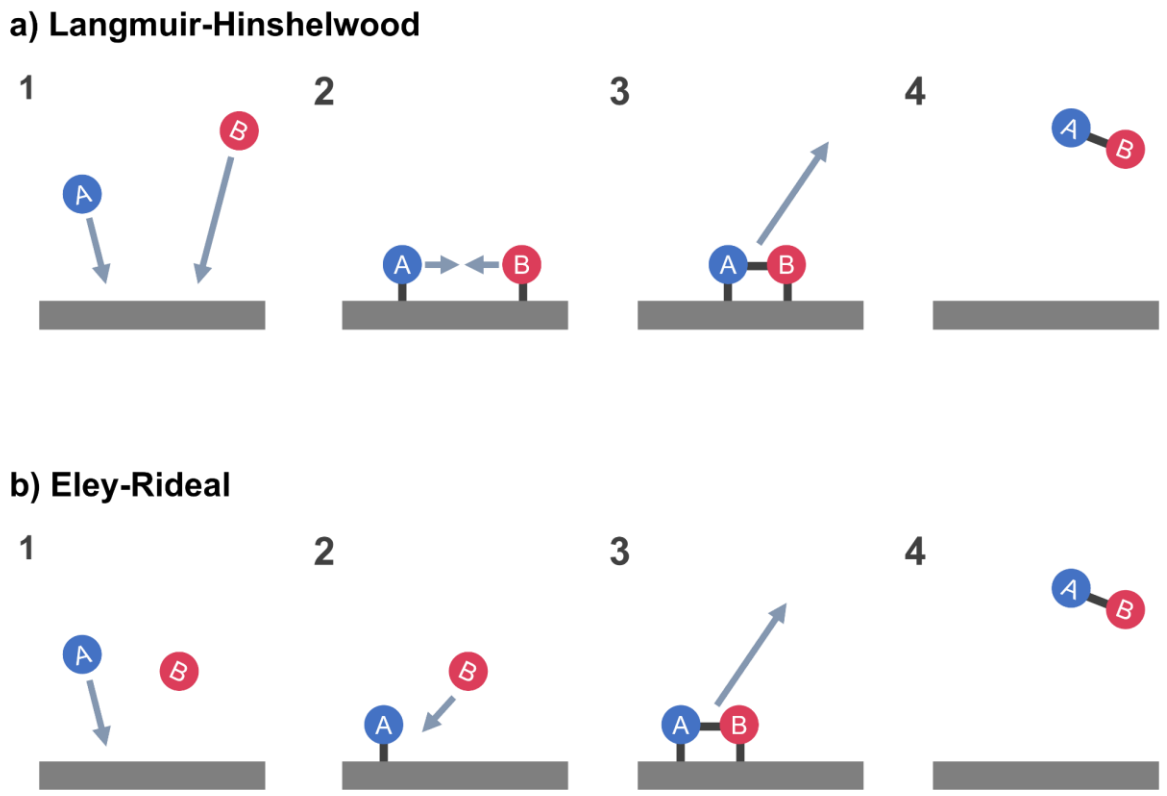

Figure 2.6. Representation of the (a) Langmuir-Hinshelwood and (b) Eley-Rideal mechanisms over a transition metal catalyst. In steps 2a and 2b, reagent B can be physisorbed to the catalyst's surface.

2.3.7. Computational Spectroscopy

Once the geometry of a compound has been optimised, further DFT calculations can be performed to predict its spectroscopic properties. One of the most common ways to calculate a chemical system's vibrational modes is the *finite displacement method*. Every ith atom in the system is moved a small distance $\pm u$ from its equilibrium position along each Cartesian direction $d \in \{x, y, z\}$. Single point energy calculations are then performed after each displacement to evaluate the forces on all atoms in the system following positive $(F_{i,d}^{+})$ and negative $(F_{i,d}^{-})$ displacements along d. The second derivative of the energy at equilibrium with respect to coordinates $u_{i,d}$ and $u_{i',d'}$ is then approximated as follows:

$$\frac{\partial F_{i,d}}{\partial u} \approx \frac{\partial^2 E_0}{\partial u_{i,d} \partial u_{i',d'}} = \frac{F_{i,d}^{+} - F_{i,d}^{-}}{2u} \tag{2.39}$$

Each second derivative calculated using the finite displacement method corresponds to an element of the Hessian ($\mathbf{H}$), a $3N \times 3N$ matrix describing the curvature of the PES, where N is the total number of atoms in the system. The mass-weighted Hessian ($\mathbf{H}_{mw}$) is then calculated as follows:

$$\mathbf{H}_{mw} = \mathbf{M}^{-1/2}\mathbf{H}\mathbf{M}^{1/2} \tag{2.40}$$

where $\mathbf{M}$ is a diagonal matrix containing the masses of all atoms in the system. Each eigenvalue of $\mathbf{H}_{mw}$ (λ_i) corresponds to a normal vibrational mode ν_i (**Equation 2.41**). Depending on the symmetry of the system, five (for linear molecules) or six (for non-linear molecules) of these modes will correspond to rotation and translation. As these operations do not change the energy of the system, their corresponding eigenvalues should, in principle, equal zero, but small numerical inaccuracies in the calculation of the Hessian can result in low magnitude imaginary frequencies.[117]

$$\nu_i = \frac{\sqrt{\lambda_i}}{2\pi} \tag{2.41}$$

The remaining eigenvalues of $\mathbf{H}_{mw}$ correspond to vibrational modes that may be observed experimentally by infrared (IR) spectroscopy. Under the double harmonic approximation, in which higher-order contributions to the energy and electric dipole moment $\boldsymbol{\mu}$ are neglected,[118,119] the IR intensity of the ith vibrational mode I_i can be approximated as follows:

$$I_i \approx \frac{n_{pd}\pi}{3c}\left|\frac{d\boldsymbol{\mu}}{dQ_i}\right|^2 \tag{2.42}$$

where n_{pd} is the particle density and c is the speed of light. Normal-mode coordinates (Q_i) are calculated as follows:

$$Q_i = \frac{u_{i,d}}{X_{i,d}} \tag{2.43}$$

where $X_{i,d}$ is the ith eigenvector of the mass-weighted Hessian along d.

2.4. Transition State Theory

When studying the mechanism of a chemical reaction, a critical step is the identification of its associated minimum energy path (MEP), the pathway along the potential energy surface (PES) from the reactant to the product with the smallest changes in energy between the intermediates. While a reaction *can* proceed via many possible pathways, the MEP is, by definition, the most energetically favourable, and is thus the most statistically likely pathway to occur.

Once the energetic minima of the MEP have been optimised, work can begin on identifying the *transition states*, intermediates corresponding to energetic maxima between each elementary step. On the PES, these states correspond to *first-order saddle points*, where the energy of the system is at a maximum along the MEP and at a minimum in all other directions. Due to the negative curvature at this point in the direction of the MEP, a single negative vibrational eigenvalue will be present. As the frequency is equal to the square root of the corresponding vibrational eigenvalue, this will result in the presence of a single imaginary frequency corresponding to motion along the MEP (e.g. bond formation or dissociation).[120] In vanishingly rare cases, higher-order saddle points can indicate the presence of alternative mechanisms that must be taken into consideration. For instance, a 2019 computational study by Pradhan and Lourderaj[121] showed that the denitrogenation of 1-pyrazoline can theoretically proceed via a second-order saddle point. However, in the vast majority of cases, the additional imaginary frequencies typically correspond to low intensity intramolecular rotations (e.g. terminating methyl groups).

By definition, transition states are less energetically stable than their corresponding minima, and are difficult to observe experimentally. “Long-lived” transition states have been detected via ultrafast pulse spectroscopy,[122,123] but their lifetimes rarely exceed the femtosecond scale, even if the measurement is taken at temperatures close to absolute zero. Fortunately, computational chemists have an enormous number of tools at their disposal to predict the chemical structures of transition states once the MEP has been identified.

2.4.1. NEB, CI-NEB, and NEB-TS

One of the most popular ways to computationally model the MEP of a given reaction is the nudged elastic band method (NEB). In a NEB calculation, a set of images is generated across the reaction coordinate. All of the images then undergo constrained optimisation in parallel with one another, with spring forces between the images to enforce equal spacing to their neighbours. Provided the intermediate structures are correct, the optimised pathway will closely model the true MEP, allowing for the calculation of the activation energy.

Early NEB scripts were useful for generating an outline of a reaction's MEP, but it often took multiple attempts to accurately calculate the activation energy of the reaction. If one of the images did not correspond to a first-order saddle point, the "true" transition state of the reaction would be missed, leading to an underestimation of the activation energy. This, combined with the heavy computational resources required to run even a single NEB calculation from start to finish, was one of the largest practical barrier for researchers when the field was in its infancy.

To amend this, a refinement of NEB designed specifically for the calculation of activation energies was developed by Henkelman and Jónsson[124] called the climbing image nudged elastic band method (CI-NEB). In a CI-NEB calculation, the image with the highest energy after optimisation is unrestrained by spring forces, and is allowed to "climb" up the energy profile until it reaches the saddle point. The other images are optimised normally, and provide the purpose of defining the rest of the MEP.

In the twenty years since its development, CI-NEB has generally been acknowledged by the computational chemistry community as the superior modelling method to NEB. However, both methods suffer from slow convergence, particularly for large systems. In 2021, a new approach called NEB-TS was developed by Ásgeirsson *et al.*[125] to improve the efficiency of PES searches. A NEB-TS calculation is divided into two halves. In the first half, CI-NEB is used to approximate the minimum energy path until the forces acting on the climbing image drop below a user-defined threshold. Next, a new transition state search begins from the climbing image along an eigenvector of the initial Hessian. The search continues uphill along this trajectory until it reaches a saddle point. If the initial CI-NEB calculation was carried out successfully, this saddle point will correspond to the true transition state (**Figure 2.7**).

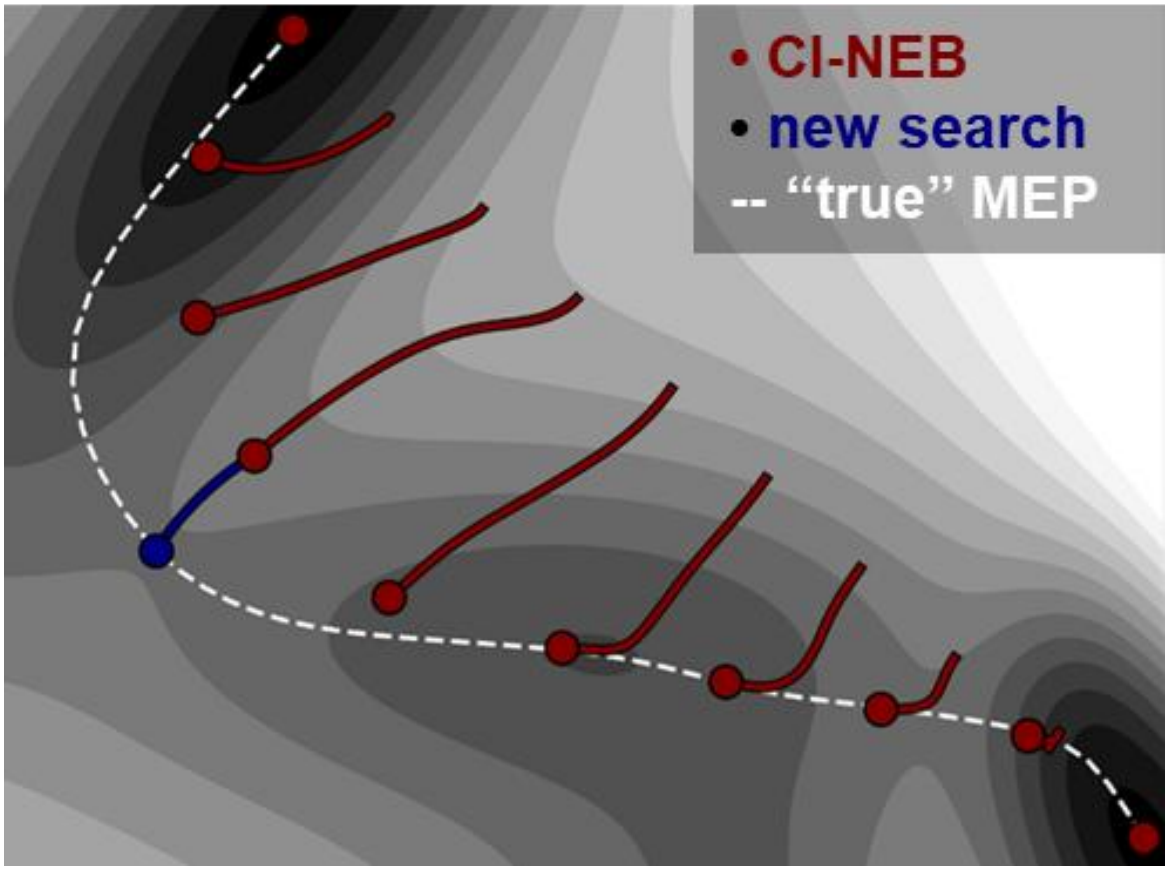

Figure 2.7. Points of a NEB-TS calculation on a potential energy surface. The saddle point search begins with a CI-NEB calculation (crimson). Once the force threshold has been reached, a new search starts (blue) starts from the climbing image until a saddle point is found. Adapted from Ásgeirsson *et al.* (2021).[125]

The original NEB-TS paper[125] included a benchmarking study, comparing the performance of NEB-TS and CI-NEB on over a hundred different reactions. This study confirmed that NEB-TS offers a substantial improvement in both efficiency and accuracy over its predecessors. Provided the user is careful with their choice of force threshold, NEB-TS can provide a significant increase in the speed of transition state searches, making it an attractive choice for modellers looking to study large systems at the DFT level.

2.4.2. The Dimer Method

Alongside their work on the nudged elastic band method, Henkelman and Jónsson[126] also developed the dimer method, a local search algorithm that uses first derivatives of the system's potential energy to identify saddle points on the potential energy surface. By definition, a NEB calculation requires multiple images to construct a model of the MEP, and the accuracy of the results will always be limited by the number of

images the chemist can afford to model along the reaction coordinate. Five image NEB calculations are generally satisfactory for most systems of interest to surface chemists, but more images may be required for high accuracy simulations work.[127] In contrast, the dimer method only requires a single trial structure corresponding to the transition state. As shown in **Figure 2.8**, the dimer method can be broken down into four stages. First, a vector across the PES known as the dimer axis ($\boldsymbol{u}_\xi$) is defined by conducting a frequency calculation on a trial structure $\boldsymbol{q}$ and extracting a negative vibrational mode corresponding to the chemical process in question (e.g. bond formation). Next, the energies and forces of $\boldsymbol{q}$ and the structure corresponding to the "end" of the dimer axis ($\boldsymbol{q} + \delta\boldsymbol{u}_\xi$) are evaluated. In the third stage, the dimer axis is rotated through a pre-defined angle ϕ_1 so that it becomes parallel to the direction of maximum negative curvature across the PES. Finally, a second rotation is performed about the angle that minimises the negative curvature along the dimer (ϕ_{min}). The search then continues along a new vector $\boldsymbol{q} + \epsilon\overline{\boldsymbol{N}}$, which moves "uphill" in an orthogonal direction from $\boldsymbol{u}_\xi$. Here, ϵ is a trial step size for the movement of the atoms between iterations. Following the recommendations of Heyden, Bell, and Keil,[128] ϵ = ±0.01 Å per atom was judged to be satisfactory for all transition state calculations in this work.

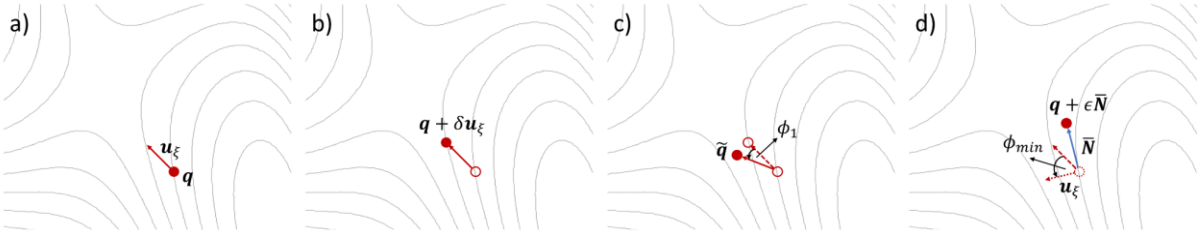

Figure 2.8. The four steps of the improved dimer method: (a) defining the dimer axis; (b) evaluating the forces and energies of the endpoints; (c) rotating the dimer axis to minimise the curvature; (d) continuing the search in an orthogonal direction if a saddle point has not been found. Adapted from Bucko (2024).[129]

An advantage of the improved dimer method is that the Hessian does not need to be explicitly evaluated at any point. Instead, the termination condition of the transition state search is governed by a user-determined force threshold. After each iteration, the potential energy is maximised along the dimer axis and minimised in all other directions. In principle, if the force threshold is tight enough, the search will continue until a saddle point is reached, indicating that a transition state has been found. Due to the expense of evaluating the Hessian for each individual atom, this makes dimer

calculations particularly attractive for transition states searches involving large numbers of atoms. The efficiency of dimer calculations in recent years has been further improved by the development of the improved dimer method, a variant of the original algorithm developed by Heyden, Bell, and Kiel[128] that significantly reduces the numerical noise associated with the PES search.

The dimer method is significantly less computationally demanding than NEB-based methods, but it is not an approach without its flaws. By definition, NEB calculations optimise images at each step along the MEP associated with the reaction. If the mechanism of the reaction is well known, the chances of atoms “hopping” to positions that correspond to incorrect saddle points on the PES are relatively small. The dimer method, meanwhile, can often prematurely end the PES search at higher-order saddle points. A cheap and straightforward way to validate dimer calculations that has since been adopted as standard practice is to run an additional frequency calculation on the optimised structure. If a single imaginary frequency is present, the structure corresponds to a saddle point on the PES, thus confirming that a true transition state has been found.

2.5. References

1. D. J. Griffiths and D. F. Schroeter, *Introduction to Quantum Mechanics*, Cambridge University Press, 3rd edn., **2018**.
2. J. Macek, *J. Phys. B At. Mol. Phys.*, **1968**, 1, 831.
3. M. Born and R. Oppenheimer, *Ann. Phys.*, **1927**, 389, 457–484.
4. H. L. Accorinti and J. C. M. González, *Philos. Perspect. Quantum Chem.*, **2022**, 107–124.
5. L. Pauling and E. B. Wilson, *Introduction to Quantum Mechanics with Applications to Chemistry*, McGraw-Hill Book Company, **1935**.
6. E. U. Condon, *Am. J. Phys.*, **1947**, 15, 365–374.
7. H. Mustroph, *ChemPhysChem*, **2016**, 17, 2616–2629.
8. P. R. Bunker, *J. Mol. Spectrosc.*, **1972**, 5, 478–494.
9. P. W. Atkins and R. S. Friedman, *Molecular Quantum Mechanics*, Oxford University Press, 4th edn., **2005**.
10. C. D. Gelatt and U. von Barth, *Phys. Rev. B*, **1980**, 21, 2222.
11. J. F. Janak, *Solid State Commun.*, **1976**, 20, 151–153.
12. Y. Minami, K. Araki, T. D. Dao, T. Nagao, M. Kitajima, J. Takeda and I. Katayama, *Sci. Rep.*, **2015**, 5, 15870.
13. Y. Fuseya, M. Ogata and H. Fukuyama, *J. Phys. Soc. Jpn.*, **2015**, 84, 012001.
14. K. C. Chitrada, K. S. Raja, R. Gakhar and D. Chidambaram, *J. Electrochem. Soc.*, **2015**, 162, H380.
15. F. Wang, G. Hong and L. Li, *Chem. Phys.*, **2001**, 263, 271–278.
16. P. Hohenberg and W. Kohn, *Phys. Rev.*, **1964**, 136, B864.

17. C. J. Cramer, *Essentials of Computational Chemistry: Theories and Models*, John Wiley & Sons, 2nd edn., **2004**.
18. W. Kohn and L. J. Sham, *Phys. Rev.*, **1965**, 140, A1133–A1138.
19. L. H. Thomas, *Math. Proc. Camb. Philos. Soc.*, **1927**, 23, 542–548.
20. E. Fermi, *Z Phys*, **1928**, 48, 73–79.
21. I. G. Kaplan, *Mol. Phys.*, **2018**, 116, 658–665.
22. A. D. Becke, *J. Chem. Phys.*, **2014**, 140, 18A301.
23. C. Lee, W. Yang and R. G. Parr, *Phys. Rev. B*, **1988**, 37, 785–789.
24. A. D. Becke, *J. Chem. Phys.*, **1993**, 98, 1372–1377.
25. J. P. Perdew, K. Burke and M. Ernzerhof, *Phys. Rev. Lett.*, **1996**, 77, 3865–3868.
26. J. H. McGuire, *Electron Correlation Dynamics in Atomic Collisions*, Cambridge University Press, **2005**.
27. D. R. Hartree, *Math. Proc. Camb. Philos. Soc.*, **1928**, 24, 89–110.
28. V. Fock, *Z. Für Phys.*, **1930**, 61, 126–148.
29. M. Hofmann and H. F. Schaefer, in *Encyclopedia of Physical Science and Technology*, Academic Press, New York, 3rd edn., **2003**, pp. 487–506.
30. S. H. Vosko, L. Wilk and M. Nusair, *Can. J. Phys.*, **1980**, 58, 1049–1258.
31. F. Jensen, *Introduction to Computational Chemistry*, John Wiley & Sons, 3rd edn., **2017**.
32. M. Fuchs, J. L. F. Da Silva, C. Stampfl, J. Neugebauer and M. Scheffler, *Phys. Rev. B - Condens. Matter Mater. Phys.*, **2002**, 65, 2452121–24521213.
33. A. van de Walle and G. Ceder, *Phys. Rev. B - Condens. Matter Mater. Phys.*, **1999**, 59, 14992–15001.
34. P. Morgante and R. Peverati, *Int. J. Quantum Chem.*, **2020**, 120, e26332.
35. S. Lehtola, C. Steigemann, M. J. T. Oliveira and M. A. L. Marques, *SoftwareX*, **2018**, 7, 1–5.
36. M. Ernzerhof and G. E. Scuseria, *J. Chem. Phys.*, **1999**, 110, 5029–5036.
37. G. L. Oliver and J. P. Perdew, *Phys. Rev. A*, **1979**, 20, 397–403.
38. S. Moroni, D. M. Ceperley and G. Senatore, *Phys Rev Lett*, **1995**, 75, 689.
39. M. Levy and J. P. Perdew, *Phys. Rev. A*, **1985**, 32, 2010–2021.
40. Y. Wang and J. P. Perdew, *Phys. Rev. B*, **1991**, 43, 8911–8916.
41. E. H. Lieb and S. Oxford, *Int. J. Quantum Chem.*, **1981**, 19, 427–439.
42. A. Laestadius and F. M. Faulstich, *J. Chem. Phys.*, **2020**, 152, 234112.
43. A. Vela, V. Medel and S. B. Trickey, *J. Chem. Phys.*, **2009**, 130, 244103.
44. G. Kin-Lic Chan and N. C. Handy, *Phys. Rev. A*, **1999**, 59, 3075–3077.
45. M. Lewin, E. H. Lieb and R. Seiringer, *Phys. Rev. B*, **2019**, 100, 035127.
46. A. D. Becke, *J. Chem. Phys.*, **1986**, 84, 4524–4529.
47. Y. Zhang and W. Yang, *Phys. Rev. Lett.*, **1998**, 80, 890–890.
48. E. Engel and S. H. Vosko, *Phys. Rev. B*, **1993**, 47, 13164–13174.
49. B. Hammer, L. B. Hansen and J. K. Nørskov, *Phys. Rev. B - Condens. Matter Mater. Phys.*, **1999**, 59, 7413–7421.
50. A. O. de la Roza and G. A. DiLabio, *Non-Covalent Interactions in Quantum Chemistry and Physics: Theory and Applications*, Elsevier, **2017**.
51. S. Grimme, J. Antony, S. Ehrlich and H. Krieg, *J. Chem. Phys.*, **2010**, 132.
52. S. Grimme, *J. Comput. Chem.*, **2004**, 25, 1463–1473.
53. S. Grimme, *J. Comput. Chem.*, **2006**, 27, 1787–1799.
54. P. Fulde, P. Thalmeier and G. Zwicknagl, in *Solid State Physics*, Elsevier, **2006**, vol. 60, pp. 1–180.
55. Y.-G. Wang, D. Mei, J. Li and R. Rousseau, *J. Phys. Chem. C*, **2013**, 117, 23082–23089.

56. J. Hubbard, *Proc. R. Soc. Lond. Ser. Math. Phys. Sci.*, **1963**, 276, 238–257.
57. A. Liechtenstein, V. I. Anisimov and J. Zaanen, *Phys. Rev. B*, **1995**, 52, R5467.
58. M. Cococcioni, *Correl. Electrons Models Mater. Model. Simul.*, **2012**, 2.
59. N. E. Kirchner-Hall, W. Zhao, Y. Xiong, I. Timrov and I. Dabo, *Appl. Sci.*, **2021**, 11, 2395.
60. G. Beridze and P. M. Kowalski, *J. Phys. Chem. A*, **2014**, 118, 11797–11810.
61. C. Møller and M. S. Plesset, *Phys. Rev.*, **1934**, 46, 618–622.
62. A. Görling and M. Levy, *Phys. Rev. B*, **1993**, 47, 13105–13113.
63. D. C. Langreth and J. P. Perdew, *Phys. Rev. B*, **1980**, 21, 5469–5493.
64. J. Villard, M. P. Bircher and U. Rothlisberger, *Chem. Sci.*, **2024**, 15, 4434–4451.
65. W. Setyawan and S. Curtarolo, *Comput. Mater. Sci.*, **2010**, 49, 299–312.
66. N. W. Ashcroft and N. D. Mermin, *Solid State Physics*, Saunders College Publishing, **1976**.
67. C. Hammond, *The Basics of Crystallography and Diffraction*, Oxford University Press, 4th edn., **2015**.
68. F. Bloch, *Z. Für Phys.*, **1929**, 52, 555–600.
69. H. J. Monkhorst and J. D. Pack, *Phys. Rev. B*, **1976**, 13, 5188.
70. S. Zhu, K. Xie, Q. Lin, R. Cao and F. Qiu, *Adv. Colloid Interface Sci.*, **2023**, 315, 102905.
71. R. Tran, Z. Xu, B. Radhakrishnan, D. Winston, W. Sun, K. A. Persson and S. P. Ong, *Sci. Data*, **2016**, 3, 160080.
72. P. Chen, Y. Gao and M. R. Castell, *Appl. Phys. Lett.*, **2020**, 117, 1–5.
73. K. W. Kolasinski, *Surface Science: Foundations of Catalysis and Nanoscience*, John Wiley & Sons, 2nd edn., **2012**.
74. R. S. Mulliken, *J. Chem. Phys.*, **1955**, 23, 1833–1840.
75. S. C. North, K. R. Jorgensen, J. Pricetolstoy and A. K. Wilson, *Front. Chem.*, **2023**, 11.
76. R. S. Mulliken, *J. Chem. Phys.*, **1971**, 55, 288–309.
77. S. Saha, R. K. Roy and P. W. Ayers, *Int. J. Quantum Chem.*, **2009**, 109, 1790–1806.
78. F. L. Hirshfeld, *Theor. Chim. Acta*, **1977**, 44, 129–138.
79. I. Choudhuri and D. G. Truhlar, *J. Chem. Theory Comput.*, **2020**, 16, 5884–5892.
80. R. F. W. Bader, *Acc. Chem. Res.*, **1985**, 18, 9–15.
81. K. E. Laidig and R. F. W. Bader, *J. Chem. Phys.*, **1990**, 93, 7213–7224.
82. W. Tang, E. Sanville and G. Henkelman, *J. Phys. Condens. Matter*, **2009**, 21, 084204.
83. P. L. A. Popelier, *Theor. Chem. Acc.*, **2001**, 105, 393–399.
84. F. De Proft, C. Van Alsenoy, A. Peeters, W. Langenaeker and P. Geerlings, *J. Comput. Chem.*, **2002**, 23, 1198–1209.
85. B. Han, C. M. Isborn and L. Shi, *J. Chem. Theory Comput.*, **2021**, 17, 889–901.
86. C. Fonseca Guerra, J.-W. Handgraaf, E. J. Baerends and F. M. Bickelhaupt, *J. Comput. Chem.*, **2004**, 25, 189–210.
87. T. A. Manz and D. S. Sholl, *J. Chem. Theory Comput.*, **2010**, 6, 2455–2468.
88. T. A. Manz and D. S. Sholl, *J. Chem. Theory Comput.*, **2011**, 8, 2844–2867.
89. T. A. Manz and N. Gabaldon Limas, *RSC Adv.*, **2016**, 6, 47771–47801.
90. N. Gabaldon Limas and T. A. Manz, *RSC Adv.*, **2016**, 6, 45727–45747.
91. J. J. Philips, M. A. Hudspeth, P. M. Browne and J. E. Peralta, *Chem. Phys. Lett.*, **2010**, 495, 146–150.
92. T. A. Manz, *RSC Adv.*, **2022**, 12, 31617–31628.

93. A. E. Reed, R. B. Weinstock and F. Weinhold, *J. Chem. Phys.*, **1985**, 83, 735–746.
94. L. Lodeiro and T. Rauch, *Comput. Phys. Commun.*, **2022**, 277, 108384.
95. D. Preziosi, M. Alexe, D. Hesse and M. Salluzzo, *Phys. Rev. Lett.*, **2015**, 115, 157401.
96. M. Mirjolet, H. B. Vasili, A. Valadkhani, J. Santiso, V. Borisov, P. Gargiani, M. Valvidares, R. Valentí and J. Fontcuberta, *Phys. Rev. Mater.*, **2021**, 5, 095002.
97. F. Iga, M. Tsubota, M. Sawada, H. B. Huang, S. Kura, M. Takemura, K. Yaji, M. Nagira, A. Kimura, T. Jo, T. Takabatake, H. Namatame and M. Taniguchi, *Phys. Rev. Lett.*, **2004**, 93, 257207.
98. C. Jia, K. Wohlfeld, Y. Wang, B. Moritz and T. P. Devereaux, *Phys. Rev. X*, **2016**, 6, 021020.
99. C. Y. Liu, K. Ruotsalainen, K. Bauer, R. Decker, A. Pietzsch and A. Föhlisch, *Phys. Rev. B*, **2022**, 106, 035104.
100. D. Mücke, I. Cooley, B. Liang, Z. Wang, S. Park, R. Dong, X. Feng, H. Qi, E. Besley and U. Kaiser, *Nano Lett.*, **2024**, 24, 3014–3020.
101. J. S. Du, Y. Bae and J. J. De Yoreo, *Nat. Rev. Mater.*, **2024**, 9, 229–248.
102. C. J. Russo and R. F. Egerton, *MRS Bull.*, **2019**, 44, 935–941.
103. G. Santarossa, A. Vargas, M. Iannuzzi, C. A. Pignedoli, D. Passerone and A. Baiker, *J. Chem. Phys.*, **2008**, 129, 234703.
104. F. Lei, C. Tang, S. Wang and W. He, *J. Alloys Compd.*, **2011**, 509, 5187–5189.
105. A. Bafekry, B. Akgenc, M. Ghergherehchi and F. M. Peeters, *J. Phys. Condens. Matter*, **2020**, 32, 355504.
106. S. Wang, *Phys. Chem. Chem. Phys.*, **2011**, 13, 11929–11938.
107. D. Yan, L. Jiao, C. Chen, X. Jia, R. Li, L. Hu, X. Li, Y. Zhai, P. E. Strizhak, Z. Zhu, J. Tang and X. Lu, *Nano Lett.*, **2024**, 24, 2912–2920.
108. X. Yue, L. Cheng, E. Baráth, R. V. Jagadeesh and Q. Xiang, *Electron*, **2024**, 2, e16.
109. X. W. Lv, J. Gong, S. Wang, X. Yan, C. Sun, X. Hu, Z. Lai, Y. Liu, H. Wang, Z. Y. Yuan and J. Geng, *Adv. Energy Mater.*, **2025**, 2501129.
110. R. Prins, *Top. Catal.*, **2018**, 61, 714–721.
111. D. D. Eley and E. K. Rideal, *Nature*, **1940**, 146, 401–402.
112. D. D. Eley and D. C. Pepper, *Trans. Faraday Soc.*, **1947**, 43, 559–591.
113. E. W. Kuipers, A. Vardi, A. Danon and A. Amirav, *Phys. Rev. Lett.*, **1991**, 66, 116–119.
114. C. T. Rettner, *Phys. Rev. Lett.*, **1992**, 69, 383–386.
115. C. Stampfl and M. Scheffler, *Phys. Rev. Lett.*, **1997**, 78, 1500–1503.
116. R. Baxter and P. Hu, *J. Chem. Phys.*, **2002**, 116, 4379–4381.
117. D. S. Sholl and J. A. Steckel, *Density Functional Theory: A Practical Introduction*, John Wiley & Sons, **2022**.
118. J. Neugebauer, M. Reiher, C. Kind and B. A. Hess, *J. Comput. Chem.*, **2002**, 23, 895–910.
119. D. Porezag and M. R. Pederson, *Phys. Rev. B*, **1996**, 54, 7830–7836.
120. D. Heidrich and W. Quapp, *Theor. Chim. Acta*, **1986**, 70, 89–98.
121. R. Pradhan and U. Lourderaj, *Phys. Chem. Chem. Phys.*, **2019**, 21, 12837–12842.
122. J. C. Polanyi and A. H. Zewail, *Acc. Chem. Res.*, **1995**, 28, 119–132.
123. M. Maiuri, M. Garavelli and G. Cerullo, *J. Am. Chem. Soc.*, **2020**, 142, 3–15.
124. G. Henkelman, B. P. Uberuaga and H. Jónsson, *J. Chem. Phys.*, **2000**, 113, 9901–9904.

125. V. Ásgeirsson, B. O. Birgisson, R. Bjornsson, U. Becker, F. Neese, C. Riplinger and H. Jónsson, *J. Chem. Theory Comput.*, **2021**, 17, 4929–4945.
126. G. Henkelman and H. Jónsson, *J. Chem. Phys.*, **1999**, 111, 7010–7022.
127. G. Henkelman and H. Jónsson, *J. Chem. Phys.*, **2000**, 113, 9978–9985.
128. A. Heyden, A. T. Bell and F. J. Keil, *J. Chem. Phys.*, **2005**, 123, 224101.
129. T. Bucko, *VASP Wiki*, **2024**. Last accessed 10 April 2025. www.vasp.at/wiki/index.php/File:IDM.png

3. Catalytic hydrogenation of furfural derivatives over Pd(111) and Pt(111)

Work from this chapter is due to be reproduced in the following publication: M. Quayle, Z. Wu, M. Pera-Titus, and A. Roldan. *Mechanistic insights into the catalytic hydrogenation of furfural derivatives over Pd and Pt.* J. Catal. **2026**.

3.1. Introduction

Furfural and its derivatives are precursors to several useful compounds in organic synthesis. Their amenability to both oxidation and hydrogenation has been readily exploited by organic chemists, leading to the development of cheap synthetic routes for a variety of platform chemicals. Examples include tetrahydrofuran (THF), a polar solvent and polymer precursor commonly used in the textiles industry;[1–3] dimethylfuran, a high-octane, energy dense biofuel;[4,5] 5-aminolevulinic acid, a biodegradable herbicide that has shown promise in neurology as a visualising agent for malignant tumors;[6–8] and 5-hydroxymethylfurfural (HMF), a feedstock with a wide variety of uses in the pharmaceutical and food industries.[9–12]

Advances in green polymer chemistry have enabled the transformation of furfural derivatives into bio-based monomers, paving the way for recyclable polymers with tailored functionalities.[13] For instance, HMF can be readily oxidised to 2,5-furandicarboxylic acid (FDCA).[14,15] As a feedstock, FDCA is a renewable precursor to polyethylene terephthalate (PET), the most common component of disposable plastic bottles,[16] but it also readily polymerises with other furfural-based monomers. A series of biogenic polymers, largely consisting of FDCA and its fellow furfural derivative, succinic acid,[17,18] have been developed by Lomelí-Rodríguez *et al.*[19,20] for use in the coatings industry. While PET remains the industry standard for the plastic packaging of soft drinks, FDCA can also undergo polycondensation to polyethylene furan-2,5-dicarboxylate (PEF),[21] a fully recyclable, heat resistant plastic that is being investigated as an eco-friendly replacement to PET.[22]

In keeping with the Twelve Principles of Green Chemistry,[23,24] many furfural-based reactions have been developed into one-pot catalytic schemes.[5,25,26] By restricting themselves to a single vessel, synthetic chemists can minimise the need to purify or handle any intermediates associated with the reaction. Several economic and

environmental advantages are associated with one-pot reactions; chief among them, lower solvent usage, lower processing costs, and a sharp reduction in the generation of waste. For instance, the ketone (*E*)-1-(furan-2-yl)-5-methylhex-1-en-3-one (ALD-1) can be synthesised directly from furfural via a one-pot aldol condensation with methyl isobutyl ketone (MIBK). As shown in **Scheme 3.1**, the C=C double bond on the branching chain of ALD-1 is reduced over both Pd and Pt, generating ALD-2. However, the subsequent hydrogenation of ALD-2's ring system to ALD-3 is catalyst dependent. Over Pd/Al_2O_3, catalysis is highly selective towards ALD-3. Even at temperatures as mild as 80 °C, the furanic ring system is fully hydrogenated, with conversion reaching 100% within hours.[26] Over Pt/Al_2O_3, however, catalytic activity and selectivity towards ALD-3 was poor, resulting in ALD-2 being the dominant product.

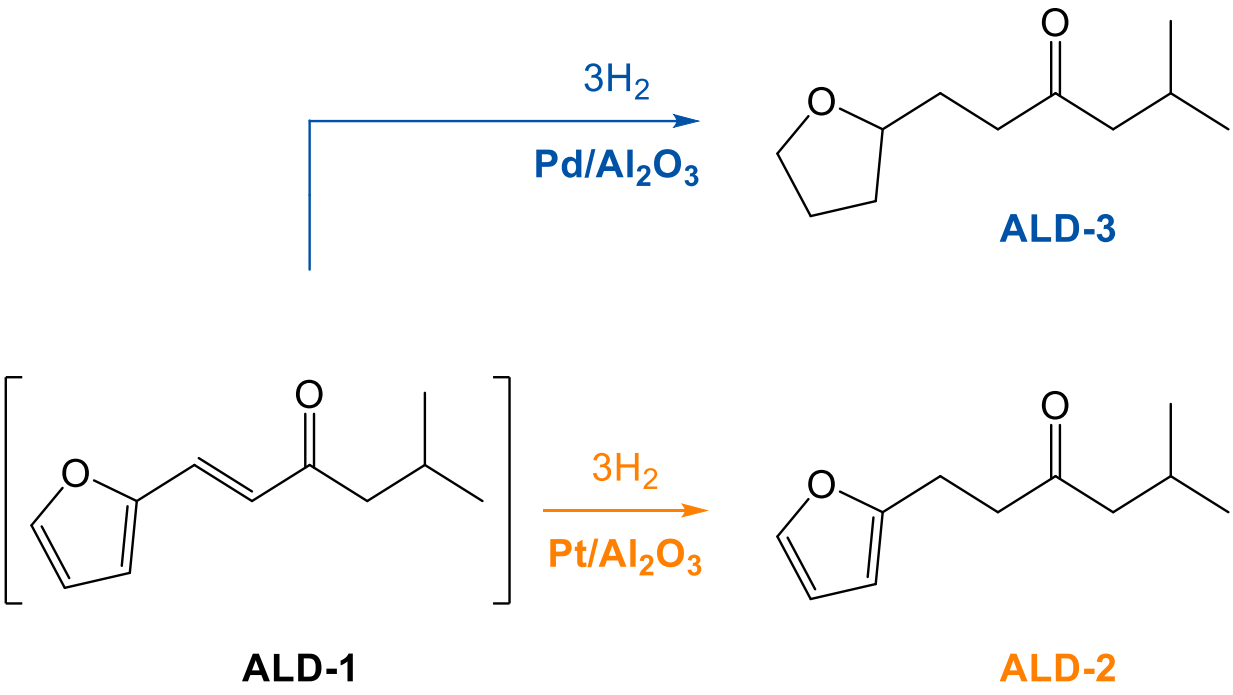

Scheme 3.1. A selection of ALD-1 hydrogenation routes. The ring system of the dominant organic product is untouched over Pt/Al_2O_3 (orange), but fully hydrogenated over Pd/Al_2O_3 (blue).

To better understand the mechanistic underpinnings of ALD-1 hydrogenation, comprehensive DFT reaction profiles were constructed using slab models of Pd and Pt. Transition state modelling was then employed to quantify the thermodynamic and kinetic barriers associated with both chain and ring hydrogenation. In parallel, the optimised structures were subjected to partial charge analysis to map the distribution of electron density across the substrates. For both Pd and Pt, the (111) surface was

chosen, as it is among the most catalytically active surfaces in prior experimental studies on Pd- and Pt-catalysed hydrogenation.[27–30]

Typically, when an unsaturated organic compound binds to the surface of a metal nanoparticle, its C=C double bonds will rarely be reduced by gas phase molecular hydrogen. Instead, H_2 adsorbs on the surface and dissociates into a pair of individual hydrogen atoms, which then migrate across the surface to the substrate. Hydrogenation then proceeds via a Langmuir-Hinshelwood type mechanism, as has been repeatedly observed both experimentally and theoretically for a variety of transition metal catalysts.[31–36] With this in mind, intermediates were generated for each product by adding hydrogen atoms to the substrate one at a time to ensure the construction of a physically accurate picture of the reaction profile. This approach allowed for the direct comparison of Pd- and Pt-catalysed hydrogenation, highlighting differences in adsorption energetics, activation barriers, and the electronic factors governing selectivity.

3.2. Methods

All spectroscopic validation of the DFT calculations (**Section 3.6**) was undertaken by Zhuoli Wu at the Cardiff Catalysis Institute. Spin-polarised single point energy calculations were conducted by Dr Alberto Roldan (**Figure 3.7**) to determine the radical character of the chain hydrogenation intermediates. All remaining computational work in this chapter was undertaken by the author.

DFT models of all possible hydrogenation intermediates of ALD-1 over Pd(111) and Pt(111) were constructed in VASP.[37] After benchmarking (**Section 3.3**), all calculations were carried out under the constraints of the generalised gradient approximation (GGA) at the RPBE-D3(0) level.[38,39] Gas phase species were optimised at the centre of 20×20×20 $Å^3$ unit cells, which were then sampled with 1×1×1 Monkhorst-Pack $\boldsymbol{k}$ point meshes.[40] Unit cells of the metal slabs and the optimised surfaces were each sampled with 13×13×13 and 3×3×1 Monkhorst-Pack meshes, respectively.

All atoms were modelled using the projector augmented wave (PAW) potentials of Kresse and Joubert.[41,42] The plane-wave cutoff energy was set to 500 eV, the ionic convergence threshold was set to 0.03 eV/Å, and the electronic convergence threshold was set to 1×10^{-5} eV. Each surface was represented with a *p*(6×6×5) slab

separated by a 20 Å vacuum layer along the z-axis. To improve convergence, the bottom three layers were frozen after the initial step of each calculation. The transition states associated with each hydrogenation step were identified using the improved dimer method. A round of frequency analysis was conducted on all transition states to confirm the presence of a single imaginary frequency along the reaction coordinate. Further detail on the experimental validation of the DFT calculations and the parameters employed in transition state analysis can be found in **Section A.1** and **Section A.2**, respectively.

3.3. Preliminary Calculations

Functional benchmarking tests were performed with PBE-D3(0), revPBE-D3(0), and RPBE-D3(0). In anticipation of future simulations work on the reductive amination of ALD-1 over Ru(0001) (**Chapter 4**), Ru was benchmarked alongside Pd and Pt. After the optimisation of H_2 and NH_3 in the gas phase (**Table 3.1**), The lattice constants and bulk moduli (**Tables 3.2** and **3.3**) were calculated from the metal unit cells. The adsorption energies of NH_3@Pd(111), NH_3@Ru(0001), and monoatomic H (**Table 3.4**) were then calculated. Following the findings of previous studies on the binding conformations of hydrogen[43–47] and ammonia[46,48–51] on Pd(111), Pt(111), and Ru(0001), the monoatomic H atoms were placed over fcc hollow sites, and the NH_3 molecules were placed over top sites, with the central N atom facing the surface.

All three functionals predicted the bond lengths of molecular hydrogen and ammonia to within ±0.01 Å of experiment.[52,53] The average bond angle of NH_3 was predicted to within ±0.5% of the experimental value of 106.7° (**Figure 3.1**).[54] As shown in **Table 3.2**, all three functionals were able to predict the lattice constants of Pd, Pt, and Ru to within ±1% of experiment.[55] While RPBE-D3(0) slightly underpredicted the bulk moduli of all three metals (**Table 3.3**), its predicted adsorption energies for H over fcc hollow sites showed the best agreement with experiment. Consequently, it was selected for all remaining DFT modelling work in this chapter. Meanwhile, revPBE-D3(0) performed well in the lattice constant and bulk moduli tests, but incorrectly predicted that the dissociative adsorption of H_2 over Pt(111) was endoergic.

RPBE-D3(0): NH_3	
Bond length error	0.59%
Bond angle error	0.47%

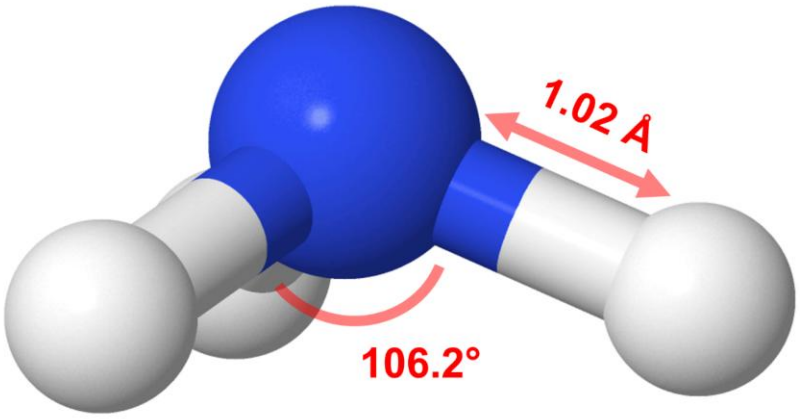

Figure 3.1. A molecule of gas phase NH_3 optimised at the RPBE-D3(0) level. Measurements were compared to the experimental values provided in **Table 3.1**.

H_2 (g) + NH_3 (g)	PBE-D3(0)	revPBE-D3(0)	RPBE-D3(0)	Exp.	Ref.
H–H (Å)	0.75	0.75	0.75	0.74	52
avg. N–H (Å)	1.02	1.02	1.02	1.02	53
avg. θ (°)	106.3	106.2	106.2	106.7	54

Table 3.1: Functional benchmarking of H_2 (blue) and NH_3 (green) optimisation in the gas phase against experimental values.

Regardless of functional or catalyst choice, the magnitude of NH_3's adsorption energy of was overestimated. For NH_3@Pd(111), PBE-D3(0) overbound by almost 100 kJ mol^{-1}. A 2024 paper by Borkar and Shetty[49] demonstrated that adding a zero point energy (ZPE) correction to this figure only exacerbated this issue (E_{ads} = –195.8 kJ mol^{-1}). In the computational literature, Ford *et al.*[48] were able to obtain a reasonable estimate for the adsorption energy of NH_3 over Pt(111) (E_{ads} = –90.7 kJ mol^{-1}) using the 1991 Perdew-Wang functional (PW91),[56] suggesting that this issue is likely a shortcoming of PBE-family functionals rather than a fundamental failure of DFT modelling.

Lattice Constants	PBE-D3(0)	revPBE-D3(0)	RPBE-D3(0)	Exp.	Ref.
fcc Pd, a (Å)	3.88	3.87	3.92	3.89	55
fcc Pt, a (Å)	3.92	3.90	3.94	3.92	55
hcp Ru, a (Å)	2.69	2.68	2.69	2.71	55
hcp Ru, c (Å)	4.25	4.23	4.25	4.28	55

Table 3.2. Calculated Pd, Pt, and Ru lattice constants against values measured via X-ray crystallography.

Bulk Moduli	PBE-D3(0)	revPBE-D3(0)	RPBE-D3(0)	Exp.	Ref.
Pd (GPa)	193	186	156	180	55
Pt (GPa)	281	275	240	278	55
Ru (GPa)	328	331	311	320	57

Table 3.3. Calculated bulk moduli of Pd, Pt, and Ru against experimental values.

E_{ads}	PBE-D3(0)	revPBE-D3(0)	RPBE-D3(0)	Lit.	Ref.
H_2@Pd(111)	–58.0	–48.2	–56.2	–43.4	43
H_2@Pt(111)	–24.2	+7.1	–36.7	–41.5	44
H_2@Ru(0001)	–56.2	–48.8	–45.6	–86.8	45
NH_3@Pd(111)	–173.2	–170.2	–169.7	–195.8 (PBE-ZPE), –73.6 (exp.)	49,50
NH_3@Ru(0001)	–146.1	–142.2	–134.4	–44.4	46

Table 3.4. Adsorption energies of monoatomic H over hollow sites (blue) and NH_3 over top sites (green) against values from the literature. Energies reported in kJ mol^{-1}. Unless stated otherwise, literature values have been taken from experiment.

After the optimisation of the metal slabs, the surface energies of Pd(111), Pt(111), and Ru(0001) were then calculated following **Equation 2.24**. The calculated surface energy for Pd(111) was within 2% of the experimental value of de Boer *et al.*,[58] and the RPBE-D3(0) surface energy for Pt(111) showed good agreement with the computational value of Singh-Miller and Marzari[59] ($\gamma = 1.49$ J m^{-2}), calculated using PBE without dispersion corrections. However, both the RPBE-D3(0) and PBE surface energies for Pt(111) were drastically smaller than the experimental value of Tyson and Miller[60] ($\gamma = 2.49$ J m^{-2}). The value for the surface energy of Ru(0001) from the same paper ($\gamma = 3.04$ J m^{-2}) is closer to the calculated value of 3.27 J m^{-2}, but in this case, RPBE-D3(0) was shown to slightly overestimate the surface energy, being larger than

both the experimental value and the computational value of Vega *et al.*[61] ($\gamma = 2.95$ J m^{-2}), calculated using the PBEsol functional of Constantin *et al.*[62,63] with no dispersion corrections. It should be highlighted that, due to the difficulty of preparing pristine Ru(0001) and Pt(111) crystals, Tyson and Miller's figures were approximated by expressing the surface energy as a function of the surface tension of the metal in the liquid phase. While this technique allows for the approximation of the "average" surface energy of a metal's high-index lattice planes, it lacks the sensitivity to resolve facet-specific surface energies. Moreover, the authors make the assumption that all surfaces present in the metal will melt and roughen at identical temperatures to one another; an assumption that is likely to oversimplify the complex, facet-dependent behaviour of real materials.

Surface Energies	RPBE-D3(0)	Literature	References
γ, Pd(111)	2.04	2.00 (exp.)	58
γ, Pt(111)	1.55	1.49 (PBE), ~2.49 (exp.)	59, 60
γ, Ru(0001)	3.27	2.95 (PBEsol), ~3.04 (exp.)	60, 61

Table 3.5. Surface energies of Pd(111) and Pt(111) calculated at the RPBE-D3(0) level (blue) against values from the computational literature. Values reported in J m^{-2}.

To ensure that RPBE-D3(0) correctly captured the binding conformations of aromatic hydrocarbons, furan molecules were placed over Pd(111) and Pt(111) at 0°, 45°, and 90° angles to the surface normal and the plane normal of the ring system. In agreement with previous work on the bonding conformations of furan and its derivatives,[64,65] RPBE-D3(0) calculations successfully predicted that the flat conformation was preferred in all cases; a preference that can be attributed to the maximisation of orbital overlap between the π-system of the furan ring and the d-orbitals of the atoms on the metal surface.

a) Furan, 0°	
E_{ads} (kJ mol^{-1})	–159.4
min. d(C–M) (Å)	2.10
d(O–M) (Å)	2.87

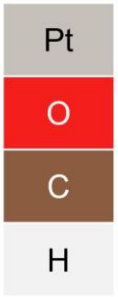

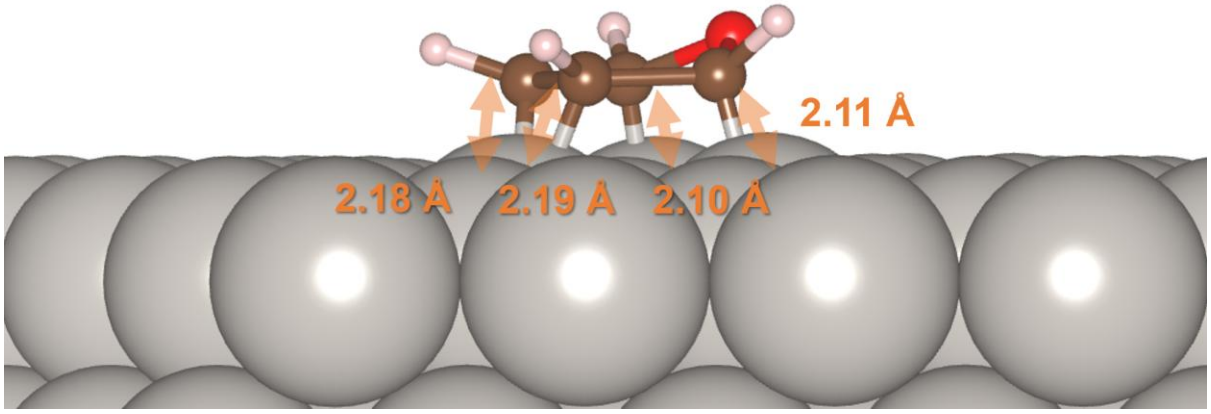

b) Furan, 45°	
E_{ads} (kJ mol^{-1})	–48.3
min. d(C–M) (Å)	3.15
d(O–M) (Å)	3.48

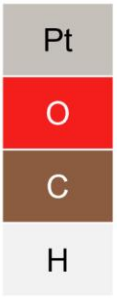

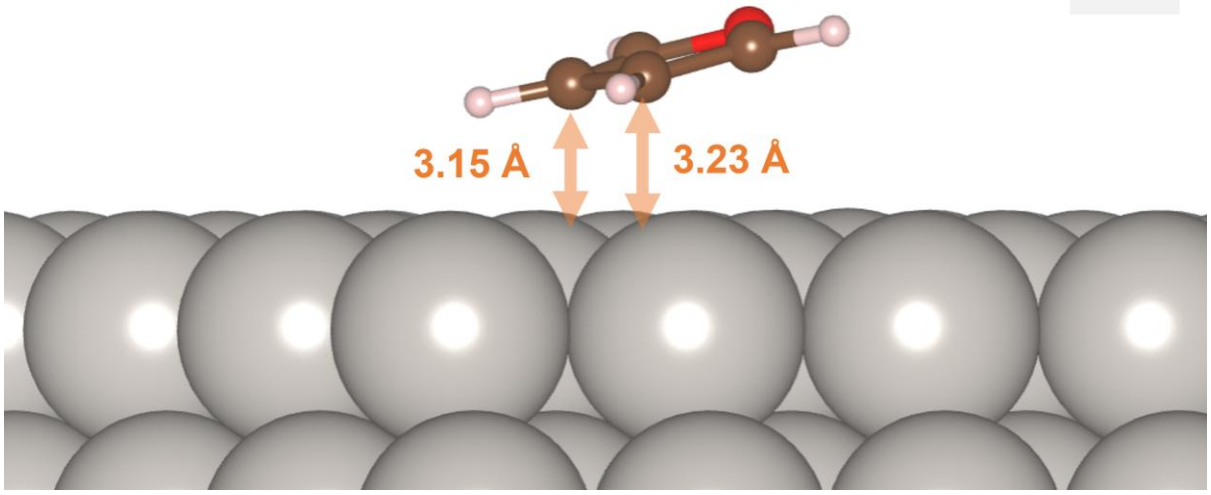

c) Furan, 90°	
E_{ads} (kJ mol^{-1})	+2.0
min. d(C–M) (Å)	3.03
d(O–M) (Å)	4.70

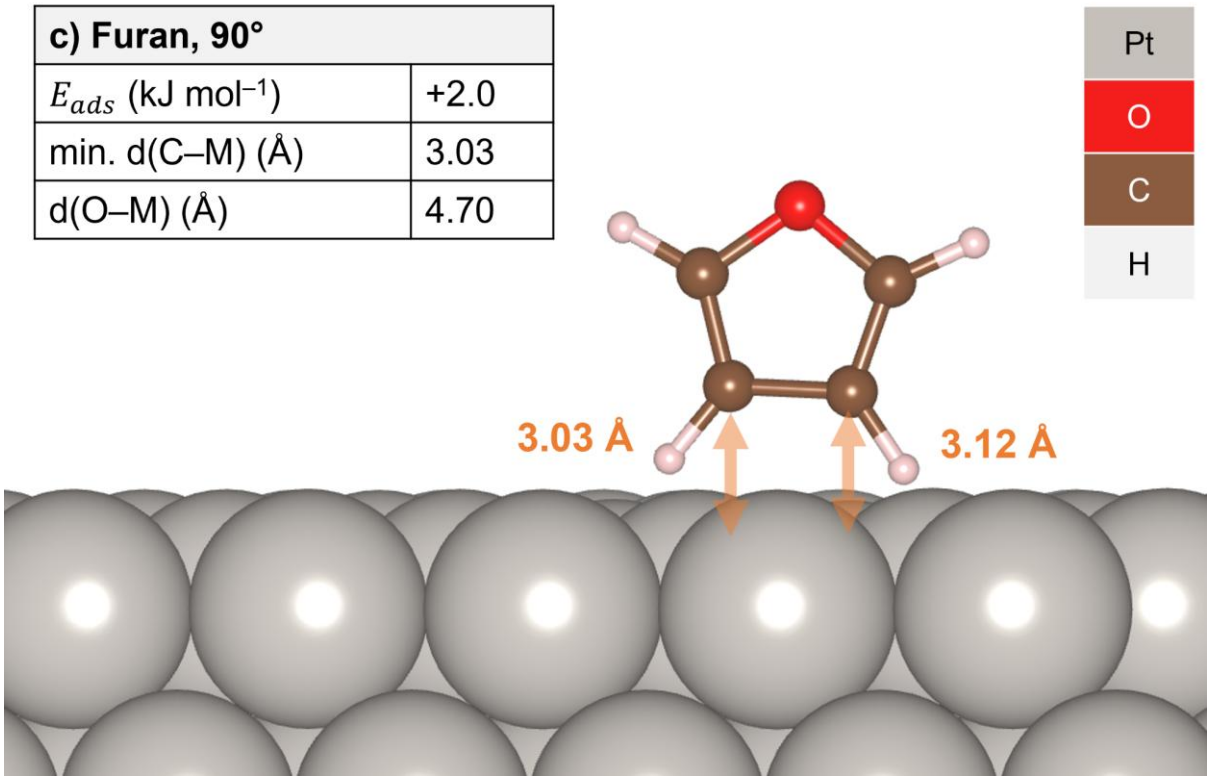

Figure 3.2. Furan molecules adsorbed over Pt(111) at (a) 0°, (b) 45°, and (c) 90° angles relative to the surface.

Angle	E_{ads} Pd(111)	E_{ads} Pt(111)
0°	–174.0	–159.4
45°	–91.7	–48.3
90°	–80.5	+2.0

Table 3.6. Stability of adsorbed furan at 0°, 45°, and 90°. Figures reported in kJ mol^{-1}.

Further optimisation at the RPBE-D3(0) level showed that furfural and ALD-1 adopted similar binding conformations (**Figures 3.3** and **3.4**), with the alkyl chain positioning itself away from the surface. As discussed by Liu *et al.*[66] in their work on the effects of dispersion corrections on furfural catalysis, the zero-damping D3 dispersion correction lead to mild overbinding (**Table 3.7**). However, furfural's conformational geometry remained effectively unchanged by the introduction of a dispersion correction. The same cannot be said about the activation energies on intermediary transition states. In previous studies of PBE-family functionals, dispersion corrections have been shown to significantly increase the accuracy of estimating activation energies.[39,67,68] Provided that the structures corresponding to the elementary steps are modelled in a consistent fashion, the activation energies of

reactions on the surface will, in principle, be more accurate if a dispersion correction is employed. The only steps with significant potential for error are the adsorption of H_2 and ALD-1, both of which are known experimentally to readily adsorb to both Pd(111) and Pt(111), and the desorption of the products. As the geometry of the adsorbates was effectively unchanged, the decision was made to keep the D3(0) dispersion correction in all subsequent calculations at the compromise of overbinding to ensure the activation energy barriers for all reactions on the surface were modelled as accurately as possible.

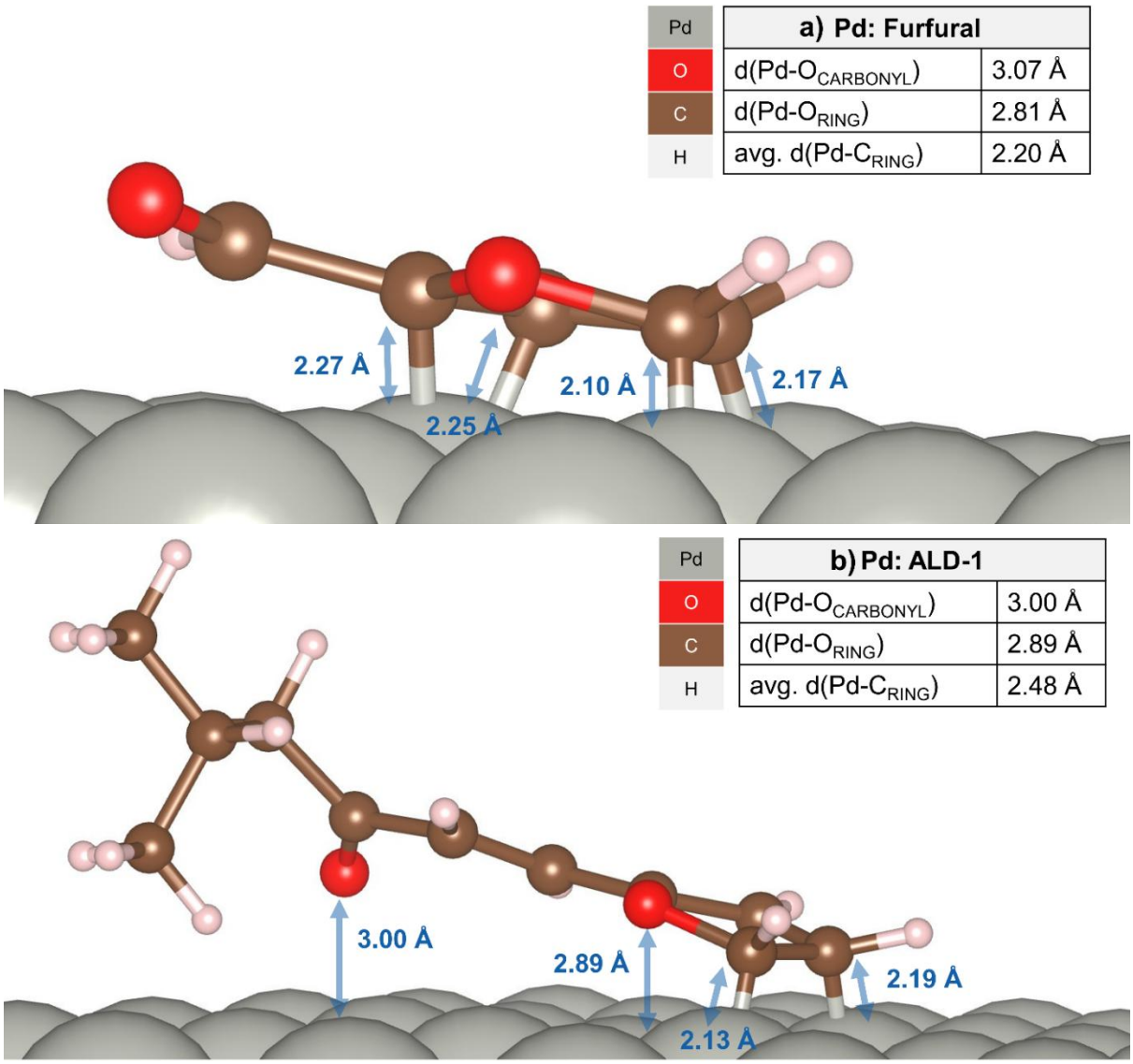

Figure 3.3. Binding conformations of (a) furfural and (b) ALD-1 over Pd(111).

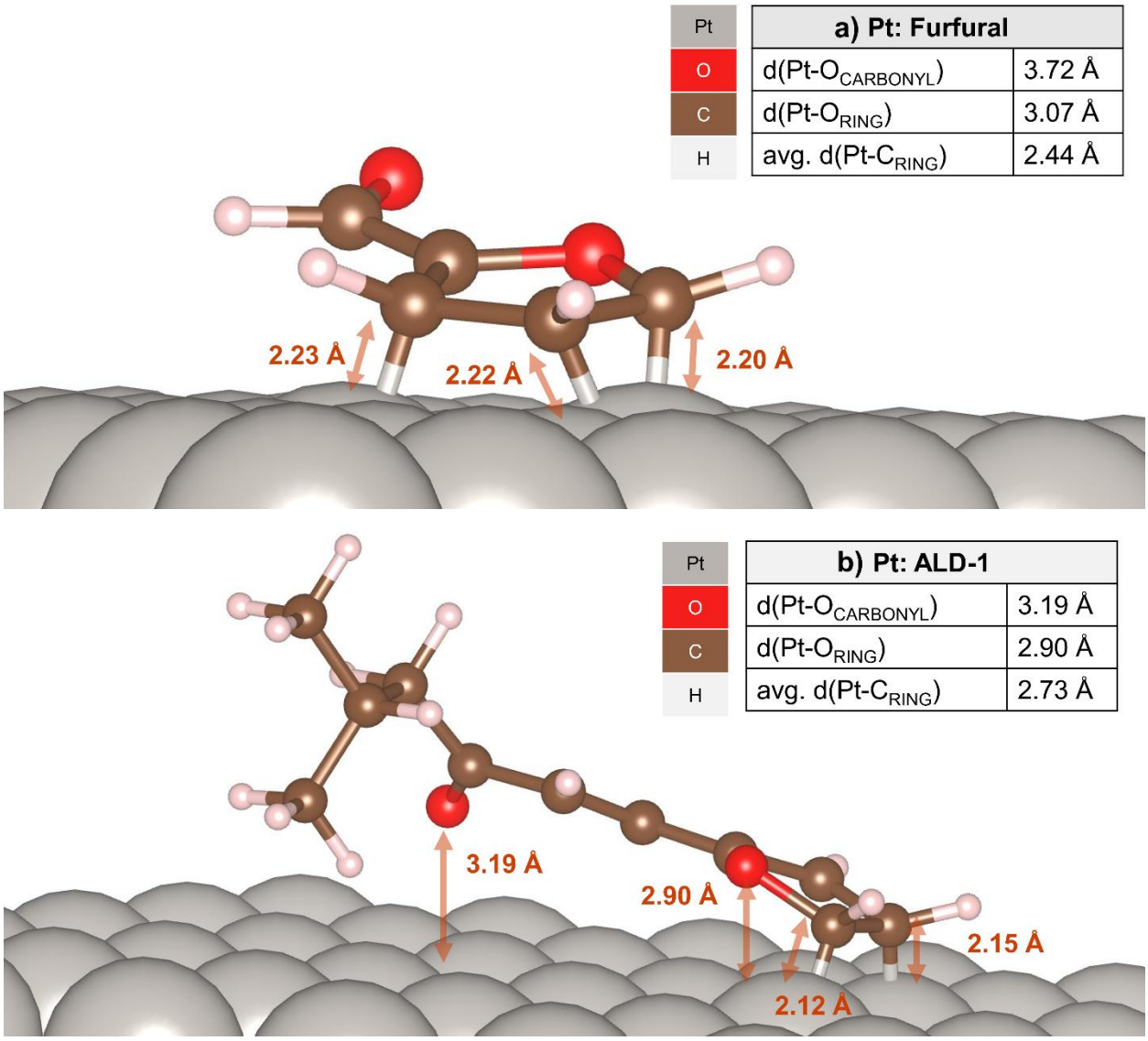

Figure 3.4. Binding conformations of (a) furfural and (b) ALD-1 over Pt(111).

E_{ads}	Pd(111)	Pt(111)	References
Furfural, RPBE-D3(0)	–244.1	–101.3	—
ALD-1, RPBE-D3(0)	–230.3	–179.5	—
Furfural, PBE	–89.7	—	66
Furfural, PBE-D3(0)	–190.1	–102.3	66,69

Table 3.7. Calculated adsorption energies of furfural and ALD-1 at the RPBE-D3(0) level (blue) against PBE and PBE-D3(0) values from the literature (pink). Values reported in kJ mol^{-1}.

3.4. Chain Hydrogenation

The names and structures of the intermediates associated with chain hydrogenation are given in **Scheme 3.2**. The hydrogenation of ALD-1 can occur at four possible sites: the chain C=C bond, the carbonyl group, and the two C=C bonds of the ring system. Henceforth, the C2=C3 and C4=C5 bonds will be referred to as the ortho and para hydrogenation sites, respectively.

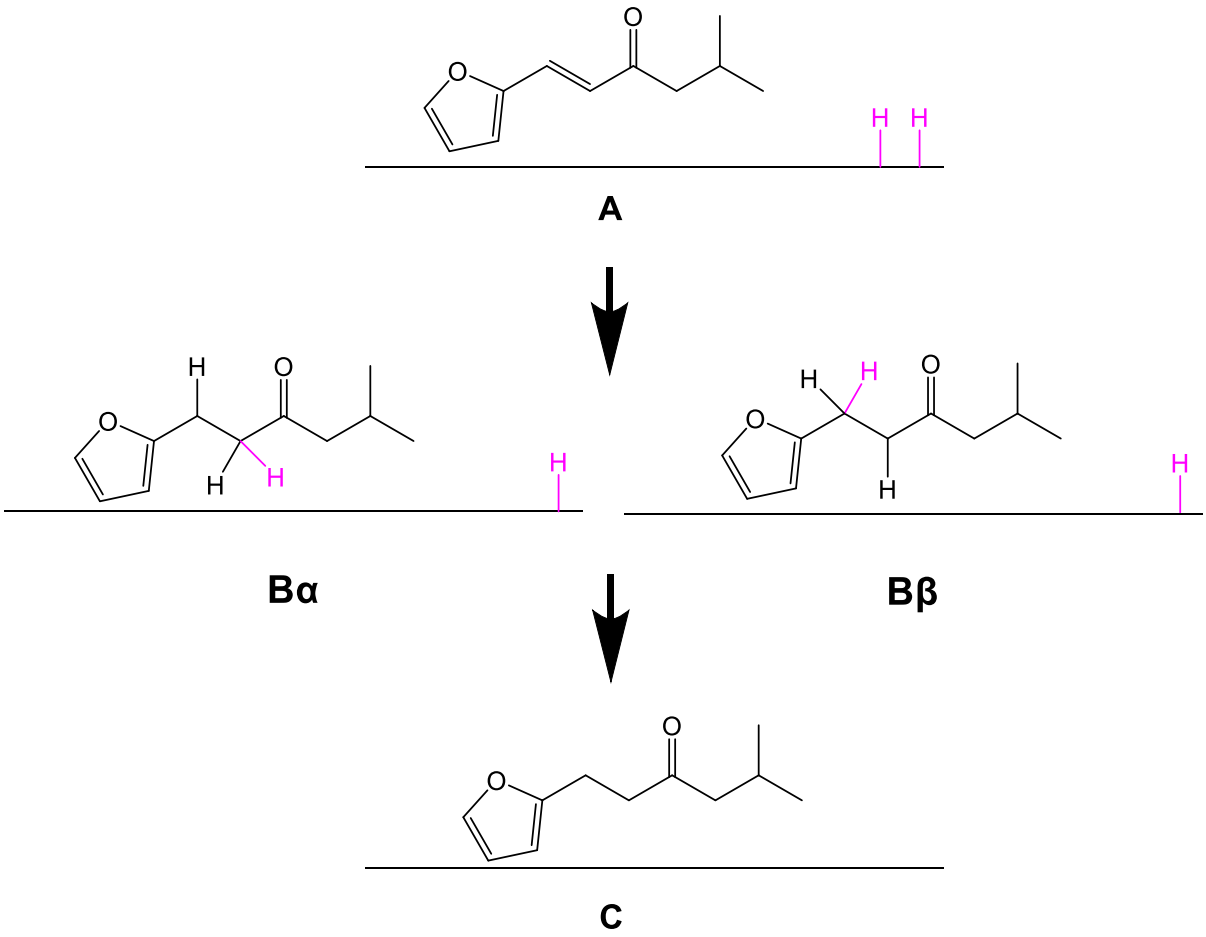

Scheme 3.2. Intermediates associated with the chain hydrogenation of ALD-1 to ALD-2. H adatoms from dissociated H_2 are highlighted in pink.

As reported by Jiang *et al.*,[26] the first site of ALD-1 to undergo hydrogenation over transition metal catalysts is the chain C=C bond. As such, this site was the first to be considered. As shown in **Figure 3.5**, the total activation energy barriers for chain hydrogenation were low for both Pd(111) (E_A = +46.5 kJ mol^{-1}) and Pt(111) (E_A = +33.9 kJ mol^{-1}). The activation energy barriers for β-hydrogenation over both Pd(111) (E_A =

+109.9 kJ mol^{-1}) and Pt(111) (E_A = +131.8 kJ mol^{-1}) were more than twice as large as the corresponding barriers for hydrogenation at the α-carbon.

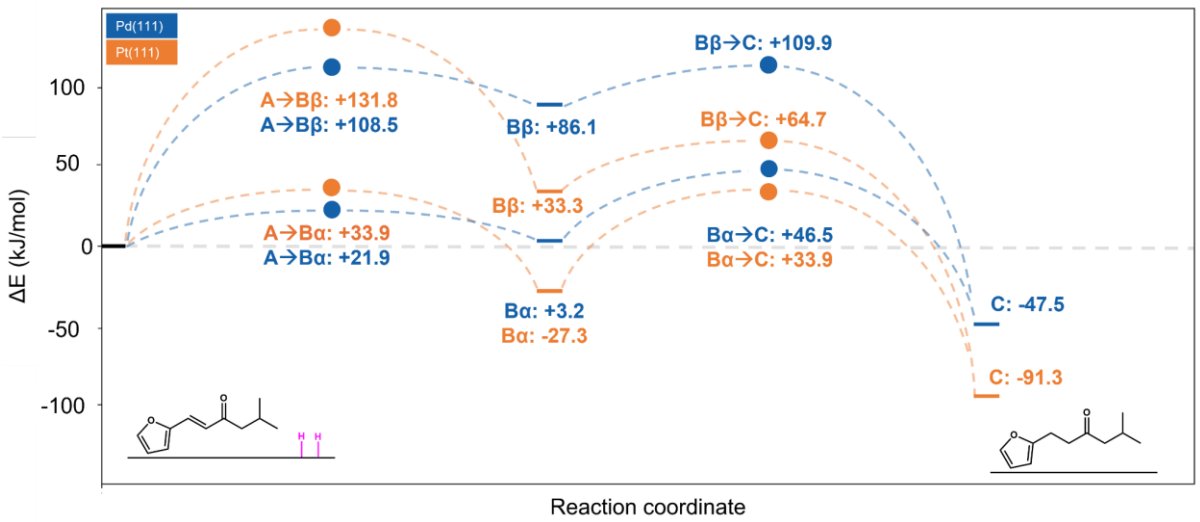

Figure 3.5. The energy profile for the chain hydrogenation of ALD-1 over Pd(111) (blue) and Pt(111) (orange). Transition states between minima are marked with coloured circles. Inset are schematic representations of A (left) and C (right).

The computational work of Jia *et al.*[70] on the hydrogenation of unsaturated ketones found that α-hydrogenation is driven by the distribution of partial charges across the molecule. DDEC6 population analysis confirmed that this charge redistribution is taking place ALD-1 in the gas phase (**Figure 3.6a**). Due to its proximity to a partially positive C=O carbon (q = +0.44 e), electron density accumulated at the α-carbon (q = –0.23 e) to prevent the formation of a localised positive charge. When ALD-1 binds to the catalyst through its ring system, this buildup in electron density at the α-carbon likely facilitates the attack of H adatoms from the surface. To verify this hypothesis, a second round of DDEC6 population analysis was conducted on ALD-1 adsorbed to Pd(111) and Pt(111). As shown in **Figures 3.6b** and **3.6c**, the discrepancy in negative charge between the vinyl carbons is preserved over both Pd(111) and Pt(111). Regardless of catalyst, the charges on the C=C carbons did not change by more than ±0.01 units of elementary charge. The DDEC6 partial charges of the H and O atoms are provided in the appendix.

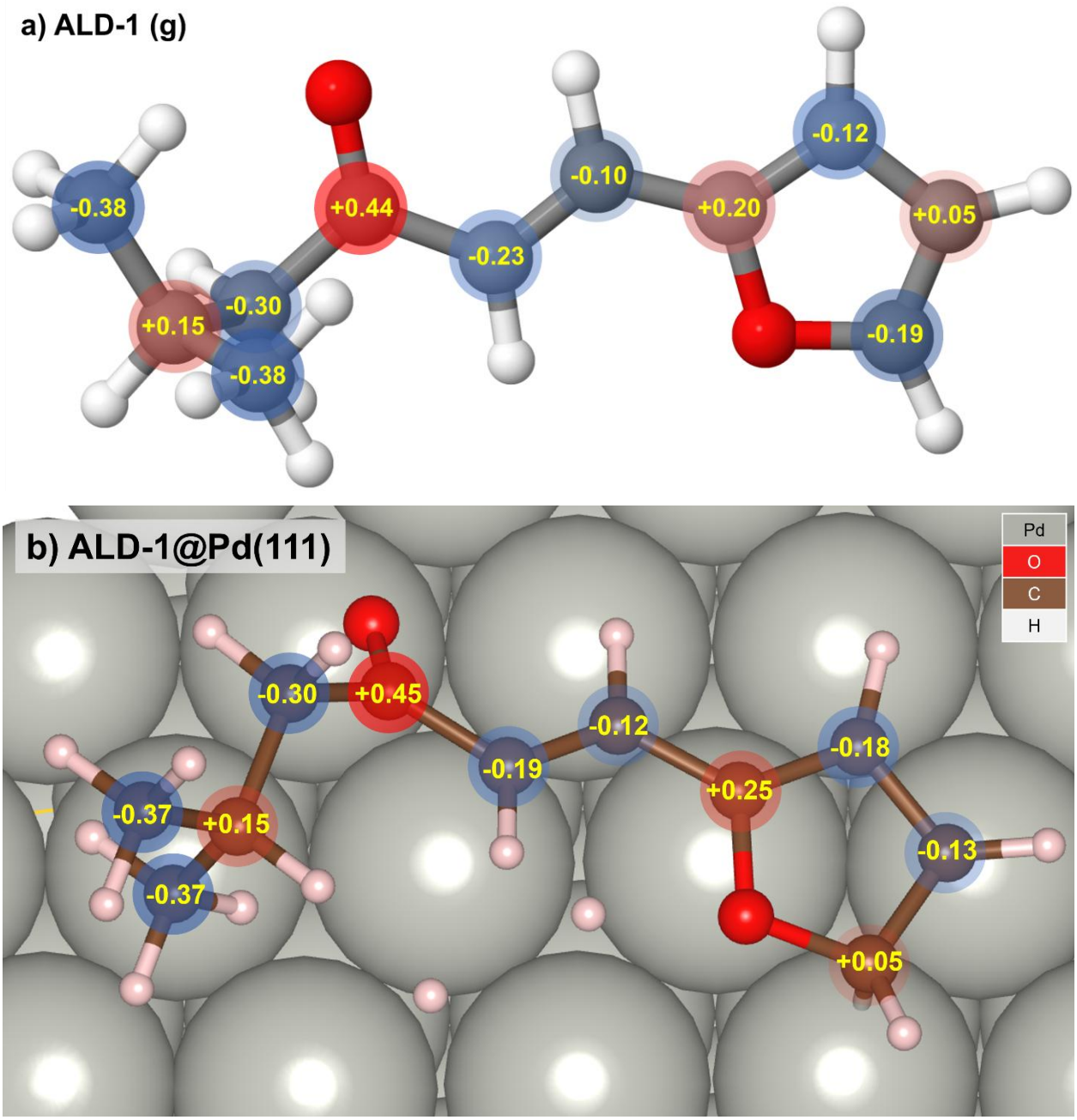
a) ALD-1 (g)
-0.38
+0.44
-0.10
-0.12
+0.20
+0.05
-0.23
-0.30
+0.15
-0.38
-0.19
b) ALD-1@Pd(111)
Pd
O
C
H
-0.30
+0.45
-0.12
-0.18
-0.19
+0.25
-0.37
+0.15
-0.13
-0.37
+0.05

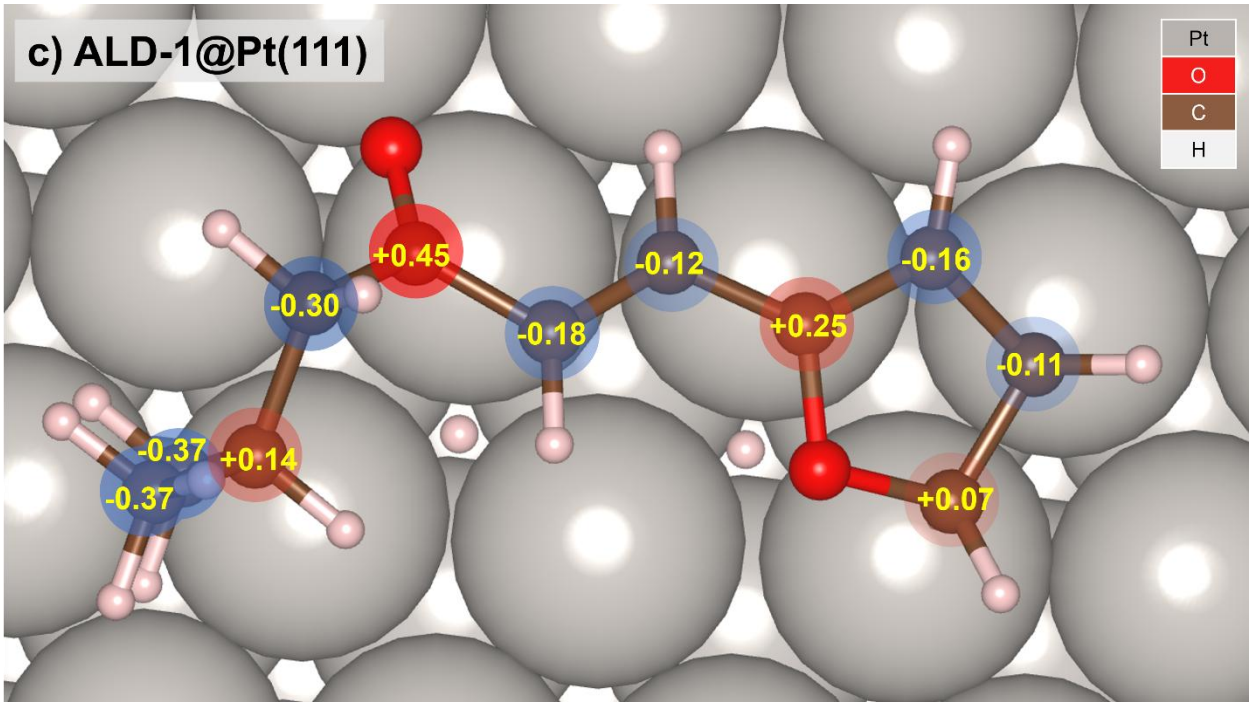

Figure 3.6. DDEC6 charge analysis of ALD-1 (a) in the gas phase and adsorbed to (b) Pd(111) and (c) Pt(111). Carbon atoms with partial positive and negative charges are highlighted in red and blue, respectively. Figures given in units of elementary charge.

The radical character of the chain hydrogenation intermediates was assessed by a supplemental round of spin-polarised single point energy calculations. As shown in **Figure 3.7,** the magnetic moments of the Bα adsorbate atoms were negligible over both Pd(111) and Pt(111) ($|m| \leq 0.005\ \mu_B$). While a small magnetic moment was observed on the α-carbon of Bβ over Pd(111) ($m = 0.042\ \mu_B$), significant delocalisation of an unpaired electron was observed in Bβ@Pt(111) between the α-carbon ($m = 0.351\ \mu_B$) and the oxygen of the carbonyl group ($m = 0.182\ \mu_B$). Although the ease with which radical species can delocalise likely contributes to the marked stability of the Bβ intermediate over Pt(111), the absence of intermediates with radical character along the more energetically favourable α-hydrogenation pathway suggests that charge distribution is a stronger predictor of stability than radical stability.

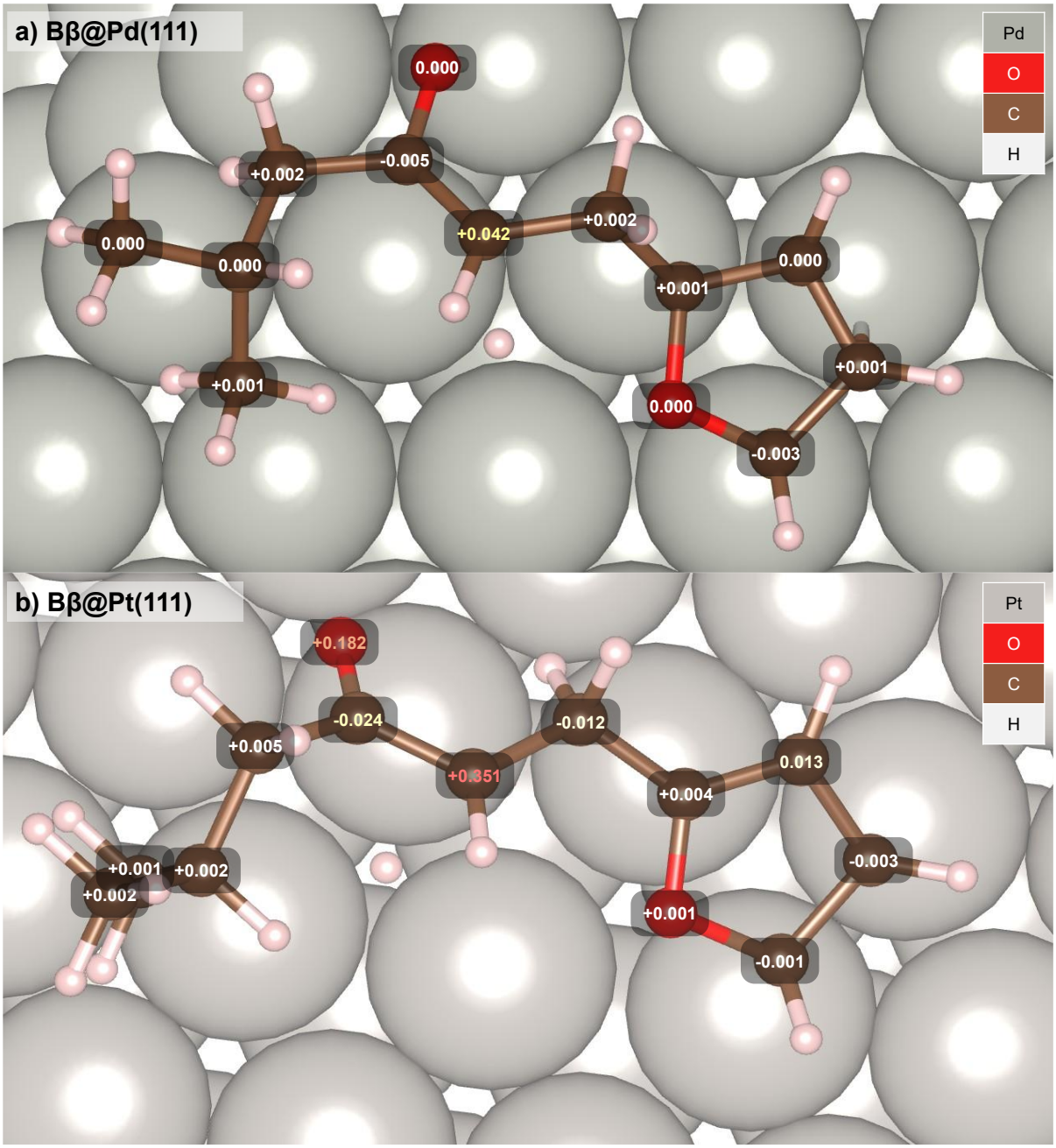

Figure 3.7. Detected magnetic moments in adsorbate C and O atoms in the Bβ intermediates over (a) Pd(111) and (b) Pt(111).

In addition to occurring at a carbon with a more localised negative charge, α-hydrogenation further benefits from the favourable sterics of the A→Bα transition state. This is illustrated in the optimised transition state structures corresponding to A→Bα and A→Bβ hydrogenation over Pt(111) (**Figure 3.8**). While the interatomic distances between the carbon and the migratory H atom are similar in both cases, the α-carbon is able to adopt a favourable vector of approach with an H–C_α–H angle of 100.1°; a figure close to the H–C_α–H bond angle of 107.5° in the sp^3-hybridised product. In contrast, hydrogenation can only be initiated at the β-carbon through an unfavourable

bond formation angle of 94.3°. While this barrier may be surmountable at high temperatures, it is likely that α-hydrogenation mechanism will dominate regardless of whether a Pd or Pt catalyst is used.

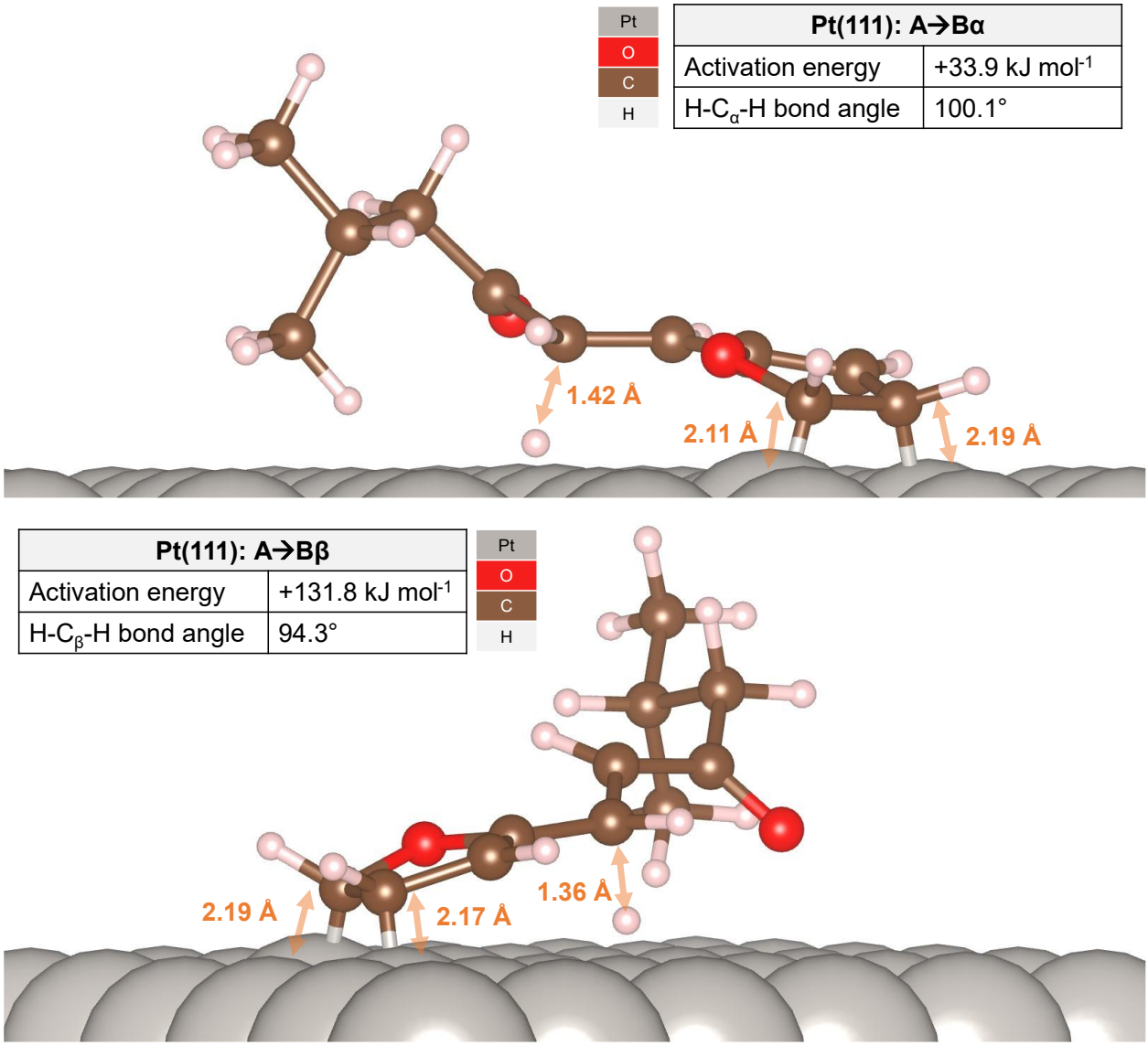

Figure 3.8. Optimised transition state structure for α- and β-hydrogenation over Pt(111).

3.5. Ring Hydrogenation

A comprehensive schematic of the intermediates associated with ring hydrogenation is provided in **Scheme 3.3.** A reaction profile for ortho hydrogenation is provided in **Figure 3.9**. In agreement with experiment, the activation energy for ring hydrogenation was substantially lower over Pd(111) (+69.1 kJ mol^{-1}) than over Pt(111) (+114.0 kJ mol^{-1}). In both cases, ortho hydrogenation was energetically favoured over para hydrogenation. Over both Pd(111) and Pt(111), the preferred order of hydrogenation was B2, then C_{ORTHO}, then D4, then E. A complete table of intermediate energies and activation energy barriers is provided in the appendix (**Section A.3**).

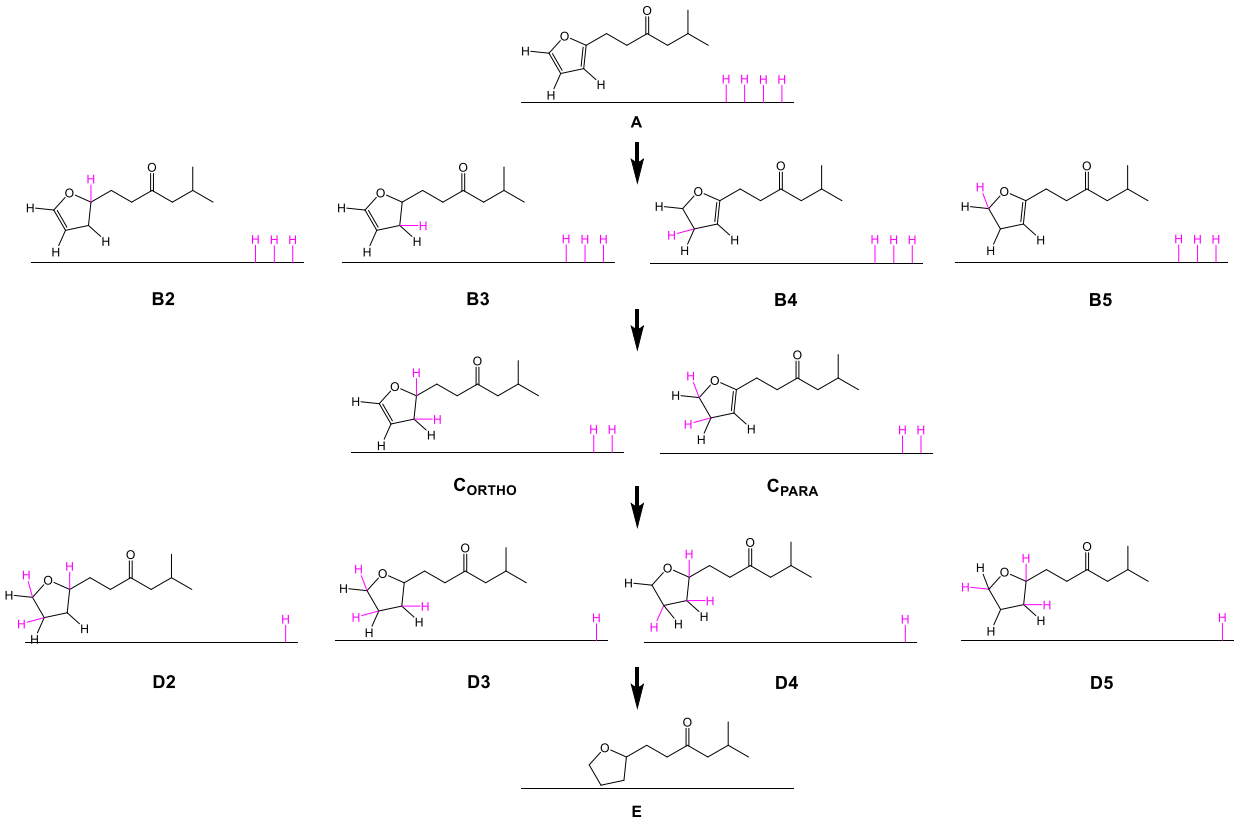

Scheme 3.3. Intermediates associated with the ring hydrogenation of ALD-2. H adatoms from dissociated H_2 are highlighted in pink.

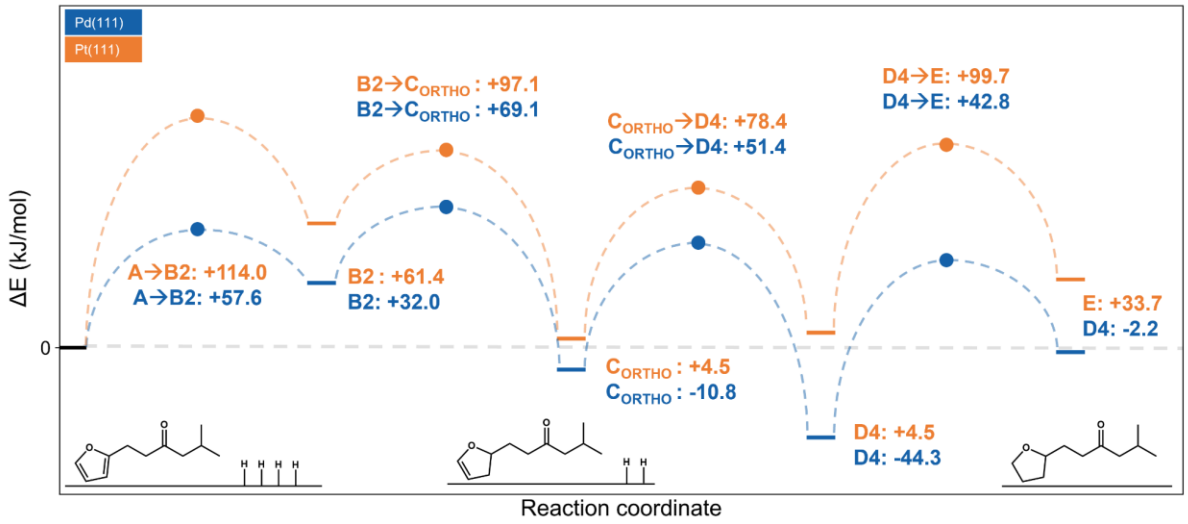

Figure 3.9. The energy profile for ortho ring hydrogenation of ALD-2 over Pd(111) (blue) and Pt(111) (orange). Transition states between minima are marked with coloured circles. Inset are schematic representations of A (left), C_{ORTHO} (centre), and E (right).

A profile depicting the minimum energy path associated with para hydrogenation is provided in **Figure 3.10**. As with ortho hydrogenation, the energetically optimal order of carbon hydrogenation was identical regardless of catalyst: B5, then C_{PARA}, then D3, then E. The activation energy for para hydrogenation over Pd(111) (E_A = +96.1 kJ mol^{-1}) was shown to be almost 40% higher than the corresponding activation energy barrier for ortho hydrogenation. While the energetic difference between the routes is relatively large, it is plausible that Pd-catalysed para hydrogenation could compete with ortho hydrogenation at conventional operating temperatures of 180 °C.[26]

The large energy barrier associated with para hydrogenation over Pt(111) (E_A = +208.3 kJ mol^{-1}) is likely insurmountable under operating temperatures and pressures. It should be noted that if the hydrogenation of the para product first takes place at carbon-2 (C_{PARA}→D2), hydrogenation over both Pd(111) (E_A = +314.1 kJ mol^{-1}) and Pt(111) (E_A = +326.0 kJ mol^{-1}) becomes even more insurmountable. The transition state corresponding to the hydrogenation of carbon-3 over Pt(111) (C_{PARA}→D3), a step with a particularly high activation energy, is given in **Figure 3.11**. The migration of the H atom to the ring carbon is hindered by an unfavourable angle of approach (70.6°), as well as the large interatomic distance between carbon-2 (2.01 Å) and the catalyst surface (2.08 Å).

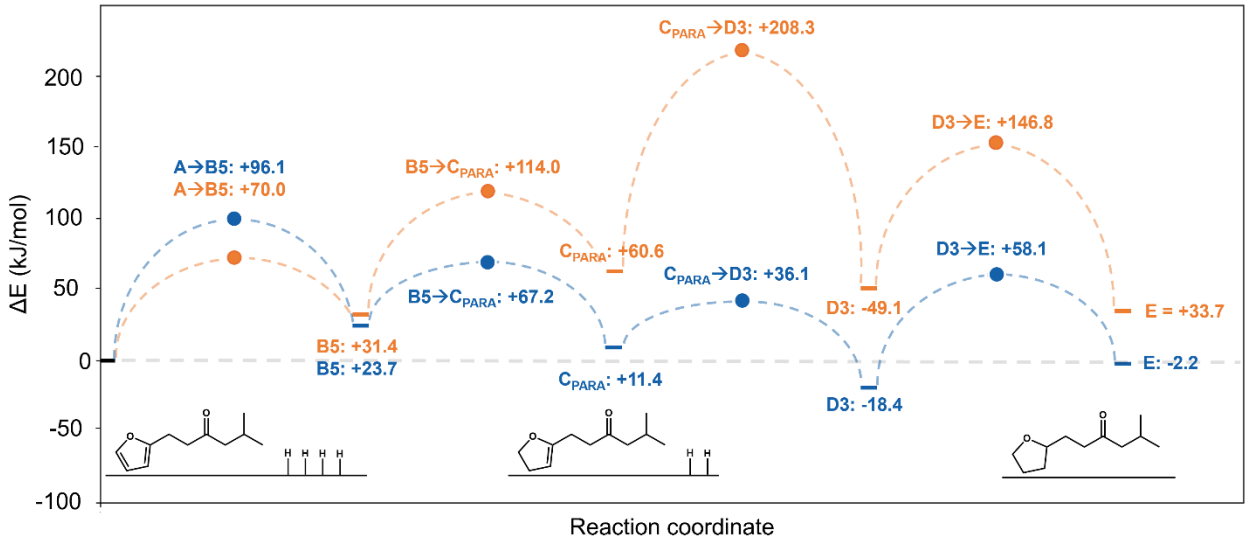

Figure 3.10. The minimum energy path for para hydrogenation over Pd(111) (blue) and Pt(111) (orange). Transition states between minima are marked with coloured circles. Inset are schematic representations of A (left), C_{PARA} (centre), and E (right).

Pt(111): C_{PARA}→D3	
Activation energy	+208.3 kJ mol^{-1}
H-C_{α}-H bond angle	70.6°

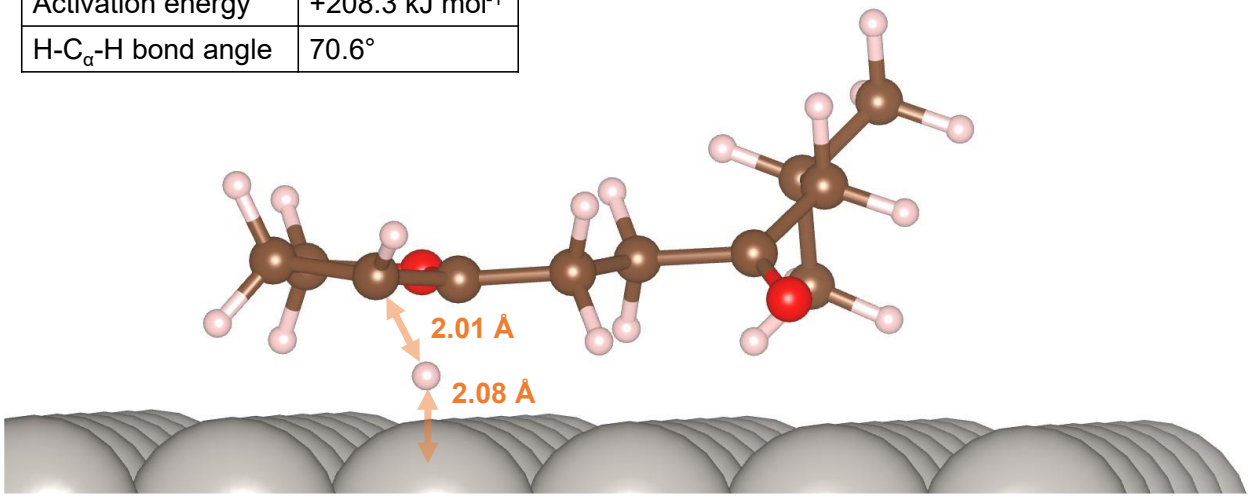

Figure 3.11. Optimised transition state structure for the hydrogenation of the para product to the intermediate D3 over Pt(111).

As shown in **Figure 3.12a**, carbon-2 (q = +0.21 e) had the greatest partial positive charge of any of the ring carbons in the gas phase due to its proximity to an electronegative O atom at the 1-position. Over both Pd(111) and Pt(111), all of the ring carbons became more positively charged; a likely consequence of electrons in the π-system being donated into the d-orbitals of the surface metal atoms. Unlike the chain C=C bond of ALD-1, catalyst choice had a marked effect on the polarisation of ALD-

2's ring carbons. Over Pt, all of the ring carbons became more positively charged; particularly, carbon-2 (Δq = +0.07 e) and carbon-3 (Δq = +0.08 e). This suggests that ortho hydrogenation is a "selectivity bottleneck" that must be surpassed if the reduction of ALD-2's ring system is to be thermodynamically feasible. If carbon-3 is hydrogenated first, even more electron density is siphoned away from the ring system, further destabilising it.

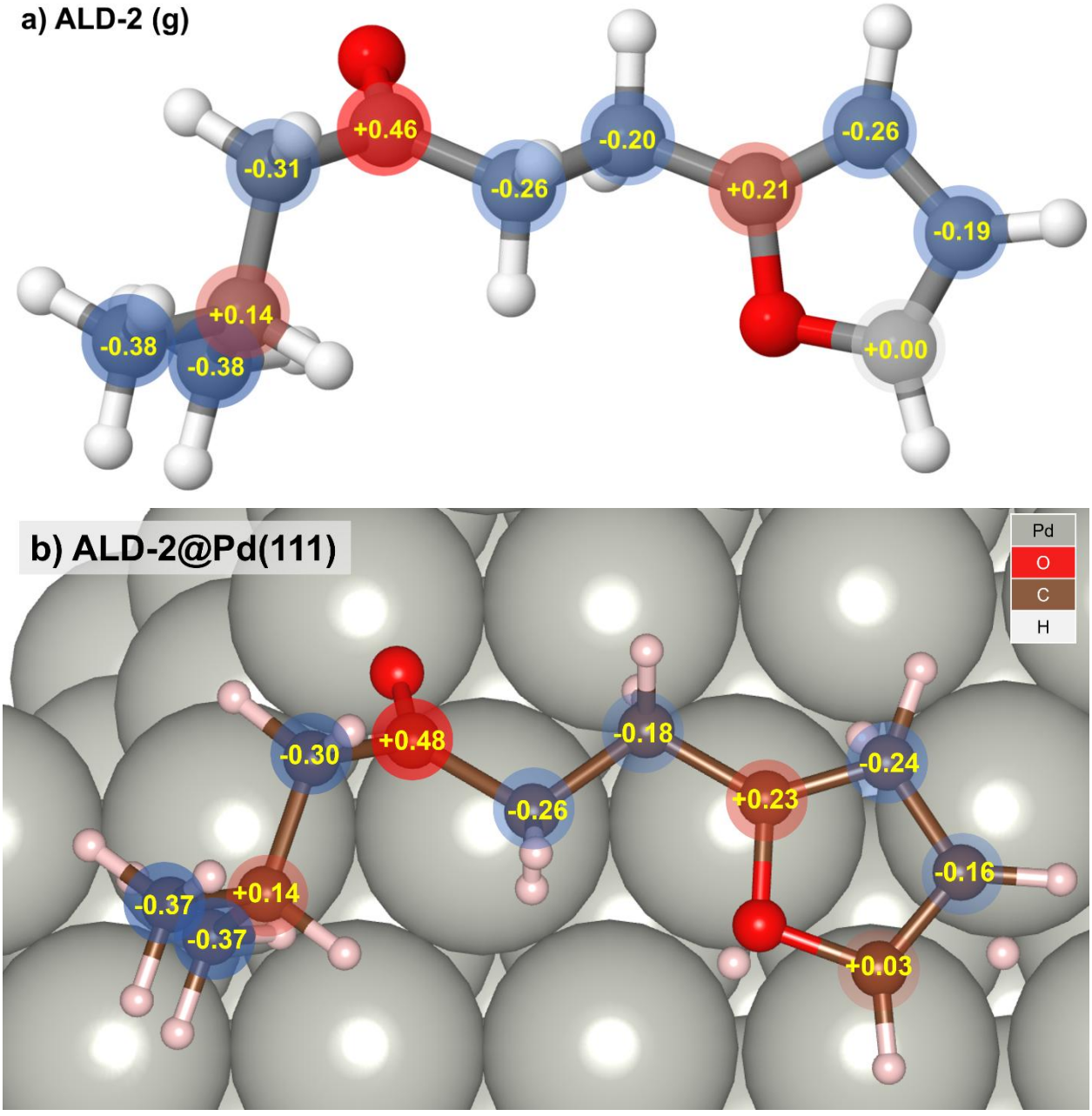

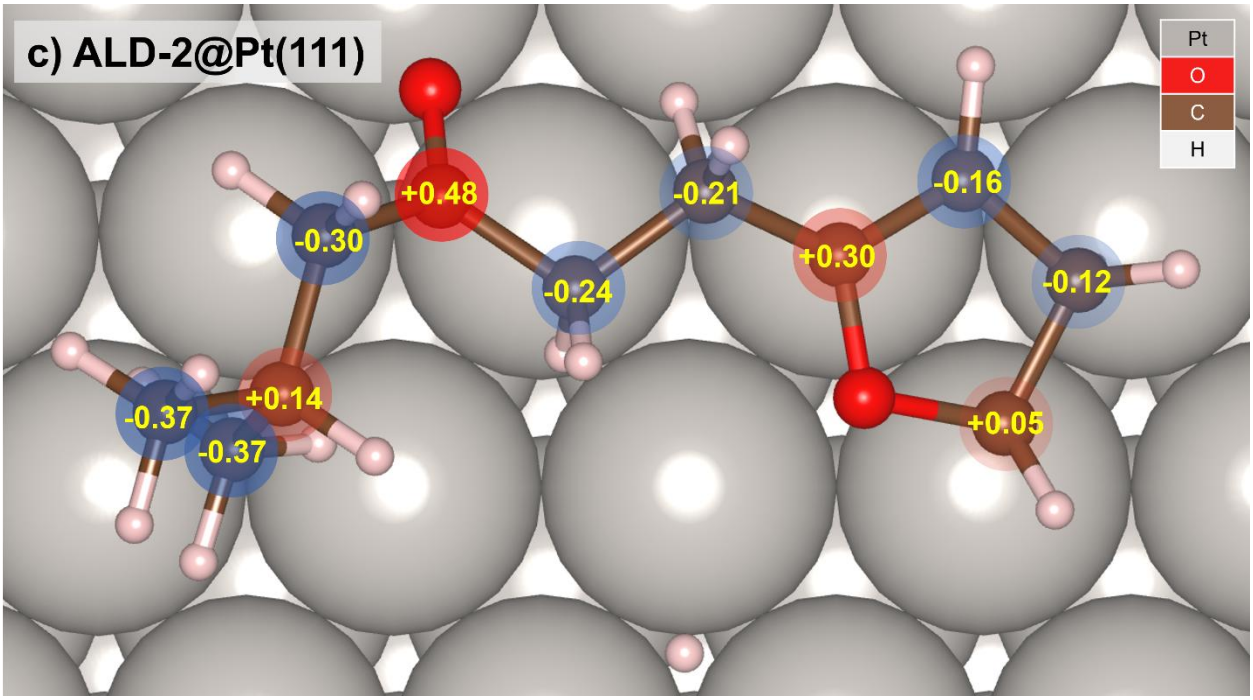

Figure 3.12. DDEC6 charge analysis of ALD-2 (a) in the gas phase and adsorbed to (b) Pd(111) and (c) Pt(111). Carbon atoms with partial positive and negative charges are highlighted in red and blue, respectively. Figures given in units of elementary charge.

The extent to which positive charge accumulates at carbon-2 during ortho hydrogenation was assessed by conducting a final round of DDEC6 charge analysis on the B2→C and B3→C transition states. Over both Pd(111) and Pt(111) (**Figures 3.13a** and **3.13c**), hydrogenation at the 2-position led to a significant reduction in localised positive charge. Conversely, this problem was greatly exacerbated over Pd(111) when carbon-3 was hydrogenated first (**Figure 3.13b**), leading to the generation of a highly positive partial charge (q = +0.35 e) on carbon-2. Over Pt(111), a transition state for B3→C hydrogenation (**Figure 3.13d**) was identified with an effectively unchanged carbon-2 partial charge from ALD-2 (Δq = –0.01 e), but this preservation of further charge accumulation came at the cost of significantly distorting the bonds connecting carbon-2 to carbon-5 and the hydrogenated α,β-chain ($\angle$ = 128.3°). This disparity in the localisation of positive charge explains why the activation energy for B3→C is far higher than the corresponding activation energy for B2→C over both Pd(111) and Pt(111). Regardless of catalyst choice, the optimal thermodynamic pathway was shown to begin with the immediate hydrogenation of carbon-2 to minimise the accumulation of a point positive charge at this position.

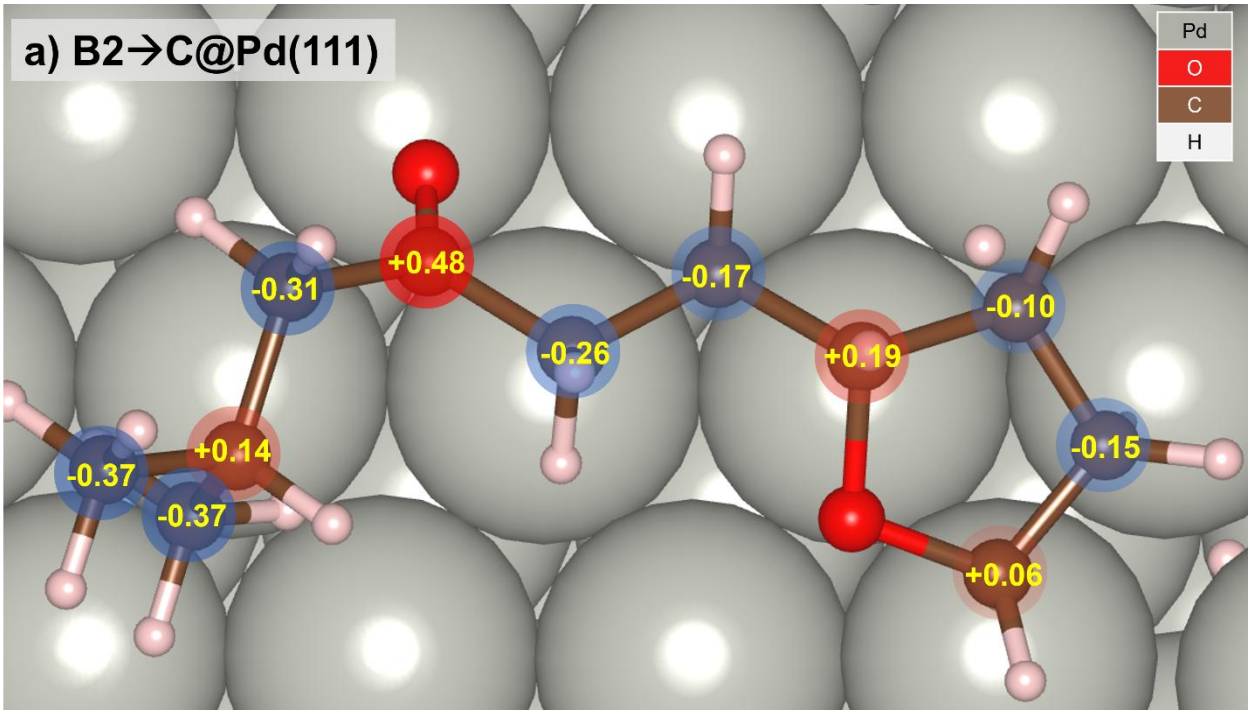
a) B2→C@Pd(111)
Pd
O
C
H
+0.48
-0.31
-0.17
-0.10
-0.26
+0.19
+0.14
-0.37
-0.37
-0.15
+0.06

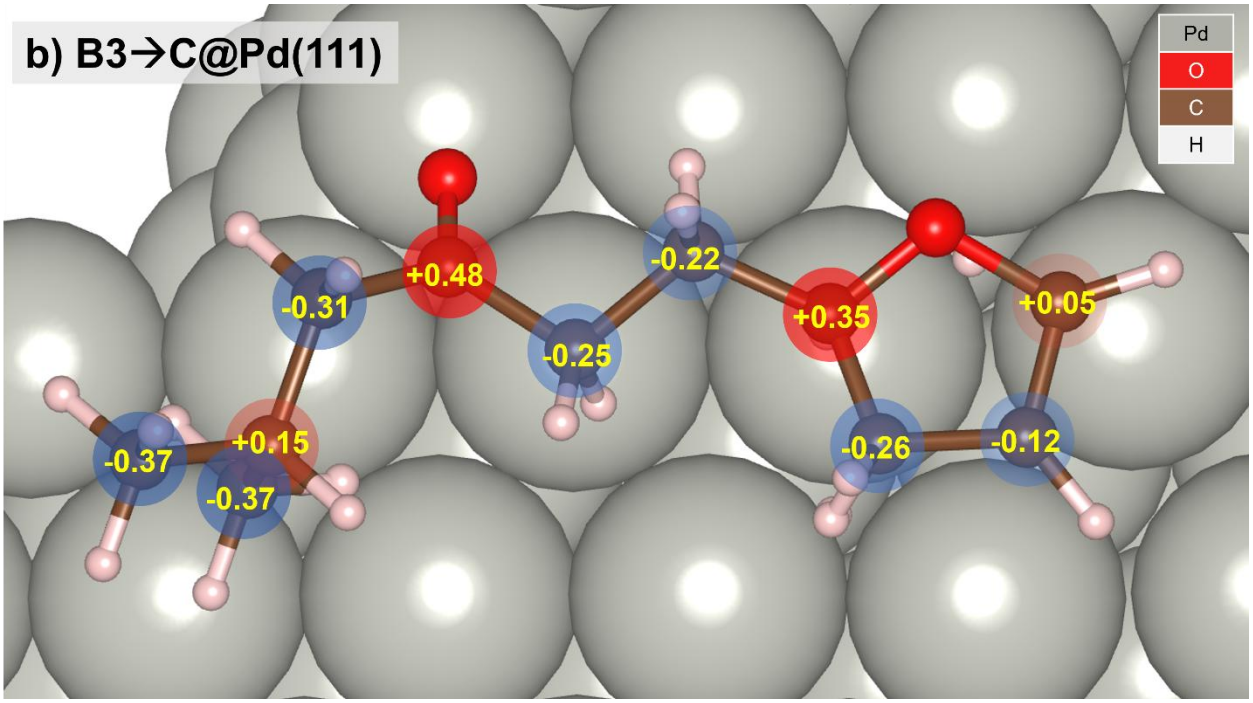
b) B3→C@Pd(111)
Pd
O
C
H
+0.48
-0.22
-0.31
+0.35
+0.05
-0.25
+0.15
-0.37
-0.37
-0.26
-0.12

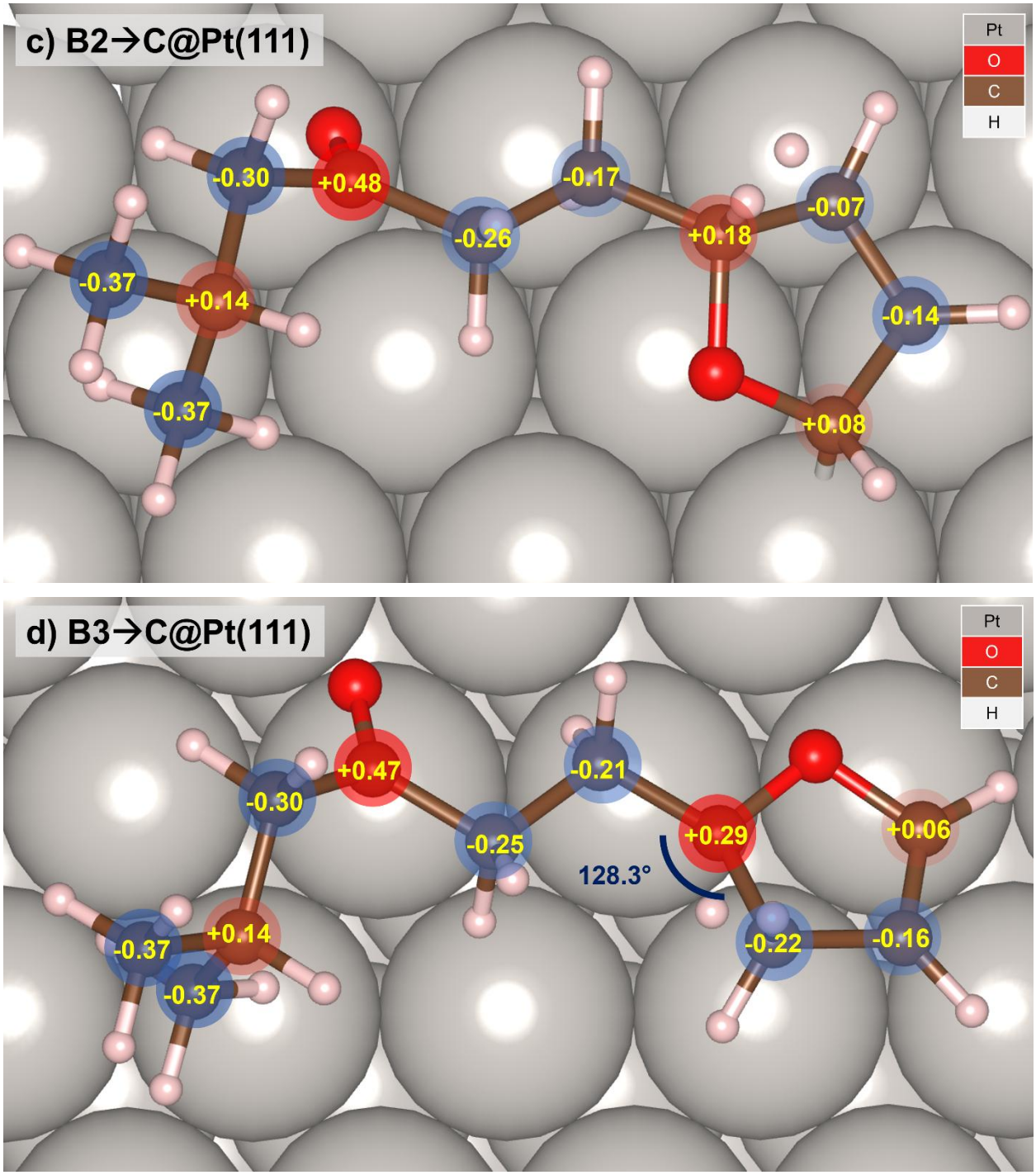

Figure 3.13. DDEC6 charge analysis of a selection of ortho hydrogenation transition states: (a) B2→C@Pd(111); (b) B3→C@Pd(111); (c) B2→C@Pt(111); (d) B3→C@Pt(111). Carbon atoms with partial positive and negative charges are highlighted in red and blue, respectively. Figures given in units of elementary charge.

A profile of the minimum energy pathway for the total hydrogenation of ALD-1 to ALD-3 is provided in **Figure 3.14**. The complete path shows a marked preference for ortho hydrogenation over both Pd and Pt, and that the poor selectivity of Pt-catalysis towards ring hydrogenation is the result of steep energetic penalties associated with the accumulation of positive charge on the ring carbons.

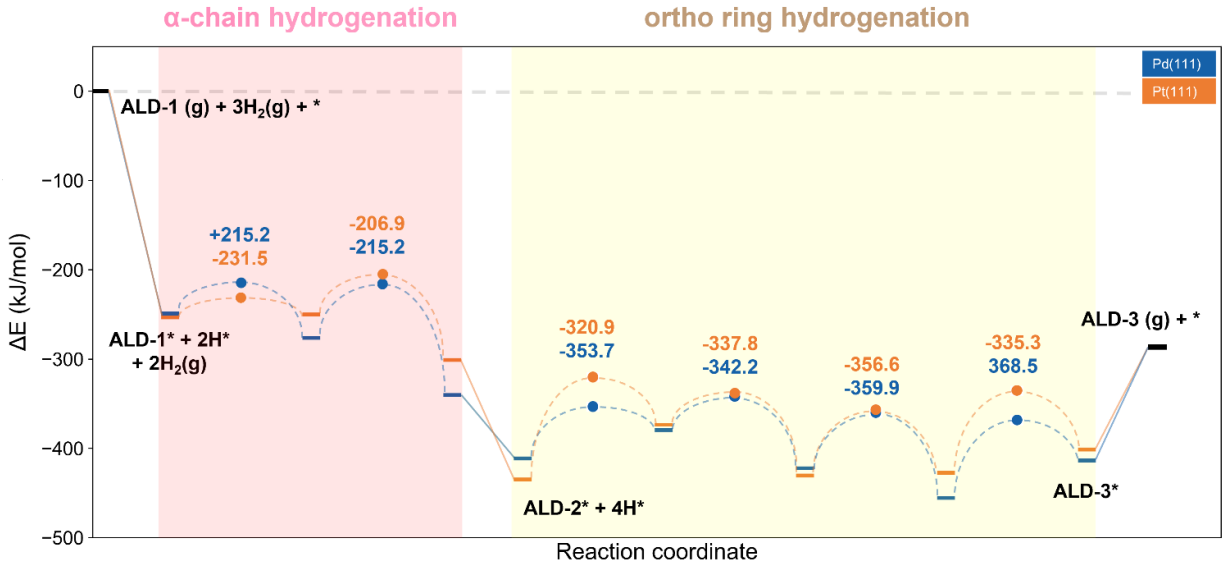

Figure 3.14. The minimum energy pathway for the hydrogenation of ALD-1 to ALD-3 over Pd(111) and Pt(111). After binding to the catalyst in the gas phase, ALD-1 undergoes α-chain hydrogenation (pink) to ALD-2, and ortho ring hydrogenation (cream) to ALD-3. All dissociated hydrogens (H*) are bound at hollow sites.

3.6. Experimental Validation

GC-MS (**Figure 3.15**) confirmed that ALD-1 readily hydrogenates over Pd/Al_2O_3. Within five minutes, ALD-1 was completely consumed. The yield of ALD-3 plateaued at 100% within two hours, showing that Pd is fully selective towards ring hydrogenation. Over Pt/Al_2O_3, however, the dynamics of the reaction proved to be more complicated. Hydrogenation of ALD-1 was initially slow. For the first two hours, there were still traces of ALD-1 in solution. The production of ALD-2 via chain hydrogenation dominated the early stages of the reaction. For comparison, ALD-2 was nearly consumed within an hour over Pd/Al_2O_3 under the same conditions. At the three-hour mark, there was a “crossover” between the yields of the hydrogenation products as the remaining molecules of ALD-2 underwent reduction to ALD-3.

When the reaction was left to run overnight, the yields of both ALD-2 and ALD-3 sharply declined, resulting in final yields of 33% and 12%, respectively, leaving 55%

of the product unaccounted for. At temperatures above 150 °C, it is well known that furfural and its derivatives readily undergo polymerisation and ring opening over Pt.[13,71–73] Following the work of Mizugaki *et al.*[71] on the conversion of furfural to 1,2-pentanediol, it is likely that opening the ring in the presence of H_2 will result in the formation a diol. The stereochemistry of this diol will depend on whether ring cleavage occurs at the C2-O or C5-O bond. In the case of furfural over Pt nanoparticles,[13,71] ring cleavage typically occurs after the reduction of the carbonyl group. However, if the ring is opened before this can happen, branching hydroxy ketones and long-chain alkenes will be generated. If these molecules are generated at our chosen operating temperatures, they will likely polymerise, either with themselves or unreacted molecules of ALD-1, ALD-2, and ALD-3 bound to the surface.

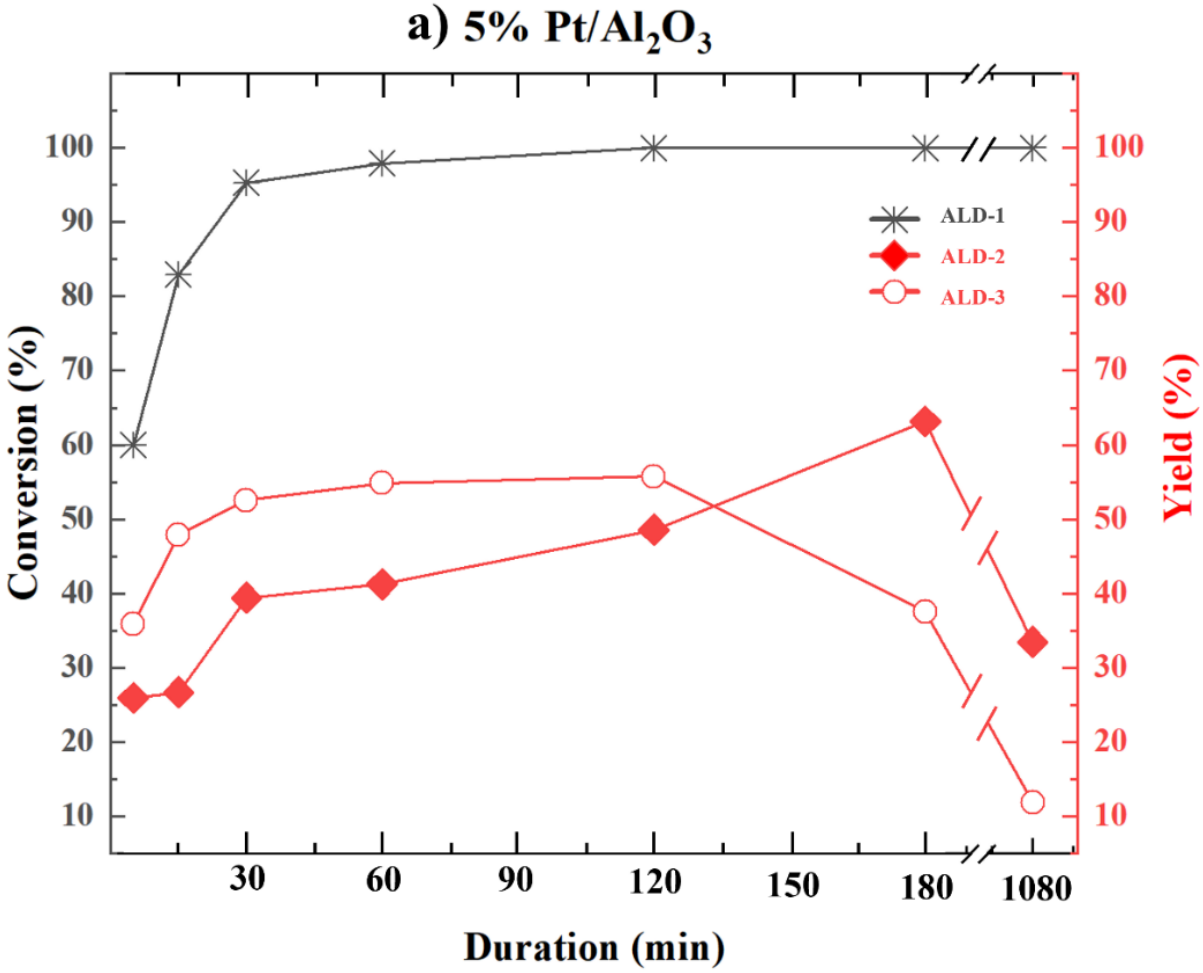

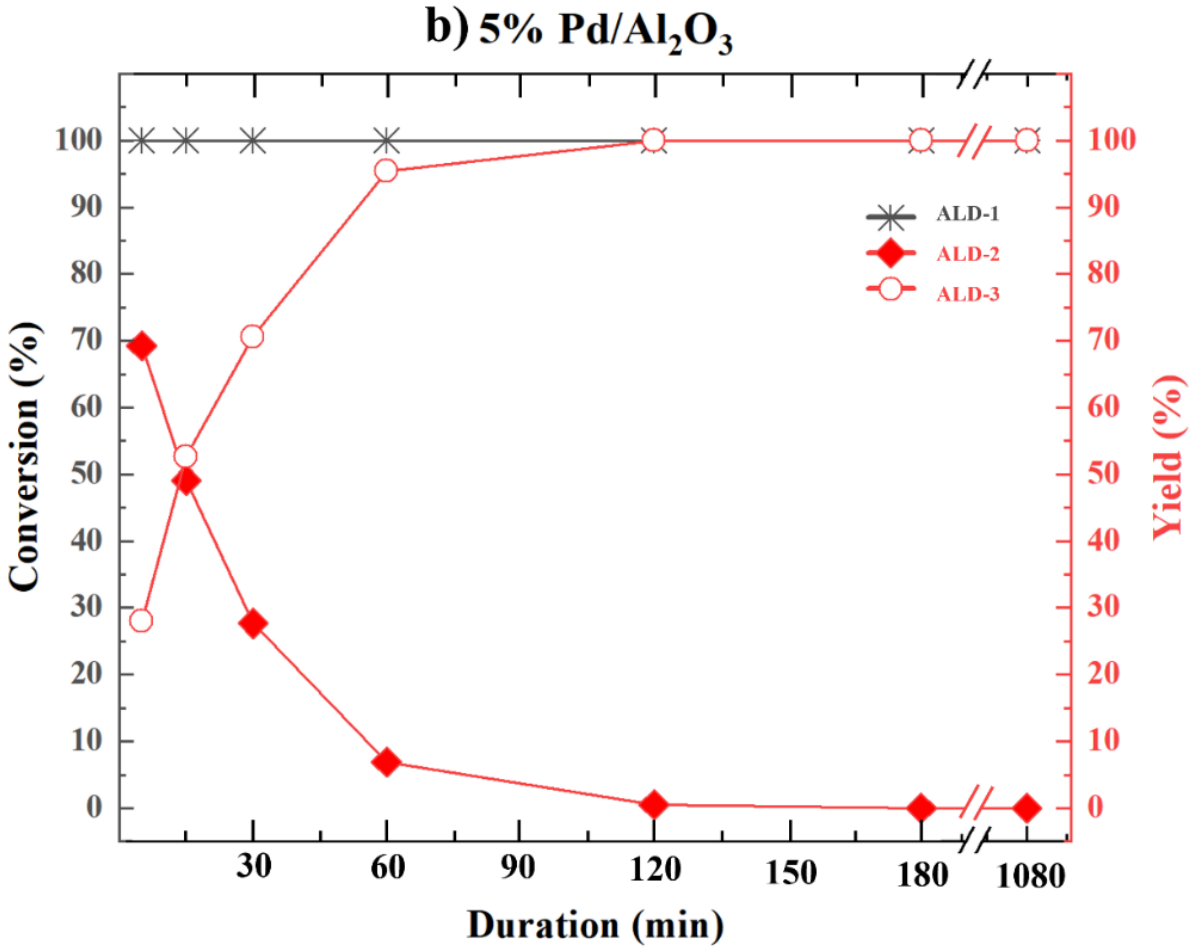

Figure 3.15. GC-MS plots of the evolution of ALD-1 to the chain hydrogenation product ALD-2 and the fully hydrogenated ketone ALD-3 over (a) Pd/Al_2O_3 and (b) Pt/Al_2O_3. Measurements taken at 5, 15, 30, 60, 120, 180, and 1080 minutes.

If any of these compounds undergo ring opening on the surface, a complex web of side reactions emerges, significantly impacting the distribution of the products. It was only by combining spectroscopic and computational methods that the true nature of the reaction became clear: The low yields of ALD-3 over Pt/Al_2O_3 are the result of a complex combination of factors that would have been highly challenging to discern with GC-MS or DFT in isolation; namely, high energy barriers associated with ring hydrogenation, the facilitation of Pt-catalysed ring cleavage, and a range of polymerisation side reactions.

3.7. Conclusions and Perspectives

In conclusion, accessible energy pathways for the chain (E_A = +33.9 kJ mol^{-1}) and ring (E_A = +69.1 kJ mol^{-1}) hydrogenation of ALD-1 over Pd(111) were identified through a combination of computational modelling and spectroscopic analysis. While chain hydrogenation over Pt(111) was thermodynamically accessible, the reduction of ALD-1's furanic ring system was limited by high activation energy barriers barring both ortho and para hydrogenation. Over both surfaces, the selectivity towards α-hydrogenation was found to be driven by both the distribution of charge on the carbon chain and the sterics of the routes' respective transition states.

An aspect of this work that warrants further study is the characterisation of the compounds making up the remaining 55% of the product mixture formed over Pt/Al_2O_3. A hypothetical mechanism for Pt-catalysed diol formation is provided in **Scheme 3.4**. If the ring system is hydrogenated before cleavage, the C2-O bond breaks, forming 9-methyldecane-1,7-diol; otherwise, the ring will break at the C5-O bond, forming 2-methyldecane-4,7-diol. If previous experimental studies on the Pt-catalysed ring cleavage of furfural are indicative of ALD-2 and ALD-3's chemistry on Pd/Al_2O_3,[13,71–73] the initial step is expected to be the hydrogenation of the ketone to an alcohol, followed by cleaving the C2-O or C5-O bond. However, if the ring system opens before the C=O bond can be reduced, branching diketones and hydroxy ketones will be generated. At the chosen operating temperature of 180 °C, these compounds will likely polymerise; either with themselves, or with unreacted molecules of ALD-1, ALD-2, and ALD-3 bound to the surface.

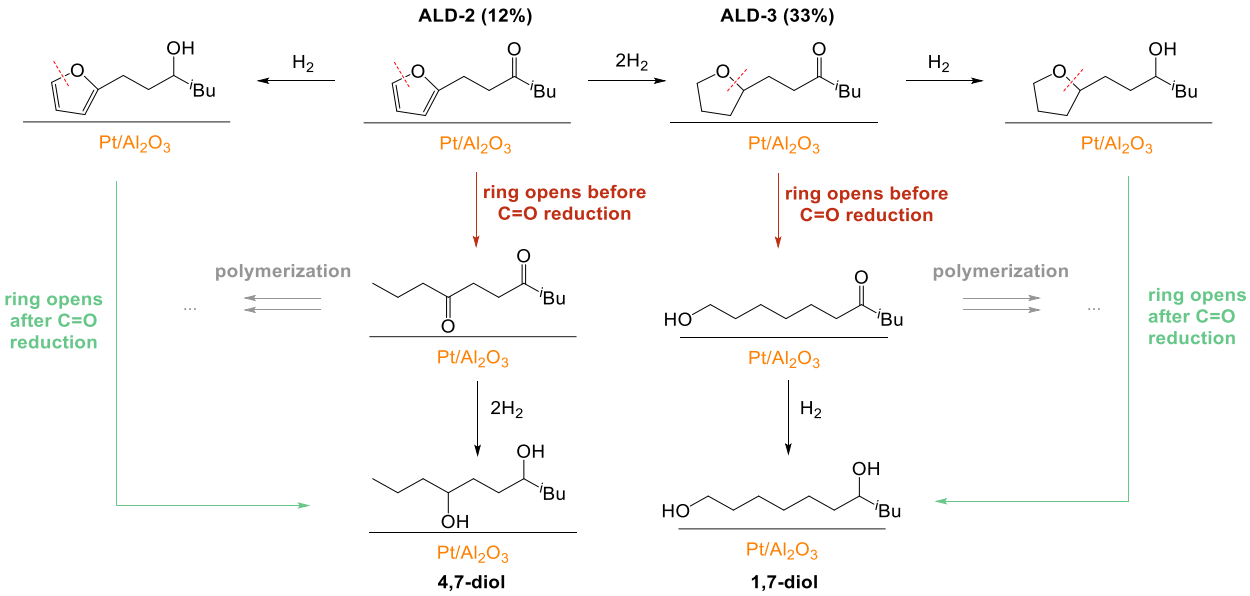

Scheme 3.4. Hypothetical mechanism for the formation of diols, diketones, and polymerised hydrocarbons over Pt/Al_2O_3.

While the mechanism depicted in **Scheme 3.4** remains speculative, it offers a plausible explanation for the significant loss in mass balance observed when ALD-1 is hydrogenated in the presence of Pt nanoparticles, highlighting the need for further experimental analysis relating to ring opening and polymerisation. It is the hope of the author that this chapter showcases how combining computational modelling with spectroscopic techniques can help deepen our collective understanding of the mechanistic chemistry involved in Pd and Pt catalysis.

3.8. References

1. D. T. Win, *Au J Technol*, **2005**, 8, 185–190.
2. S. Wang, V. Vorotnikov and D. G. Vlachos, *Green Chem.*, **2014**, 16, 736–747.
3. G. Pruckmayr, P. Dreyfuss and M. P. Dreyfuss, *Kirk-Othmer Encycl. Chem. Technol.*, **2000**.
4. L. Hu, L. Lin and S. Liu, *Ind. Eng. Chem. Res.*, **2014**, 53, 9969–9978.
5. S. De, S. Dutta and B. Saha, *ChemSusChem*, **2012**, 5, 1826–1833.
6. Á. Szabolcs, M. Molnár, G. Dibó and L. T. Mika, *Green Chem.*, **2013**, 15, 439–445.
7. M. A. Ravutsov, M. M. Marinova, A. Kurutos and S. P. Simeonov, *Sustain. Chem. Pharm.*, **2024**, 38, 101491.
8. I. Y. Eyüpoglu, M. Buchfelder and N. E. Savaskan, *Nat. Rev. Neurol.*, **2013**, 9, 141–151.
9. J. Slak, B. Pomeroy, A. Kostyniuk, M. Grilc and B. Likozar, *Chem. Eng. J.*, **2022**, 429.
10. G. Trapasso, G. Mazzi, B. Chícharo, M. Annatelli, D. Dalla Torre and F. Aricò, *Org. Process Res. Dev.*, **2022**, 26, 2830–2838.
11. N. Esmaeili, M. J. Zohuriaan-Mehr, H. Bouhendi and G. Bagheri-Marandi, *Korean J. Chem. Eng.*, **2016**, 33, 1964–1970.
12. M. Musolino, J. Andraos and F. Aricò, *ChemistrySelect*, **2018**, 3, 2359–2365.
13. J. Zhu and G. Yin, *ACS Catal.*, **2021**, 11, 10058–10083.
14. S. E. Davis, L. R. Houk, E. C. Tamargo, A. K. Datye and R. J. Davis, *Catal. Today*, **2011**, 160, 55–60.
15. M. Sajid, X. Zhao and D. Liu, *Green Chem.*, **2018**, 20, 5427–5453.
16. P. Sahu, A. Thorbole and R. K. Gupta, *ACS Sustain. Chem. Eng.*, **2024**, 12, 6811–6826.
17. Y. N. Palai, A. Shrotri and A. Fukuoka, *ACS Catal.*, **2022**, 12, 3534–3542.
18. W. Zhu, F. Tao, S. Chen, M. Li, Y. Yang and G. Lv, *ACS Sustain. Chem. Eng.*, **2019**, 7, 296–305.
19. M. Lomelí-Rodríguez, J. R. Corpas-Martínez, S. Willis, R. Mulholland and J. A. Lopez-Sanchez, *Polymers*, **2018**, 10, 1–19.
20. M. Lomelí-Rodríguez, M. Martín-Molina, M. Jiménez-Pardo, Z. Nasim-Afzal, S. I. Cauët, T. E. Davies, M. Rivera-Toledo and J. A. Lopez-Sanchez, *J. Polym. Sci. Part Polym. Chem.*, **2016**, 54, 2876–2887.
21. E. De Jong, M. A. Dam, L. Sipos and G. J. M. Gruter, *ACS Symp. Ser.*, **2012**, 1105, 1–13.
22. A. J. J. E. Eerhart, A. P. C. Faaij and M. K. Patel, *Energy Environ. Sci.*, **2012**, 5, 6407–6422.
23. P. T. Anastas and J. C. Warner, *Green Chemistry: Theory and Practice*, Oxford University Press, **2000**.
24. S. L. Y. Tang, R. L. Smith and M. Poliakoff, *Green Chem.*, **2005**, 7, 761–762.
25. A. García-Ortiz, J. D. Vidal, M. J. Climent, P. Concepción, A. Corma and S. Iborra, *ACS Sustain. Chem. Eng.*, **2019**, 7, 6243–6250.
26. S. Jiang, C. Ma, E. Muller, M. Pera-Titus, F. Jérôme and K. De Oliveira Vigier, *ACS Catal.*, **2019**, 9, 8893–8902.
27. W. Zhang, Y. Shi, Y. Yang, J. Tan and Q. Gao, *Chin. J. Catal.*, **2022**, 43, 3116–3125.
28. G. Li, J. Han, H. Wang, X. Zhu and Q. Ge, *ACS Catal.*, **2015**, 5, 2009–2016.
29. F. Zaera and G. A. Somorjai, *J. Am. Chem. Soc.*, **1984**, 106, 2288–2293.

30. P. A. Sheth, M. Neurock and C. M. Smith, *J. Phys. Chem. B*, **2003**, 107, 2009–2017.
31. F. E. Massoth, P. Politzer, M. C. Concha, J. S. Murray, J. Jakowski and J. Simons, *J. Phys. Chem. B*, **2006**, 110, 14283–14291.
32. S. Sitthisa, T. Sooknoi, Y. Ma, P. B. Balbuena and D. E. Resasco, *J. Catal.*, **2011**, 277, 1–13.
33. M. Pirmoradi and J. R. Kastner, *Chem. Eng. J.*, **2021**, 414, 128693.
34. I. K. M. Yu, F. Deng, X. Chen, G. Cheng, Y. Liu, W. Zhang and J. A. Lercher, *Nat. Commun.*, **2022**, 13, 7154.
35. P. Liu, W. Qiu, C. Zhang, Q. Tan, C. Zhang, W. Zhang, Y. Song, H. Wang and C. Li, *ChemCatChem*, **2019**, 11, 3296–3306.
36. R. Baxter and P. Hu, *J. Chem. Phys.*, **2002**, 116, 4379–4381.
37. J. Hafner and G. Kresse, in *Properties of Complex Inorganic Solids*, Springer, **1997**, 69–82.
38. B. Hammer, L. B. Hansen and J. K. Nørskov, *Phys. Rev. B*, **1999**, 59, 7413–7421.
39. S. Grimme, J. Antony, S. Ehrlich and H. Krieg, *J. Chem. Phys.*, **2010**, 132.
40. H. J. Monkhorst and J. D. Pack, *Phys. Rev. B*, **1976**, 13, 5188.
41. G. Kresse and D. Joubert, *Phys. Rev. B*, **1999**, 59, 1758.
42. P. E. Blöchl, *Phys. Rev. B*, **1994**, 50, 17953.
43. H. Conrad, G. Ertl and E. E. Latta, *Surf. Sci.*, **1974**, 41, 435–446.
44. R. A. Olsen, G. J. Kroes and E. J. Baerends, *J. Chem. Phys.*, **1999**, 111, 11155–11163.
45. P. Feulner and D. Menzel, *Surf. Sci.*, **1985**, 154, 465–488.
46. L. R. Danielson, M. J. Dresser, E. E. Donaldson and J. T. Dickinson, *Surf. Sci.*, **1978**, 71, 599–614.
47. M. Y. Chou and J. R. Chelikowsky, *Phys. Rev. Lett.*, **1987**, 59, 1737–1740.
48. D. C. Ford, Y. Xu and M. Mavrikakis, *Surf. Sci.*, **2005**, 587, 159–174.
49. S. S. Borkar and M. Shetty, *J. Phys. Chem. C*, **2024**, 128, 12916–12930.
50. K. K. Al-Shammeri and J. M. Saleh, *J. Phys. Chem.*, **1986**, 90, 2906–2910.
51. G. B. Fisher, *Chem. Phys. Lett.*, **1981**, 79, 452–458.
52. G. J. Kubas, *J. Organomet. Chem.*, **2014**, 751, 33–49.
53. K. B. Nilsson, PhD Thesis, Uppsala University, **2005**.
54. W. M. Haynes, D. R. Lide and T. J. Bruno, *CRC Handbook of Chemistry and Physics*, CRC Press, 97th edn., **2016**.
55. C. Kittel, *Introduction to Solid State Physics*, Wiley New York, 8th edn., **2005**.
56. J. P. Perdew, K. Burke and Y. Wang, *Phys. Rev. B*, **1996**, 54, 16533–16539.
57. G. P. Papapolymerou and V. Bontozoglou, *React. Kinet. Catal. Lett.*, **1996**, 58, 199–205.
58. F. R. de Boer, W. Mattens, R. Boom, A. R. Miedema and A. K. Niessen, *Cohesion in Metals: Transition Metal Alloys*, **1988**.
59. N. E. Singh-Miller and N. Marzari, *Phys. Rev. B*, **2009**, 80, 235407.
60. W. R. Tyson and W. A. Miller, *Surf. Sci.*, **1977**, 62, 267–276.
61. L. Vega, J. Ruvireta, F. Viñes and F. Illas, *J. Chem. Theory Comput.*, **2018**, 14, 395–403.
62. L. A. Constantin, J. P. Perdew and J. M. Pitarke, *Phys. Rev. B*, **2009**, 79, 075126.
63. J. P. Perdew, A. Ruzsinszky, G. I. Csonka, O. A. Vydrov, G. E. Scuseria, L. A. Constantin, X. Zhou and K. Burke, *Phys. Rev. Lett.*, **2008**, 100, 136406.
64. A. Banerjee and S. H. Mushrif, *ChemCatChem*, **2017**, 9, 2828–2838.

65. S. Wang, V. Vorotnikov and D. G. Vlachos, *Green Chem.*, **2014**, 16, 736–747.
66. B. Liu, L. Cheng, L. Curtiss and J. Greeley, *Surf. Sci.*, **2014**, 622, 51–59.
67. N. Mardirossian and M. Head-Gordon, *Mol. Phys.*, **2017**, 115, 2315–2372.
68. A. Castro-Alvarez, H. Carneros, D. Sánchez and J. Vilarrasa, *J. Org. Chem.*, **2015**, 80, 11977–11985.
69. S. H. Pang and J. W. Medlin, *ACS Catal.*, **2011**, 1, 1272–1283.
70. F. Jia and B. Zhang, *ChemPhysChem*, **2023**, 24, 1–11.
71. T. Mizugaki, T. Yamakawa, Y. Nagatsu, Z. Maeno, T. Mitsudome, K. Jitsukawa and K. Kaneda, *ACS Sustain. Chem. Eng.*, **2014**, 2, 2243–2247.
72. M. Y. Byun and M. S. Lee, *J. Ind. Eng. Chem.*, **2021**, 104, 406–415.
73. Z. Fu, Z. Wang, W. Lin, W. Song and S. Li, *Appl. Catal. Gen.*, **2017**, 547, 248–255.

4. Reductive amination of furfural derivatives over Pd(111) and Ru(0001)

4.1. Introduction

Amines are essential compounds in the energy, agricultural, and pharmaceutical sectors.[1–4] As such, it is of critical importance that the mechanistic chemistry behind amination is properly understood so that the selectivity and yield of industrially scalable syntheses can be maximised. Historically, amines were produced on an industrial scale through the N-alkylation and nucleophilic substitution of alkyl halides.[5,6] While the yields of these processes are high, they each share a number of environmental drawbacks; chief among them, the generation of large volumes of waste halide salts. Consequently, green chemists have shifted their attention to reductive amination, a family of reactions where amines are synthesised from carbonyls via an imine intermediate. While reductive amination can be conducted with a wide range of amines and reducing agents,[7–9] it is typically performed with molecular hydrogen and ammonia over a metal catalyst. The general mechanism for "classical" reductive amination over NH_3 and H_2 is well known, and has been extensively studied by physical chemists (**Scheme 4.1**).[10–14] The reaction begins with NH_3 acting as a hard nucleophile and attacking the carbonyl centre through the lone pair on the nitrogen, forming a hemiaminal intermediate. Water is then eliminated, forming an imine, and H_2 hydrogenates the C=N bond to generate the final amine.

Due to its low operating costs and high selectivity, reductive amination is currently the most popular way to produce amines at the industrial scale.[15] If the feedstock has only one carbonyl group to attack, the only waste product typically generated via classical reductive amination is water. Variants of this mechanism such as the Leuckart-Wallach reaction[8,16] have shown great utility in the pharmaceutical industry, and has been used successfully by medicinal chemists to synthesise antibiotics and anti-HIV agents.[9,17]

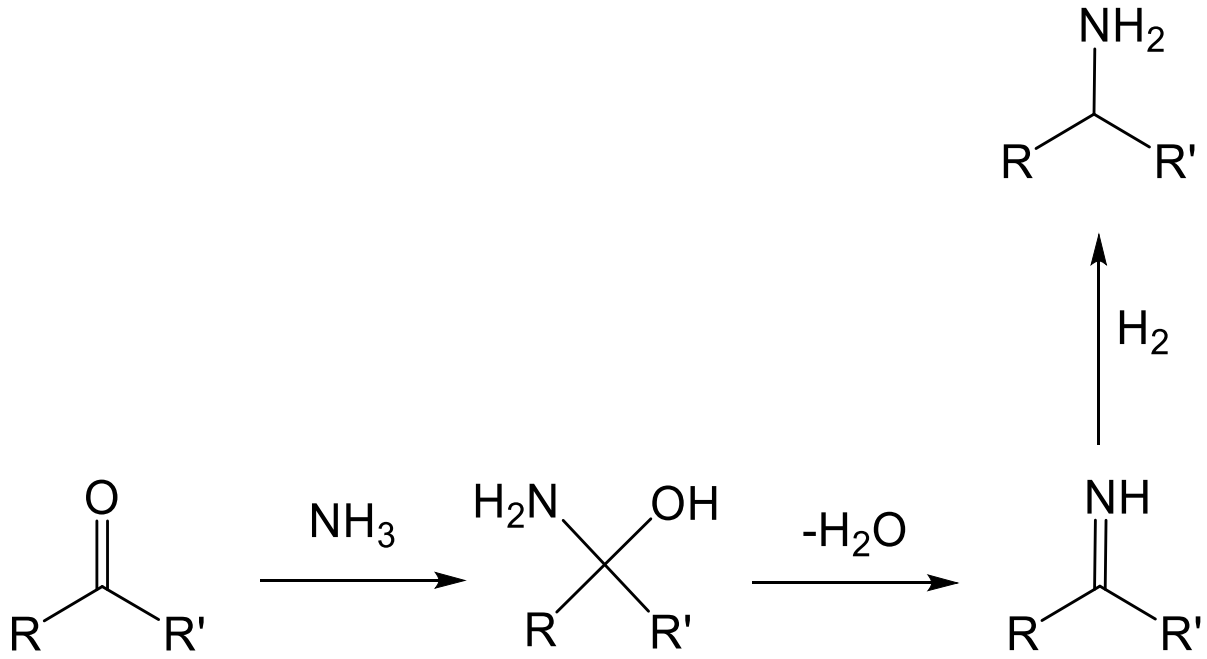

Scheme 4.1. General mechanism for the classical reductive amination of a carbonyl through a hemiaminal and an imine intermediate.

However, reductive amination is not without its drawbacks. A common problem with the classical route is that H_2 tends to over-reduce carbonyls to their corresponding alcohols.[18] Pressurised ammonia is also a dangerous reagent to work with in large quantities. If used in excess, it can lead to catalytic spoiling and the corrosion of the walls of the reaction vessels.[12,19] Nevertheless, while precautions must be taken, reductive amination remains one of the most environmentally friendly ways to synthesise amines known to synthetic chemists.

The hydrogenation of ALD-1 over Pd(111) and Pt(111) featured in the previous chapter was originally reported by Jiang *et al.*[20] in 2019 as part of a larger one-pot reductive amination scheme (**Scheme 4.2**). The initial step of the reaction, an aldol condensation with methyl isobutyl ketone (MIBK) over an Amberlyst-26 catalyst bed, takes place under identical conditions as the initial step of **Scheme 3.1**. After ALD-1 is formed, H_2 and NH_3 were introduced into the reaction vessel. Over Pd/Al_2O_3, the dominant product was the fully hydrogenated primary amine, AMI-3. Even under mild conditions, Pd/Al_2O_3 proved to be a highly selective catalyst, with a final AMI-3 yield of 92% after 12 hours. However, over Ru/C, the dominant product was an amine with its ring system untouched (AMI-2).

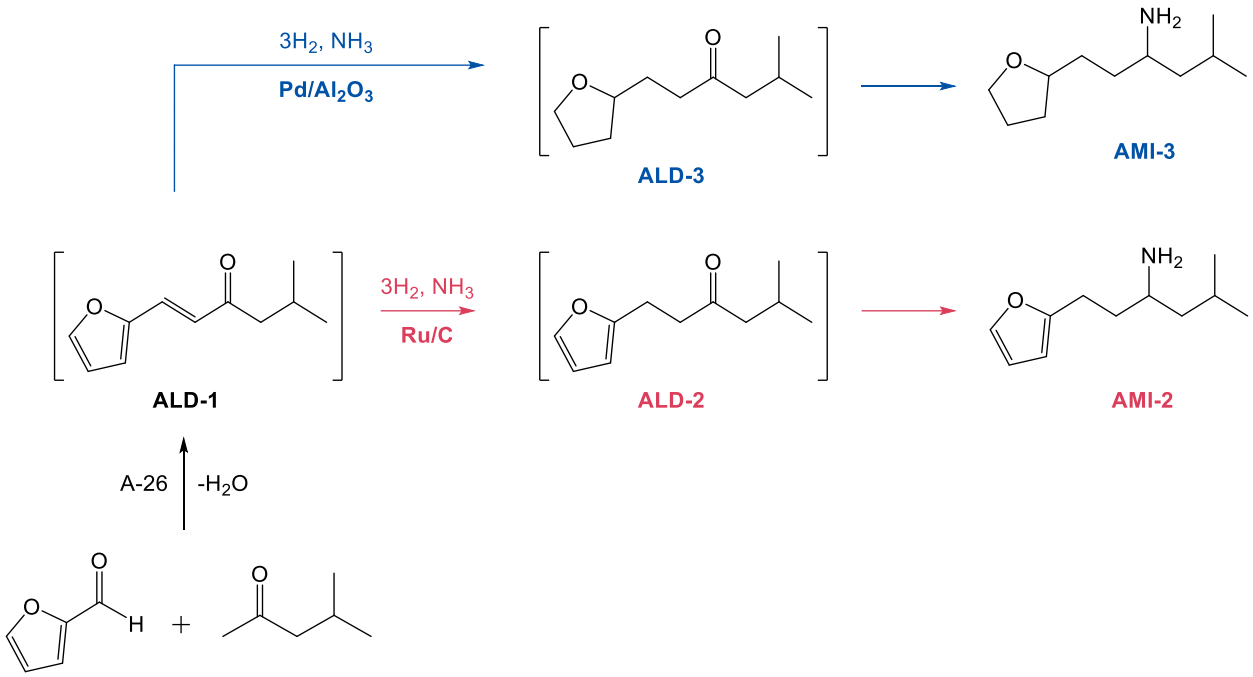

Scheme 4.2. One pot reductive amination from furfural and MIBK over Pd/Al_2O_3 and Ru/C. Reaction conditions: ALD-1 (0.2 g), NH_3 (5 bar), H_2 (20 bar), 120 °C, 12 h. Conversion of ALD-1 was over 99% for both catalysts.

As an expansion of the author's previous modelling work on the Pd- and Pt-catalysed hydrogenation of ALD-1, a second investigation was undertaken on its reductive amination over Pd(111) and Ru(0001). Following the methodology of the previous chapter, **Section 4.3** details the construction of a reaction profile for the chain and ring hydrogenation of ALD-1 over Ru(0001), with the aim of providing a mechanistic explanation for the preservation of the unsaturated ring system over this catalyst. As described in **Section 4.4**, new rounds of transition state analysis were then carried out for the three main sub-reactions associated with reductive amination over transition metal catalysts: (1) the formation of the hemiaminal via the nucleophilic addition of NH_3; (2) the formation of the imine via the elimination of water; (3) the formation of the final amine by hydrogenating the C=N bond of the imine. Like molecular hydrogen, ammonia does not typically react with adsorbed substrates from the gas phase. Following Langmuir-Hinshelwood kinetics, it was assumed that the initial step of the reaction would be the adsorption of both the furfural derivative and NH_3 to the metal surface, followed by nucleophilic substitution at the carbonyl group.

4.2. Methods

DFT models of all possible reductive amination intermediates of ALD-1 over Pd(111) and Ru(0001) were optimised in VASP.[21] All calculations were carried out under the constraints of the generalized gradient approximation (GGA) at the RPBE-D3(0) level.[22,23] Gas phase species were optimised at the centre of 20×20×20 $Å^3$ unit cells, which were then sampled with 1×1×1 Monkhorst-Pack $\boldsymbol{k}$ point meshes.[24] Unit cells of the bulk and the slab models were each sampled with 13×13×13 and 3×3×1 Monkhorst-Pack meshes, respectively.

All atoms were modelled using the projector augmented wave (PAW) potentials of Kresse and Joubert.[25,26] The plane-wave cutoff energy was set to 500 eV, the ionic convergence threshold was set to 0.03 eV/Å, and the electronic convergence threshold was set to 1×10^{-5} eV. Each surface was represented with a *p*(6×6×5) slab separated by 20 Å of vacuum along the z-axis. To improve convergence, the bottom three layers were frozen after the initial step of each calculation. The transition states associated with each hydrogenation and amination were identified using the improved dimer method and validated with a round of frequency analysis.

4.3. Hydrogenation

Similarly to Pd and Pt, it is known from the experimental findings of Jiang *et al.*[20] that that the hydrogenation of ALD-1 first occurs over Ru at the chain site. In all the products resulting from Ru catalysis, the α,β-double bond present in ALD-1 was reduced. It can be inferred from this result that the barrier associated with chain hydrogenation is low. A complete energetic profile for chain hydrogenation over Ru(0001) is provided in **Figure 4.1**. The reaction profiles for chain hydrogenation over Pd(111) and Pt(111) (**Figure 3.5**) have been superimposed over the data for Ru(0001) for comparison. The bonding conformations of ALD-1 over all three surfaces is provided in **Figure 4.2.** Transition state analysis revealed that chain hydrogenation is facile over all three metals, with activation energies under +50 kJ mol^{-1} in all cases. Like Pd(111) and Pt(111), α-hydrogenation was the most favourable hydrogenation route over Ru(0001), with an activation energy of +48.8 kJ mol^{-1}.

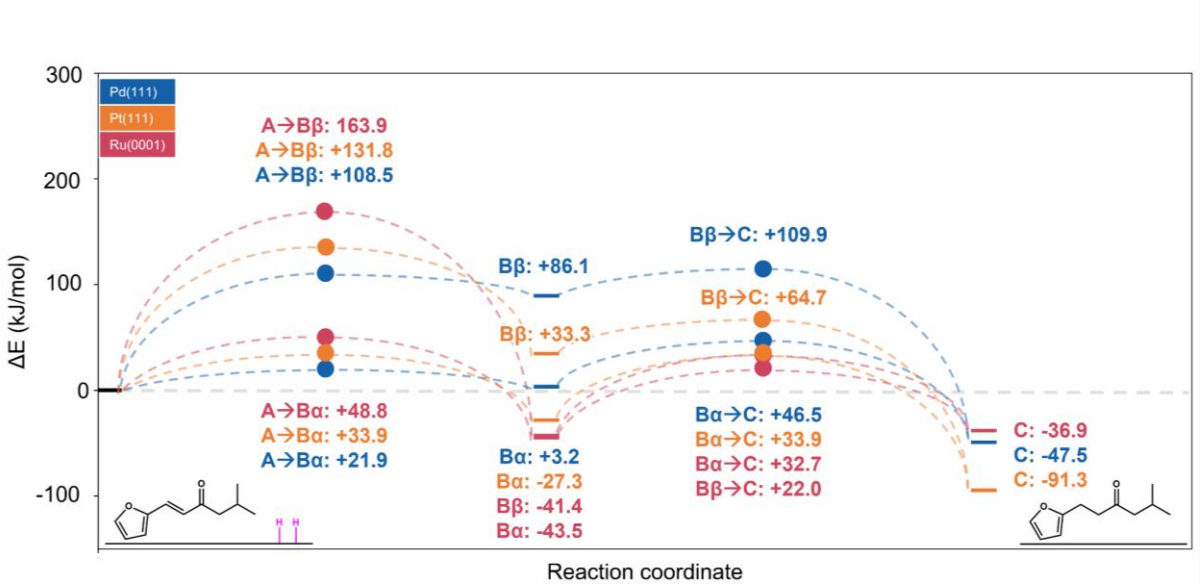

Figure 4.1. Reaction profile for the chain hydrogenation of ALD-1 over Pd(111) (blue), Pt(111) (orange), and Ru(0001) (red). Transition states between minima are marked with coloured circles. Inset are schematic representations of A (left) and C (right).

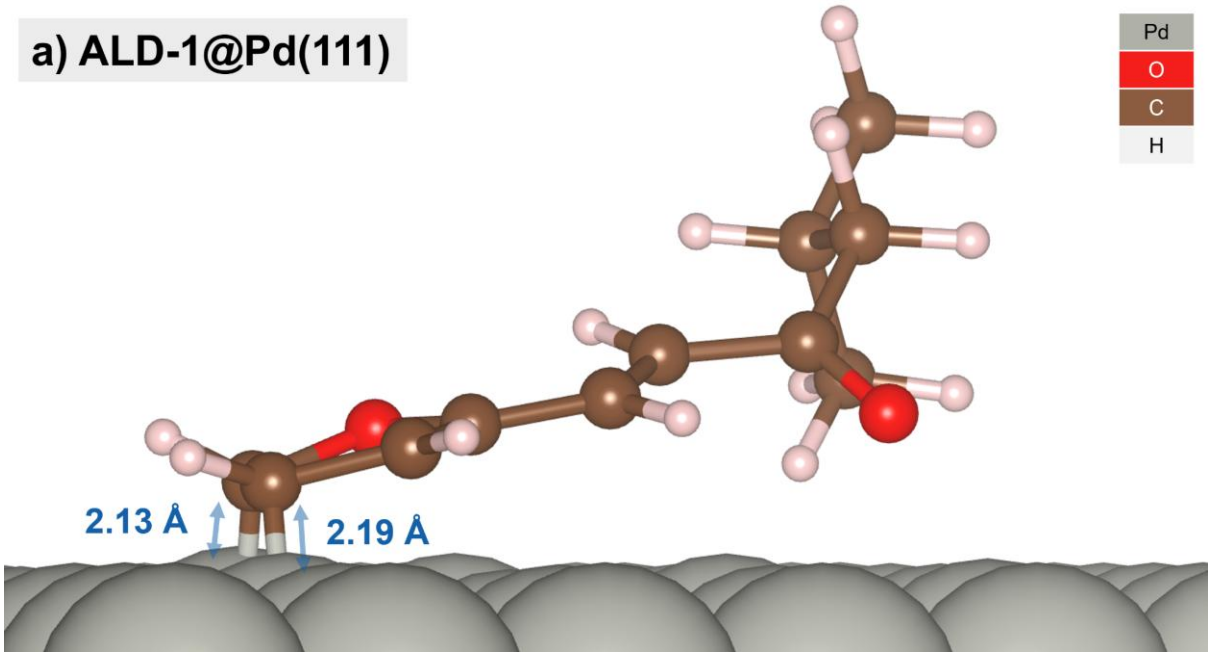

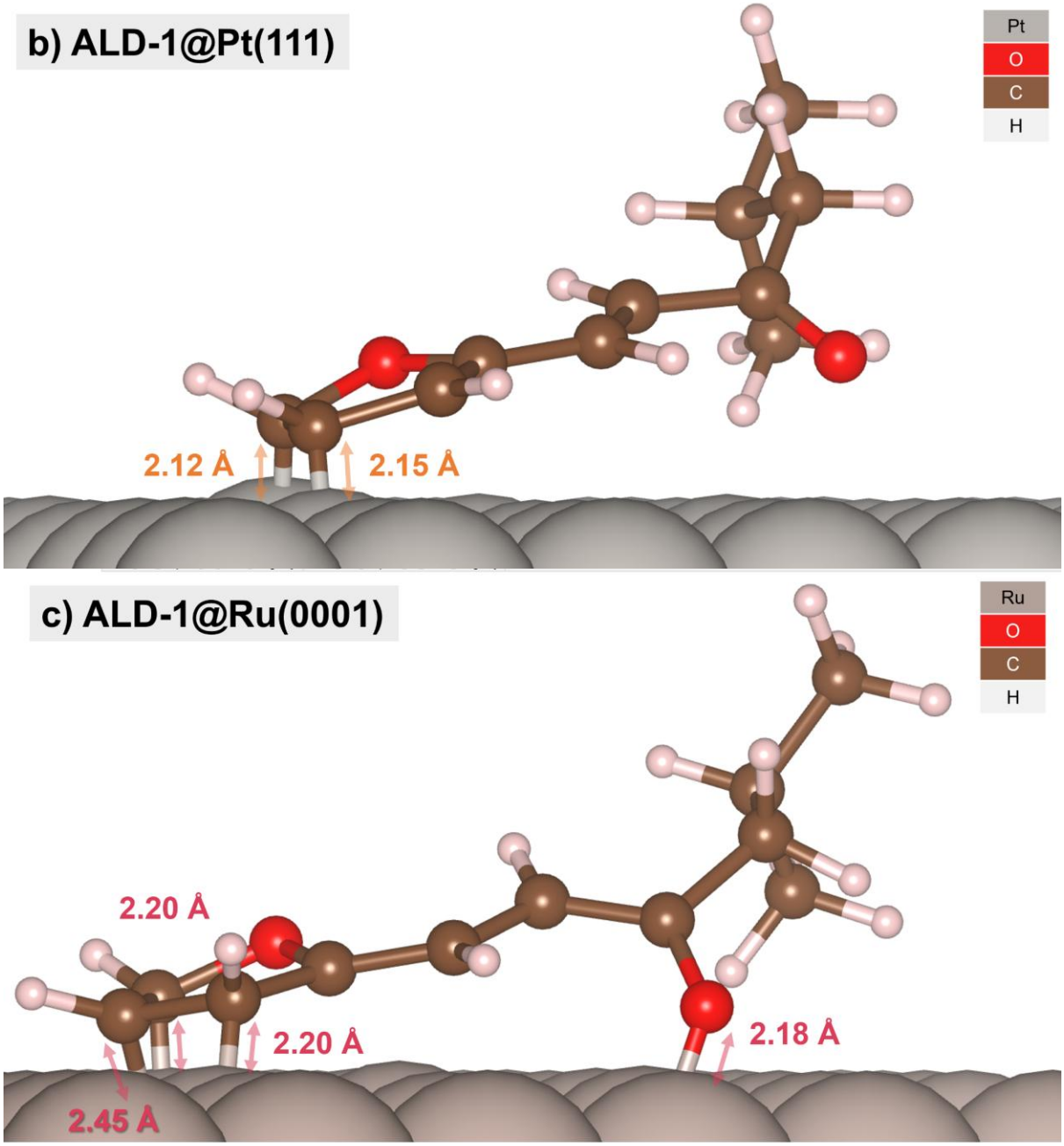

Figure 4.2. Adsorption configurations of ALD-1 over (a) Pd(111), (b) Pt(111), and (c) Ru(0001).

The difference in activation energies between α- and β-hydrogenation (ΔE_A = +115.1 kJ mol^{-1}) was at its largest over Ru(0001). If, as hypothesised in **Chapter 3**, the selectivity towards α-hydrogenation is driven by the accumulation of negative charge on the α-carbon, the disparity in electron density between C_α and C_β should be even larger over Ru(0001) than over Pd(111) and Pt(111). However, DDEC6 population analysis (**Figure 4.3**) revealed that the charge distribution of ALD-1 and ALD-2 over Ru(0001) was effectively identical the distribution of the adsorbate over

Pd(111) and Pt(0001). It should be noted that, unlike Pd(111) and Pt(111), the most energetically favourable bonding confirmation of ALD-1 over Ru(0001) exhibited a formal Ru–O bond through the carbonyl O atom ($d = 2.18$ Å), leading to a substantial reduction in the partial charge of the carbonyl C atom from +0.44 e (**Figure 3.6a**) to +0.36 e (**Figure 4.3a**). Ru's oxophilicity has been well documented in the experimental and theoretical literature.[27–30] Ru has a Kepp oxophilicity[27] of 0.4; a value that places its tendency to form oxygen bonds on par with atomic hydrogen. For comparison, Pt and Pd each have Kepp oxophilicities of 0.0 and 0.1, respectively. Across the optimised intermediates adsorbed to Ru(0001), close contact between the C=O group and the metal surface was frequently prioritised over contact with the ring system, increasing the migration distance between H adatoms and the C=C bonds. It can thus be inferred that Ru(0001)'s poor selectivity towards ring hydrogenation is a result of both unfavourable charge distribution and poor sterics.

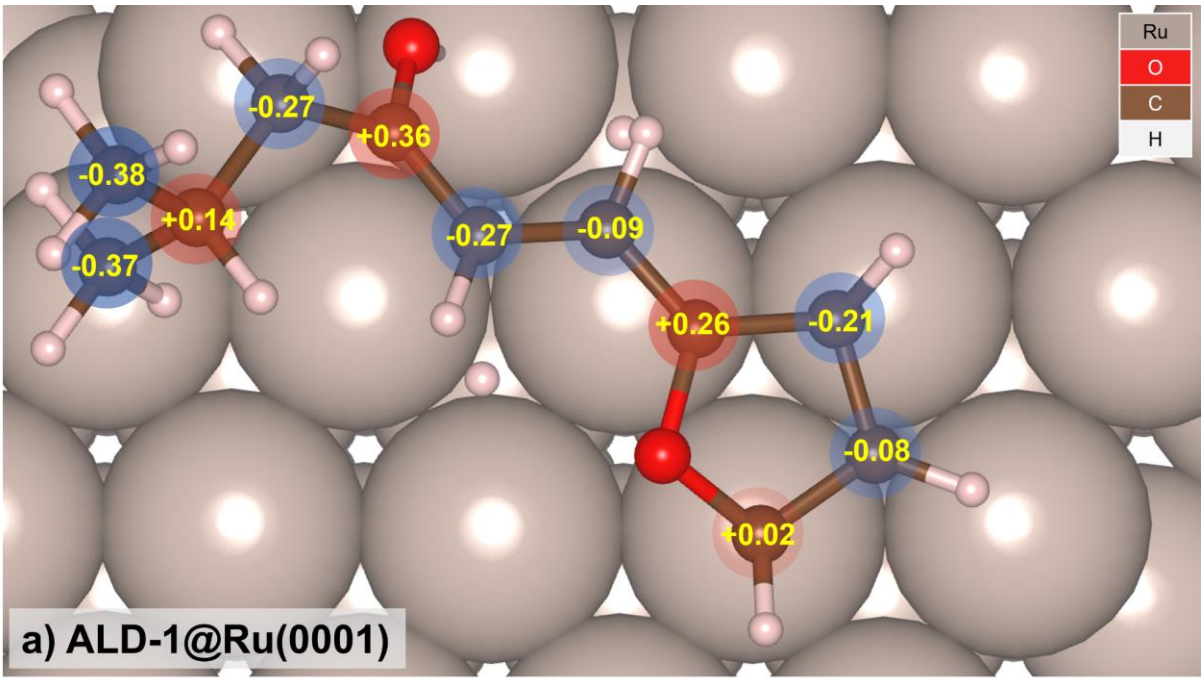

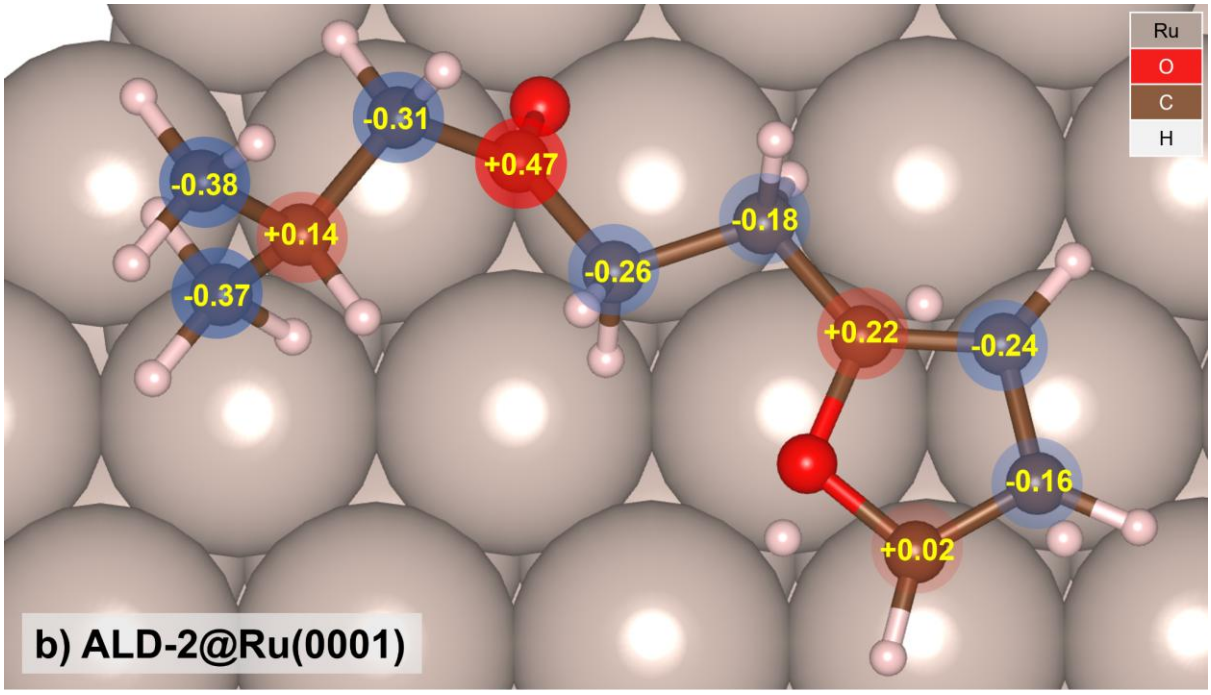

Figure 4.3. DDEC6 charge analysis of (a) ALD-1 and (b) ALD-2 adsorbed to Ru(0001). Carbon atoms with partial positive and negative charges are highlighted in red and blue, respectively. Figures given in units of elementary charge.

Reaction profiles for the ortho and para hydrogenation of ALD-2's ring system over all three metals are provided in **Figure 4.4** and **4.5**, respectively. Unlike Pd(111) and Pt(111), transition state analysis showed that the activation energy for ortho hydrogenation over Ru(0001) (E_A = +134.0 kJ mol^{-1}) was higher than the corresponding figure for para hydrogenation (E_A = +109.7 kJ mol^{-1}). While this figure is slightly smaller than the calculated activation energy barrier for Pt(111) ring hydrogenation (E_A = +114.0 kJ mol^{-1}), this difference is within the ±4 kJ mol^{-1} limit of chemical accuracy.[31] It can thus be inferred that Pt(111) and Ru(0001) are equally poor catalysts for the ring hydrogenation of ALD-2.

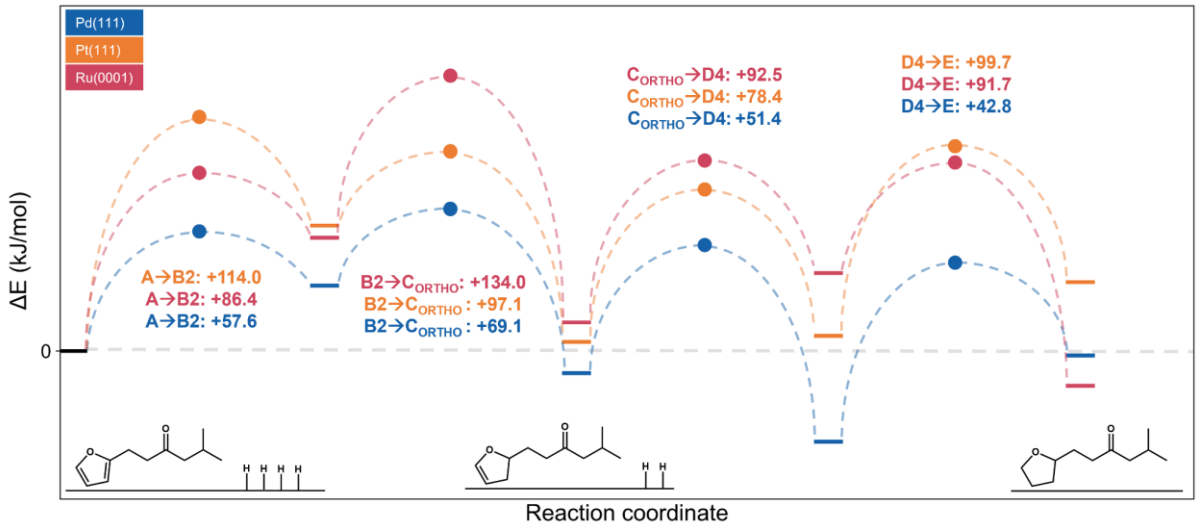

Figure 4.4. Reaction profile for the ortho hydrogenation of ALD-2 over Pd(111) (blue), Pt(111) (orange), and Ru(0001) (red). Transition states between minima are marked with coloured circles. Inset are schematic representations of A (left), C$_{ORTHO}$ (centre), and E (right).

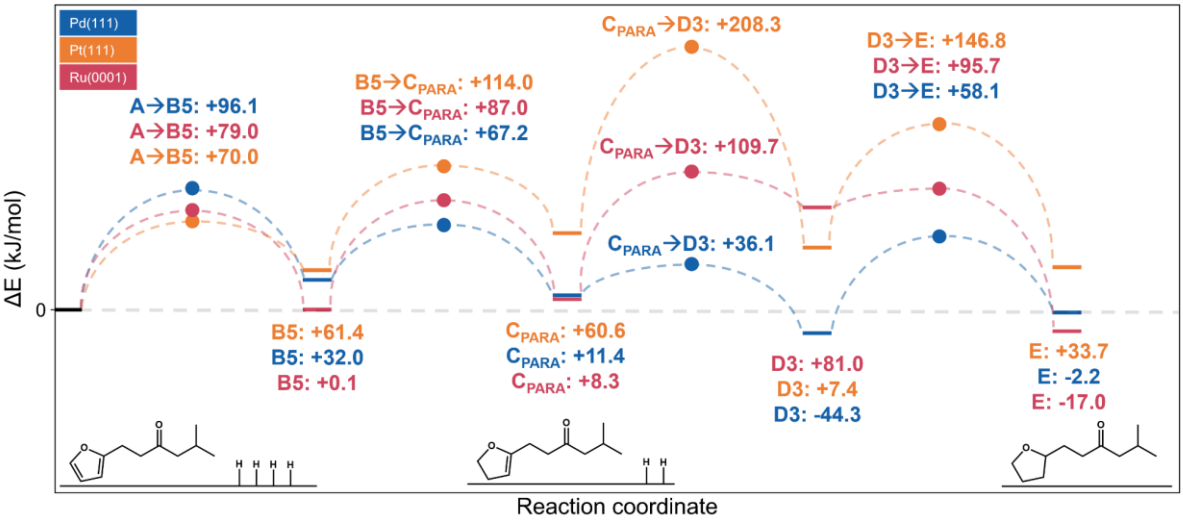

Figure 4.5. Reaction profile for the para hydrogenation of ALD-2 over Pd(111) (blue), Pt(111) (orange), and Ru(0001) (red). Transition states between minima are marked with coloured circles. Inset are schematic representations of A (left), C$_{PARA}$ (centre), and E (right).

As shown by DDEC6 analysis of the B2→C and B3→C transition states over Ru(0001) (**Figure 4.6**), hydrogenation at carbon-3 led to a substantial build-up of partial positive charge on carbon-2 (q = +0.31 e). As observed over Pd(111) and Pt(111), this problem could, in theory, be mitigated by initially hydrogenating carbon-2 (q = +0.18 e). However, over Ru(0001), a lower energy transition state was accessible through an attack at carbon-5 (**Figure 4.7**). Similarly to ortho hydrogenation

over Pd(111) and Pt(111), para hydrogenation over Ru(0001) was at its most energetically favourable when the C=C carbon with the greatest localised positive charge was hydrogenated first. The relative energy difference between the A4→B and A5→B transition states over Ru(0001) was negligible ($|\Delta E| = 0.6$ kJ mol^{-1}), but the same cannot be said for the B5→C and B4→C states ($|\Delta E| = 35.6$ kJ mol^{-1}), highlighting a clear preference for initial hydrogenation at carbon-5. However, when compared to Pd(111), the activation energies of both ortho and para hydrogenation remain high over Ru(0001). It can thus be inferred that neither of these processes will be energetically competitive with Pd-catalysed ring hydrogenation at the operating temperature of 180 °C employed by Jiang *et al.*[20]

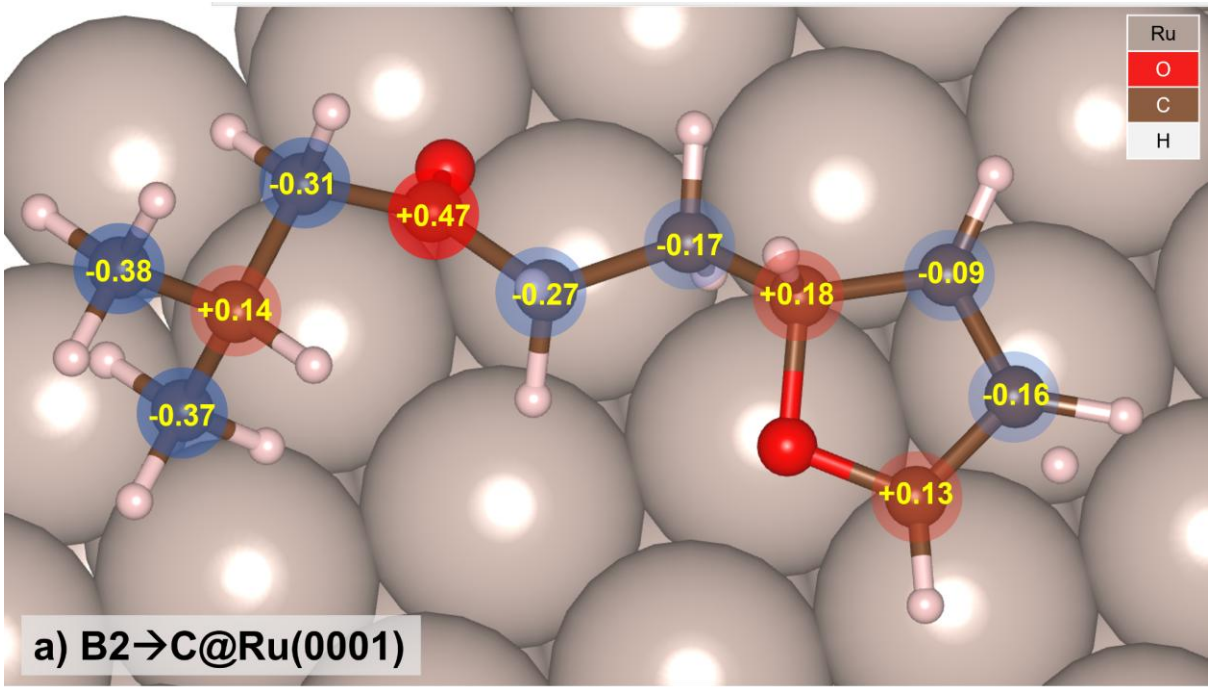

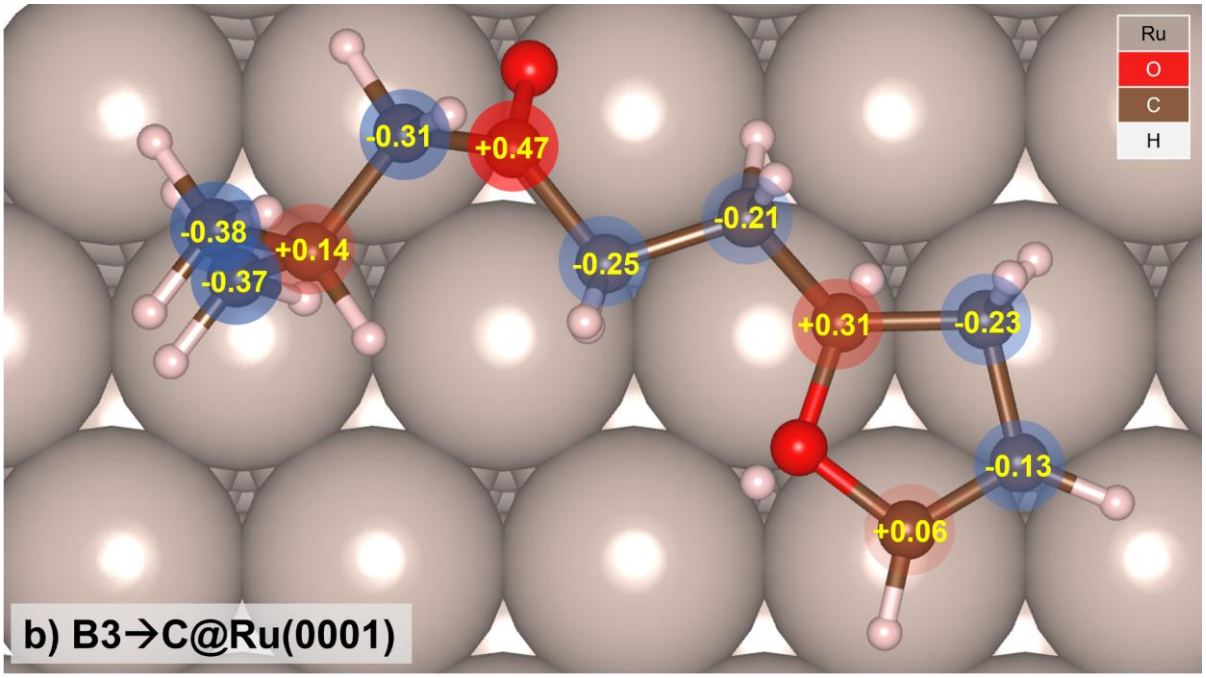

Figure 4.6. DDEC6 charge analysis of the (a) B2→C@Ru(0001) and (b) B3→C@Ru(0001) ortho hydrogenation transition states. Carbon atoms with partial positive and negative charges are highlighted in red and blue, respectively. Figures given in units of elementary charge.

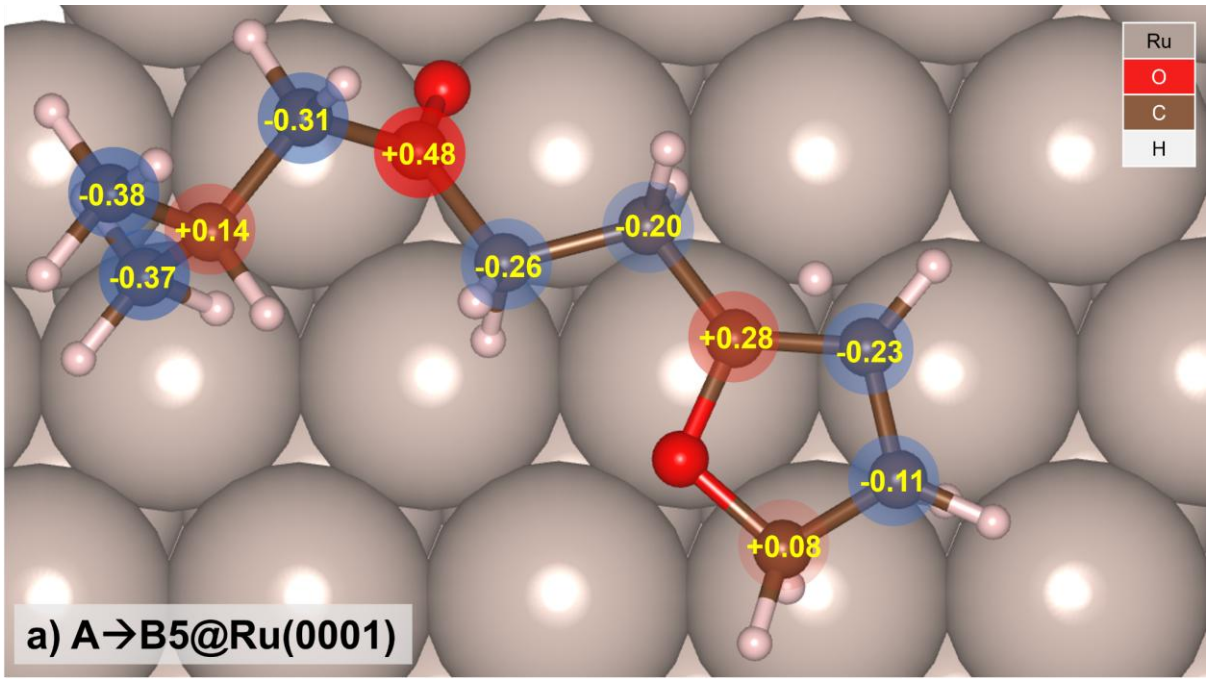

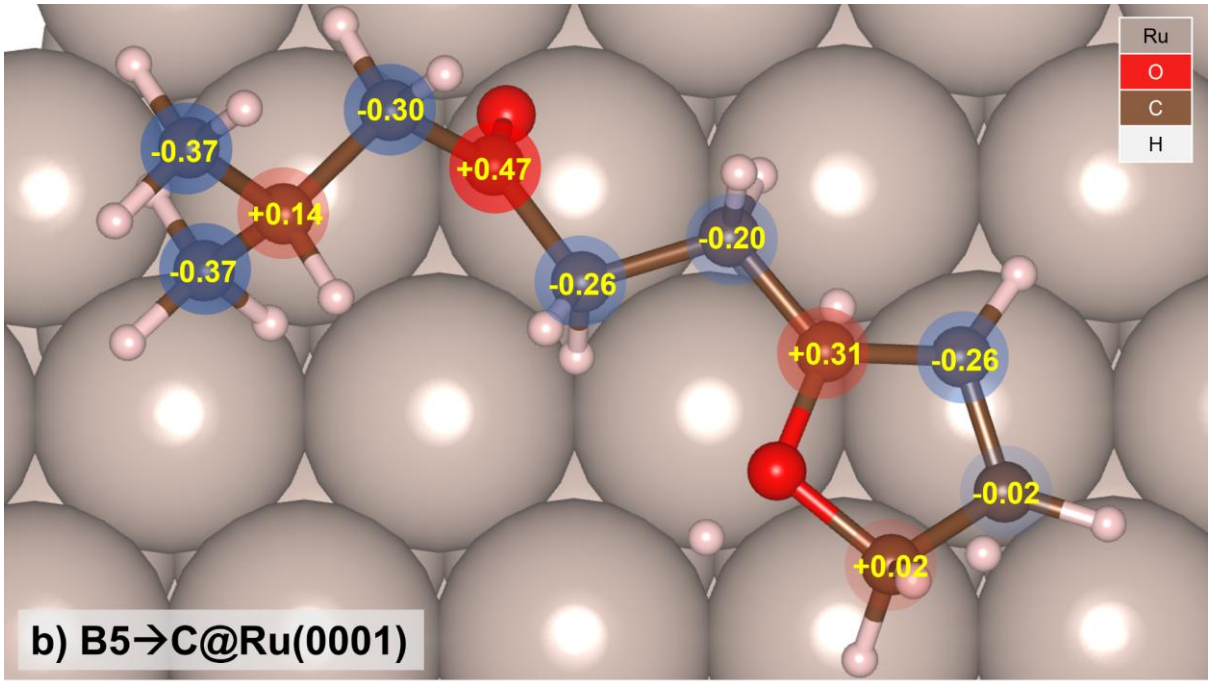

Figure 4.7. DDEC6 charge analysis of the (a) A→B5@Ru(0001) and (b) B5→C@Ru(0001) para hydrogenation transition states. Carbon atoms with partial positive and negative charges are highlighted in red and blue, respectively. Figures given in units of elementary charge.

4.4. Amination

After NH_3 and H_2 adsorb to the surface of the catalyst, amination typically proceeds via three sequential sub-reactions: (1) the carbonyl C undergoes nucleophilic attack, forming a hemiaminal after proton rearrangement; (2) the hydroxyl group of the hemiaminal is protonated and eliminated as water, generating an imine; (3) the imine is hydrogenated at its C=N double bond, giving the final product. H_2 is known to readily dissociate over Pd(111), Pt(111), and Ru(0001), but the number of N–H bonds cleaved during the dissociation of ammonia is known to vary with metal composition and temperature.[32–34] Following the work of Liu *et al.*[32] on the dissociation of ammonia over transition metal nanoparticles, it was assumed that the rate-limiting effects of the decomposition of $*NH_3$ would be smaller at 120 °C than those of the elimination of water from the carbonyl; especially for Ru(0001), a catalyst that DFT has shown to be particularly effective at stabilising $*NH_2$, *NH, and *N species. Alongside ammonia itself, it is likely that the amine can be formed from a multitude of its decomposition products on the surfaces of the nanoparticles. However, in the interests of simplifying the investigation, $*NH_2$ was selected as a reagent for transition state searches due to the ease with which trial single-step mechanisms could be constructed.

Using the same methodology employed for chain and ring hydrogenation, energetic profiles were constructed for each amination sub-reaction. Due to the compounds' similarities in structure and the spatial separation between the ring system and the carbonyl group, it was assumed that the activation energies of ALD-2 and ALD-3 amination would be similar to one other, and that the ring system had little effect on the reactivity of the carbonyl group. Consequently, to conserve computational resources, all transition state calculations were performed on ALD-3 and its derivatives.

In contrast with the reaction profiles generated for hydrogenation, the DFT profiles for amination showed mixed agreement with experiment.[20] The activation energies of hemiaminal formation (**Section 4.4.1**) were substantially higher than expected over both metals, erroneously suggesting that amination is catalytically unviable over Pd(111) and Ru(0001). Additionally, the transition states associated with imine formation (**Section 4.4.2**) proved challenging to model with the improved dimer method, necessitating the adoption of a simplified mechanism (**Scheme 4.4**) to provide an upper bound for the activation energy. Unlike hemiaminal formation, however, this upper bound proved to be relatively low over both Pd(111) (E_A = +78.9 kJ mol^{-1}) and Ru(0001) (E_A = +83.9 kJ mol^{-1}), suggesting the existence of a lower energy pathway that can be readily accessed over both catalysts. Furthermore, the hydrogenation of the imine to the amine (**Section 4.4.3**) was shown to readily catalysed by both Pd(111) and Ru(0001). Taken together, these findings indicate that, despite methodological limitations, reductive amination remains viable over transition metal catalysts.

4.4.1. Carbonyl to Hemiaminal

The intermediates associated with the generation of the hemiaminal via nucleophilic addition are provided in **Scheme 4.3**. Two initial steps for this sub-reaction were considered: the protonation of the carbonyl O (BO) and the attack of the NH_2 from the surface (BN). A reaction profile for the minimum energy pathway (MEP) of ALD-3 to HEMI-3 is provided in **Figure 4.8**. The direct attack of adsorbed NH_2 proved to be energetically inaccessible over both Pd(111) (E_A = +196.5 kJ mol^{-1}) and Ru(0001) (E_A = +187.2 kJ mol^{-1}). While the BN→C transition state remained equally

inaccessible over both metals ($|\Delta E_A| = 2.4$ kJ mol^{-1}), a wide gulf in stability was observed for the A→BN state ($|\Delta E_A| = 98.6$ kJ mol^{-1}).

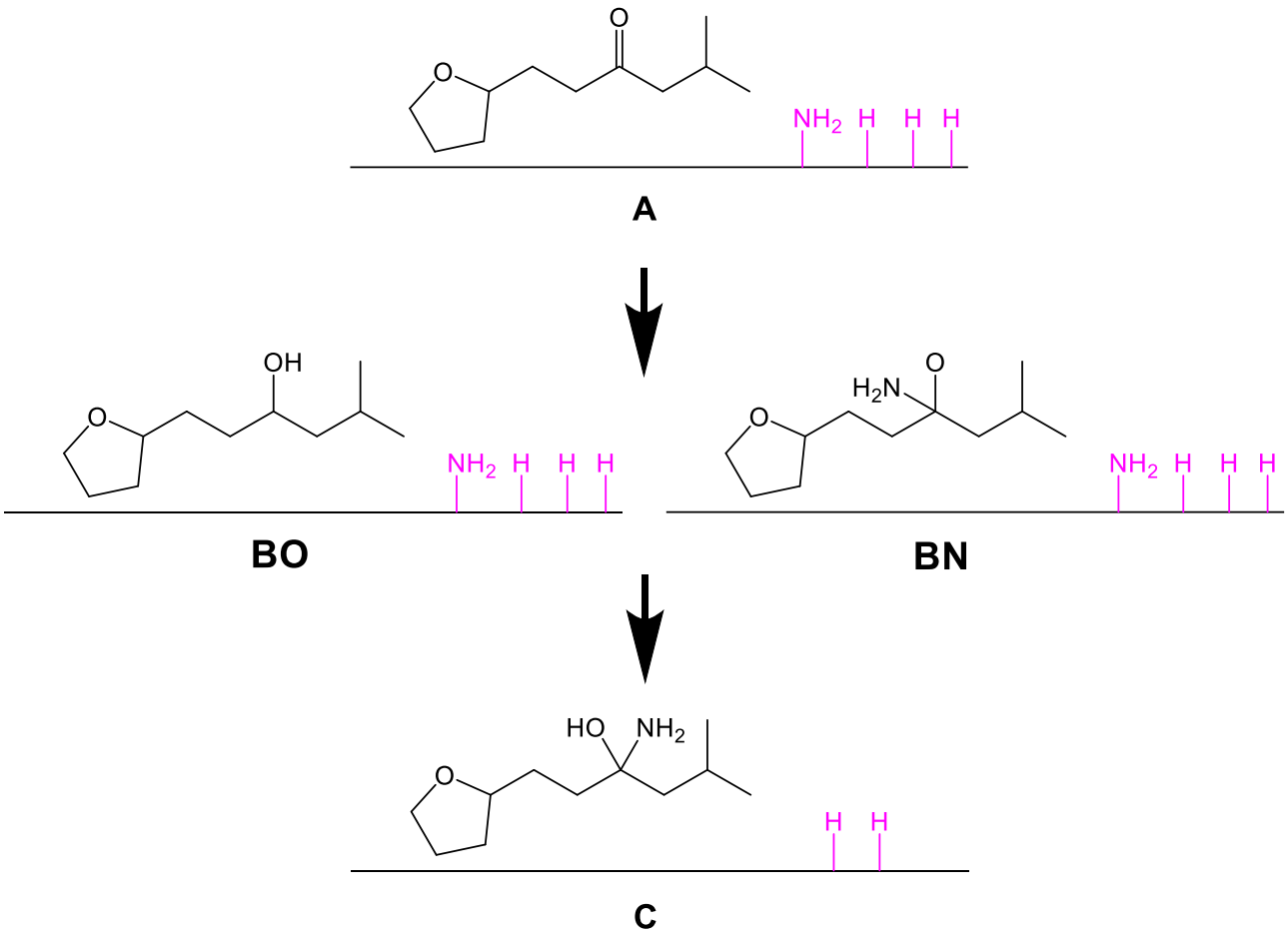

Scheme 4.3. Intermediates associated with the nucleophilic addition of ALD-3 and dissociated ammonia to HEM-3. Adsorbed H and NH_2 highlighted in pink.

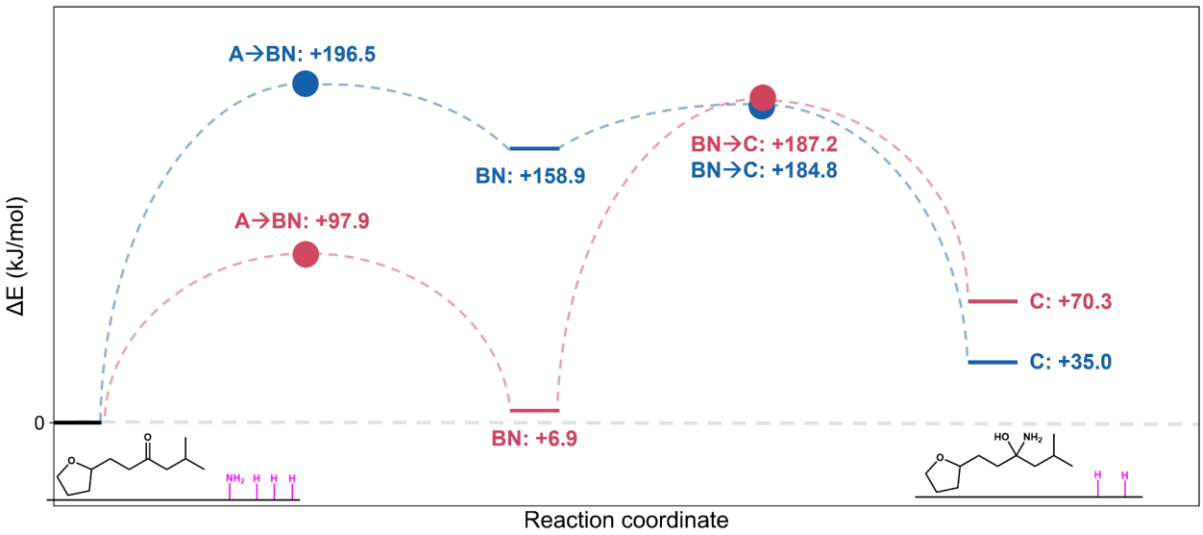

Figure 4.8. Minimum energy path for the amination of ALD-3 to HEM-3 over Pd(111) (blue) and Ru(0001) (red). Transition states between minima are marked with coloured circles. Inset are schematic representations of A (left) and C (right).

As shown in **Figure 4.9**, the A→BN transition state over Pd(111) adopts a strained conformation with a C_{α}–$C_{CARBONYL}$–C_{tBu} bond angle of 113.2°. Over Ru(0001), this angle (116.2°) was closer to the idealised sp^2-sp^3 intermediary value of 115°. While this strain likely contributes to the destabilisation of the transition state over Pd(111), it is improbable that such a minor change in geometry would incur an energetic penalty of nearly 100 kJ mol^{-1}. DFT is known to underestimate the stability of compounds with strong localised charges;[35–38] a problem that has shown to be further exacerbated in calculations where solvent is not accounted for.[37,38] Therefore, while the amination of ALD-3 to HEM-3 was not predicted to be energetically viable, the calculated activation energies for this sub-reaction are likely computational artefacts resulting from the neglect of solvation and limitations in the DFT methodology.

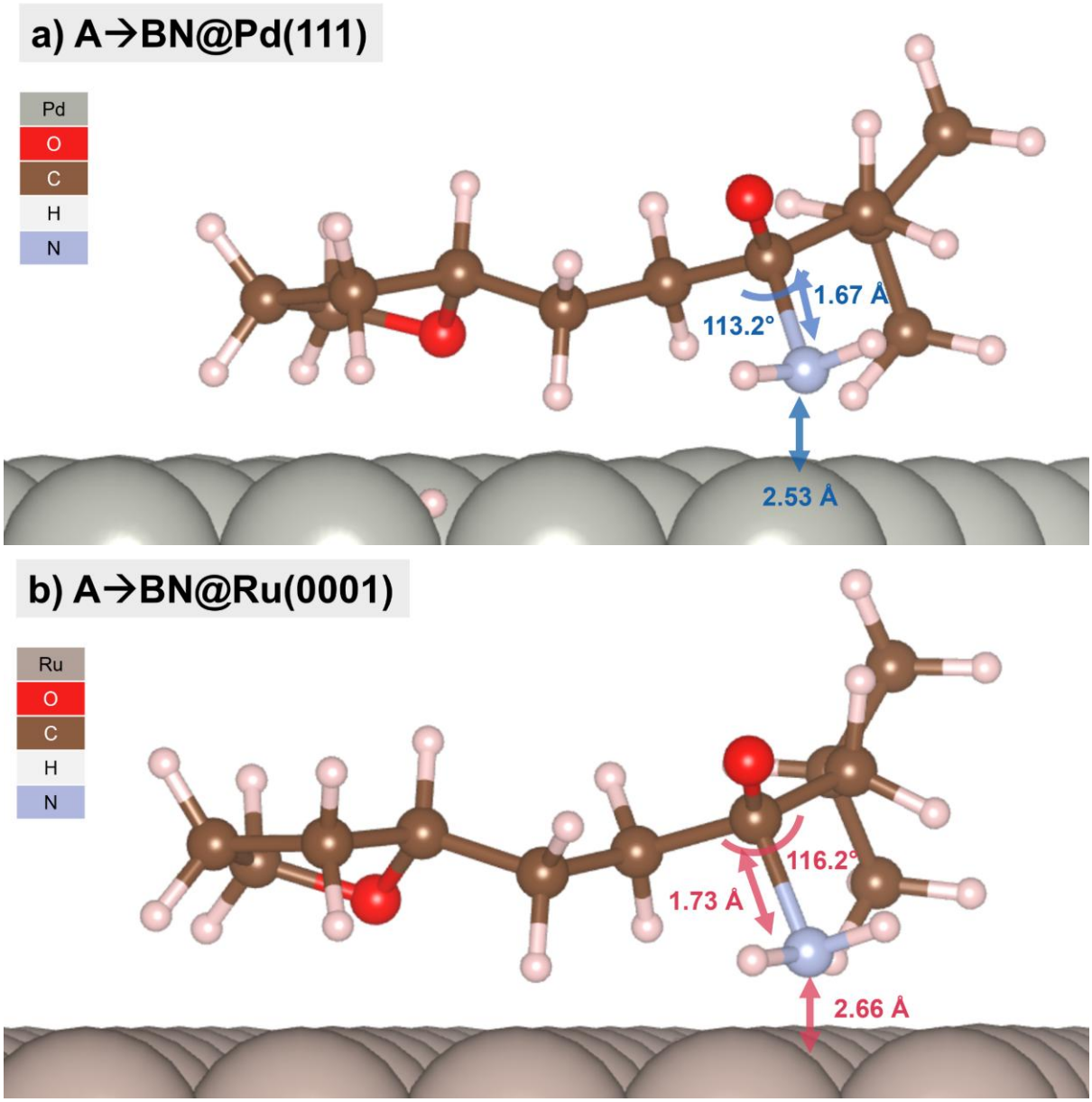

Figure 4.9. A→BN transition states over (a) Pd(111) and (b) Ru(0001).

4.4.2. Hemiaminal to Imine

Computationally modelling the dehydration of the hemiaminal to the imine with the improved dimer method proved challenging. In the liquid phase, this sub-reaction typically proceeds via a single-step intramolecular elimination, and is known to be highly sensitive to solvent.[10,39] As shown in **Scheme 4.4a**, the alcohol forms a bond with a proton on the neighbouring amine group. As the N–H bond breaks, a C=N bond forms, leading to the cleavage of the R–O bond and the elimination of the alcohol group as a water molecule.

There are several difficulties associated with constructing a DFT model of this mechanism. In solution, hemiaminals are short-lived and typically require extensive

stabilisation from neighbouring functional groups or co-ordinating metal ions to be spectroscopically detected at room temperature.[40–42] They can be further stabilised by forming networks of hydrogen bonds with molecules of polar solvents,[39,43] but modelling these networks at the DFT level typically requires the implementation of expensive explicit solvation codes, making them impractical for reactions whose intermediates feature large numbers of atoms.

This issue is further complicated by the difficulty of locating viable transition states on the PES for intramolecular elimination. Due to the wide array of configurations that the leaving group can adopt when it is cleaved from its host, imaginary frequencies corresponding to the cleavage and formation of multiple bonds are often coupled with "spurious" imaginary vibrational nodes,[44,45] making it challenging to isolate single-order saddle points on the PES for these reactions. Guess transition states generated by the improved dimer method for the single-step elimination were heavily contaminated with extra imaginary frequencies.

In the hope of finding an upper bound for the activation energy of imine dehydrogenation, a trial multi-step mechanism was used in lieu of the single-step mechanism. As illustrated in **Scheme 4.4b**, the mechanism begins with the assumption that the energetic cost of protonating the alcohol group to R–$^{+}$OH$_2$ is negligible in comparison to the cleavage of the C–O bond. A simplified transition state was then isolated in which bond cleavage occurs independently of proton transfer. The carbocation generated by this step was then assumed to rapidly undergo a water-mediated deprotonation to the final imine. To prevent artificially lowering the total energy of the system by introducing an extra H atom, one of the H adatoms was used to protonate the R–OH group. The number of adatoms was then restored in the final structure by moving one of the H atoms from the R–NH$_2$ group to the surface.

a) experimental single-step elimination

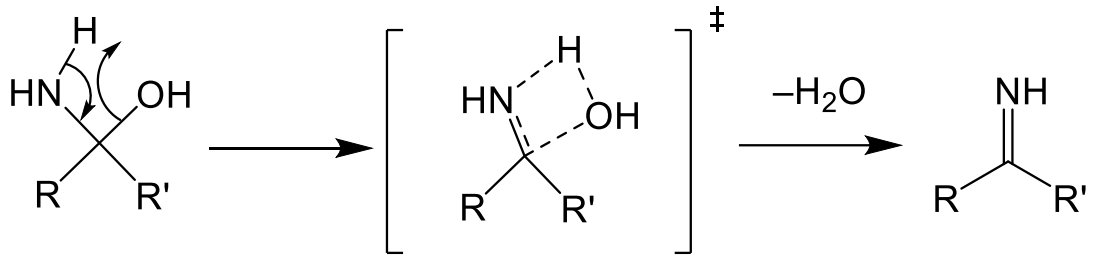

b) trial multi-step elimination

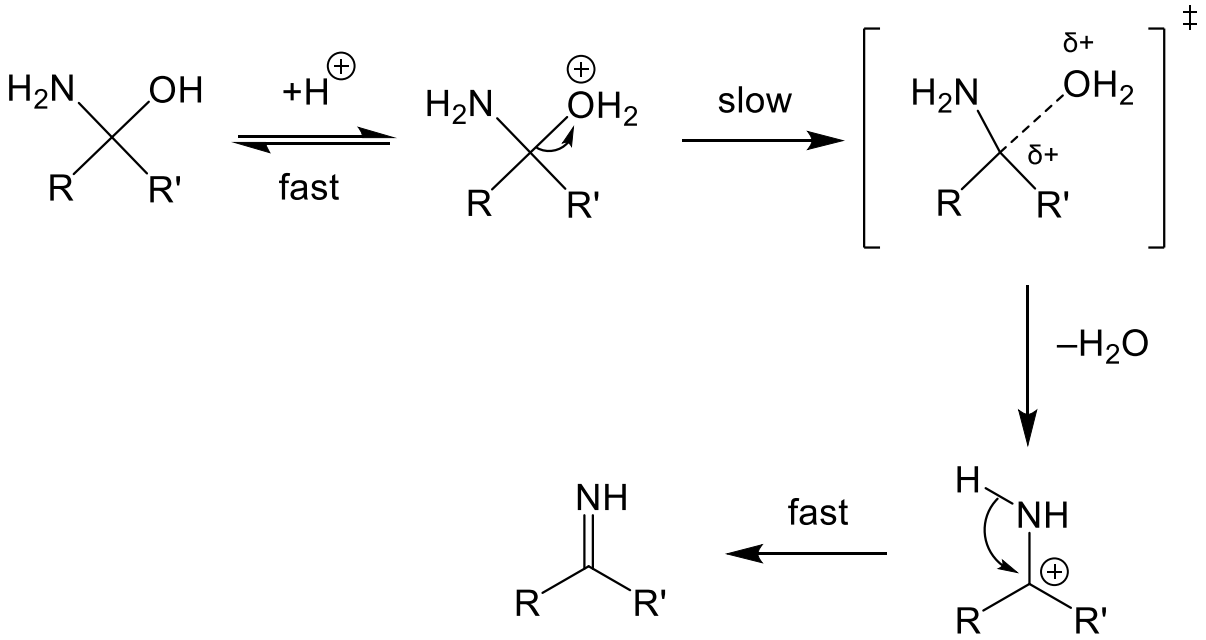

Scheme 4.4. Single-step (a) and multi-step (b) elimination mechanisms for the dehydration of a hemiaminal to an imine.

A reaction profile for the trial multi-step elimination is provided in **Figure 4.10**. The upper bound activation energies for the conversion of HEM-3 to IMI-3 proved to be relatively accessible over both Pd(111) (E_A = +78.9 kJ mol^{-1}) and Ru(0001) (E_A = +83.9 kJ mol^{-1}). Despite their energetic similarities, the A→B transition states over each surface showed a marked difference in conformation. Over Pd(111), the O–H bonds in the leaving OH_2 group were identical in length (d = 1.01 Å), slightly shorter than the experimental O–H bond length of gaseous H_2O (d = 1.05 Å).[46] Meanwhile, over Ru(0001), the O–H bond closest to the surface was stretched to 1.18 Å. This suggests that the cleavage of water from HEM-3 could be aided over Ru(0001) by bonding interactions between the OH_2 group and the metal surface.

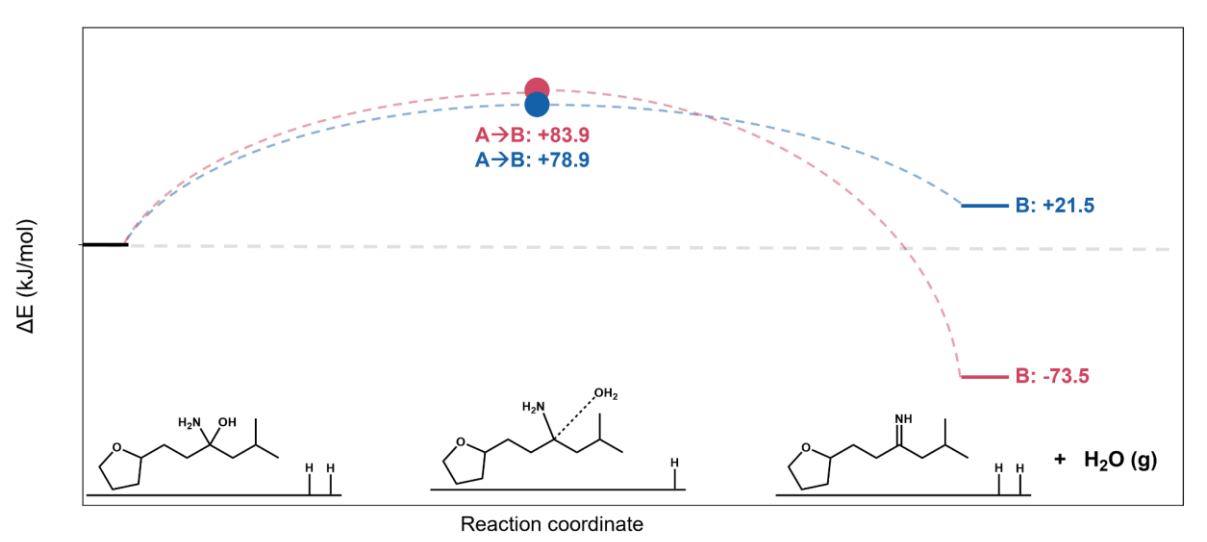

Figure 4.10. Reaction profile for the trial multi-step elimination over Pd(111) (blue) and Ru(0001) (red). Transition states between minima are marked with coloured circles. Inset are schematic representations of the hemiaminal (left), the E1 transition state (centre), and the final imine (right). Proton transfer steps have been assumed to be energetically negligible.

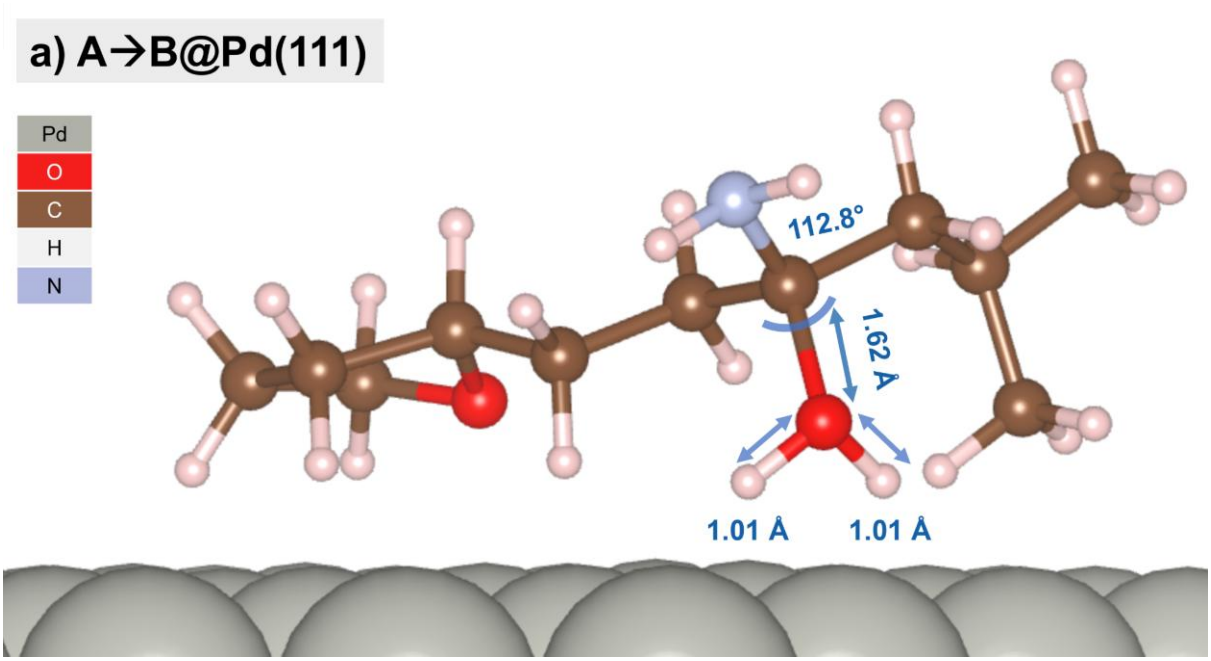

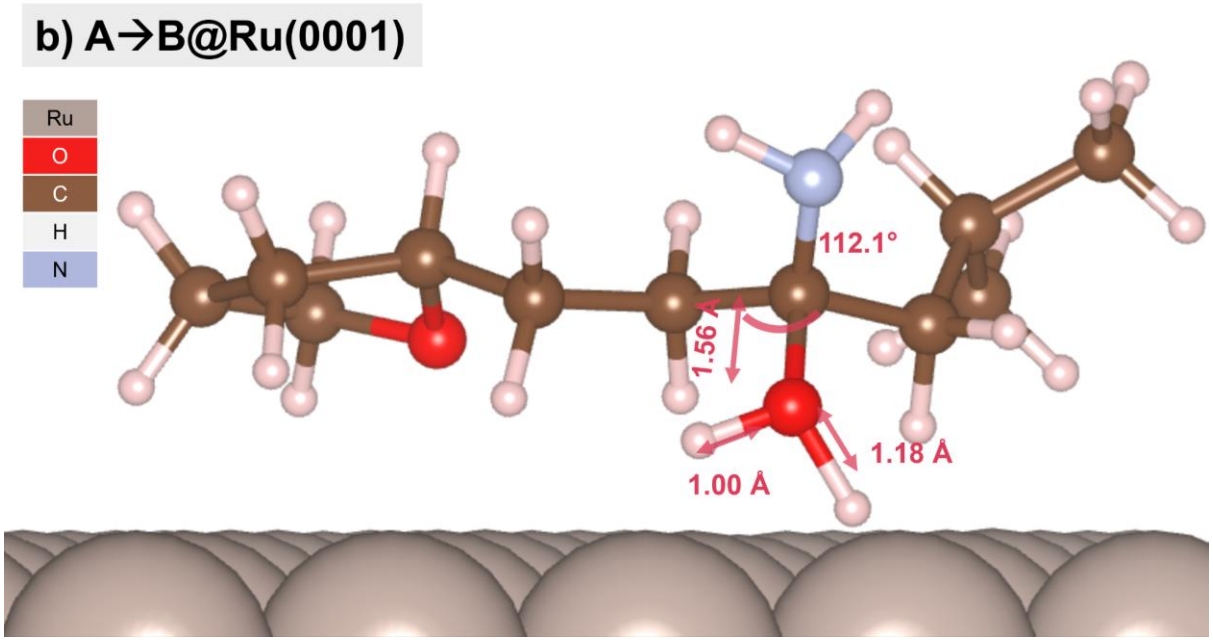

Figure 4.11. Multi-step transition states over (a) Pd(111) and (b) Ru(0001).

4.4.3. Imine to Amine

While the first two sub-reactions proved challenging to model with the improved dimer method, accessible transition states were successfully located for the final hydrogenation of the imine to the amine. As shown in **Scheme 4.5**, hydrogenation of the C=N bond can first occur at either the carbon (BC) or the nitrogen (BN). In agreement with experiment, the reduction of the C=N bond to the final amine proved to be facile over both catalysts. The activation energy for the imine hydrogenation of IMI-2 was approximately half as large over Pd(111) (E_a = +40.1 kJ mol^{-1}) than the Ru(0001) (E_a = +75.6 kJ mol^{-1}). A complete reaction profile for this process is provided in **Figure 4.12**. Over both Pd(111) and Ru(0001), a marked preference for initial hydrogenation at the nitrogen was observed; a process likely driven by the substantial difference in Pauling electronegativity between N ($\chi_P = 3.04$) and C ($\chi_P = 2.55$).[47,48] This preference was particularly apparent over Pd(111), where the activation energy for C-hydrogenation (E_a = +245.1 kJ mol^{-1}) was almost five times larger than that for N-hydrogenation.

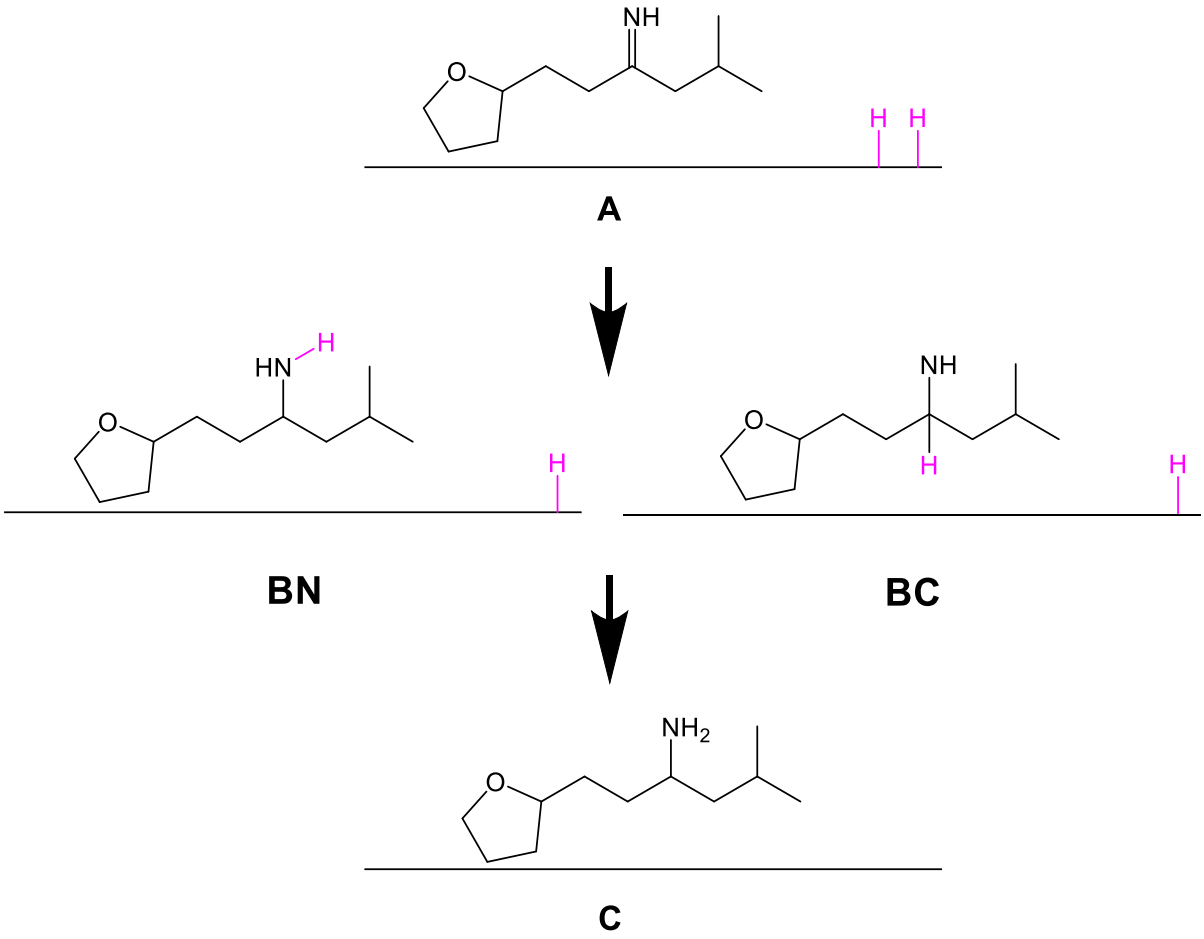

Scheme 4.5. Intermediates associated with the hydrogenation of IMI-3 to AMI-3. H adatoms from dissociated H_2 are highlighted in pink.

DDEC6 charge analysis (**Figure 4.13**) revealed that the charge distribution of the adsorbate was effectively identical over both catalysts. As expected, a large charge gradient was observed across the C=N bond ($|\Delta q| = 0.90$ e), with negative charge congregating at the N atom. It is likely that, similarly to the α-hydrogenation of the chain C=C bond in **Section 4.3**, this localised build-up in electron density is responsible for the marked preference for the N-hydrogenation of the imine over both Pd(111) and Ru(0001).

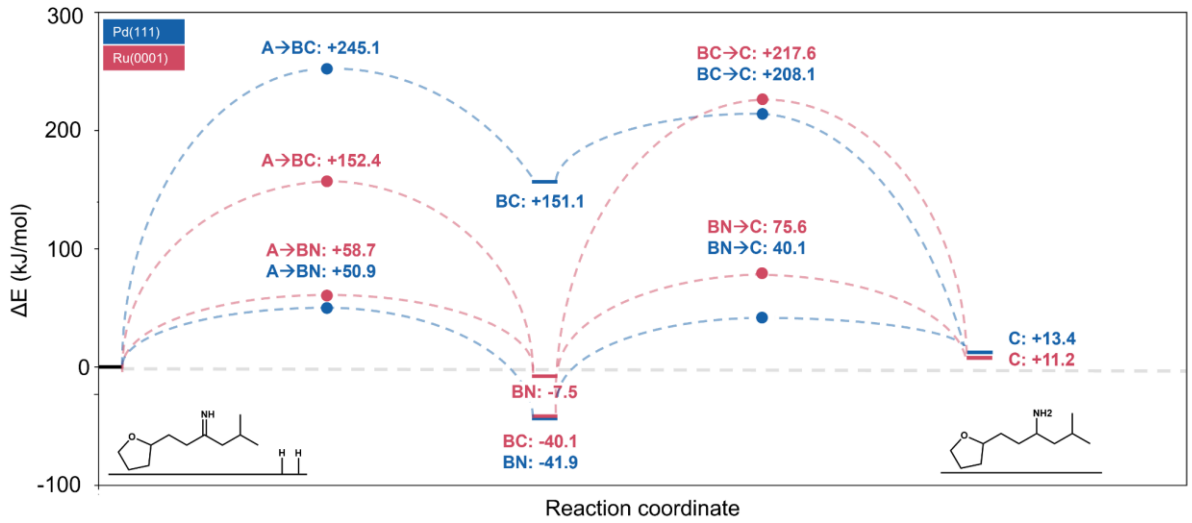

Figure 4.12. Reaction profile for the hydrogenation of IMI-3 to AMI-3 over Pd(111) (blue) and Ru(0001) (red). Transition states between minima are marked with coloured circles. Inset are schematic representations of A (left) and C (right).

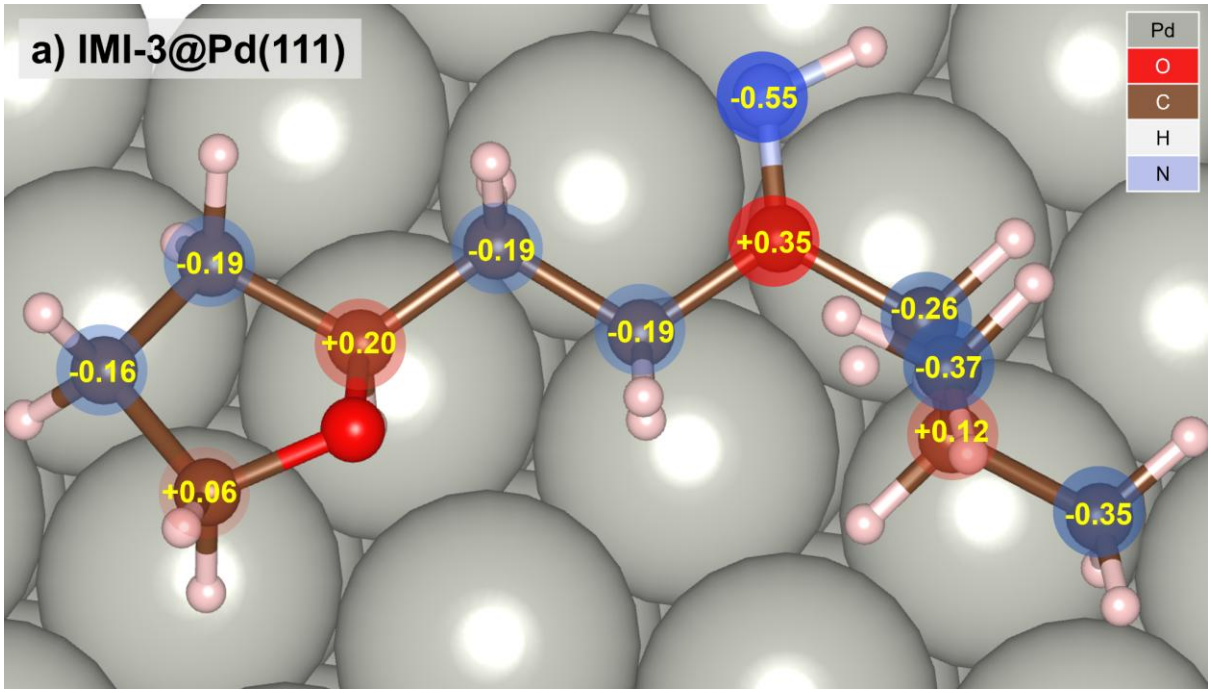

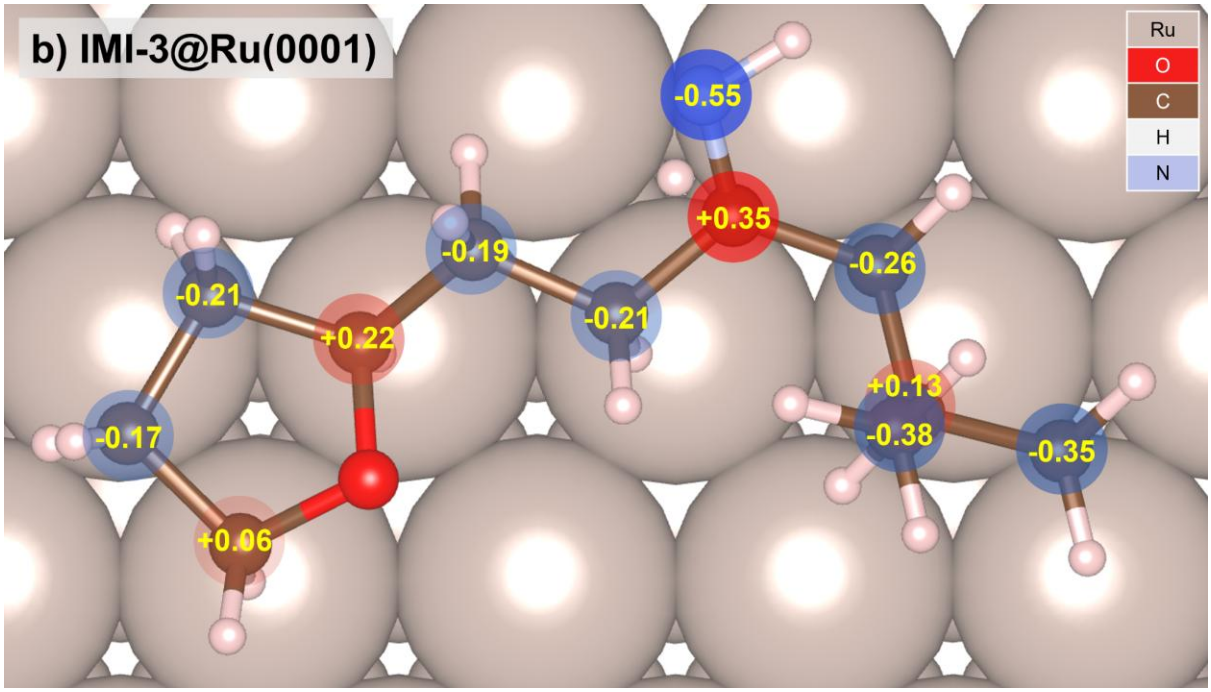

Figure 4.13. DDEC6 charge analysis of IMI-3 adsorbed to (a) Pd(111) and (b) Ru(0001). Atoms with partial positive and negative charges are highlighted in red and blue, respectively. Figures given in units of elementary charge.

4.5. Conclusions and Perspectives

In agreement with experiment, the RPBE-D3(0) profile successfully predicted that the ring hydrogenation of ALD-1 is more energetically favourable over Pd(111) than Ru(0001). While chain hydrogenation was shown to be readily catalysed by both metals, high energy barriers associated with ring hydrogenation were identified for both the ortho and para mechanisms over Ru(0001). Conversely, DFT was shown to overestimate the activation energies associated with amination. While the upper bounds associated with the trial elimination mechanism were shown to be relatively accessible at operating temperatures of 180 °C, attempts to locate low-energy single step elimination transition states with the improved dimer method were unsuccessful.

The first facet of this reaction that should be investigated in future work is the role that solvation plays in the stabilisation of intermediates and transition states over Pd(111) and Ru(0001). Both experimental and theoretical studies have shown that solvent mediation is a critical factor in low-temperature reductive amination.[7,49–51] It is likely that MIBK, the solvent used by Jiang *et al.*[20] in their work on this synthesis, helps facilitate the amination of ALD-2 and ALD-3. Due to the computational costs associated with explicit solvation, individually encasing the adsorbates in a solvation shell of MIBK molecules was deemed unfeasible for this investigation. While implicit

solvation codes such as VASPsol[52,53] can mimic the bulk properties of solvents, localised effects such as the formation of hydrogen bonding networks are neglected. Furthermore, benchmarking work by Oğuz *et al.*[54] has shown that VASPsol introduces non-negligible errors in the energetic profiles. The authors highlight that these errors were especially pronounced for amines and alcohols. In light of these issues, the VASPsol code was not employed in this thesis. However, the possibility remains that other solvation packages may be able to successfully capture the stabilising effects of solvent at the DFT level.

Another facet of this reaction that should be investigated in future work is the viability of non-Langmuir-Hinshelwood mechanisms. While ring, chain, and imine hydrogenation were successfully modelled at the DFT level with Langmuir-Hinshelwood mechanisms, the same could not be said for the formation of the hemiaminal and the imine. A mechanistic pathway not considered in this investigation was the Eley-Rideal mechanism,[55,56] a route in which ammonia attacks the carbonyl from the gas or liquid phase instead of adsorbing to the catalyst and migrating across the surface. As noted in **Section 2.3.6**, the Langmuir-Hinshelwood mechanism is generally favoured in heterogeneous catalysis,[56–59] but it has been experimentally shown by Guo *et al.*[14] that the Eley-Rideal mechanism outcompetes the corresponding Langmuir-Hinshelwood mechanism for the reductive amination of cyclopentanone over Ru/Nb_2O_5. While a solvent-mediated Langmuir-Hinshelwood mechanism remains the likely candidate for this reaction's minimum energy pathway over Pd and Ru nanoparticles, the possibility of reductive amination proceeding via an alternative, lower energy mechanistic pathway cannot be discounted without further experimental and computational work. Nevertheless, it is the hope of the author that the work conducted in this chapter provides a theoretical bedrock for future research on green reductive amination and helps inform the design of new processes in heterogeneous catalysis.

4.6. References

1. S. A. Lawrence, *Amines: Synthesis, Properties and Applications*, Cambridge University Press, **2004**.
2. D. Crosby and J. Bowers, *J. Agric. Food Chem.*, **1968**, 16, 839–843.
3. J. Hack, N. Maeda and D. M. Meier, *ACS Omega*, **2022**, 7, 39520–39530.
4. W. Zawodny and S. L. Montgomery, *Catalysts*, **2022**, 12, 595.
5. F. Moulines, M. Kalam-Alami, V. Martinez and D. Astruc, *J. Organomet. Chem.*, **2002**, 643–644, 125–129.
6. Y. Ju and R. S. Varma, *Green Chem.*, **2004**, 6, 219–221.
7. F. Jameel and M. Stein, *J. Catal.*, **2022**, 405, 24–34.
8. R. Baltzly and O. Kauder, *J. Org. Chem.*, **1951**, 16, 173–177.
9. S. C. Lee and S. B. Park, *Chem. Commun.*, **2007**, 3714–3716.
10. J. Clayden, N. Greeves and S. Warren, *Organic Chemistry*, Oxford University Press, 2nd edn., **2012**.
11. T. Irrgang and R. Kempe, *Chem. Rev.*, **2020**, 120, 9583–9674.
12. K. Murugesan, T. Senthamarai, V. G. Chandrashekhar, K. Natte, P. C. J. Kamer, M. Beller and R. V. Jagadeesh, *Chem. Soc. Rev.*, **2020**, 49, 6273–6328.
13. M. Ortega, B. Garrido, D. Gómez, A. A. Fernandez-Andrade, M. E. Domine, R. Jiménez and L. E. Arteaga-Pérez, *ChemCatChem*, **2024**, 0, e202401476.
14. W. Guo, T. Tong, X. Liu, Y. Guo and Y. Wang, *ChemCatChem*, **2019**, 11, 4130–4138.
15. A. García-Ortiz, J. D. Vidal, M. J. Climent, P. Concepción, A. Corma and S. Iborra, *ACS Sustain. Chem. Eng.*, **2019**, 7, 6243–6250.
16. E. R. Alexander and R. B. Wildman, *J. Am. Chem. Soc.*, **1948**, 70, 1187–1189.
17. M. J. Kukla, H. J. Breslin, C. J. Diamond, P. P. Grous, C. Y. Ho, M. Miranda, J. D. Rodgers, R. G. Sherrill, E. De Clercq, R. Pauwels, K. Andries, L. J. Moens, M. A. C. Janssen and P. A. J. Janssen, *J. Med. Chem.*, **1991**, 80, 3187–3197.
18. N. Wang, J. Liu, X. Li and L. Ma, *Catal. Commun.*, **2023**, 175, 106620.
19. P. Schmitz, G. Reniers and P. Swuste, *J. Loss Prev. Process Ind.*, **2021**, 70, 104395.
20. S. Jiang, C. Ma, E. Muller, M. Pera-Titus, F. Jérôme and K. De Oliveira Vigier, *ACS Catal.*, **2019**, 9, 8893–8902.
21. J. Hafner and G. Kresse, in *Properties of Complex Inorganic Solids*, Springer, **1997**, pp. 69–82.
22. B. Hammer, L. B. Hansen and J. K. Nørskov, *Phys. Rev. B*, **1999**, 59, 7413–7421.
23. S. Grimme, J. Antony, S. Ehrlich and H. Krieg, *J. Chem. Phys.*, **2010**, 132.
24. H. J. Monkhorst and J. D. Pack, *Phys. Rev. B*, **1976**, 13, 5188.
25. G. Kresse and D. Joubert, *Phys. Rev. B*, **1999**, 59, 1758.
26. P. E. Blöchl, *Phys. Rev. B*, **1994**, 50, 17953.
27. K. P. Kepp, *Inorg. Chem.*, **2016**, 55, 9461–9470.
28. T. Reier, M. Oezaslan and P. Strasser, *ACS Catal.*, **2012**, 2, 1765–1772.
29. S. Zhu, X. Qin, F. Xiao, S. Yang, Y. Xu, Z. Tan, J. Li, J. Yan, Q. Chen, M. Chen and M. Shao, *Nat. Catal.*, **2021**, 4, 711–718.
30. J. Zhou, W. An, Z. Wang and X. Jia, *Catal. Sci. Technol.*, **2019**, 9, 4314–4326.
31. J. Sauer, *Acc. Chem. Res.*, **2019**, 52, 3502–3510.
32. X. Lu, J. Zhang, W.-K. Chen and A. Roldan, *Nanoscale Adv.*, **2021**, 3, 1624–1632.
33. Z. Jiang, P. Qin and T. Fang, *Appl. Surf. Sci.*, **2016**, 371, 337–342.

34. D. G. Löffler and L. D. Schmidt, *J. Catal.*, **1976**, 41, 440–454.
35. S. G. Dale and E. R. Johnson, *J. Chem. Phys.*, **2015**, 143, 184112.
36. C. Sutton, T. Körzdörfer, V. Coropceanu and J.-L. Brédas, *J. Phys. Chem. C*, **2014**, 118, 3925–3934.
37. R. M. Hoekstra, J. P. Telo, Q. Wu, R. M. Stephenson, S. F. Nelsen and J. I. Zink, *J. Am. Chem. Soc.*, **2010**, 132, 8825–8827.
38. M. Renz, M. Kess, M. Diedenhofen, A. Klamt and M. Kaupp, *J. Chem. Theory Comput.*, **2012**, 8, 4189–4203.
39. M.-S. Li, Y.-W. Dong, M. Quan and W. Jiang, *Angew. Chem.*, **2022**, 134, e202208508.
40. D. A. Evans, G. Borg and K. A. Scheidt, *Angew. Chem. Int. Ed.*, **2002**, 41, 3188–3191.
41. A. Kwiecień, M. Barys and Z. Ciunik, *Molecules*, **2014**, 19, 11160–11177.
42. M. Barys, Z. Ciunik, K. Drabent and A. Kwiecień, *New J. Chem.*, **2010**, 34, 2605–2611.
43. L. Xu, S. Hua and S. Li, *Chem. Commun.*, **2013**, 49, 1542–1544.
44. A. Mirzanejad and L. Muechler, *ChemPhysChem*, **2025**, 26, e202400786.
45. D. Asturiol, M. Duran and P. Salvador, *J. Chem. Theory Comput.*, **2009**, 5, 2574–2581.
46. F. H. Stillinger, *Science*, **1980**, 209, 451–457.
47. L. Pauling, *The Nature of the Chemical Bond*, Cornell University Press, 3rd edn., **1960**.
48. A. L. Allred, *J. Inorg. Nucl. Chem.*, **1961**, 17, 215–221.
49. S. Song, Y. Wang and N. Yan, *Mol. Catal.*, **2018**, 454, 87–93.
50. K. K. Popov, J. L. P. Campbell, O. Kysilka, J. Hošek, C. D. Davies, M. Pour and P. Kočovský, *J. Org. Chem.*, **2022**, 87, 920–943.
51. J. Zhang, J. Yin, X. Duan, C. Zhang and J. Zhang, *J. Catal.*, **2023**, 420, 89–98.
52. K. Mathew, R. Sundararaman, K. Letchworth-Weaver, T. A. Arias and R. G. Hennig, *J. Chem. Phys.*, **2014**, 140, 084106.
53. K. Mathew, V. S. Kolluru, S. Mula, S. N. Steinmann and R. G. Hennig, *J. Chem. Phys.*, **2019**, 151.
54. I. C. Oğuz, D. Vassetti and F. Labat, *Theor. Chem. Acc.*, **2021**, 140, 1–13.
55. P. W. Atkins, J. De Paula and J. Keeler, *Physical Chemistry*, Oxford University Press, 12th edn., **2023**.
56. E. W. Kuipers, A. Vardi, A. Danon and A. Amirav, *Phys. Rev. Lett.*, **1991**, 66, 116–119.
57. C. T. Rettner, *Phys. Rev. Lett.*, **1992**, 69, 383–386.
58. C. Stampfl and M. Scheffler, *Phys. Rev. Lett.*, **1997**, 78, 1500–1503.
59. R. Baxter and P. Hu, *J. Chem. Phys.*, **2002**, 116, 4379–4381.

5. Pyrolysis of sinapic acid over CeO_2(111)

Work from this chapter has been reproduced in the following publication: T. Kulik, N. Nastasiienko, B. Palianytsia, M. Quayle, A. Nastasiienko, P. R. Davies, D. Wass, and A. Roldan. *Catalytic Pyrolysis of Sinapic Acid on Nanoceria: Surface Complexes, Valorisation of Products, Experimental, and Atomistic Approaches.* ChemSusChem. **2025**, 19, (1), e202501249. https://doi.org/10.1002/cssc.202501249.

5.1. Introduction

Ceria (CeO_2) is an intriguing material to study from both a synthetic and computational point of view. Throughout the twentieth century, ceria's primary use in heterogeneous catalysis was as a support for transition metal catalysts. To this day, Cu/CeO_2 remains one of the most popular catalysts for the water-gas shift reaction, a cost-effective industrial process for the production of molecular hydrogen.[1,2] Beyond its role as a support, pure ceria has shown promise as a redox catalyst. When ceria nanoparticles are introduced into a reaction vessel, O atoms on the surface will rapidly react with surrounding species, causing neighbouring Ce atoms to oscillate between the Ce^{4+} and Ce^{3+} oxidation states. This process is known as redox cycling,[3] and its efficiency – and consequently, ceria's effectiveness as a redox catalyst – is highly dependent on nanoparticle size and the concentration of oxygen vacancies in the structure.[4–7]

Ceria's utility as a redox catalyst has not gone unnoticed in the field of catalytic biomass pyrolysis. A spectroscopic study by Shao *et al.*[8] showed that ceria is an effective catalyst for the extraction of acetic acid, glycol aldehyde, and other high-value carbonyls from waste straw and bagasse. Subsequent work by Wan *et al.*[9] highlighted nanoceria's utility as a selective catalyst in the pyrolytic extraction of linear ketones from waste plant matter.

Due to the hundreds, if not thousands, of different compounds that may be present in a sample of organic matter, modelling catalytic processes involving biomass at the DFT level remains challenging. In these cases, it is often practical to select a *model compound*, a molecule whose structure and chemical properties have proven to be broadly representative of more complex compounds. In the case of biomass pyrolysis, an excellent example of such a compound is sinapic acid (SA). In nature, SA is plentiful and easy to handle, and it can be extracted in high concentrations from food waste.[10]

SA is particularly abundant in strawberries,[11] but smaller concentrations have been detected in cranberries,[12] lemons,[13] and blueberries.[14] Even higher concentrations of SA have been detected in herbs and spices such as rosemary[15] and borage.[16] As shown in **Scheme 5.1**, sinapic acid decomposes into an array of aromatic compounds when it is subjected to high temperatures. Under these conditions, SA is readily decarboxylated to 4-vinylsyringol (4VS), a powerful antioxidant that has been investigated by medicinal chemists as a treatment for colon cancer.[15,17] Devinylation of 4VS yields syringol, a flavouring agent that imparts a "wood-smoked" taste to barbecued meat and barrel-aged alcoholic drinks.[18,19] Demethoxylation to guaiacol and subsequent deoxygenation of the methoxy group[20] yields *o*-cresol, which can be further broken down to useful bulk chemicals such as phenol, toluene, and benzene.[21,22]

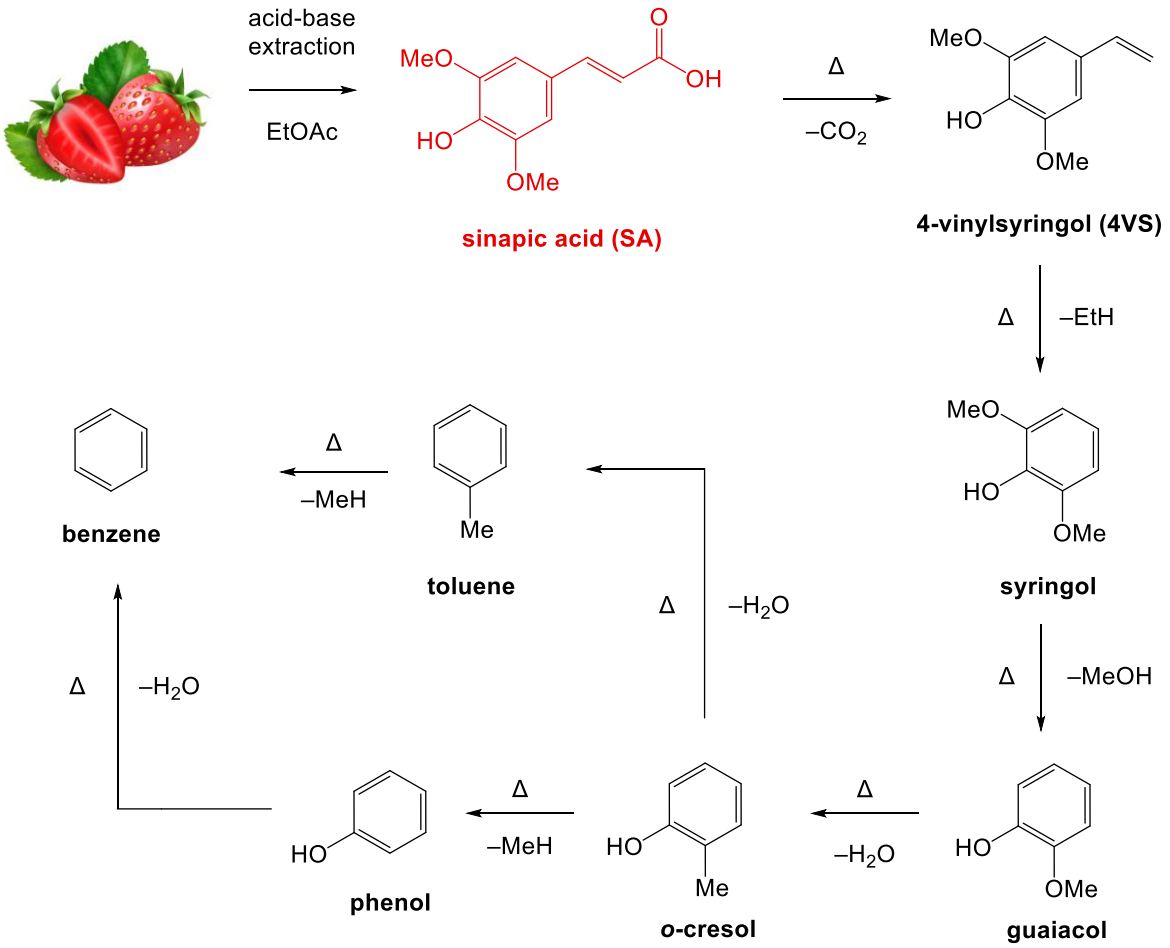

Scheme 5.1. Selection of common pyrolysis routes for SA (red) following its extraction from biomass. SA can be sourced in high yields from strawberries via an acid-base extraction into ethyl acetate (EtOAc).[11]

Ceria is a difficult material to model at the DFT level. The electrons in Ce's 4f orbitals are highly localised and experience strong on-site Coulomb interactions. As these interactions are poorly described by GGA functionals,[23] the degree of delocalisation experienced by the 4f electrons will be overestimated. If unaccounted for, this will lead to significant inaccuracies in ceria's electronic structure, but DFT+U corrections (**Section 2.2.5**) can help alleviate this problem by introducing a Hubbard correction parameter (U_{eff}) to the DFT energy.

The focus of the final computational chapter of this work is ceria's utility as a heterogeneous catalyst in biomass-based chemistry. To better understand the role that ceria plays in SA pyrolysis, a series of IR spectra were generated by conducting frequency analysis on optimised DFT structures of the adsorbate. The computational work of the author (**Sections 5.3** and **5.5**) was then validated using *in situ* diffuse reflectance Fourier-transform infrared (DRIFTS) spectroscopy, temperature-programmed desorption mass spectrometry (TPD-MS), thermogravimetric analysis (TGA), and differential thermal analysis (DTA) by the members of the Tetiana Kulik Group at the Chuiko Institute of Surface Chemistry in Kyiv, Ukraine (**Section 5.4**).

5.2. Methods

All DFT calculations were carried out in VASP[24,25] at the PBE-D3(0) level.[26,27] Gas phase SA and its conjugate base were optimised in the centre of a 20×20×20 Å^3 unit cell sampled with a 1×1×1 Monkhorst-Pack mesh.[28] Oxygen-terminating CeO_2(111), the facet with the lowest surface energy for ceria,[29] was represented with a *p*(7×7×2) slab (Ce = 98, O = 196), as recommended by Engel *et al*.[30] to balance accuracy and computational cost for catalytic modelling at the PBE-D3(0) level. Each slab was separated with a 20 Å vacuum layer along the z-axis. The Brillouin zones of the unit cell and the slab were sampled with 13×13×13 and 3×3×1 Monkhorst-Pack meshes,[28] respectively. The plane-wave cutoff energy was set to 500 eV, the ionic convergence threshold to 0.03 eV/Å, and the electronic convergence threshold to 1×10^{-5} eV. Following established benchmarking work for ceria,[30–32] the rotationally invariant DFT+U scheme of Liechtenstein *et al.*[33] was used to more accurately describe the electrons in the Ce 4f orbitals, with a Hubbard correction parameter U_{eff} of 4 eV (U = 5 eV, J = 1 eV). Infrared spectra were generated from the optimised structures using an in-house code. The transition state associated with decarboxylation was identified

using the improved dimer method.[34,35] Experimental details relating to spectroscopy are provided in the appendix (**Section A.5**).

5.3. Preliminary Work

The electronic structure of the catalyst was investigated by modelling the partial density of states (PDOS) of the CeO_2(111) unit cell (**Figure 5.1**). A clear band gap was observed, with high occupation in the d-orbitals near the Fermi energy ($E_F = 5.52$ eV). However, the width of the band gap ($E_G = 2.21$ eV) was substantially lower than the experimental value for nanoceria, which, depending on the preparation method and the size of the nanoparticles, can range from 2.7 – 3.7 eV, with gaps larger than 3 eV being the most common.[36–38] As PDOS data was only recorded for electrons in the Ce orbitals, ceria's second O_{2p}-Ce_{5d} band gap with a width between 5.5 – 6.0 eV[39–41] was not observed; a likely consequence of Ce's 5d and 6s electrons being donated into the 2p orbitals of the O atoms.[42]

The underestimation of metal oxide band gaps (e.g. CeO_2, NiO, MgO) is a well-documented deficiency of DFT.[32,43–47] As shown in **Table 5.1**, the degree of error can be slightly reduced under the rotationally invariant DFT+U scheme of Liechtenstein *et al.*[33] by increasing U_{eff}, but this comes at the cost of introducing further errors in both the lattice parameters and the Gibbs free energy of formation (ΔG_f°) of the catalyst. As such, a Hubbard correction parameter U_{eff} of 4 eV (U = 5 eV, J = 1 eV) was used for all subsequent optimisation work, following the recommendations of previous benchmarking work on ceria.[30]

Benchmarking	U_{eff}				
	0 eV	4 eV	7 eV	Exp.	Ref.
3d-4f band gap (eV)	2.08	2.21	2.70	~3.00	[30,32,43–47]
a (Å)	5.43	5.43	5.49	5.41	[30,36,48]
ΔG_f° (eV)	–12.0	–11.4	–10.5	–11.3	30,32

Table 5.1. The effects of U_{eff} on the band gap, lattice parameter (a), and Gibbs free energy of formation (ΔG_f°) of CeO_2. All calculations were conducted with the PBE-D3(0) functional. The benchmarking data for $U_{eff} = 0$ eV and $U_{eff} = 7$ eV, and the formation energies for all U_{eff} values, were taken from Engel *et al.*[30]

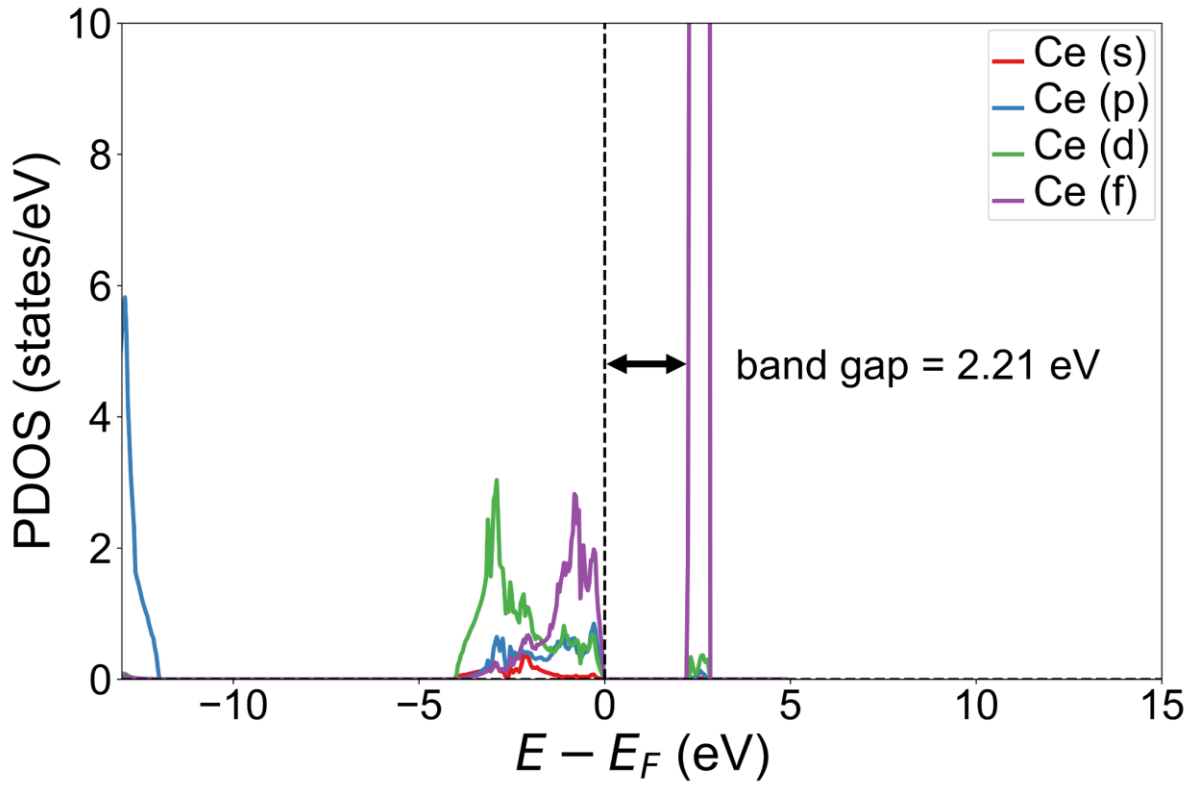

Figure 5.1. Projected density of states plot for electrons in the s (red), p (blue), d (green), and f (purple) orbitals in Ce.

As shown in **Tables 5.2** and **5.3**, the lattice parameters and ionic bond lengths of the optimised CeO_2 unit cell were each within 0.4% of experiment. Following the assumption that the energetic barrier associated with the dissociation of SA's acidic proton would be easily surmountable at pyrolytic temperatures, both SA and its conjugate base were optimised in the gas phase. The latter was then used for all DFT calculations on the $CeO_2(111)$ surface. Following the observations of previous studies of hydrogen clustering on $CeO_2(111)$,[49] the acidic hydrogen was placed on an O top site. Two binding conformations were tested for the conjugate base: (1) the molecule lies parallel to the surface and binds to the catalyst through its aromatic ring system; (2) the molecule adopts a perpendicular conformation and binds to a Ce atom through its COO^- group (**Figure 5.2**). In agreement with experimental studies on the binding configurations of aromatic compounds on ceria,[50,51] a pronounced preference for the flat conformation was observed, albeit at the cost of overbinding.

fcc CeO_2	PBE–D3(0)	Exp.	Ref.
a (Å)	5.43	5.41	34, 35
$d(Ce^{4+}, O^{2-})$ (Å)	2.37	2.37	52

Table 5.2. Lattice parameters and ionic spacing of fcc CeO_2.

CeO_2(111)	Perpendicular	Parallel
E_{ads} (kJ mol^{-1})	–82.6	–237.1
d(Ce—$O_{CARBONYL}$) (Å)	2.93	2.80
d(Ce—H_{TOP}) (Å)	0.98	0.98

Table 5.3. Adsorption energies and interatomic distances of dissociated SA in the parallel and perpendicular configurations over CeO_2(111).

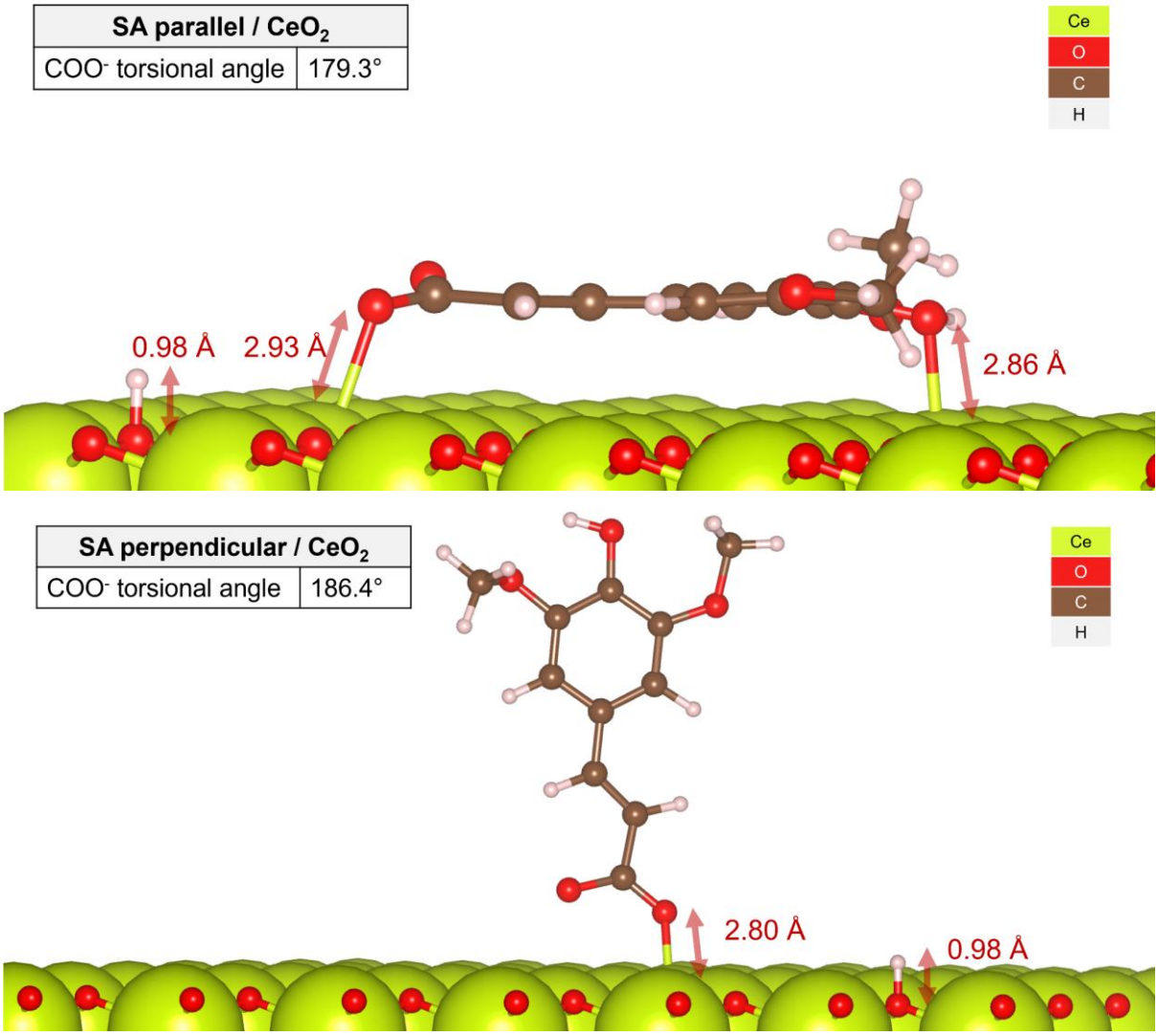

Figure 5.2. Dissociated sinapic acid over CeO_2(111) in the parallel (top) and perpendicular (bottom) configurations.

5.4. Experimental Spectra

5.4.1. TPD-MS

Throughout the pyrolysis of SA, a range of ions were detected by TPD in the gas phase (**Figure 5.3**). Above 310 °C, gaseous products with molar masses of 154, 139, 111, 93, and 96 were detected by mass spectrometry (**Figure 5.4**). Analysis of the ions' mass-to-charge ratios (m/z) confirmed the formation of $^{+}CH_3$ ($m/z = 15$), H_2O^{+} ($m/z = 18$), CO^{+} and $^{+}C_2H_4$ ($m/z = 28$), CH_3O^{+} ($m/z = 31$), and CO_2^{+} ($m/z = 44$). In agreement with the experimental work of Nunes *et al.*,[53] this fragment range is indicative of the formation of syringol ($M_r = 154$) in the gas phase. A complete list of pyrolysis products is provided in **Table 5.4**. The vapour pressure of the system was at its highest between 250 and 450 °C, suggesting that the gasification of the products was at its most intense between these temperatures. Further information on vapour pressure analysis is provided in the appendix (**Figure A.6**).

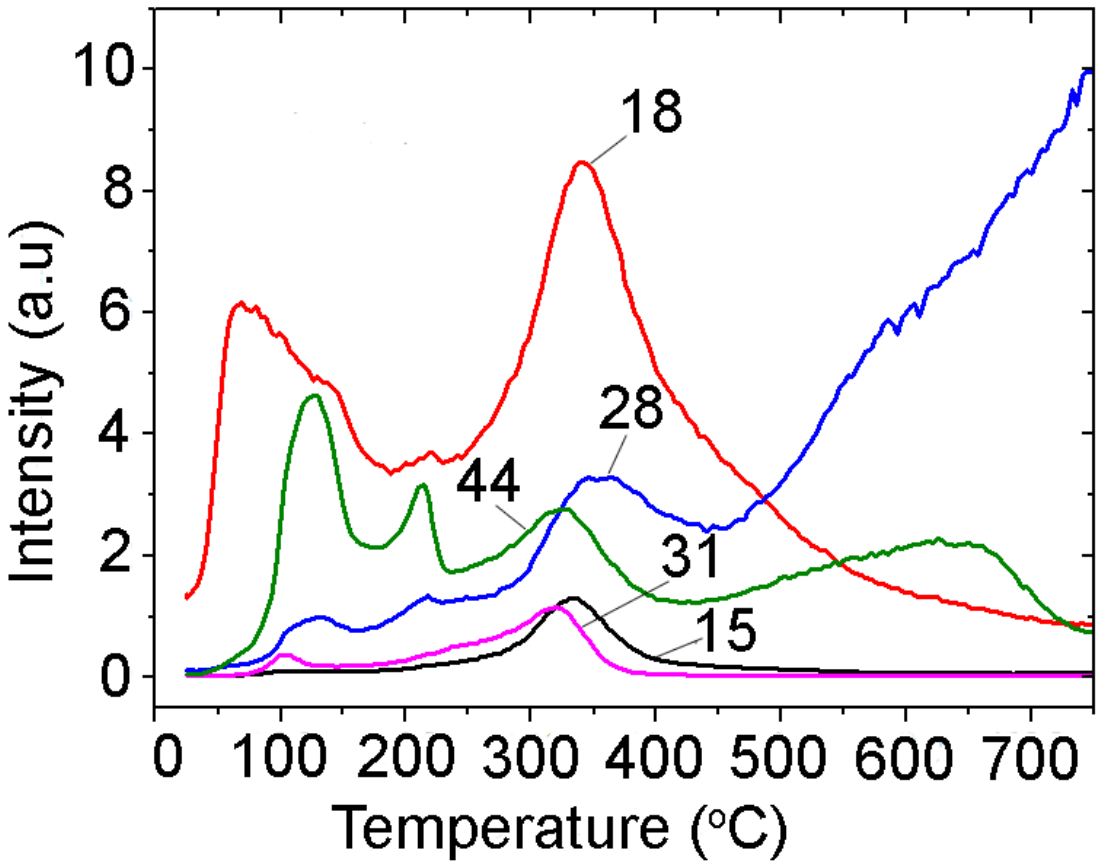

Figure 5.3. TPD spectra for ions with mass-to-charge ratios of 15 (purple), 18 (red), 28 (blue), 31 (black), and 44 (green).

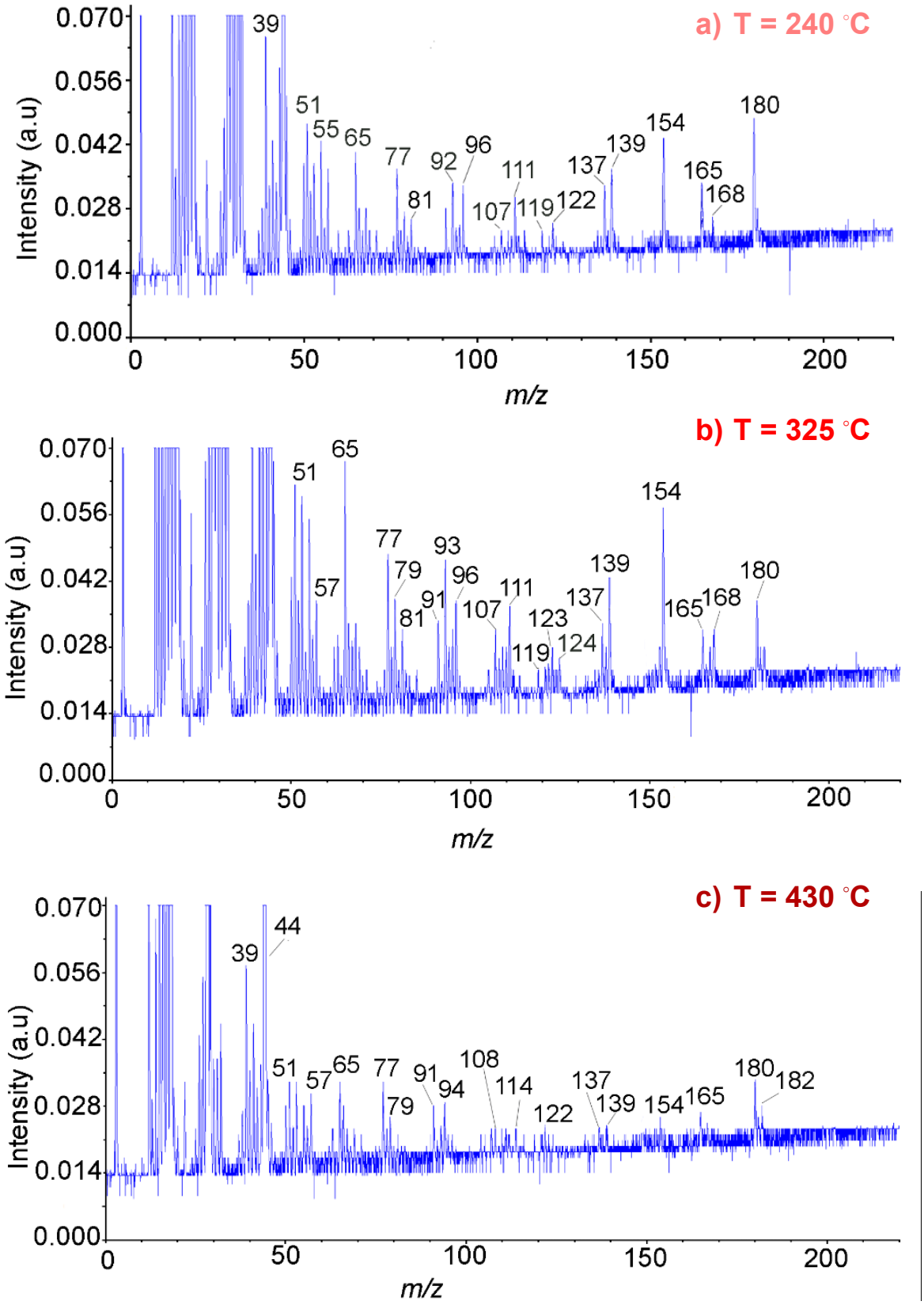

Figure 5.4. Mass spectra of SA@CeO_2 (1.2 mmol/g) pyrolysis products. Spectra recorded at 240 °C (a), 325 °C (b), and 430 °C (c).

Compounds	Main fragments (*m/z*)	Temp. range (ºC)	References
Benzene	78, 77	300 – 380	53
Toluene	91, 92	325	53
o-cresol	107, 108	340	53
Pyrocatechol	110, 64	325	53
Indene	116, 115	330 – 500	53
Pyrogallol	126, 52, 80, 108	320 – 450	53
Naphthalene	128	210 – 500	53
Syringol	154, 139, 111, 93, 96	310	53
4-methyl syringol	168, 153, 125	325	54
4VS	180, 165, 137	237	55
Xanthene	182, 181, 152	230 – 750	53, 56
4-propenyl syringol	194, 179, 167	327	55

Table 5.4. Pyrolysis products of SA detected over CeO_2.

5.4.2. FT-IR

The FT-IR spectra of SA over CeO_2 (**Figure 5.5**) proved to be highly sensitive to heat. As the temperature increased from 20 °C to 470 °C, the shoulder region corresponding to the C=O vibrational mode at 1664 cm^{-1} began to fade, disappearing entirely by 170 °C. The peaks at 1263 cm^{-1} and 1273 cm^{-1}, both of which correspond to vibrations of the O–H hydroxyl bond, also vanished at this temperature. The peaks at 1606 cm^{-1} and 1639 cm^{-1}, each of which correspond to C=C vibrational modes, were still visible at 170 °C, but both showed a marked decrease in intensity as the temperature continued to increase, becoming nearly imperceptible at 260 °C. The diminishing intensity of these peaks indicates the thermal degradation of both carboxylate and aromatic surface complexes. At 200 °C, a broad band emerges at 1633 cm^{-1}, which can be partially attributed to the decomposition of aromatic moieties in SA. This band is consistent with the formation of free vinyl groups following CO_2 elimination, typically absorbing near 1645 cm^{-1}.

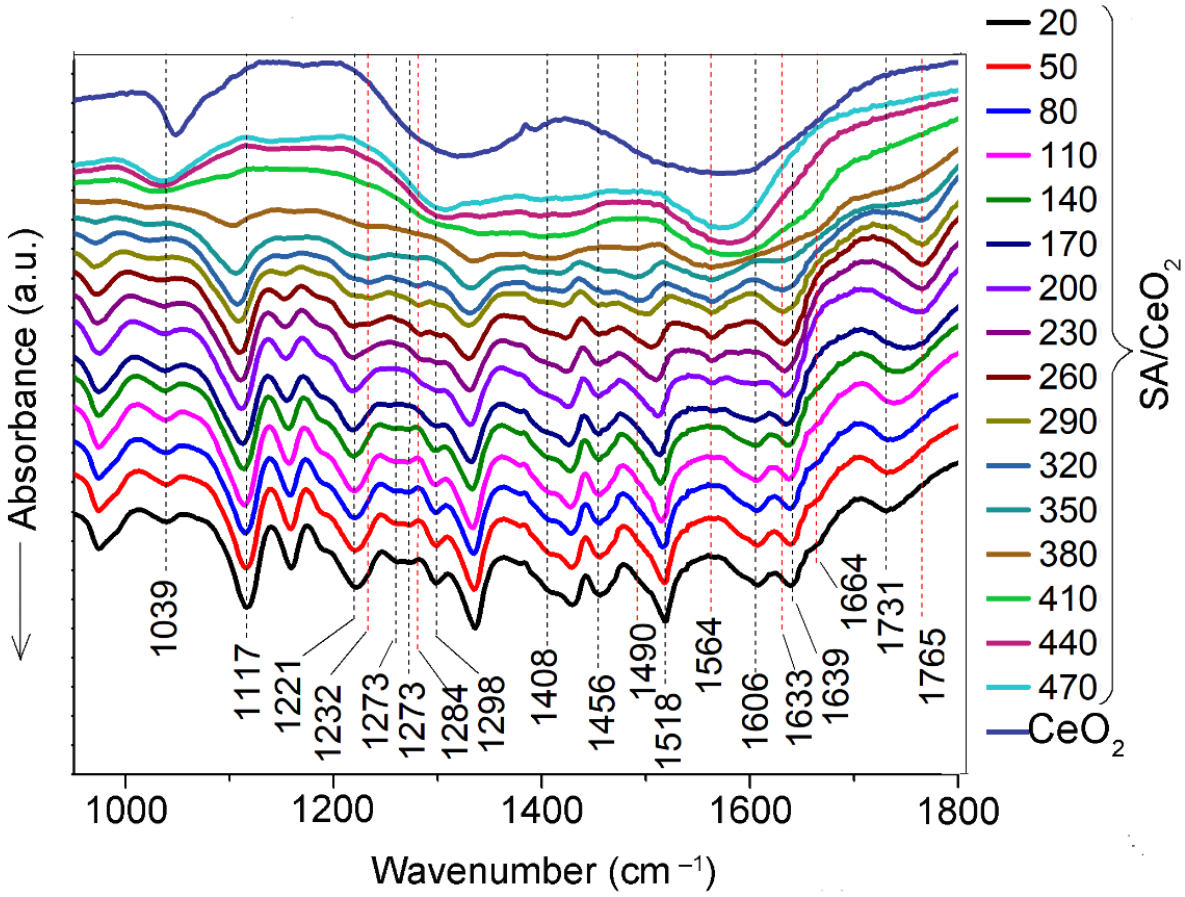

Figure 5.5. FT-IR spectra of pure CeO_2 and SA@CeO_2 (0.6 mmol g^{-1}) after heating from 20 °C (black) to 470 °C (turquoise).

5.5. Computational Spectra

The simulated IR spectrum for SA in the gas phase (**Figure 5.6**) showed satisfactory agreement with experiment. The wavenumbers of all key peaks were correctly identified. In particular, the symmetrical stretch of the α,β-double bond (1302 cm^{-1}) was captured within a single wavenumber of the experimental value (1303 cm^{-1}). However, the model underestimated the intensities of the vibrational modes at 1495 cm^{-1} and 1206 cm^{-1}, and slightly overestimated the modes in the 2800–3100 cm^{-1} range.

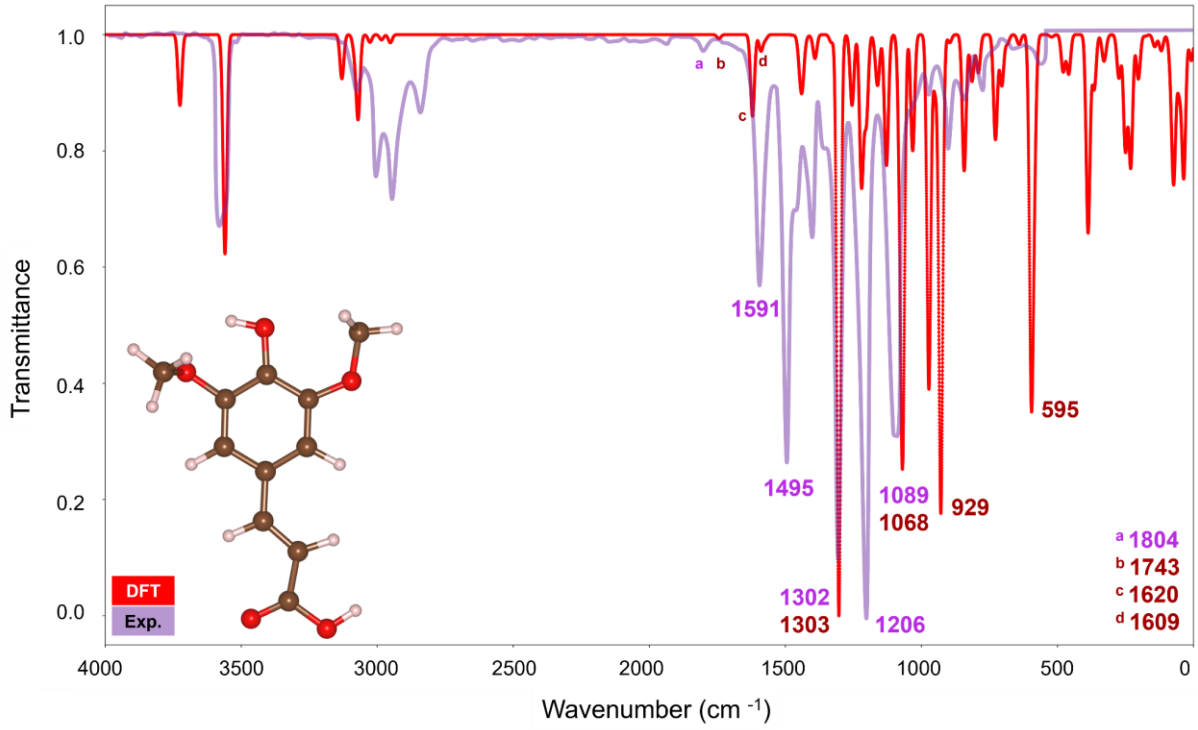

Figure 5.6. Simulated (red) and experimental (lilac) IR spectra of SA. Both spectra recorded in the gas phase. A representation of the optimised structure of SA at the PBE–D3(0) level is provided in the inset (C = brown, H = white, O = red). Experimental IR data adapted from the National Institute of Standards and Technology (NIST).[57]

The predicted IR spectrum of the flat conformation of SA over CeO_2(111) (**Figure 5.7**) bore little resemblance to the experimental spectra. After the transmittance of the vibrational modes were normalised, a sharp peak at 1801 cm^{-1} corresponding to a symmetrical carboxylic acid C–O stretch dwarfed the rest of the spectrum. While the model correctly predicted the presence of a peak corresponding to an alkene stretch at 1563 cm^{-1}, it underestimated the relative intensity of this mode with respect to the peak at 1801 cm^{-1}. The peak at 755 cm^{-1}, the only other wavenumber with an intensity distinguishable from background noise, corresponded to an asymmetric methoxy stretch, which was found to be coupled with a carboxylic acid C–O scissoring mode.

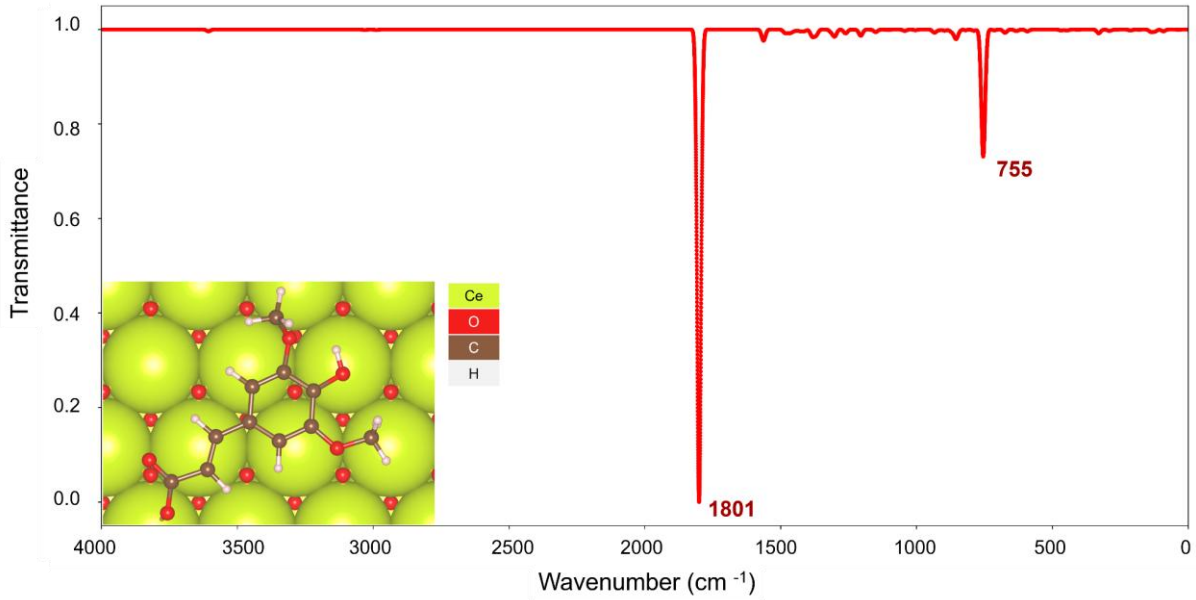

Figure 5.7. Simulated IR spectra of SA's conjugate base in the parallel configuration over CeO_2(111). An optimised structure of the adsorbate at the PBE-D3(0) level is provided in the inset.

As shown in **Table 5.4**, SA can undergo decarboxylation to 4VS when subjected to high temperatures and pressures. Previous experimental studies on the CeO_2-catalysed pyrolysis of caffeic and coumaric acid[55,58] were accompanied by the formation of a selection of decarboxylated compounds; chief among them, pyrocatechin, vinyl guaiacol, and vinyl phenol. With this in mind, a second round of atomistic simulations was carried out to investigate the possibility that the decarboxylation of SA was being catalysed by CeO_2(111). The simulated IR spectrum of 4VS over CeO_2(111) (**Figure 5.8**) bore a much closer resemblance to the experimental spectrum. The peak of highest intensity corresponds to an asymmetric methoxy stretch at 1215 cm^{-1}. Two peaks from the methoxy group at the 6-position showed high intensity: an asymmetric stretch (1085 cm^{-1}) on the C–O bond, and a scissoring mode (901 cm^{-1}) centred on the oxygen. The fingerprint region was bookended by an asymmetric stretching frequency on the vinyl C=C (1618 cm^{-1}).

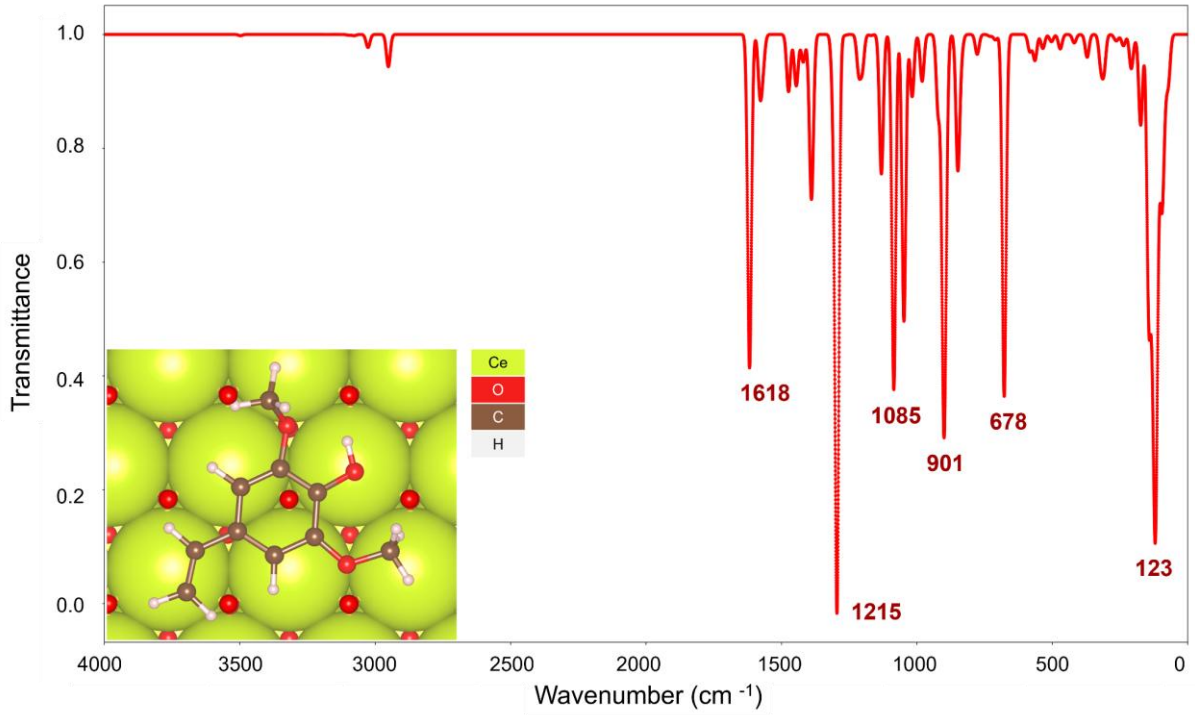

Figure 5.8. Simulated IR spectra of 4VS in the parallel configuration over CeO_2(111). An optimised structure of the adsorbate at the PBE-D3(0) level is provided in the inset.

While the spectra of adsorbed 4VS showed much stronger agreement with experiment than adsorbed SA, this interpretation of the data only holds true if the energy barriers associated with CO_2 formation are within reach under experimental conditions. An upper bound for the decarboxylation barrier heights was determined by freezing the surface and constructing a guess TS structure corresponding to an S_N2 mechanism. This structure was then used as a starting point for a TS search using the improved dimer method. This search yielded an elementary step with a corresponding activation energy of +189 kJ mol^{-1} (**Figure 5.9**). While relatively high, decarboxylation activation energies exceeding +150 kJ mol^{-1} are common for cyclic hydrocarbons,[59,60] and are likely to be surmounted at 170 °C (i.e. the temperature at which the FT-IR peak for C=O vibration disappeared entirely). It should also be noted that, while an S_N2 mechanism is a likely candidate for the minimum energy pathway associated with decarboxylation, lateral interactions between neighbouring adsorbates may facilitate the cleavage of the carbonyl group. Even if the PBE-D3(0) figure of +189 kJ mol^{-1} is an overestimation of the "true" activation energy barrier for decarboxylation, it is a good predictor that this process is feasible over nanoceria at pyrolysis temperatures, thus explaining the similarities between the experimental FT-IR data and the calculated IR spectrum for 4VS@CeO_2.

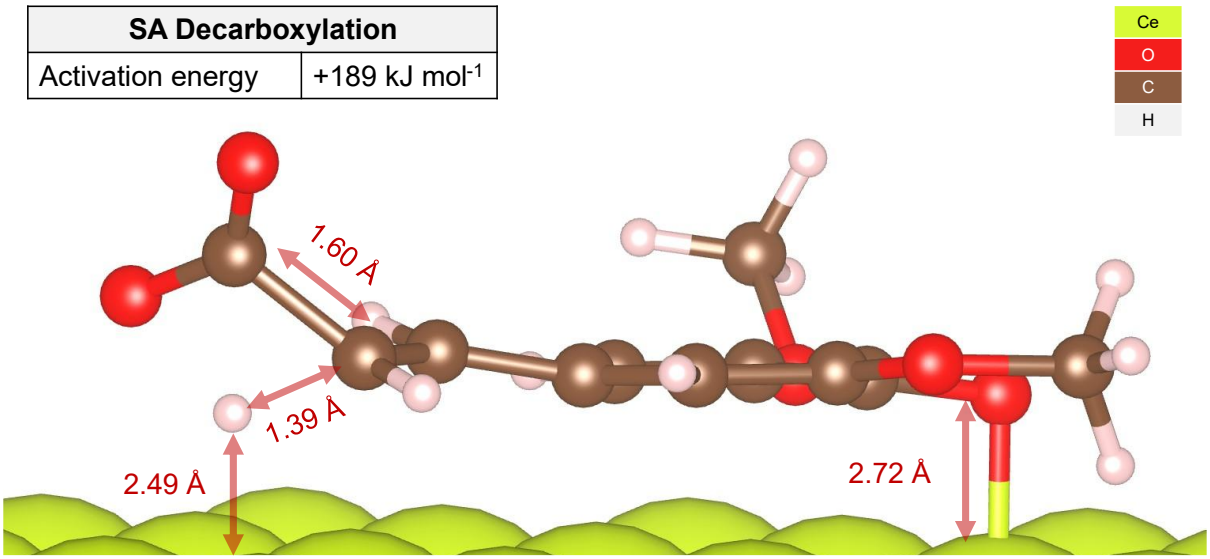

Figure 5.9. Representation of the S_N2 transition state associated with the decarboxylation of SA's conjugate base to 4VS over CeO_2(111).

5.6. Conclusions and Perspectives

The combination of DFT modelling and experimental spectroscopic techniques yielded valuable mechanistic insights into the pyrolysis of SA over CeO_2(111). The gradual disappearance of the bands associated with carboxylate and hydroxyl functional groups and the accessible mechanism identified for decarboxylation suggests that the formation of 4VS is highly favourable at high temperatures over nanoceria.

One area worthy of future study is the role of O vacancies and other surface defects on nanoceria pyrolysis; an area neglected in this thesis so that more attention could be directed towards computational spectroscopy and transition state analysis. When an O^{2-} ion is removed from the surface of a ceria nanoparticle, it typically leaves behind two electrons from its 2p orbitals.[61] The electrons typically localise on a pair of Ce^{4+} ions (thus reducing them to Ce^{3+}), but in rarer cases, they can form a localised, negatively charged vacancy in place of the O atom.[62–64] The effects that O vacancies have on the electronic structure and catalytic properties of nanoceria are challenging to model at the DFT level. The distribution of the electrons throughout the material is known to be highly sensitive to the presence of impurities and surface morphology.[65]

Furthermore, the work of Wan *et al.*[9] on ceria-catalysed pyrolysis suggests that, while (111) facets are the most catalytically active facets for ceria nanorods and nano-polyhedra, catalysis over cubic nanoparticles is dominated by the CeO_2(100) facet.

While the study in question used xylan as a model compound rather than SA, it is possible that a lower energy pathway for decarboxylation may be more accessible on other facets of the nanoparticles; particularly, if cubic particles are being formed under reaction conditions. Future work should aim to incorporate these defect states into atomistic models to more accurately reflect the conditions present during high-temperature pyrolysis and to uncover their role in bond activation and product selectivity.

5.7. References

1. H.-M. Kim, Y.-H. Lee, M.-J. Park and D.-W. Jeong, *Int. J. Hydrog. Energy*, **2023**, 48, 29142–29152.
2. T. Montini, M. Melchionna, M. Monai and P. Fornasiero, *Chem. Rev.*, **2016**, 116, 5987–6041.
3. M. Melchionna and P. Fornasiero, *RSC Appl. Interfaces*, **2024**, 1, 70–79.
4. F. Esch, S. Fabris, L. Zhou, T. Montini, C. Africh, P. Fornasiero, G. Comelli and R. Rosei, *Science*, **2005**, 309, 752–755.
5. D. R. Mullins, S. H. Overbury and D. R. Huntley, *Surf. Sci.*, **1998**, 409, 307–319.
6. A. Trovarelli, *Catalysis by Ceria and Related Materials*, World Scientific, **2002**, vol. 2.
7. L. Wu, H. J. Wiesmann, A. R. Moodenbaugh, R. F. Klie, Y. Zhu, D. O. Welch and M. Suenaga, *Phys. Rev. B*, **2004**, 69, 125415.
8. S. Shao, C. Liu, X. Xiang, X. Li, H. Zhang, R. Xiao and Y. Cai, *Renew. Energy*, **2021**, 177, 1372–1381.
9. Y. Wan, K. Ding, J. C.-H. Lam, D. Zhong and S. Zhang, *Fuel Process. Technol.*, **2023**, 241, 107584.
10. N. Nićiforović and H. Abramovič, *Compr. Rev. Food Sci. Food Saf.*, **2014**, 13, 34–51.
11. W. R. Russell, A. Labat, L. Scobbie, G. J. Duncan and G. G. Duthie, *Food Chem.*, **2009**, 115, 100–104.
12. Y. Zuo, C. Wang and J. Zhan, *J. Agric. Food Chem.*, **2002**, 50, 3789–3794.
13. Y.-C. Wang, Y.-C. Chuang and Y.-H. Ku, *Food Chem.*, **2007**, 102, 1163–1171.
14. F. A. Ayaz, S. Hayirlioglu-Ayaz, J. Gruz, O. Novak and M. Strnad, *J. Agric. Food Chem.*, **2005**, 53, 8116–8122.
15. N. Nićiforović and H. Abramovič, *Compr. Rev. Food Sci. Food Saf.*, **2014**, 13, 34–51.
16. M. Wettasinghe, F. Shahidi, R. Amarowicz and M. M. Abou-Zaid, *Food Chem.*, **2001**, 75, 49–56.
17. H. Kuwahara, A. Kanazawa, D. Wakamatu, S. Morimura, K. Kida, T. Akaike and H. Maeda, *J. Agric. Food Chem.*, **2004**, 52, 4380–4387.
18. C. Srinivasulu, M. Ramgopal, G. Ramanjaneyulu, C. M. Anuradha and C. Suresh Kumar, *Biomed. Pharmacother.*, **2018**, 108, 547–557.
19. B. M. Schneider, in *Chemistry of Alcoholic Beverages*, ACS Publications, **2023**, pp. 159–172.
20. K. Agrawal, A. M. Verma and N. Kishore, *ChemistrySelect*, **2019**, 4, 6013–6025.

21. B. R. Albuquerque, S. A. Heleno, M. B. P. P. Oliveira, L. Barros and I. C. F. R. Ferreira, *Food Funct.*, **2021**, 12, 14–29.
22. N. Chakinala and A. G. Chakinala, *Ind. Eng. Chem. Res.*, **2021**, 60, 5331–5351.
23. P. Fulde, P. Thalmeier and G. Zwicknagl, in *Solid State Physics*, Elsevier, **2006**, vol. 60, pp. 1–180.
24. J. Hafner and G. Kresse, in *Properties of Complex Inorganic Solids*, Springer, **1997**, pp. 69–82.
25. G. Kresse and D. Joubert, *Phys. Rev. B*, **1999**, 59, 1758.
26. J. P. Perdew, K. Burke and M. Ernzerhof, *Phys. Rev. Lett.*, **1996**, 77, 3865.
27. S. Grimme, J. Antony, S. Ehrlich and H. Krieg, *J. Chem. Phys.*, **2010**, 132.
28. H. J. Monkhorst and J. D. Pack, *Phys. Rev. B*, **1976**, 13, 5188.
29. A. S. Kholtobina, A. Forslund, A. V. Ruban, B. Johansson and N. V. Skorodumova, *Phys. Rev. B*, **2023**, 107, 035407.
30. J. Engel, S. Francis and A. Roldan, *Phys. Chem. Chem. Phys.*, **2019**, 21, 19011–19025.
31. A. Bruix, J. A. Rodriguez, P. J. Ramírez, S. D. Senanayake, J. Evans, J. B. Park, D. Stacchiola, P. Liu, J. Hrbek and F. Illas, *J. Am. Chem. Soc.*, **2012**, 134, 8968–8974.
32. C. Loschen, J. Carrasco, K. M. Neyman and F. Illas, *Phys. Rev. B*, **2007**, 75, 035115.
33. A. Liechtenstein, V. I. Anisimov and J. Zaanen, *Phys. Rev. B*, **1995**, 52, R5467.
34. G. Henkelman and H. Jónsson, *J. Chem. Phys.*, **1999**, 111, 7010–7022.
35. A. Heyden, A. T. Bell and F. J. Keil, *J. Chem. Phys.*, **2005**, 123, 224101.
36. M. Fronzi, A. Soon, B. Delley, E. Traversa and C. Stampfl, *J. Chem. Phys.*, **2009**, 131.
37. J. Li, A. Kalam, A. S. Al-Shihri, Q. Su, G. Zhong and G. Du, *Mater. Chem. Phys.*, **2011**, 130, 1066–1071.
38. E. K. Goharshadi, S. Samiee and P. Nancarrow, *J. Colloid Interface Sci.*, **2011**, 356, 473–480.
39. H.-T. Chen and J.-G. Chang, *J. Chem. Phys.*, **2010**, 132, 214702.
40. E. Wuilloud, B. Delley, W.-D. Schneider and Y. Baer, *Phys. Rev. Lett.*, **1984**, 53, 202–205.
41. J.-M. Costantini, K. Béneut, M. Guillaumet and G. Lelong, *Materials*, **2024**, 17.
42. R. Gillen, S. J. Clark and J. Robertson, *Phys. Rev. B—Condensed Matter Mater. Phys.*, **2013**, 87, 125116.
43. K. Terakura, T. Oguchi, A. R. Williams and J. Kübler, *Phys. Rev. B*, **1984**, 30, 4734–4747.
44. J. Muscat, A. Wander and N. M. Harrison, *Chem. Phys. Lett.*, **2001**, 342, 397–401.
45. I. de P. R. Moreira, F. Illas and R. L. Martin, *Phys. Rev. B*, **2002**, 65, 155102.
46. Z.-X. Shen, R. S. List, D. S. Dessau, B. O. Wells, O. Jepsen, A. J. Arko, R. Barttlet, C. K. Shih, F. Parmigiani, J. C. Huang and P. A. P. Lindberg, *Phys. Rev. B*, **1991**, 44, 3604–3626.
47. C. Ataide, R. Pelá, M. Marques, L. Teles, J. Furthmüller and F. Bechstedt, *Phys. Rev. B*, **2017**, 95, 045126.
48. V. Esposito and E. Traversa, *J. Am. Ceram. Soc.*, **2008**, 91, 1037–1051.
49. D. Fernández-Torre, J. Carrasco, M. V. Ganduglia-Pirovano and R. Pérez, *J. Chem. Phys.*, **2014**, 141, 014703.
50. J. N. Jocz, Y. Lyu, B. J. Hare and C. Sievers, *Langmuir*, **2022**, 38, 458–471.
51. C. Li, Y. Nakagawa, M. Tamura, A. Nakayama and K. Tomishige, *ACS Catal.*, **2020**, 10, 14624–14639.

52. *Fm3̄m* CeO_2, The Materials Project. Last accessed 23 May 2025. https://next-gen.materialsproject.org/materials/mp-20194.
53. C. A. Nunes, C. F. Lima, L. C. A. Barbosa, J. L. Colodette, A. F. G. Gouveia and F. O. Silvério, *Bioresour. Technol.*, **2010**, 101, 4056–4061.
54. C. F. Lima, L. C. A. Barbosa, M. N. N. Silva, J. L. Colodette and F. O. Silvério, *J. Anal. Appl. Pyrolysis*, **2015**, 112, 164–172.
55. N. Nastasiienko, T. Kulik, B. Palianytsia, M. Larsson, T. Cherniavska and M. Kartel, *Colloids Interfaces*, **2021**, 5, 48.
56. S. M. Schimming, O. D. LaMont, M. König, A. K. Rogers, A. D. D'Amico, M. M. Yung and C. Sievers, *ChemSusChem*, **2015**, 8, 2073–2083.
57. *3,5-Dimethoxy-4-hydroxycinnamic acid*, NIST Chemistry WebBook. Last accessed 15 July 2025. https://webbook.nist.gov/cgi/inchi?ID=C530596&Type=IR-SPEC&Index=2.
58. N. Nastasiienko, T. Kulik, M. Ilchenko, B. Palianytsia, A. Nastasiienko, G. Shaw, P. Davies, D. Wass and M. Kartel, *Chem. Phys. Technol. SurfaceKhimiya Fiz. Ta Tekhnologiya Poverhni*, **2024**, 15.
59. S. Zhou, Y. Wang and J. Gao, *JACS Au*, **2021**, 1, 233–244.
60. C. A. Jr. Lewis and R. Wolfenden, *Biochemistry*, **2009**, 48, 8738–8745.
61. H.-F. Wang, H.-Y. Li, X.-Q. Gong, Y.-L. Guo, G.-Z. Lu and P. Hu, *Phys. Chem. Chem. Phys. PCCP*, **2012**, 14, 16521–16535.
62. H.-J. Freund and G. Pacchioni, *Chem. Soc. Rev.*, **2008**, 37, 2224.
63. J. Carrasco Rodríguez, N. López and F. Illas, *Phys. Rev. Lett.*, **2004**, 93, 225502.
64. M. V. Ganduglia-Pirovano, A. Hofmann and J. Sauer, *Surf. Sci. Rep.*, **2007**, 62, 219–270.
65. O. Hellman, N. V. Skorodumova and S. I. Simak, *Phys. Rev. Lett.*, **2012**, 108, 135504.

6. Conclusions and Future Work

The final chapter of this thesis summarises the main findings of the two reactions investigated: the hydrogenation and reductive amination of ALD-1 over Pd(111), Pt(111), and Ru(0001) in **Section 6.1**; and the ceria-catalysed pyrolysis of SA in **Section 6.2**. Each of these sections is supplemented by a selection of suggestions for future work in the field.

6.1. ALD-1 Hydrogenation and Reductive Amination

As observed experimentally, sequential chain and ring hydrogenation of ALD-1 to ALD-3 was shown to be facile over Pd(111). The high activation energies associated with ring hydrogenation over Pt(111) and Ru(0001) were shown to originate from the buildup of positive charge at the ortho site of the furanic ring system. While the high yields of ALD-3 over Pd(111) were verified via GC-MS (**Figure 3.14**), the exact structure and yield distribution of the side products over Pt(111) remained elusive. Furfural derivatives will often polymerise with one another on the surface of Pt nanoparticles.[1–3] While polymerisation was likely a major source of by-products, lateral interactions between adsorbates had to be neglected out of computational necessity due to the large number of atoms in the system. While ALD-2 was correctly identified through TS analysis as the likely dominant product of Pt-catalysed ALD-1 hydrogenation, a complete picture of the mechanistic chemistry driving this reaction would require each side product to be identified experimentally.

Another aspect of this reaction that requires further investigation is the role of solvation on each elementary step's activation energy. In the thirty years since VASP's release,[4,5] there remains no clear consensus on the best way to account for solvation effects in DFT models of heterogeneous catalytic systems. Explicit solvation models, wherein each molecule of solvent is modelled at the atomic level, remain unfeasible for large systems (**Figure 6.1c**). A more practical approach is implicit solvation (**Figure 6.1a**), a model in which the solvent is treated as a continuous "averaged" potential. This method is especially popular in the field of computational biochemistry, where modelling the interactions of large proteins with individual molecules of solvent would be impractical.

The implementation of implicit solvation for periodic DFT packages is non-trivial. For VASP users, the most common implicit solvation plugin is VASPsol, developed by Mathew *et al.*[6,7] in 2014. While VASPsol remains an acceptable choice for systems with heavy solvent dependencies, a review by Oğuz *et al.*[8] revealed a number of systematic errors relating to geometry optimisation and transition state calculations. These issues were particularly pronounced for amines and other organic molecules with nitrogen-based functional groups. Due to the heavy focus on amine chemistry in **Chapter 4**, VASPsol was not considered in this work to ensure consistency and comparability with the DFT calculations conducted in **Chapter 3**.

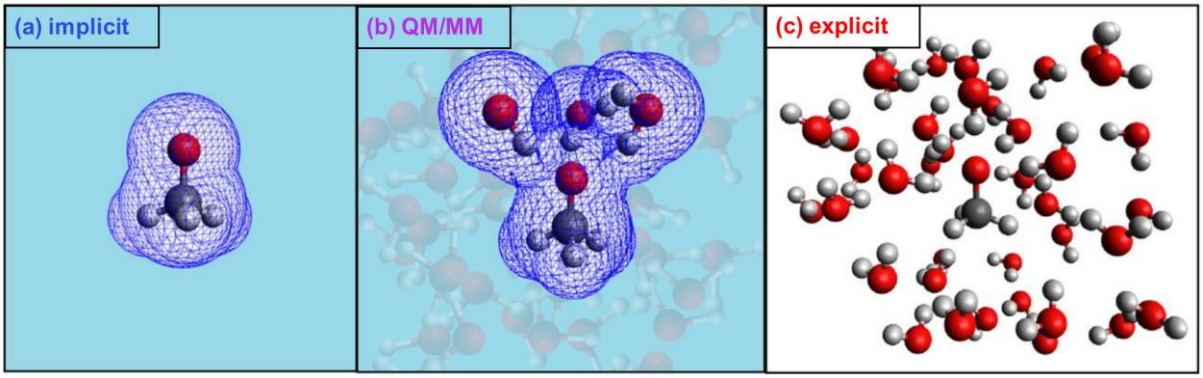

Figure 6.1. MeO^- anions in water, as represented by (a) implicit, (b) QM/MM, and (c) explicit solvation models. The cavity boundaries in the implicit and hybrid models are highlighted by a dark blue mesh. Adapted from Pliego and Riveros (2020).[9]

A potential method that could be employed in future work on the hydrogenation and amination of furfural derivatives is QM/MM solvation (**Figure 6.1b**). In a QM/MM calculation, the region of greatest interest to theoreticians, colloquially referred to as the "QM region", is modelled at the DFT level. Typically, the QM region encompasses the solute and a small selection of neighbouring solvent molecules. The rest of the solvent molecules in the "MM region" are then modelled using classical molecular mechanics, drastically reducing the cost of the calculation. QM/MM has proven especially popular in the field of computational biochemistry, as it allows theoreticians to model the effects of localised solvation has on large, complex molecules such as proteins. The largest barriers in contemporary QM/MM research are the extensive parameterisation that must be conducted to ensure that the boundary separating the QM and MM region is properly modelled and the poor transferability of QM/MM codes across catalytic systems, but such a study could allow for new insights into the effects of solvent on the hydrogenation and amination of ALD-1 and other furfural derivatives.

Another low-cost solvation technique that warrants consideration in future computational studies in this area is microsolvation. Instead of simulating the solvation of the entire system, solvent molecules are placed at key sites around the structure to capture the effects of total solvation as accurately as possible. In the case of polar solvents, priority is given to parts of the system with localised charges or functional groups that are known to form extensive networks of hydrogen bonds; a property that has been shown in previous computational studies to drastically improve the stability of solvated organic molecules.[10–12] By design, microsolvation is not intended to be a substitute for complete solvation models, but it has proven to be a useful technique in the field of computational organic chemistry. For instance, in a DFT study on the structural chemistry of triazole-water clusters ($TZ(H_2O)_{1\text{-}8}$), Hattab *et al.*[13] used microsolvation modelling to demonstrate the existence of strongly stabilising networks of hydrogen bonds between the solvent molecules and the nitrogen atoms in TZ's ring system. As shown in **Figure 6.2**, the most stable clusters were those with eight water molecules in compressed, cube-like configurations, linked together by hydrogen bonds; a stabilising factor that would have been exceedingly difficult to model without explicitly modelling the water molecules.

6.2. Sinapic Acid Pyrolysis

While DFT analysis of pyrolysed SA successfully predicted the formation of 4VS over CeO_2(111), computational modelling molecular spectra remains a formidable challenge. For small molecules in the gas phase, frequency analysis can often approximate the individual wavenumbers of IR peaks. For catalytic systems, however, complications quickly arise. The broadness of an IR peak is a trivially simple property to measure experimentally, but it remains extremely challenging to model at the DFT level due to highly sensitivity to the formation of hydrogen bonds and intramolecular proton shuttling; a problem that is further exacerbated for compounds in the liquid phase.[14–16] For an accurate infrared spectrum to be generated, the conformational PES of a given molecule must be extensively explored. While state-of-the-art modelling methods can predict IR spectra to extremely high degrees of accuracy, they are often dependent on an optimisation at the CCSD(T) level,[17–19] making them impractical for large catalytic systems.

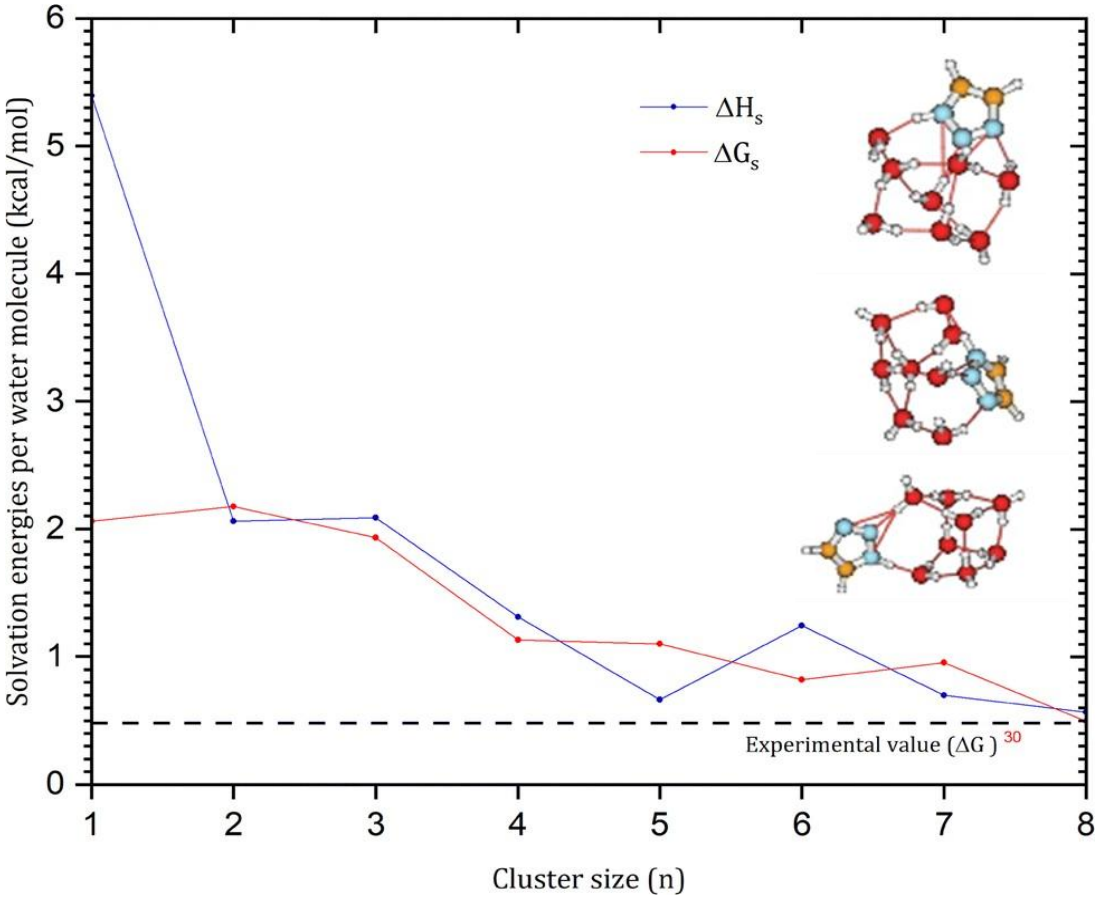

Figure 6.2. Solvation energies of $TZ(H_2O)_n$ clusters as a function of cluster size. The three most stable conformations are given on the right-hand side. Figure adapted from Hattab *et al.* (2025).[13]

The effects of O vacancies and surface defects on nanoceria-catalysed pyrolysis were also neglected in this work so that more attention could be expended on computational spectroscopy. Machine learning (ML) models have shown great promise in contemporary research on the morphological properties of ceria catalysts; particularly, doped ceria, a family of materials whose electronic structure has proven challenging to model at the DFT level.[20–22] For example, a 2022 study by Pentyala *et al.*[20] showed that ML models could successfully predict vacancy formation energies in Pd-Zr-substituted ceria. The 2024 work of Barrios Herrera *et al.*[23] further demonstrated that ML models could successfully predict the conformational geometry of Ni-doped ceria nanoparticles.

ML transition state searches have also shown great promise in the field of theoretical chemistry. ML-NEB, a transition state search method developed in 2019 by Garrido-Torres *et al.*,[24] uses machine learning to construct a simplified "surrogate" model of the PES. A classical NEB calculation, its speed greatly increased by the

simplicity of the surface, is then performed over the surrogate PES. CatTSunami, a 2025 ML model developed by Wander *et al.*,[25,26] is capable of performing transition state searches at over 25 times the speed of conventional NEB calculations within an activation energy accuracy of 91%; a feat made possible due to its training set of over 900 converged NEB calculations. Building on this work, future studies could utilise machine learning models in combination with DFT+U calculations to more effectively model the effects of O vacancies and the introduction of dopants on ceria's reactivity, with the goal of helping the development of new sustainable processes in bio-based heterogeneous catalysis.

6.3. References

1. T. Mizugaki, T. Yamakawa, Y. Nagatsu, Z. Maeno, T. Mitsudome, K. Jitsukawa and K. Kaneda, *ACS Sustain. Chem. Eng.*, **2014**, 2, 2243–2247.
2. Z. Fu, Z. Wang, W. Lin, W. Song and S. Li, *Appl. Catal. Gen.*, **2017**, 547, 248–255.
3. M. Y. Byun and M. S. Lee, *J. Ind. Eng. Chem.*, **2021**, 104, 406–415.
4. J. Hafner and G. Kresse, in *Properties of Complex Inorganic Solids*, Springer, **1997**, pp. 69–82.
5. G. Kresse and D. Joubert, *Phys. Rev. B*, **1999**, 59, 1758.
6. K. Mathew, R. Sundararaman, K. Letchworth-Weaver, T. A. Arias and R. G. Hennig, *J. Chem. Phys.*, **2014**, 140, 084106.
7. K. Mathew, V. S. Kolluru, S. Mula, S. N. Steinmann and R. G. Hennig, *J. Chem. Phys.*, **2019**, 151.
8. I. C. Oğuz, D. Vassetti and F. Labat, *Theor. Chem. Acc.*, **2021**, 140, 1–13.
9. J. R. Pliego Jr. and J. M. Riveros, *Wiley Interdiscip. Rev. Comput. Mol. Sci.*, **2020**, 10, e1440.
10. S. M. Bachrach, T. T. Nguyen and D. W. Demoin, *J. Phys. Chem. A*, **2009**, 113, 6172–6181.
11. P. L. Türtscher and M. Reiher, *J. Chem. Theory Comput.*, **2025**, 21, 5571–5587.
12. C. Liu, J. C. Y. Le Blanc, B. B. Schneider, J. Shields, J. J. I. Federico, H. Zhang, J. G. Stroh, G. W. Kauffman, D. W. Kung, C. Ieritano, E. Shepherdson, M. Verbuyst, L. Melo, M. Hasan, D. Naser, J. S. Janiszewski, W. S. Hopkins and J. L. Campbell, *ACS Cent. Sci.*, **2017**, 3, 101–109.
13. A. Hattab, A. Malloum, J. Conradie and N. Russo, *Phys. Chem. Chem. Phys.*, **2025**, 27, 21752–21761.
14. J. Jo, J. Park, S. Kwon, M. Park, J. Jung, Y. Yoo and D. Kang, *J. Environ. Chem. Eng.*, **2023**, 11, 110108.
15. T. Ebata, K. Kouyama and N. Mikami, *J. Chem. Phys.*, **2003**, 119, 2947–2950.
16. R. Biswas, W. Carpenter, G. A. Voth and A. Tokmakoff, *J. Chem. Phys.*, **2016**, 145, 154504.
17. V. Barone, M. Biczysko, J. Bloino and C. Puzzarini, *J. Chem. Phys.*, **2014**, 141, 034107.
18. C. Puzzarini, M. Biczysko, J. Bloino and V. Barone, *Astrophys. J.*, **2014**, 785, 107.

19. V. Barone, S. Alessandrini, M. Biczysko, J. R. Cheeseman, D. C. Clary, A. B. McCoy, R. J. DiRisio, F. Neese, M. Melosso and C. Puzzarini, *Nat. Rev. Methods Primer*, **2021**, 1, 38.
20. P. Pentyala, V. Singhania, V. K. Duggineni and P. A. Deshpande, *Mol. Catal.*, **2022**, 522, 112190.
21. K. Polychronopoulou, A. A. AlKhoori, A. M. Efstathiou, M. A. Jaoude, C. M. Damaskinos, M. A. Baker, A. Almutawa, D. H. Anjum, M. A. Vasiliades, A. Belabbes, L. F. Vega, A. F. Zedan and S. J. Hinder, *ACS Appl. Mater. Interfaces*, **2021**, 13, 22391–22415.
22. M. D. Krcha and M. J. Janik, *Int. J. Quantum Chem.*, **2014**, 114, 8–13.
23. L. Barrios Herrera, M. P. Lourenço, J. Hostaš, P. Calaminici, A. M. Köster, A. Tchagang and D. R. Salahub, *J. Comput. Chem.*, **2024**, 45, 1643–1656.
24. J. A. Garrido Torres, P. C. Jennings, M. H. Hansen, J. R. Boes and T. Bligaard, *Phys. Rev. Lett.*, **2019**, 122, 156001.
25. B. Wander, PhD Thesis, University of California Los Angeles, **2024**.
26. B. Wander, M. Shuaibi, J. R. Kitchin, Z. W. Ulissi and C. L. Zitnick, *ACS Catal.*, **2025**, 15, 5283–5294.

A. Appendix

All spectroscopic work relating to the hydrogenation of ALD-1 (**Section A.1**) was undertaken by Zhuoli Wu at the Cardiff Catalysis institute. All experimental analysis corresponding to the pyrolysis of SA (**Section A.3**) was undertaken by the members of the Tetiana Kulik Group at the Chuiko Institute of Surface Chemistry in Kyiv, Ukraine.

A.1. Experimental Analysis of ALD-1 Hydrogenation

A.1.1. Reagent Preparation

10.4 mmol furfural (Sigma Aldrich, 99%), 100.0 mmol methyl isobutyl ketone (Sigma Aldrich, ACS reagent, ≥98.5%), and an Amberlyst® A26 Ion Exchange Resin catalyst (Sigma Aldrich, 16-50 mesh) were reacted for 2 hours at 393 K in a 35 mL sealed glass reactor tube. The solvent was removed via rotary evaporation, giving (*E*)-1-(furan-2-yl)-4-methylpent-1-en-3-one (ALD-1) with 96% yield. Gas chromatography confirmed a purity of 97.5%.

A.1.2. Hydrogenation Analysis

Catalytic testing of the hydrogenation of ALD-1 (3.2 mmol) over Pd/Al_2O_3 (66 mg, Sigma Aldrich) and Pt/Al_2O_3 (66 mg, Sigma Aldrich) nanoparticles was conducted at 180 °C in a stainless-steel autoclave (50 mL, DG Innovative Engineering Design Solutions). Once MIBK (59.3 mmol, Sigma Aldrich) and H_2 (<99%, 20 bar, British Oxygen Company) had been fed into the reaction vessel, the yields of the hydrogenation products were monitored over an 18-hour period via gas chromatography-mass spectrometry (GC-MS).

A.1.3. Mass Spectrometry

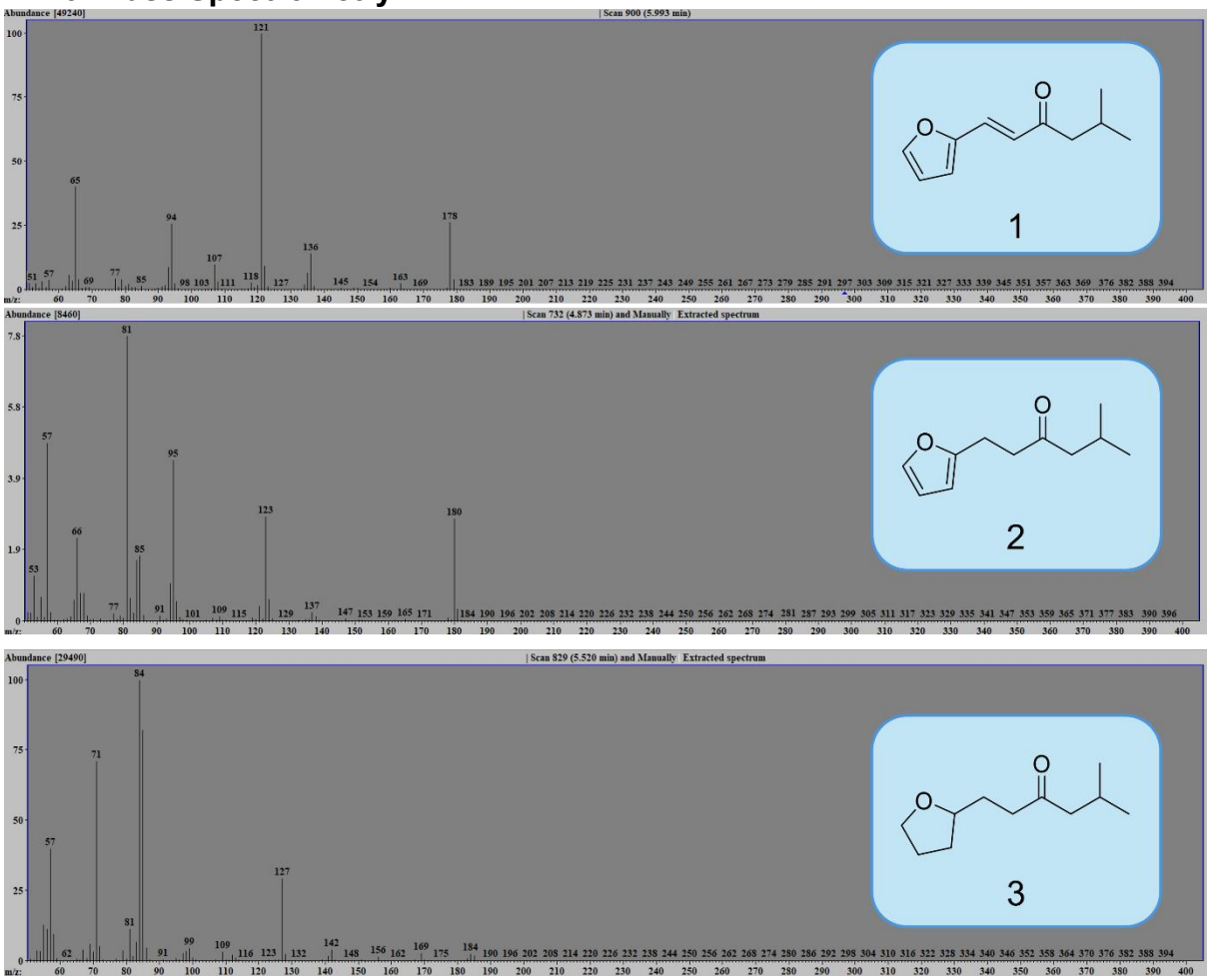

Figure A.1. Mass spectrometry plots of ALD-1, ALD-2, and ALD-3.

Pd/Al_2O_3			
Duration (min)	**Conversion, ALD-1**	**Yield, ALD-2**	**Yield, ALD-3**
1080	100%	0%	100%
180	100%	0%	100%
120	100%	1%	100%
60	100%	7%	95%
30	100%	28%	71%
15	100%	49%	53%
5	100%	69%	28%

Pt/Al_2O_3			
Duration (min)	**Conversion, ALD-1**	**Yield, ALD-2**	**Yield, ALD-3**
1080	100%	12%	33%
180	100%	39%	65%
120	100%	56%	49%
60	98%	55%	41%
30	95%	53%	39%
15	83%	48%	27%
5	60%	36%	26%

Table A.1. Hydrogenation yields over Pd/Al_2O_3 and Pt/Al_2O_3.

A.1.4. Nanoparticle Characterisation

As shown in **Figure A.2**, the nanoparticles were characterized with a Jeol 2100-JEM transmission electron microscope (TEM). The microscope was equipped with a 0.2 nm Gatan digital camera, a high-angle annular dark-field (HAADF) detector set to STEM mode, and a 3D tomographic scanner. A 150 point scan conducted in the ImageJ software package[1] revealed that the mean diameter of the nanoparticles were 4.29 nm for Pd/Al_2O_3 and 2.27 nm for Pt/Al_2O_3 (**Figure A.3**).

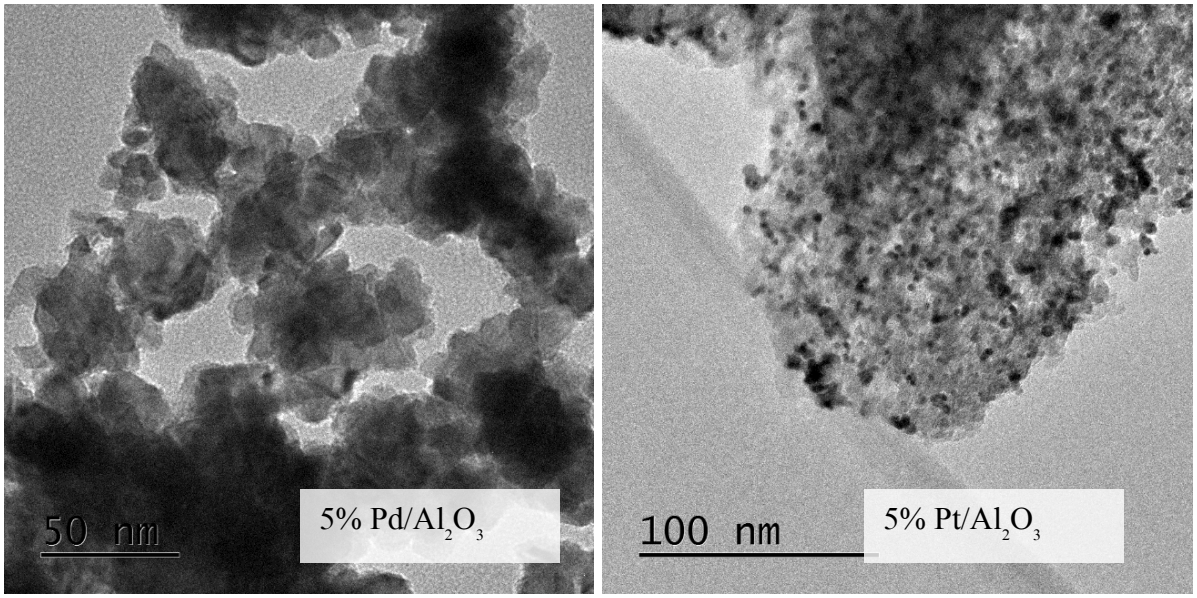

Figure A.2. 0.2 nm resolution TEM images of the Pd/Al_2O_3 (left) and Pt/Al_2O_3 (right) nanoparticles at 77 K.

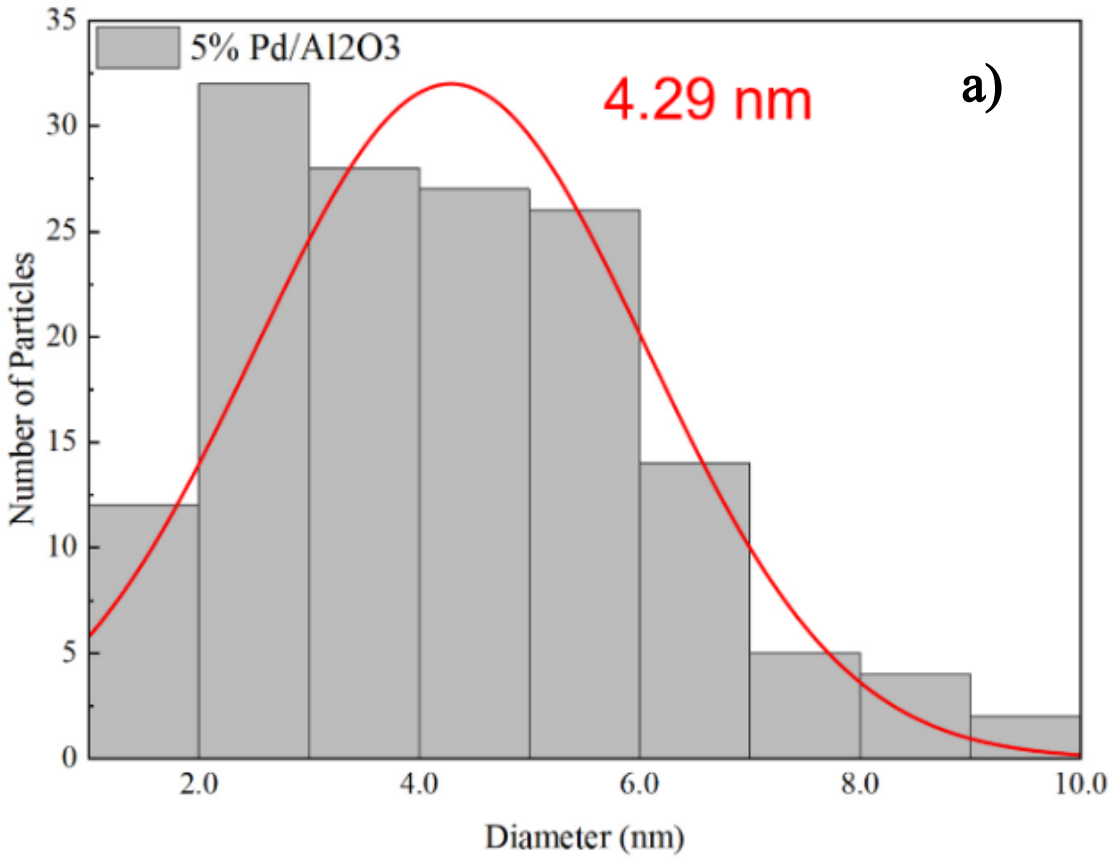

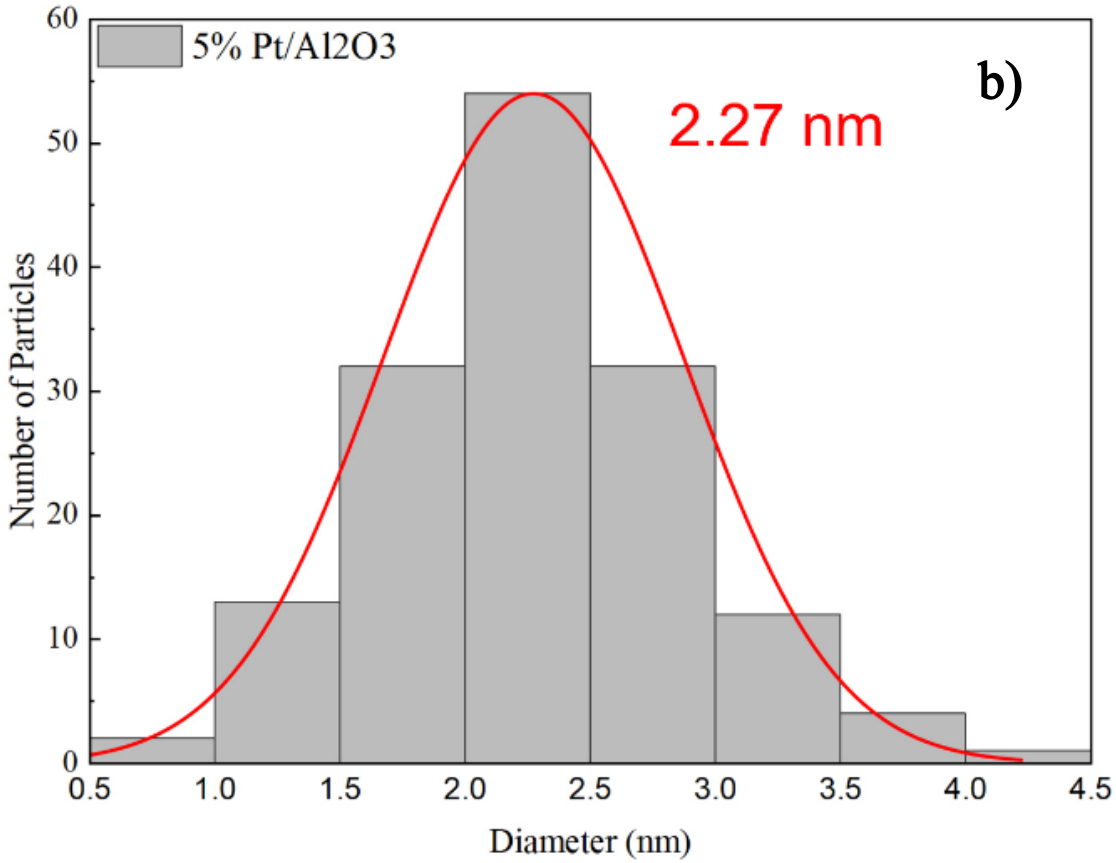

Figure A.3. Mean diameter of (a) Pd/Al_2O_3 and (b) Pt/Al_2O_3 nanoparticles.

A.2. Transition State Analysis, ALD-1 Hydrogenation

All transition states were identified using the improved dimer method.[2,3] Initial guess structures were constructed by linearly interpolating the positions of the atoms from the coordinates of the optimized intermediates. These structures were then subjected to vibrational analysis to identify the dimer axis, a vector along the potential energy surface (PES) corresponding to an imaginary vibration mode associated with bond formation. Constrained optimizations were then carried out along the dimer axis until a transition state was identified, with a trial step size of ±0.01 Å. All optimized structures were then subjected to a second round of vibrational analysis to confirm the presence of a single order saddle point on the PES. Due to the length of the adsorbate's branching chain, low-intensity imaginary frequencies corresponding to methyl group rotations were neglected. Complete raw data sets for chain hydrogenation, ring hydrogenation, and the total minimum energy path are provided in **Tables A.2**, **A.3**, and **A.4**, respectively.

Chain Hyd.	Pd(111) (kJ mol^{-1})	Pt(111) (kJ mol^{-1})	Ru(0001) (kJ mol^{-1})
A	0.0	0.0	0.0
A➞Bα	21.9	33.9	48.8
A➞Bβ	108.5	131.8	163.9
Bα	3.2	-27.3	-43.5
Bβ	86.1	33.3	-41.4
Bα→C	46.5	33.9	32.7
Bβ→C	109.9	64.7	22.0
C	-47.5	-91.3	-36.9

Table A.2. Relative ground state energies of all chain hydrogenation elementary steps over Pd(111), Pt(111), and Ru(0001). Cells marked with arrows (➞) correspond to transition states between two stable intermediates. Steps on the minimum energy path are highlighted in light blue for Pd(111), light orange for Pt(111), and light red for Ru(0001).

Ring Hyd.	Pd(111) (kJ mol^{-1})	Pt(111) (kJ mol^{-1})	Ru(0001) (kJ mol^{-1})
A	0.0	0.0	0.0
A→B2	57.6	114.0	86.4
A→B3	105.7	69.0	138.1
A→B4	76.6	77.4	79.6
A→B5	96.1	70.0	79.0
B2	32.0	61.4	55.4
B3	90.3	-15.3	122.5
B4	16.5	52.3	37.2
B5	23.7	31.4	0.1
B2→C$_{ORTHO}$	69.1	97.1	134.0
B3→C$_{ORTHO}$	392.1	205.5	135.4
B4→C$_{PARA}$	104.7	189.3	122.6
B5→C$_{PARA}$	67.2	114.0	87.0
C$_{ORTHO}$	-10.8	4.5	14.0
C$_{PARA}$	11.4	60.6	8.3
C$_{PARA}$ →D2	314.1	326.0	141.4
C$_{PARA}$→D3	36.1	208.3	109.7
C$_{ORTHO}$ →D4	51.4	78.4	92.5
C$_{ORTHO}$ →D5	66.2	65.4	93.2
D2	135.7	62.0	39.6
D3	-18.5	49.1	81.0
D4	-44.3	7.4	38.2
D5	-7.0	44.1	62.6
D2→E	180.0	134.9	221.7
D3→E	58.1	146.8	95.7
D4→E	42.8	99.7	91.7
D5→E	68.2	136.8	364.6
E	-2.2	33.7	-17.0

Table A.3. Relative ground state energies of all ring hydrogenation elementary steps over Pd(111) and Pt(111). Cells marked with arrows (→) correspond to transition states between two stable intermediates. Steps on the minimum energy path are highlighted in light blue for Pd(111), light orange for Pt(111), and light red for Ru(0001).

Total Hyd.	Pd(111) (kJ mol^{-1})	Pt(111) (kJ mol^{-1})	Ru(0001) (kJ mol^{-1})
ALD-1 (g) + 3H_2 (g) + *	0.0	0.0	0.0
ALD-1* + 2H* + 2H_2 (g)	-249.1	-253.4	-270.9
(A→Bα) + 2H_2 (g)	-215.2	-231.5	-222.1
Bα + 2H_2 (g)	-276.4	-250.2	-314.4
(Bα→C) + 2H_2 (g)	-215.2	-206.9	-238.3
ALD-2* + 2H_2 (g)	-340.4	-300.9	-307.9
ALD-2* + 4H*	-411.3	-434.9	-383.6
A→B2 / A→B5	-353.7	-320.9	-304.6
B2 / B5	-379.3	-373.6	-383.5
B2→C$_{ORTHO}$ / B5→C$_{PARA}$	-342.2	-337.8	-296.7
C$_{ORTHO}$ / C$_{PARA}$	-422.1	-430.5	-375.3
C$_{ORTHO}$→D4 / C$_{PARA}$→D3	-359.9	-356.6	-273.9
D4 / D3	-455.6	-427.5	-302.7
D4→E / D3→E	-368.5	-335.3	-288.0
ALD-3*	-413.4	-401.3	-400.6
ALD-3 (g) + *	-287.1	-287.1	-287.1

Table A.4. Relative ground state energies of all elementary steps on the minimum energy pathway associated with the hydrogenation of ALD-1 to ALD-3 over Pd(111) and Pt(111). Cells marked with arrows (➞) correspond to transition states between two stable intermediates. Steps associated with chain hydrogenation and ring hydrogenation are highlighted in pink and cream, respectively.

A.3. DDEC6 Raw Data

DDEC6 analysis[4,5] was conducted throughout **Chapter 3** (**Figures A.4** to **A.6**) and **Chapter 4** (**Figures A.7** and **A.10**). The Cartesian coordinates (x, y, z) and partial charges (q) of all adsorbates are given in **Tables A.5** to **A.11**. Due to the ease with which charge can be distributed across atoms in a metal slab, the metal atoms remained effectively neutral, regardless of adsorbate. In all calculations, the partial charge magnitude $|q|$ of every Pd, Pt, and Ru atom in the system was less than 0.05 units of elementary charge. As such, the partial charges of these elements were neglected for brevity.

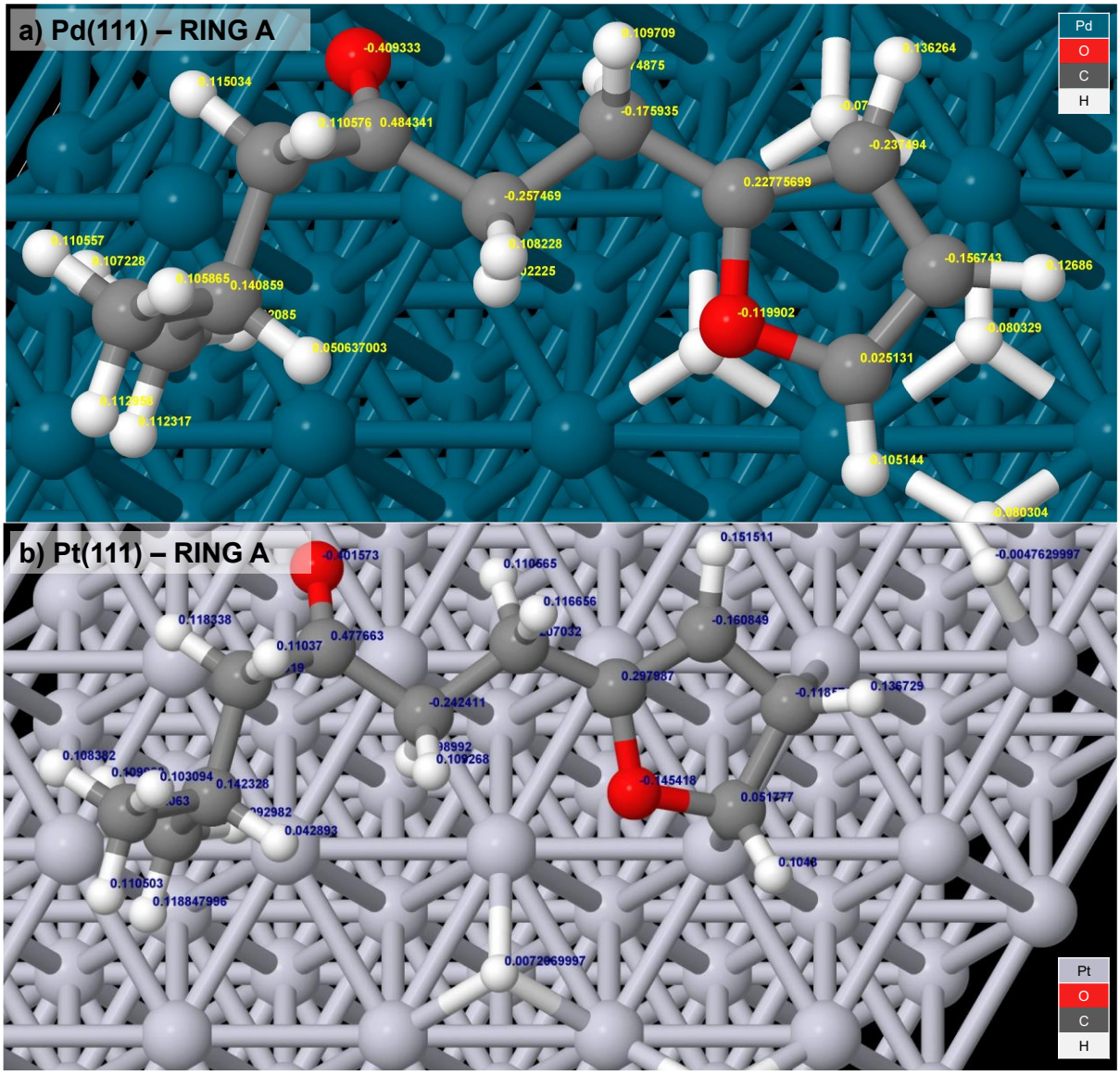

Figure A.4. DDEC6 raw data for the initial ring hydrogenation state over (a) Pd(111) and (b) Pt(111).

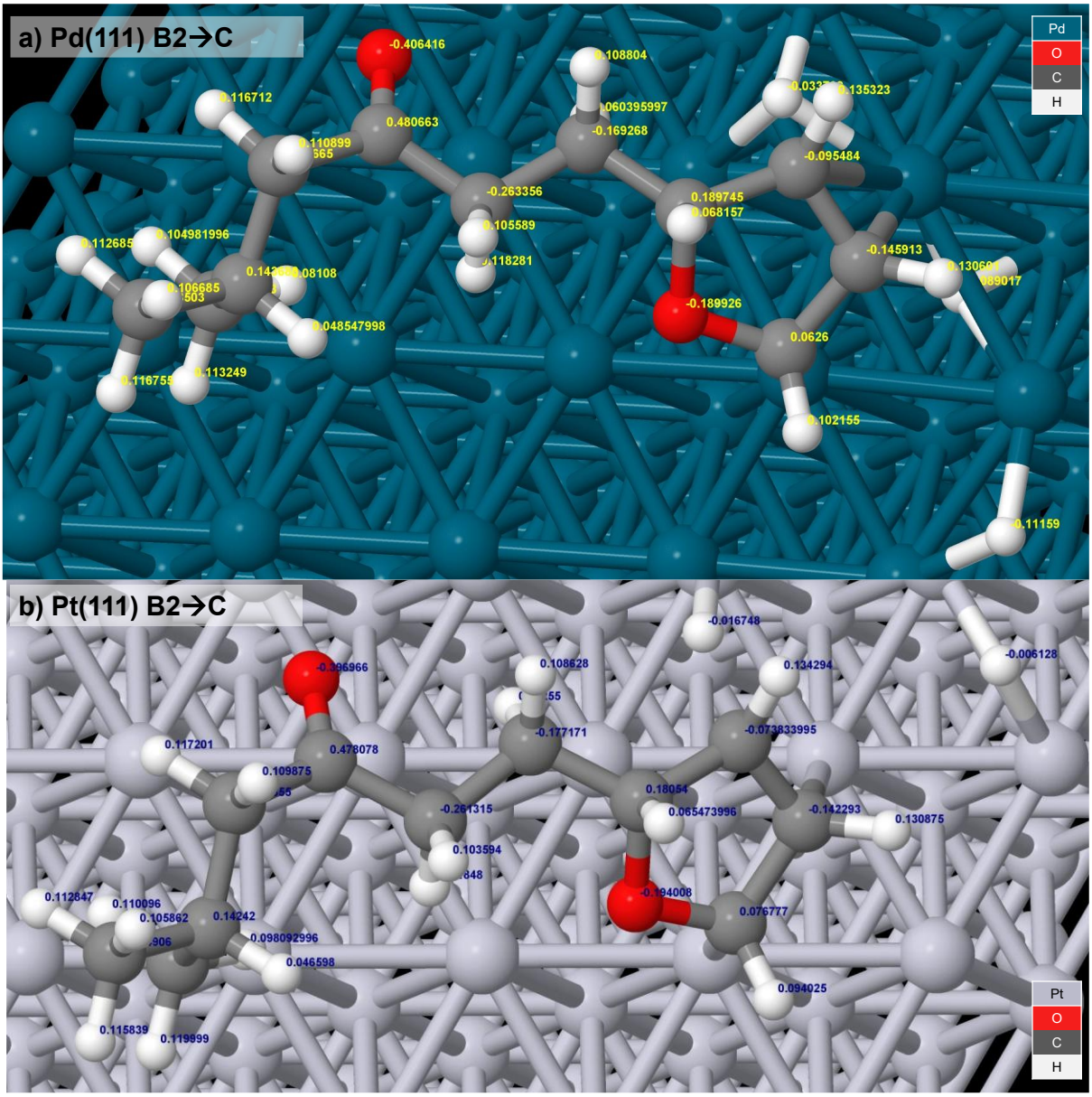

Figure A.5. DDEC6 raw data for the B2→C ring hydrogenation transition state over (a) Pd(111) and (b) Pt(111).

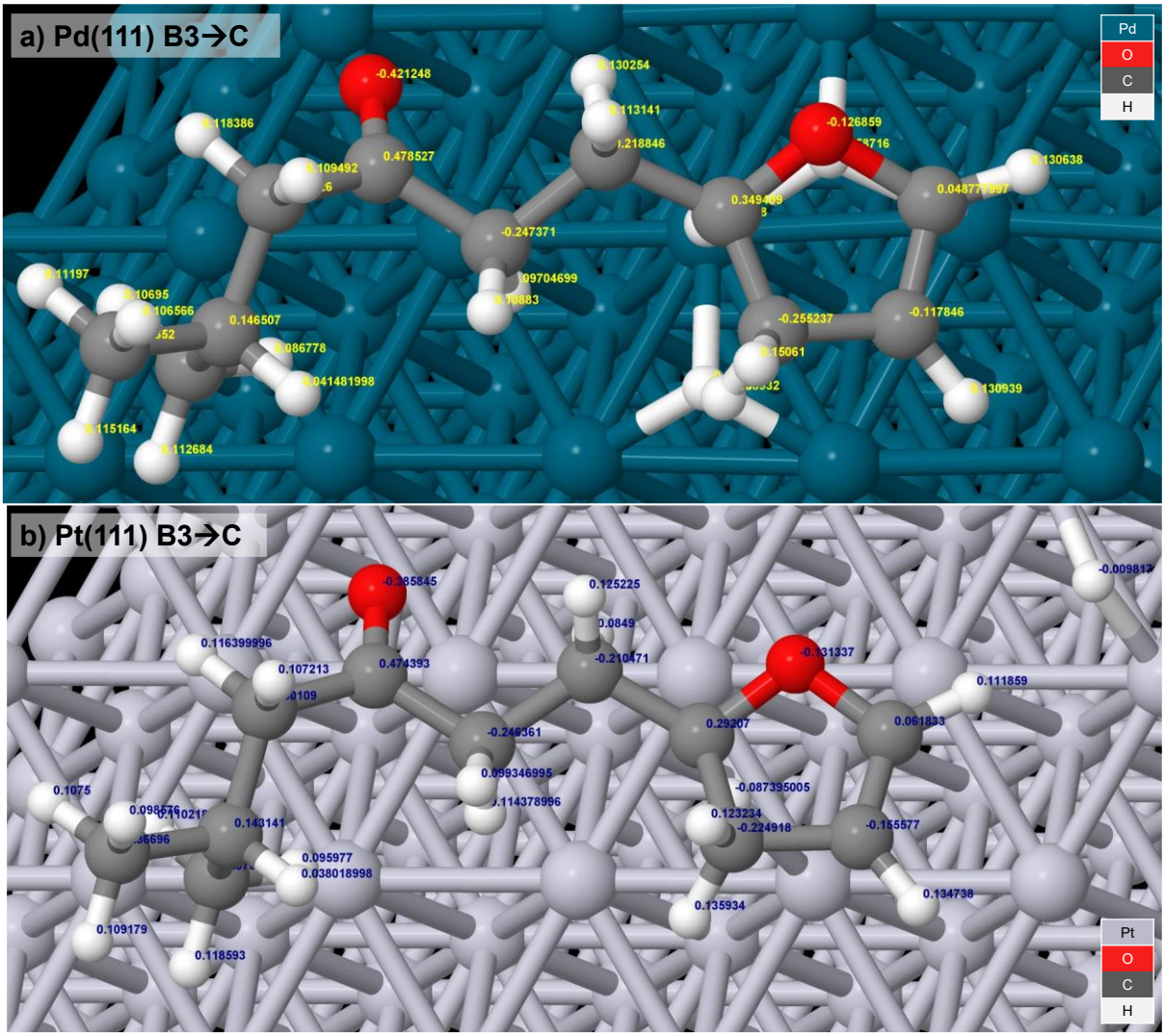

Figure A.6. DDEC6 raw data for the B3→C ring hydrogenation transition state over (a) Pd(111) and (b) Pt(111).

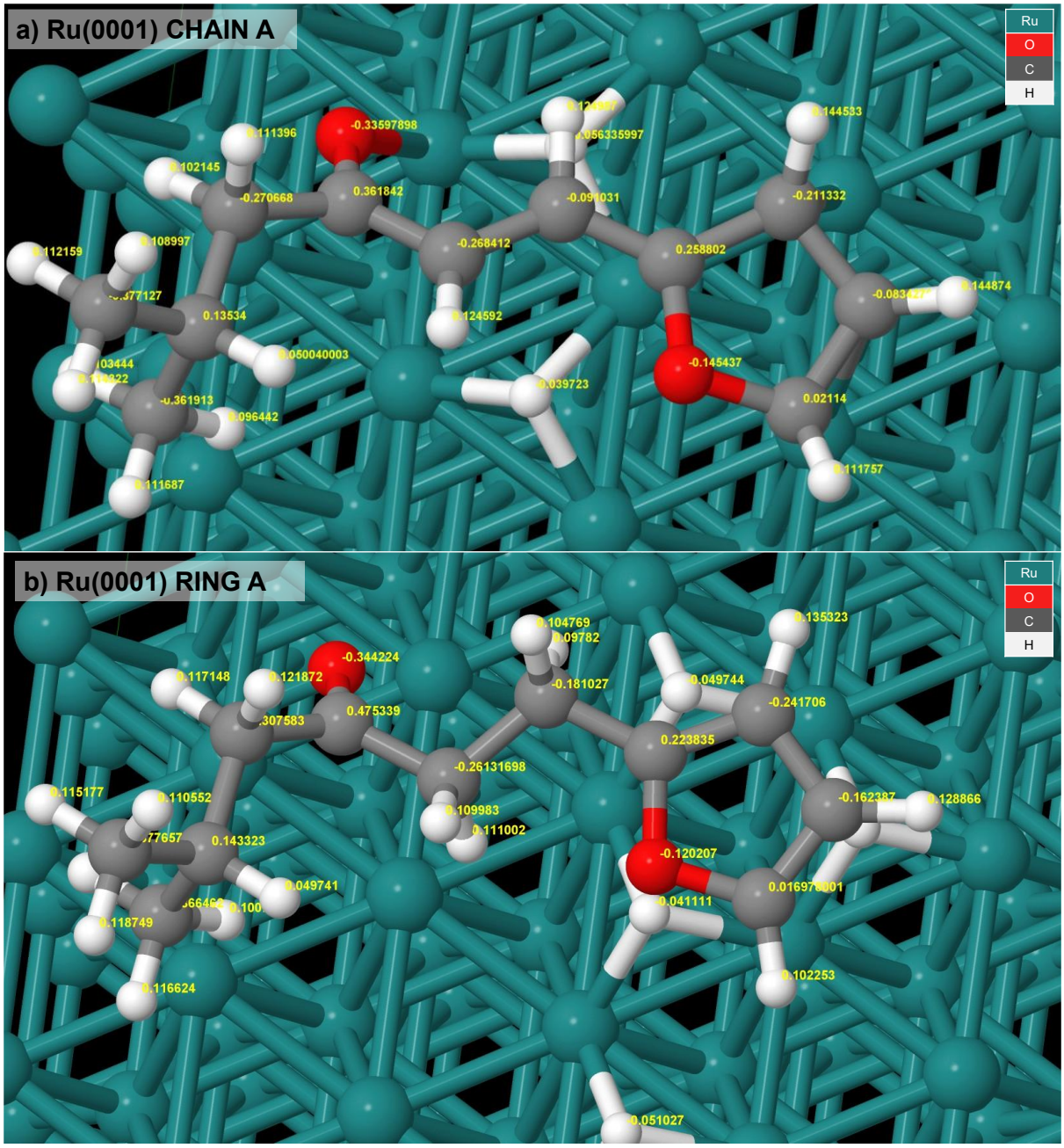

Figure A.7. DDEC6 raw data for the initial states for (a) chain and (b) ring hydrogenation over Ru(0001).

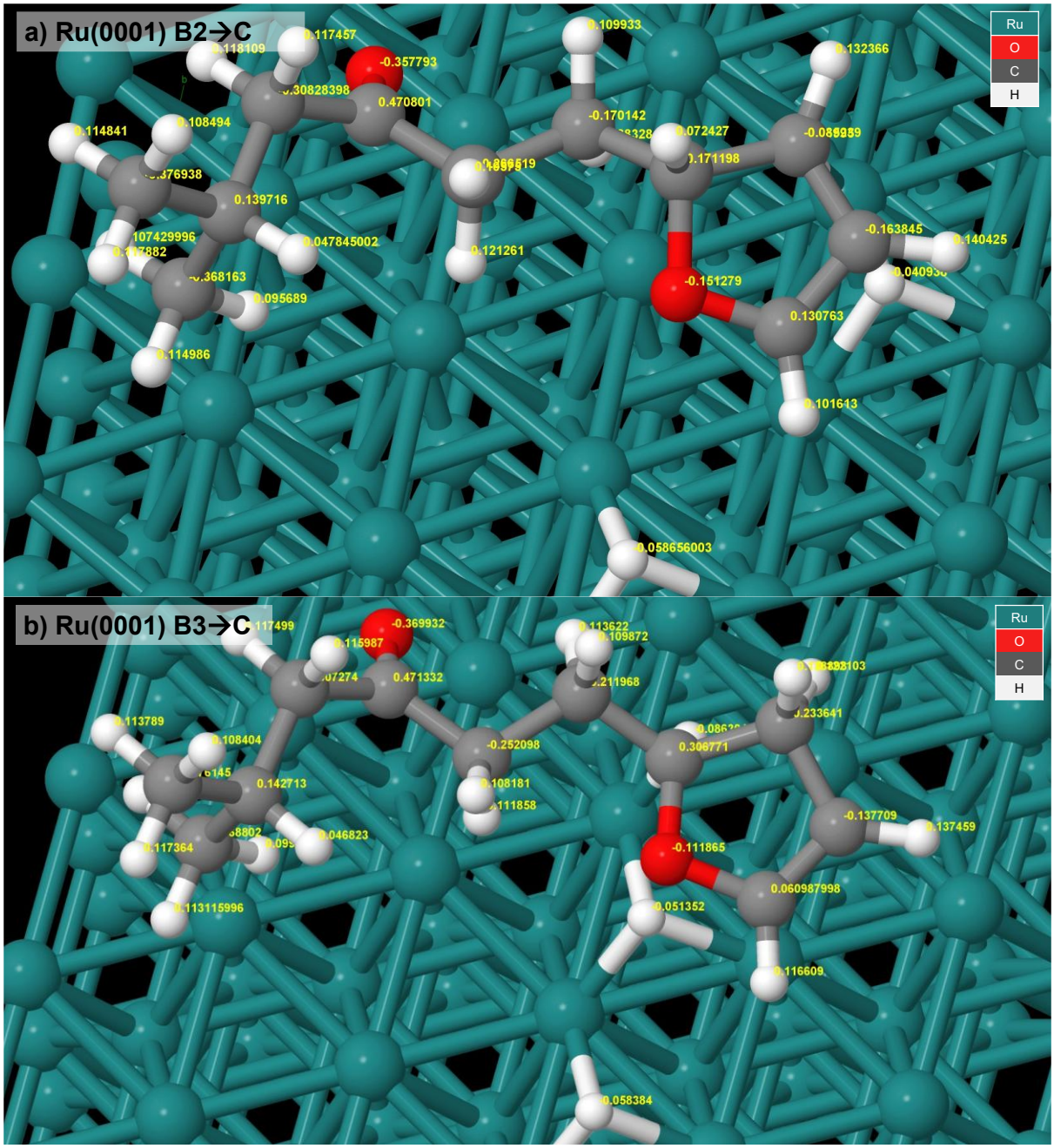

Figure A.8. DDEC6 raw data for the initial states for the (a) B2→C and (b) B3→C ortho ring hydrogenation transition states over Ru(0001).

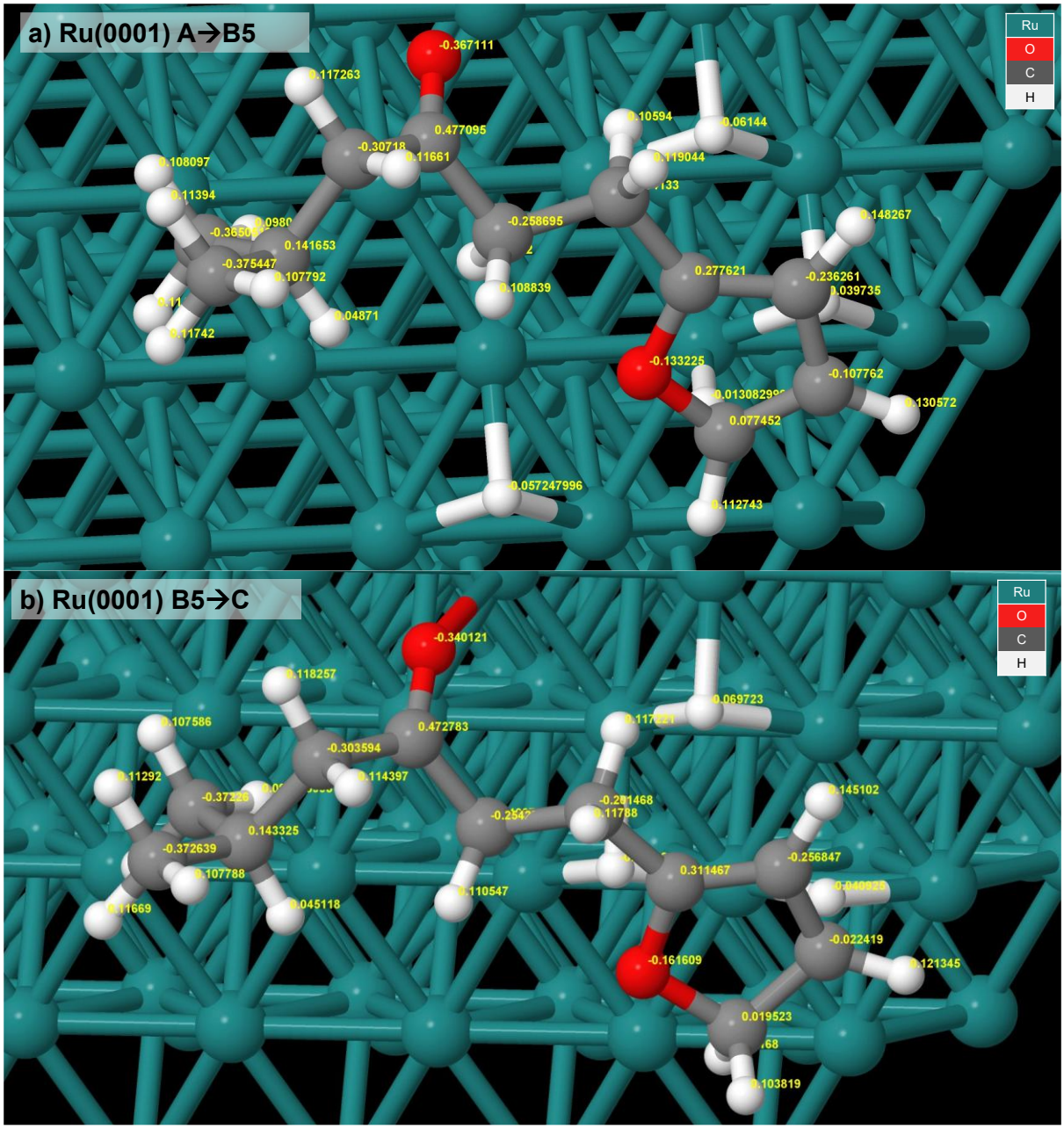

Figure A.9. DDEC6 raw data for the initial states for the (a) A→B5 and (b) B5→C para ring hydrogenation transition states over Ru(0001).

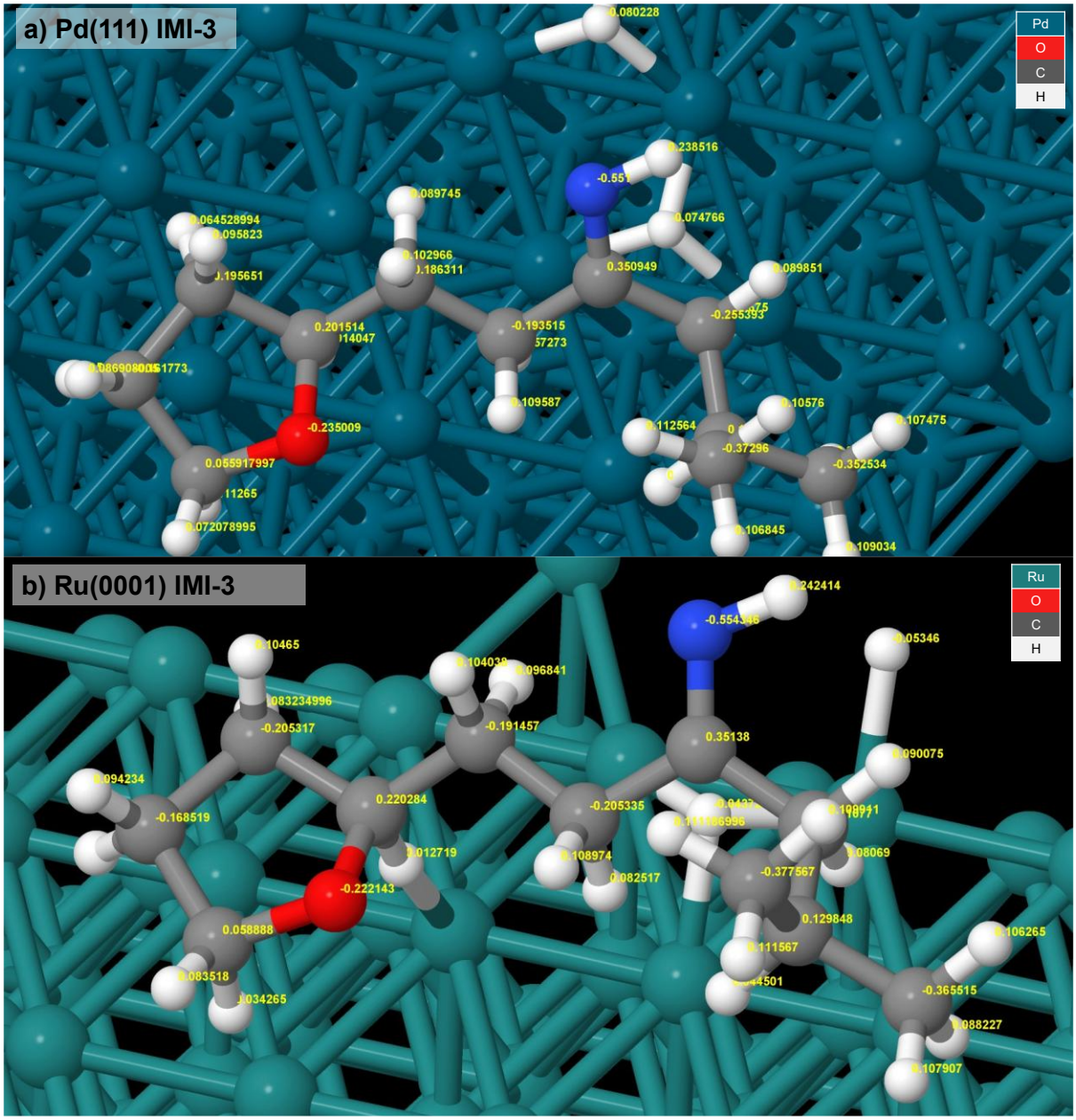

Figure A.10. DDEC6 raw data for the initial states for the IMI-3 intermediate over (a) Pd(111) and (b) Ru(0001).

A.3.1. Pd(111) and Pt(111) Hydrogenation

RING – A	Pd(111)				Pt(111)			
Element	x **(Å)**	y **(Å)**	z **(Å)**	q **(e)**	x **(Å)**	y **(Å)**	z **(Å)**	q **(e)**
O	12.84	5.78	14.68	-0.12	13.56	6.76	13.39	-0.15
O	8.86	8.62	13.99	-0.41	9.47	9.66	13.58	-0.40
C	7.53	6.00	15.91	0.14	8.10	6.71	15.25	0.14
C	8.03	7.47	15.94	-0.30	8.50	8.21	15.22	-0.30
C	10.38	7.00	14.92	-0.26	10.84	7.76	14.08	-0.24
C	9.07	7.78	14.87	0.48	9.58	8.62	14.23	0.48
C	11.6	7.91	14.69	-0.18	12.08	8.68	13.97	-0.21
C	6.87	5.68	14.55	-0.37	7.60	6.25	13.88	-0.37
C	6.55	5.76	17.07	-0.37	7.02	6.49	16.33	-0.37
C	12.90	7.16	14.67	0.23	13.33	8.11	13.39	0.30
C	14.22	7.56	14.6	-0.24	14.50	8.83	13.10	-0.16
C	15.01	6.36	14.54	-0.16	15.57	7.89	12.76	-0.12
C	14.13	5.31	14.58	0.03	14.87	6.54	12.76	0.05
H	8.40	5.34	16.03	0.05	8.99	6.11	15.52	0.04
H	8.49	7.66	16.93	0.11	8.88	8.49	16.22	0.11
H	7.18	8.16	15.81	0.12	7.62	8.83	15.02	0.12
H	10.33	6.26	14.10	0.10	10.72	7.19	13.14	0.10
H	10.47	6.44	15.86	0.11	10.94	7.03	14.89	0.11
H	11.47	8.45	13.74	0.07	12.33	9.07	14.98	0.12
H	11.65	8.69	15.47	0.11	11.81	9.55	13.36	0.11
H	6.51	4.64	14.52	0.11	7.29	5.20	13.88	0.12
H	6.01	6.35	14.36	0.11	6.75	6.86	13.54	0.11
H	7.58	5.82	13.72	0.08	8.39	6.35	13.11	0.09
H	7.04	5.95	18.04	0.11	7.38	6.81	17.33	0.10
H	5.68	6.42	16.99	0.11	6.12	7.08	16.09	0.11
H	6.20	4.72	17.07	0.11	6.74	5.43	16.39	0.11
H	14.57	8.58	14.56	0.14	13.22	11.69	11.66	0.00
H	16.09	6.29	14.44	0.13	16.55	7.97	13.24	0.14
H	14.24	4.23	14.57	0.11	14.67	2.80	11.67	0.00
H	15.42	3.81	12.15	-0.08	18.15	9.68	11.81	0.00
H	12.42	5.66	12.08	-0.08	11.83	4.43	11.66	0.01
H	15.34	5.78	11.89	-0.08	14.61	9.90	13.25	0.15
H	13.81	8.12	12.04	-0.08	15.36	5.70	13.26	0.10

Table A.5. DDEC6 raw data for the initial ring hydrogenation state over Pd(111) and Pt(111).

RING – B2→C	Pd(111)				Pt(111)			
Element	x **(Å)**	y **(Å)**	z **(Å)**	q **(e)**	x **(Å)**	y **(Å)**	z **(Å)**	q **(e)**
O	12.84	5.78	14.12	-0.19	13.66	6.92	13.40	-0.19
O	8.96	8.79	14.02	-0.41	9.68	9.71	13.49	-0.40
C	7.59	6.07	15.86	0.14	8.38	6.82	15.27	0.14
C	8.01	7.56	15.86	-0.31	8.70	8.34	15.19	-0.30
C	10.43	7.14	14.98	-0.26	11.18	8.05	14.39	-0.26
C	9.11	7.92	14.87	0.48	9.84	8.77	14.28	0.48
C	11.63	7.90	14.40	-0.17	12.35	8.95	13.96	-0.18
C	7.03	5.67	14.49	-0.37	8.03	6.26	13.88	-0.37
C	6.57	5.80	16.98	-0.37	7.20	6.60	16.24	-0.37
C	12.95	7.17	14.58	0.19	13.71	8.25	14.02	0.18
C	14.24	7.69	13.96	-0.10	14.94	8.92	13.43	-0.07
C	15.00	6.52	13.61	-0.15	15.73	7.89	12.81	-0.14
C	14.09	5.37	13.59	0.06	14.89	6.63	12.78	0.08
H	8.49	5.45	16.06	0.05	9.26	6.29	15.66	0.05
H	8.38	7.83	16.87	0.11	8.96	8.69	16.21	0.11
H	7.14	8.20	15.64	0.12	7.80	8.90	14.87	0.12
H	10.29	6.20	14.40	0.12	11.13	7.18	13.71	0.12
H	10.59	6.83	16.02	0.11	11.31	7.65	15.40	0.10
H	11.46	8.08	13.32	0.06	12.40	9.85	14.59	0.11
H	11.71	8.90	14.86	0.11	12.18	9.29	12.93	0.07
H	6.73	4.61	14.45	0.11	7.77	5.19	13.92	0.12
H	6.14	6.28	14.23	0.10	7.19	6.81	13.43	0.11
H	7.77	5.83	13.69	0.08	8.89	6.36	13.18	0.10
H	6.98	6.05	17.97	0.11	7.43	6.99	17.24	0.11
H	5.67	6.41	16.83	0.11	6.30	7.12	15.87	0.11
H	6.27	4.75	16.99	0.12	6.96	5.53	16.32	0.12
H	13.74	8.38	12.54	-0.03	14.52	10.15	12.23	-0.02
H	16.07	6.39	13.80	0.13	16.79	7.79	13.08	0.13
H	14.40	4.39	13.96	0.10	14.63	2.82	11.66	0.01
H	16.69	3.03	12.17	-0.11	18.17	9.69	11.81	-0.01
H	13.16	7.10	15.68	0.07	13.96	8.07	15.09	0.07
H	15.73	5.85	10.56	-0.09	15.41	9.76	13.94	0.13
H	14.71	8.58	14.35	0.14	15.35	5.72	13.18	0.09

Table A.6. DDEC6 raw data for the B2→C ring hydrogenation transition state over Pd(111) and Pt(111).

RING – B3→C	Pd(111)				Pt(111)			
Element	x **(Å)**	y **(Å)**	z **(Å)**	q **(e)**	x **(Å)**	y **(Å)**	z **(Å)**	q **(e)**
O	13.98	8.28	14.55	-0.13	14.82	8.78	13.78	-0.13
O	8.99	8.82	14.39	-0.42	9.82	9.57	13.41	-0.39
C	7.56	6.08	16.15	0.15	8.30	6.84	15.23	0.14
C	8.08	7.54	16.21	-0.31	8.70	8.33	15.12	-0.30
C	10.45	7.06	15.16	-0.25	11.19	7.87	14.40	-0.25
C	9.16	7.89	15.19	0.48	9.89	8.66	14.24	0.47
C	11.67	8.03	15.25	-0.22	12.42	8.72	14.05	-0.21
C	7.04	5.73	14.75	-0.37	7.95	6.25	13.86	-0.37
C	6.45	5.90	17.20	-0.37	7.09	6.70	16.18	-0.37
C	12.95	7.42	14.76	0.35	13.73	7.95	13.96	0.29
C	13.48	6.11	14.90	-0.26	14.20	6.78	14.82	-0.22
C	14.87	6.19	14.34	-0.12	15.68	6.80	14.50	-0.16
C	15.17	7.55	14.12	0.05	15.96	7.99	13.95	0.06
H	8.39	5.39	16.40	0.04	9.14	6.27	15.66	0.04
H	8.51	7.72	17.21	0.11	8.94	8.71	16.13	0.11
H	7.25	8.24	16.06	0.12	7.85	8.92	14.75	0.12
H	10.48	6.58	14.15	0.10	11.13	7.00	13.71	0.11
H	10.46	6.30	15.91	0.11	11.25	7.45	15.42	0.10
H	11.48	8.90	14.65	0.13	12.44	9.63	14.67	0.13
H	11.77	8.37	16.31	0.11	12.31	9.06	13.00	0.08
H	6.66	4.70	14.70	0.11	7.65	5.20	13.92	0.12
H	6.22	6.40	14.45	0.11	7.14	6.82	13.38	0.11
H	7.84	5.82	13.99	0.09	8.82	6.30	13.17	0.10
H	6.81	6.13	18.22	0.11	7.31	7.11	17.18	0.10
H	5.60	6.57	16.98	0.11	6.22	7.25	15.77	0.11
H	6.07	4.86	17.20	0.12	6.80	5.65	16.29	0.11
H	12.88	5.39	14.31	0.14	14.04	7.02	15.90	0.12
H	15.55	5.36	14.20	0.13	16.39	6.01	14.72	0.13
H	13.40	5.72	15.94	0.15	14.63	2.82	11.66	0.01
H	16.19	7.87	13.96	0.13	18.10	9.65	11.81	-0.01
H	12.45	5.55	12.07	-0.08	13.86	7.11	12.44	-0.09
H	12.56	7.33	12.97	-0.12	13.67	5.85	14.61	0.14
H	13.81	8.10	11.92	-0.06	16.89	8.44	13.59	0.11

Table A.7. DDEC6 raw data for the B3→C ring hydrogenation transition state over Pd(111) and Pt(111).

A.3.2. Ru(0001) Hydrogenation

Ru(0001)	CHAIN – A				RING – A			
Element	x **(Å)**	y **(Å)**	z **(Å)**	q **(e)**	x **(Å)**	y **(Å)**	z **(Å)**	q **(e)**
O	12.53	5.32	11.26	-0.15	12.38	5.53	12.19	-0.12
O	9.91	9.57	10.55	-0.34	9.73	9.46	10.92	-0.34
C	7.69	7.78	12.93	0.14	7.46	7.65	13.03	0.14
C	8.56	8.96	12.44	-0.27	8.40	8.88	12.84	-0.31
C	10.62	7.60	11.71	-0.27	10.49	7.50	12.08	-0.26
C	9.73	8.67	11.51	0.36	9.55	8.67	11.87	0.48
C	11.95	7.67	11.20	-0.09	11.96	7.96	12.18	-0.18
C	6.76	7.27	11.82	-0.36	6.65	7.38	11.75	-0.37
C	6.87	8.21	14.16	-0.38	6.52	7.90	14.22	-0.38
C	12.87	6.64	10.97	0.26	12.92	6.81	12.19	0.22
C	14.32	6.74	10.65	-0.21	14.30	6.73	12.18	-0.24
C	14.73	5.35	10.45	-0.08	14.63	5.33	12.16	-0.16
C	13.54	4.51	10.66	0.02	13.44	4.64	12.16	0.02
H	8.35	6.95	13.24	0.05	8.07	6.76	13.25	0.05
H	9.00	9.47	13.32	0.11	8.87	9.10	13.81	0.12
H	7.91	9.71	11.94	0.10	7.82	9.75	12.52	0.12
H	10.65	6.13	9.44	-0.04	10.39	6.85	11.18	0.11
H	10.30	6.73	12.28	0.12	10.21	6.91	12.95	0.11
H	12.35	8.67	11.06	0.12	12.09	8.57	13.09	0.10
H	12.11	8.68	9.23	-0.06	12.19	8.61	11.32	0.10
H	6.15	6.42	12.15	0.11	5.98	6.51	11.88	0.12
H	6.08	8.08	11.48	0.10	6.03	8.25	11.48	0.11
H	7.35	6.93	10.94	0.10	7.32	7.16	10.90	0.10
H	7.52	8.49	15.00	0.11	7.08	8.05	15.16	0.11
H	6.24	9.08	13.92	0.11	5.90	8.80	14.05	0.12
H	6.21	7.40	14.50	0.11	5.84	7.04	14.36	0.12
H	14.96	7.45	11.18	0.14	14.98	7.57	12.15	0.14
H	15.74	4.98	10.70	0.14	15.62	4.89	12.12	0.13
H	13.60	3.53	11.12	0.11	13.17	3.59	12.12	0.10
H	—	—	—	—	13.46	7.80	9.55	-0.05
H	—	—	—	—	10.74	3.11	9.57	-0.05
H	—	—	—	—	12.07	5.45	9.55	-0.04
H	—	—	—	—	14.82	5.43	9.54	-0.04

Table A.8. DDEC6 raw data for the initial states for chain and ring hydrogenation over Ru(0001).

Ru(0001)	RING – B2→C				RING – B3→C			
Element	x **(Å)**	y **(Å)**	z **(Å)**	q **(e)**	x **(Å)**	y **(Å)**	z **(Å)**	q **(e)**
O	12.31	5.32	11.93	-0.15	12.49	5.67	11.78	-0.11
O	9.76	9.52	11.07	-0.36	9.70	9.61	11.17	-0.37
C	7.44	7.72	13.16	0.14	7.47	7.62	13.16	0.14
C	8.40	8.93	12.97	-0.31	8.42	8.84	13.06	-0.31
C	10.42	7.50	12.19	-0.27	10.5	7.55	12.10	-0.25
C	9.54	8.72	11.99	0.47	9.54	8.74	12.04	0.47
C	11.89	7.76	11.82	-0.17	11.96	8.02	12.07	-0.21
C	6.68	7.42	11.86	-0.37	6.69	7.42	11.84	-0.37
C	6.47	7.99	14.32	-0.38	6.49	7.80	14.34	-0.38
C	12.82	6.66	12.33	0.17	12.92	6.96	11.63	0.31
C	14.28	6.63	11.95	-0.09	14.42	6.99	11.82	-0.23
C	14.60	5.28	11.73	-0.16	14.76	5.52	11.67	-0.14
C	13.4	4.57	11.62	0.13	13.61	4.82	11.68	0.06
H	8.05	6.84	13.42	0.05	8.07	6.71	13.35	0.05
H	8.86	9.17	13.94	0.12	8.90	8.99	14.04	0.12
H	7.83	9.82	12.64	0.12	7.84	9.75	12.83	0.12
H	10.02	6.70	11.52	0.12	10.3	6.95	11.19	0.11
H	10.33	7.12	13.22	0.11	10.29	6.91	12.97	0.11
H	12.24	8.71	12.24	0.11	12.27	8.37	13.08	0.11
H	12.00	7.86	10.72	0.09	12.06	8.89	11.40	0.11
H	6.00	6.56	11.99	0.11	6.02	6.55	11.90	0.11
H	6.08	8.29	11.54	0.11	6.09	8.31	11.60	0.11
H	7.37	7.17	11.04	0.10	7.39	7.24	11.00	0.10
H	7.01	8.16	15.27	0.11	7.03	7.91	15.29	0.11
H	5.85	8.88	14.11	0.11	5.87	8.70	14.18	0.11
H	5.79	7.13	14.46	0.12	5.82	6.93	14.42	0.12
H	14.97	7.42	12.23	0.13	14.92	7.64	11.09	0.12
H	15.58	4.86	11.54	0.14	15.77	5.11	11.61	0.14
H	13.22	3.52	11.42	0.10	13.37	3.77	11.62	0.12
H	14.82	5.44	9.47	-0.04	13.18	7.50	9.81	-0.09
H	10.77	3.11	9.58	-0.06	10.75	3.10	9.57	-0.06
H	12.75	6.65	13.44	0.07	12.05	5.43	9.50	-0.05
H	14.28	7.28	10.13	-0.09	14.67	7.37	12.82	0.14

Table A.9. DDEC6 raw data for the initial states for the B2→C and B3→C ortho ring hydrogenation transition states over Ru(0001).

Ru(0001)	RING – A→B5				RING – B5→C			
Element	x **(Å)**	y **(Å)**	z **(Å)**	q **(e)**	x **(Å)**	y **(Å)**	z **(Å)**	q **(e)**
O	12.23	5.46	11.92	-0.13	12.87	5.45	12.20	-0.16
O	9.68	9.52	11.10	-0.37	10.14	9.45	10.93	-0.34
C	7.41	7.64	13.13	0.14	7.97	7.86	13.24	0.14
C	8.36	8.87	13.01	-0.31	9.03	8.98	13.01	-0.30
C	10.40	7.49	12.15	-0.26	10.92	7.45	12.02	-0.25
C	9.49	8.70	12.01	0.48	10.04	8.68	11.91	0.47
C	11.89	7.88	12.12	-0.20	12.4	7.85	12.25	-0.20
C	6.64	7.42	11.81	-0.37	7.15	7.60	11.96	-0.37
C	6.43	7.84	14.30	-0.38	7.05	8.26	14.41	-0.37
C	12.80	6.69	12.10	0.28	13.35	6.71	12.05	0.31
C	14.18	6.57	12.20	-0.24	14.7	6.74	11.70	-0.26
C	14.50	5.21	12.05	-0.11	15.12	5.40	11.49	-0.02
C	13.28	4.54	11.72	0.08	14.01	4.53	12.01	0.02
H	8.01	6.74	13.33	0.05	8.50	6.94	13.51	0.05
H	8.83	9.04	13.99	0.12	9.60	9.12	13.95	0.11
H	7.79	9.77	12.74	0.12	8.53	9.93	12.76	0.12
H	10.19	6.84	11.28	0.11	10.84	6.92	11.05	0.11
H	10.16	6.91	13.06	0.11	10.58	6.78	12.81	0.11
H	12.14	8.52	12.98	0.12	12.52	8.26	13.27	0.12
H	12.07	8.49	11.21	0.11	12.68	8.65	11.55	0.12
H	5.97	6.55	11.87	0.11	6.39	6.82	12.14	0.12
H	6.04	8.30	11.55	0.11	6.63	8.51	11.63	0.11
H	7.35	7.24	10.98	0.10	7.79	7.26	11.13	0.10
H	6.97	7.95	15.26	0.11	7.63	8.43	15.33	0.11
H	5.81	8.74	14.15	0.11	6.50	9.18	14.18	0.11
H	5.76	6.97	14.39	0.12	6.32	7.46	14.61	0.12
H	14.87	7.40	12.33	0.15	15.27	7.64	11.51	0.15
H	15.49	4.76	12.01	0.13	14.88	5.19	9.77	-0.04
H	13.02	3.51	11.95	0.11	13.68	3.72	11.34	0.09
H	13.47	7.79	9.55	-0.06	13.41	7.80	9.54	-0.07
H	10.75	3.10	9.58	-0.06	14.25	4.11	13.01	0.10
H	13.25	4.41	10.29	-0.01	12.10	5.43	9.56	-0.06
H	14.83	5.46	9.49	-0.04	16.16	5.07	11.48	0.12

Table A.10. DDEC6 raw data for the initial states for the A→B5 and B5→C para ring hydrogenation transition states over Ru(0001).

A.3.3. Pd(111) and Ru(0001) Amination

IMI-3	Pd(111)				Ru(0001)			
Element	x **(Å)**	y **(Å)**	z **(Å)**	q **(e)**	x **(Å)**	y **(Å)**	z **(Å)**	q **(e)**
N	12.66	8.52	15.62	-0.55	8.79	10.69	12.93	-0.55
O	9.67	4.54	15.11	-0.24	10.39	6.01	12.21	-0.22
C	15.02	5.66	15.27	0.13	12.48	10.91	12.62	0.13
C	14.50	7.05	14.84	-0.26	11.07	11.33	12.15	-0.26
C	12.00	6.37	14.72	-0.19	10.20	8.90	12.11	-0.21
C	13.05	7.40	15.13	0.35	9.94	10.35	12.46	0.35
C	10.55	6.82	14.94	-0.19	8.96	8.00	12.22	-0.19
C	14.93	5.48	16.80	-0.37	12.52	10.69	14.14	-0.38
C	16.46	5.48	14.78	-0.35	13.51	11.97	12.19	-0.37
C	9.52	5.81	14.45	0.20	9.20	6.60	11.68	0.22
C	8.04	6.19	14.65	-0.20	8.08	5.56	11.89	-0.21
C	7.32	4.81	14.74	-0.16	8.83	4.21	12.00	-0.17
C	8.49	3.80	14.75	0.06	10.31	4.62	11.86	0.06
H	14.39	4.89	14.78	0.04	12.74	9.96	12.12	0.04
H	14.63	7.11	13.73	0.07	11.09	11.45	11.05	0.08
H	15.15	7.83	15.27	0.09	10.82	12.32	12.57	0.09
H	12.19	5.42	15.26	0.11	11.00	8.51	12.76	0.11
H	12.17	6.12	13.65	0.06	10.62	8.85	11.09	0.08
H	10.38	7.77	14.39	0.09	8.13	8.44	11.64	0.10
H	10.38	7.04	16.00	0.10	8.62	7.94	13.26	0.10
H	15.30	4.49	17.10	0.11	13.53	10.38	14.47	0.11
H	15.54	6.24	17.31	0.11	12.27	11.63	14.67	0.11
H	13.89	5.58	17.16	0.11	11.80	9.93	14.47	0.11
H	16.52	5.60	13.68	0.07	13.49	12.12	11.09	0.09
H	17.13	6.23	15.23	0.11	13.29	12.94	12.66	0.11
H	16.85	4.48	15.03	0.11	14.53	11.67	12.47	0.11
H	7.92	6.77	15.58	0.10	7.53	5.80	12.81	0.10
H	6.66	4.63	13.88	0.06	8.54	3.51	11.20	0.08
H	8.38	2.97	15.47	0.07	11.02	4.06	12.50	0.08
H	6.71	4.74	15.65	0.09	8.64	3.72	12.96	0.09
H	9.69	5.63	13.34	-0.01	9.38	6.70	10.54	0.01
H	7.67	6.80	13.81	0.06	7.36	5.59	11.05	0.08
H	8.64	3.37	13.73	0.01	10.66	4.49	10.79	0.03
H	13.47	9.12	15.83	0.24	8.76	11.70	13.11	0.24
H	13.86	8.05	12.07	-0.07	8.00	12.40	9.57	-0.05
H	12.46	10.49	12.17	-0.08	9.34	10.05	9.54	-0.04

Table A.11. DDEC6 raw data for the IMI-3 intermediate over Pd(111) and Ru(0001).

A.4. Transition State Analysis, Amination

To ensure consistency across the reaction profile for reductive amination, the same dimer method settings were used for both the hydrogenation (**Section A.2**) and amination steps.

Ketone → Hemi	Pd(111) (kJ mol^{-1})	Ru(0001) (kJ mol^{-1})
A	0	0
A→BN	196.5	97.9
BN	158.9	6.94
BN→C	184.8	187.2
BO→C		
C	35.0	70.3

Table A.12. Relative ground state energies of all elementary steps associated with the dehydrogenation of ALD-3 to HEM-3 over Pd(111) and Ru(0001). Cells marked with arrows (→) correspond to transition states between two stable intermediates.

Hemi → Imine	Pd(111) (kJ mol^{-1})	Ru(0001) (kJ mol^{-1})
A	0.0	0.0
A→B	78.9	83.9
B	21.5	-73.5

Table A.13. Relative ground state energies of all elementary steps associated with the dehydrogenation of HEM-3 to IMI-3 over Pd(111) and Ru(0001). Cells marked with arrows (→) correspond to transition states between two stable intermediates.

Imine → Amine	Pd(111) (kJ mol^{-1})	Ru(0001) (kJ mol^{-1})
A	0.0	0.0
A➞BN	50.9	58.7
A➞BC	245.1	152.4
BN	-41.9	-7.5
BC	151.1	-40.1
BN→C	40.1	75.6
BC→C	208.1	217.6
C	13.4	11.2

Table A.14. Relative ground state energies of all elementary steps associated with the hydrogenation of IMI-3 to AMI-3 over Pd(111) and Ru(0001). Cells marked with arrows (➞) correspond to transition states between two stable intermediates. Steps on the minimum energy path are highlighted in light blue for Pd(111) and light red for Ru(0001).

A.5. Experimental Analysis, SA Pyrolysis

A.5.1. Preparation of Reagents

Nanosized ceria (99.5%) and SA (≥98%) were purchased from Sigma-Aldrich. CeO_2 was pre-calcined at 500 °C for 2 h to remove organic matter. A series of SA/CeO_2 samples (0.1, 0.3, 0.6, 0.9, and 1.2 mmol g^{-1}) were prepared by impregnating CeO_2 (100 mg) with SA ethanolic solution (2 mL). The suspensions were stirred and dried at room temperature in air. SA was immobilized on the catalyst's surface in concentrations of 0.1 – 1.2 mmol g^{-1}.

A.5.2. Spectroscopic Details

In situ diffuse reflectance Fourier-transform infrared (DRIFTS) spectroscopy was conducted using a Thermo Nicolet Nexus FT-IR spectrometer equipped with a Nexus Smart Collector. Spectra were recorded from 20 °C to 470 °C at intervals of 30 °C. All spectra were recorded over a range of 4000 – 400 cm^{-1}. The spectroscopic resolution was ±4 cm^{-1}, the total number of scans was 50, and the scan velocity was 0.5 cm s^{-1}. Before any FT-IR spectra were taken, the CeO_2 and SA/CeO_2 samples were mixed with KBr (≥ 99%, Alfarus, Kyiv, Ukraine) in a 1:10 ratio. Pure SA was mixed with KBr at a ratio of 1:100. KBr was pre-calcined at 500°C for 2 h.

TPD-MS spectra were taken with an MX-7304 monopole mass spectrometer (Electron, Sumy, Ukraine) with an electron ionization beam, re-equipped for thermal desorption measurements.[31] At the beginning of each reading, 15 mg samples were placed in a quartz-molybdenum ampoule and pumped at room temperature to a pressure of 5×10^{-5} Pa. Heating was increased from room temperature to 750 °C at a programmed linear rate of 0.17°C s^{-1}. Volatile thermolysis products entered the ionization chamber of the mass spectrometer and were ionized and fragmented under the action of electrons. The range of the investigated masses was 1 – 220 a.m.u. The slow heating of the sample and the high pumping rate of volatile thermolysis products made it possible to neglect diffusion effects. Under these conditions, the intensity of the ion current was proportional to the rate of desorption.

Thermogravimetric analysis (TGA) and differential thermal analysis (DTA) were conducted using a TGA/DTA analyzer (Q-1500D, Budapest, Hungary). 100 mg samples were heated from room temperature to 1000 °C in an air atmosphere at a linear rate of 10 °C min^{-1}.

A.5.3. Thermal Analysis

As shown in **Figure A.11**, the TG and DTG plots plateaued at 450 °C, suggesting that the bulk of thermal decomposition occurs before this temperature is reached. 87.8% of the SA was converted into volatile products, with the remaining 12.2% being converted into coal. Supplemental temperature programmed desorption (TPD) plots are provided in **Figure A.12**. As shown in **Figure A.13**, the vapour pressure during pyrolysis was at its highest between 250 and 450 °C, suggesting that gasification of the products was at its most intense in this temperature range.

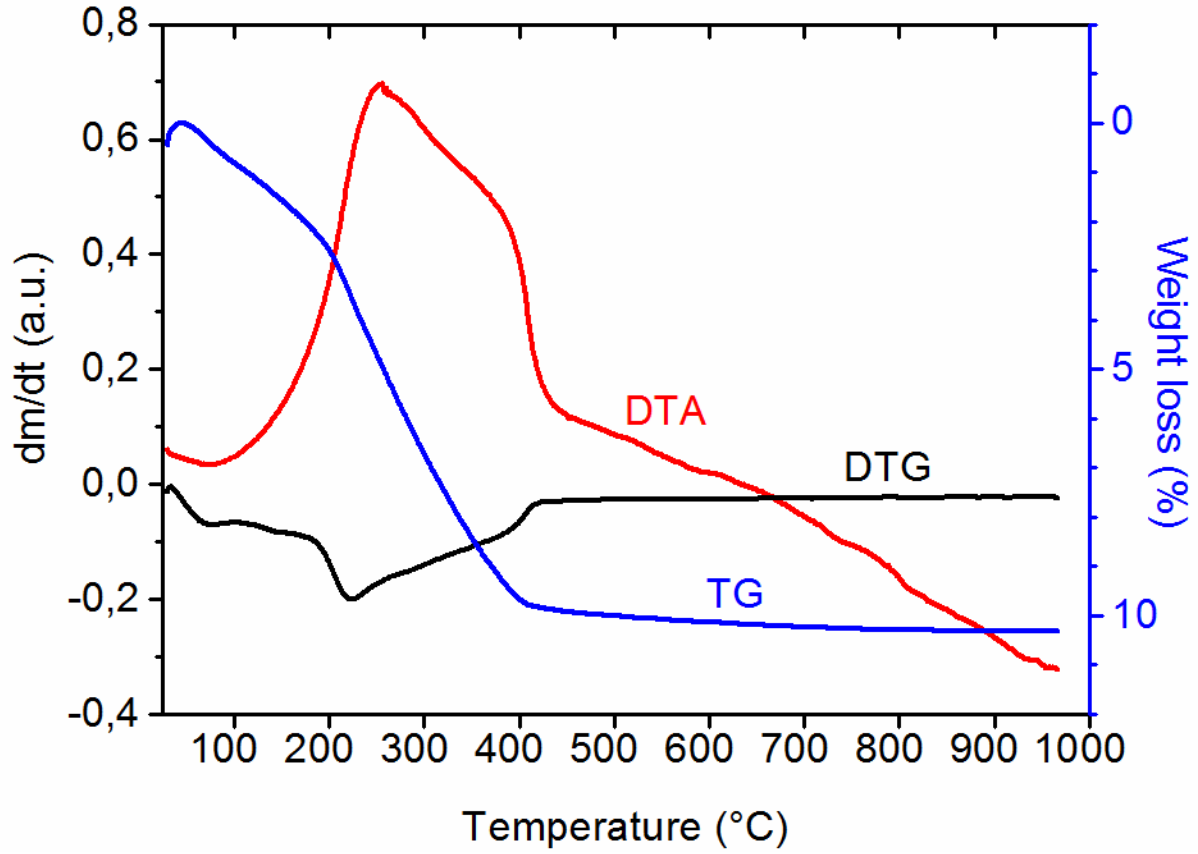

Figure A.11. Differential thermal analysis (DTA, red), differential thermogravimetric analysis (DTG, black), and thermogravimetric (TG, blue) plots for SA over CeO_2.

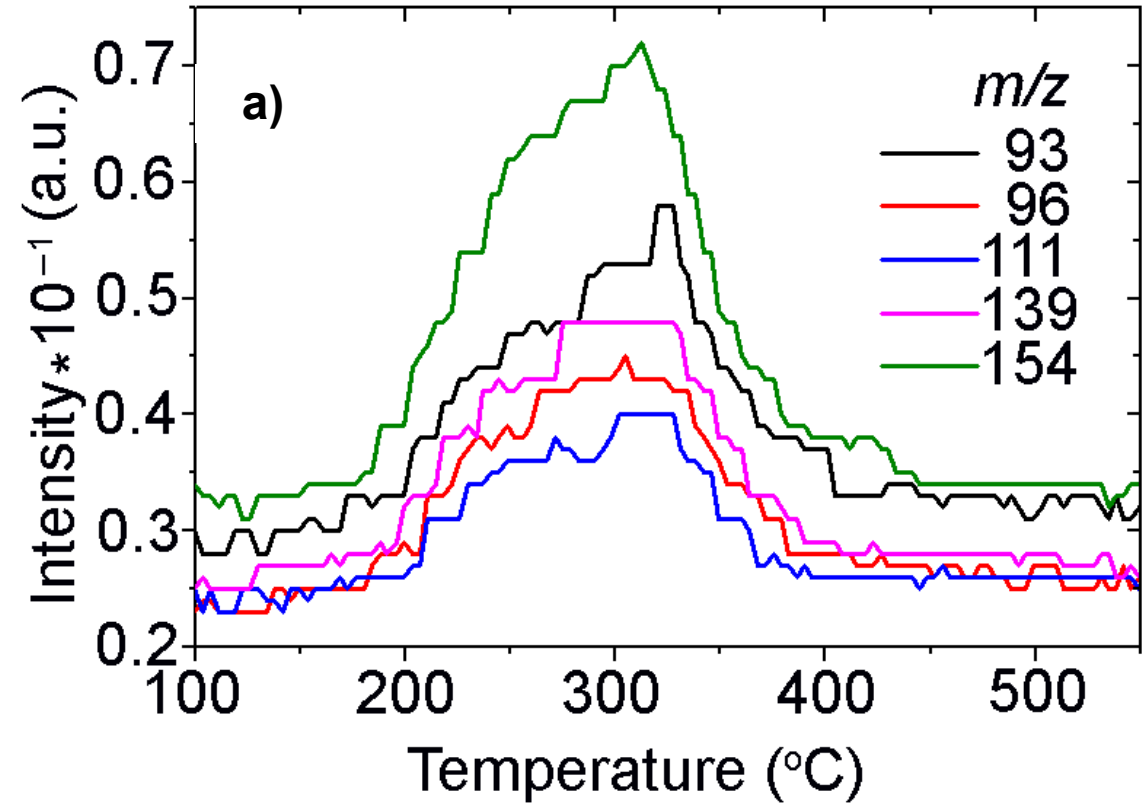
a)
m/z
93
96
111
139
154
Intensity∗10⁻¹ (a.u.)
0.7
0.6
0.5
0.4
0.3
0.2
100
200
300
400
500
Temperature (°C)

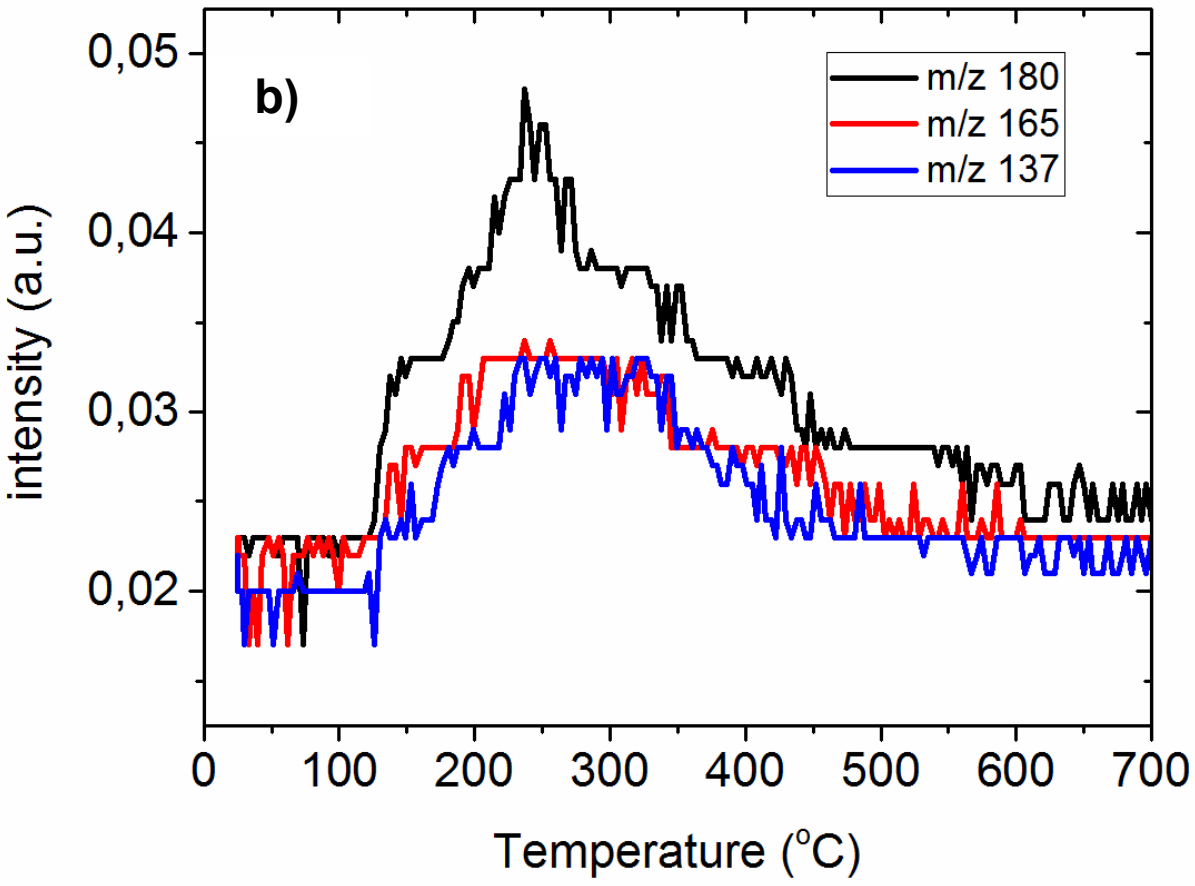
b)
m/z 180
m/z 165
m/z 137
intensity (a.u.)
0,05
0,04
0,03
0,02
0
100
200
300
400
500
600
700
Temperature (°C)

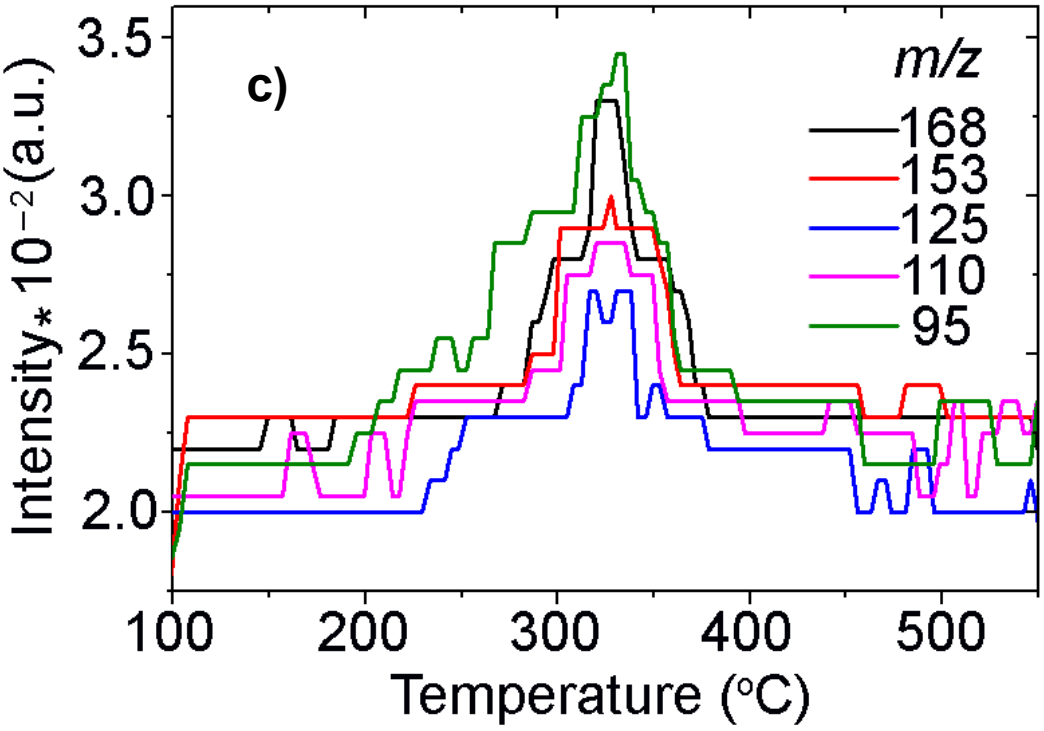

Figure A.12. TPD curves for each ion by their mass-to-charge ratio: (a) 154, 139, 111, 96, 93; (b) 180,165, 137; (c) 168, 153, 125, 110, 95.

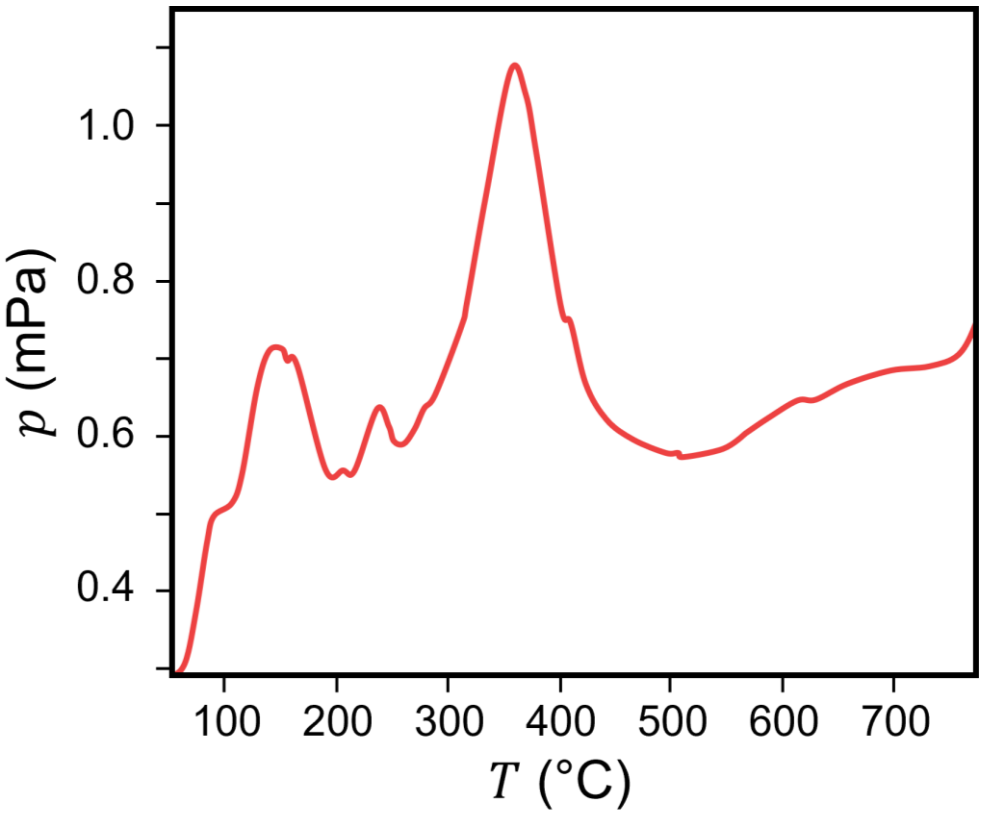

Figure A.13. Vapour pressure of the pyrolysis products as a function of temperature.

A.5. References

1. C. A. Schneider, W. S. Rasband and K. W. Eliceiri, *Nat. Methods*, **2012**, 9, 671–675.
2. A. Heyden, A. T. Bell and F. J. Keil, *J. Chem. Phys.*, **2005**, 123, 224101.
3. G. Henkelman and H. Jónsson, *J. Chem. Phys.*, **1999**, 111, 7010–7022.
4. T. A. Manz and N. Gabaldon Limas, *RSC Adv.*, **2016**, 6, 47771–47801.
5. N. Gabaldon Limas and T. A. Manz, *RSC Adv.*, **2016**, 6, 45727–45747.